

First Principles investigation on the electronic, phononic and electrocatalytic properties of 2D- dichalcogenide materials



Thesis submitted by

Arnab Das

Index No.: D-7/ISLM/33/2020

**School of Materials Science and
Nanotechnology**

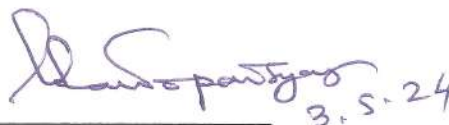
**Faculty of Interdisciplinary studies,
Law and Management (FISLM)**

Jadavpur University

Kolkata, India

CERTIFICATE FROM THE SUPERVISOR

This is to certify that the thesis entitled "**First Principles Investigation on the Electronic, Phononic, and Electrocatalytic Properties of 2D-Dichalcogenide Materials,**" submitted by Arnab Das, who registered on 04.12.2020, for the Ph.D. degree at the School of Materials Science and Nanotechnology of Jadavpur University, is entirely based on his own original work conducted under the supervision of Prof. (Dr.) Kalyan Kumar Chattopadhyay of Jadavpur University. Furthermore, I affirm that neither the thesis nor any part of it has been previously submitted for any degree, diploma, or other academic award elsewhere.



Signature of the Supervisor and

date with Official Seal

3.5.24
Dr. K. K. Chattopadhyay
Professor
Department of Physics
Jadavpur University
Kolkata-700 032

“Statement of Originality”

I, Arnab Das, registered on 04.12.2020, do hereby declare that the thesis entitled "**First Principles Investigation on the Electronic, Phononic, and Electrocatalytic Properties of 2D-Dichalcogenide Materials**" contains both literature survey and original research work conducted by myself as part of my doctoral studies.

All information presented in this thesis has been obtained and presented in accordance with existing academic rules and ethical conduct. I affirm that, as required by these rules and conduct, I have fully cited and referenced all materials and results that are not original to this work.

Furthermore, I affirm that I have thoroughly checked this thesis in accordance with the "Policy on Anti-Plagiarism, Jadavpur University, 2019," and the level of similarity, as assessed by the iThenticate software, is 3%.

Signature of Candidate:

Arnab Das

Date: 3.05.24

Certified by Supervisor:

(Signature with date, seal)

K. K. Chattopadhyay
3.5.24

Prof. Kalyan Kumar Chattopadhyay

Department of Physics,

School of Materials Science and Nanotechnology,

Jadavpur University, Kolkata-700032

Dr. K. K. Chattopadhyay
Professor
Department of Physics
Jadavpur University
Kolkata-700 032

Dedicated to my Late Father, Anupam Das

Table of Contents

Acknowledgements	4
List of Publications	5
Abstract:	6
1. Introduction and Objectives:	8
1.1. Introduction to low dimensional materials:.....	8
1.1.1. Advantages of low dimensional materials over Bulk:	9
1.1.2. Challenges in working with low dimensional materials:.....	9
1.1.3. Advantages of 2D materials compared to other low dimensional structures:	11
1.1.4. Well known 2D materials:.....	12
1.2. Understanding electrocatalytic activity and its implications in alternative energy:	16
1.2.1. Diminishing fossil fuel reserves and escalating pollution levels:	18
1.2.2. Alternative energies:.....	21
Solar energy:.....	21
1.3. Understanding the fundamentals of Fuel cells:	24
1.3.1. Efficiency of fuel cells:.....	26
1.3.2. Types of fuel cell:	28
1.3.3. Limitation of fuel cells:.....	32
1.3.4. The role of 2D materials in addressing fuel cell limitations:.....	33
1.4. Phononic process:.....	35
1.5. The benefits of computational studies based on DFT:.....	37
1.6. Aims and objectives:	41
References:.....	43
2. Theoretical Backgrounds:	51
2.1. Many-body problems & density functional theory:.....	51
2.2. Early solutions to the many-body problem: the Hartree and Hartree-Fock models	53
2.3. Density Functional Theory:.....	56
2.3.1. Observables in terms of electron density:	56
2.3.2. The Hohenberg-Kohn theorem:	57
2.3.3. The exchange-correlation functional and its approximations:	63
2.3.4. The local density approximation and generalized gradient approximation:	64
2.3.5. The Meta-GGAs and hybrid functionals:.....	66

2.3.6.	Plane wave basis sets and energy cut-off:	69
2.3.7.	The pseudopotential method:	72
2.3.8.	The projector augmented wave (PAW) method:.....	74
References:.....		77
3.	Review of past works:	79
3.1.	Introduction:	79
3.2.	Previous computational and experimental reports on the structural, electronic and electrocatalytic properties of pure/ doped TMDs and their Janus Structures:.....	83
References:.....		100
4.	Coinage metals doped 1T' WS₂ as efficient bifunctional electrocatalyst towards ORR and HER: a first principles study	
4.1.	Introduction:	105
4.2.	Theoretical Methods:.....	107
4.3.	Results and Discussions:.....	109
4.3.1.	Doping in 1T' WS ₂ :	109
4.3.2.	Oxygen reduction reaction mechanism:.....	116
4.3.3.	Hydrogen evolution reaction:	123
4.4.	Conclusion:	127
References:.....		129
5.	Zinc doping induced WS₂ accelerating the HER and ORR kinetics: A theoretical and Experimental Validation	
5.1.	Introduction:	133
5.2.	Theoretical Method:	135
5.3.	Results and discussions on HER and ORR:	136
5.4.	Conclusion:	143
References:.....		144
6.	Vibrational, thermal, electronic and optical properties of TaXY Janus monolayers (X= S, Se; Y= O, N, P): A First-principles Study	
6.1.	Introduction:	148
6.2.	Computational Methods:.....	149
6.3.	Result and discussion:.....	151
6.3.1.	Atomic Structure and stability:	151

6.3.2.	Thermal conductivity:	154
6.3.3.	Electronic Properties:	158
6.3.4.	Vibrational Properties:	160
6.3.5.	Thermal Properties:	162
6.3.6.	Optical Properties:	163
6.4.	Conclusion:	165
References:		167
7.	Grand conclusions and scopes for future works	172
7.1.	Summary of the present study:	172
7.2.	Scopes for future works:	174
Appendix		176

Acknowledgements

I extend my heartfelt gratitude to all who have supported me on my research journey. Without the guidance and encouragement of numerous individuals, this thesis would not have come to fruition. First and foremost, I am deeply grateful to my supervisor, Professor Kalyan Kumar Chattopadhyay. His mentorship has been invaluable, introducing me to the captivating realm of computational physics. Professor Chattopadhyay's guidance not only illuminated the fascinating world of research in this field but also provided me with the necessary resources for both theoretical studies and practical investigations. I am forever indebted to his scientific leadership, patient supervision, and encouragement for independent and insightful research. I also wish to express my deep appreciation for Dr. Bikram Kumar Das (Bikram Da) for his significant contributions to my academic journey. Since the inception of my PhD program, Dr. Das has been a constant source of encouragement and knowledge. His patient guidance through the intricacies of density functional theory and related computational software has been invaluable. His enthusiasm for exploring novel computational avenues has enriched my research experience immeasurably. Special thanks are due to Anibrata, my labmate and close friend, whose unwavering support has been a true blessing. He has been a pillar of strength during challenging times, offering encouragement and assistance through various setbacks. His presence has been a constant source of solace and inspiration. Acknowledgment is also owed to Souvik, another dear friend among labmates, for his insightful scientific discussions and assistance in organizing my thesis. His contributions have been invaluable to me. Finally, I extend my gratitude to Dimitra Di, whose presence has been akin to that of an elder sister, offering comfort and support during times of distress. Afternoon tea times with her have been a source of rejuvenation, lifting my spirits and helping me overcome moments of despondency. I am also deeply grateful to my lab mates and close collaborators, Dipayan, Nabamita, Koushik Da, Subhasis Da and Shuvankar, whose work alongside me has been an immense pleasure and a source of inspiration. Additionally, Saikat Da, Suvra Di, Karam Da, and Lab Seniors have also provided invaluable support throughout my PhD journey. Outside my lab, my mother, elder sisters, and close friend Beauty have been constant sources of inspiration. I'm also grateful to CSIR for providing funding throughout my five years of research endeavors. Finally, I must express my deepest gratitude to my father, who instilled in me a sense of focus from childhood and supported me unconditionally. In conclusion, I dedicate this thesis to my late father.

Arnab Das

Index No.: D-7/ISLM/33/2020

Title of the thesis: First Principles investigation on the electronic, phononic and electrocatalytic properties of 2D-dichalcogenide materials.

Name and Designation of the Supervisor:

Prof. Kalyan Kumar Chattopadhyay
Department of Physics,
School of Materials Science and Nanotechnology,
Jadavpur University,
Kolkata-32, India

List of Publications

1. **Arnab Das**, Bikram Kumar Das, K.K. Chattopadhyay, Coinage metals doped 1T' WS₂ as efficient bifunctional electrocatalyst towards ORR and HER: A first principles study, Computational Materials Science, Volume 229, 2023, 112418.

<https://doi.org/10.1016/j.commatsci.2023.112418>

2. **Arnab Das**, Dipayan Roy, Bikram Kumar Das, Md Imran Ansari, Kalyan Kumar Chattopadhyay, Sourav Sarkar, Zinc doping induced WS₂ accelerating the HER and ORR kinetics: A theoretical and experimental validation, Catalysis Today, Volume 423, 2023, 113921.

<https://doi.org/10.1016/j.cattod.2022.10.003>

3. **Arnab Das**, Souvik Bhattacharya, Bikram Kumar Das, Anibrata Banerjee, Kalyan Kumar Chattopadhyay Vibrational, thermal, electronic and optical properties of TaXY Janus monolayers (X= S, Se; Y= O, N, P): A First-principles Study.

4. Bikram Kumar Das, Anibrata Banerjee, **Arnab Das**, Kalyan Kumar Chattopadhyay, Graphyne supported Co₁₃, Fe₁₃ and Ni₁₃ nano-cluster as efficient electrocatalysts for nitrogen reduction reaction: A first principles study, Catalysis Today, Volume 423, 2023, 113906.

<https://doi.org/10.1016/j.cattod.2022.09.012>.

5. Nabanita Sen, **Arnab Das**, Supratim Maity, Shrabani Ghosh, Madhupriya Samanta, and Kalyan Kumar Chattopadhyay, Tailoring the Sb₂Se₃/rGO Heterointerfaces for Modulation of Electrocatalytic Hydrogen Evolution Performances in Acidic Media, ACS Appl. Energy Mater. 2023, 6, 1, 58–67.

<https://doi.org/10.1021/acsaem.2c01820>

6. K. Sardar, S. Thakur, **A. Das**, N. Besra, D. Banerjee, G. Majumdar and K. K. Chattopadhyay Synthesis of different manganese tungstate nanostructures for enhanced charge-storage applications: theoretical support for experimental findings, Phys.Chem.Chem. Phys 2022, 24, 28271-28282.

<https://doi.org/10.1039/1463-9084/1999>

***This thesis draws upon the findings obtained in the aforementioned publications and communicated articles, numbered 1-3.**

Abstract:

Humanity stands at a pivotal moment, confronted by dwindling fossil fuel reserves and escalating environmental pollution, heralding an unprecedented crisis. Ensuring a sustainable future demands urgent pursuit of economical, clean, and renewable energy sources. Renewable energy, encompassing resources like solar, wind, and geothermal power, emerges as a beacon of hope. Extensive research endeavours are underway to harness these resources effectively, with the ultimate aim of entirely displacing fossil fuels. Fuel cells emerge as a notable contender in this pursuit due to their high efficiency and environmentally friendly operation. Operating via a simple reaction wherein hydrogen and oxygen combine to yield water and electricity, fuel cells offer a promising avenue for sustainable energy production. However, the widespread adoption of fuel cells hinges on the development of superior cathode materials. Presently utilized materials often suffer from inefficiencies or exorbitant costs. Recent years have witnessed a surge in the research and development of two-dimensional (2D) materials, distinguished by their unique properties compared to bulk counterparts. These materials, characterized by high surface area, tunable electronic structure, and exceptional stability in harsh environments, emerge as ideal candidates for electrocatalysts in fuel cells. Computational tools and synthesis techniques have facilitated the discovery of novel, stable 2D materials, among which transition metal dichalcogenides (TMDs) hold particular promise. TMDs exhibit superior mechanical strength, excellent electrical conductivity, and resistance to poisoning, rendering them excellent electrode materials. Different structural phases of TMDs, such as 2H, 1T, and 1T', with varying electronic properties ranging from semiconducting to metallic or semimetallic, hold significant potential for fuel cell applications. Additionally, Janus structures, characterized by inherent non-uniform charge distribution across two different elemental faces, showcase promising electronic and electrocatalytic properties. Computational simulations utilizing density functional theory (DFT) have emerged as crucial tools for predicting the electrocatalytic properties of these materials. This thesis delves into the potential of TMDs as cathode electrocatalysts for fuel cells, presenting a comprehensive exploration of their properties and applications. Chapter 1 sets the stage by outlining the global energy crisis, environmental challenges, and the role of fuel cells as a solution, alongside discussions on current limitations and the promise of 2D materials, particularly TMDs. Chapter 2 delves into the intricacies of the many-body problem in quantum mechanics and its resolution using DFT,

supplemented by necessary mathematical background. Chapter 3 reviews prior research on TMDs and their Janus forms, focusing on theoretical investigations of their electronic and electrocatalytic properties, including discussions on pristine and doped/adsorbed TMDs for comparative analysis. In Chapter 4, the potential of extrinsic defects to enhance the electrocatalytic properties of 1T' phase WS₂ and its doped structures for both oxygen reduction reaction (ORR) and hydrogen evolution reaction (HER) is explored, utilizing first-principles calculations to illustrate the impact of coinage metal doping on electronic properties. Chapter 5 presents a detailed theoretical study on the electrocatalytic activity of zinc-doped WS₂ for ORR in alkaline electrolytes, alongside HER activity of Zn-doped WS₂, investigating how doping influences electronic structure and performance. Finally, in Chapter 6, the electronic, thermal, and structural attributes of Janus forms derived from TaS₂ and TaSe₂ structures are explored, involving the replacement of sulphur or selenium sites with oxygen, nitrogen, and phosphorus atoms. This investigation aims to elucidate the impact of modification on electronic behavior, thermal stability, and overall structural integrity, expanding our understanding of these Janus structures and their potential suitability in optoelectronic applications.

1. Introduction and Objectives:

1.1. Introduction to low dimensional materials:

Materials with dimensions smaller than 100 nanometers in at least one direction, demonstrating unique physical properties compared to their bulk counterparts, are commonly known as low-dimensional materials [1]. These materials classified into zero-dimensional (0D) [1], one-dimensional (1D) [2], or two-dimensional (2D) [3] based on the dimensionality of their structures are discussed below

1. Zero-dimensional (0D): These materials are confined in all three dimensions. Examples include quantum dots or nanoparticles, where their size is extremely small, leading to unique quantum effects and properties.

2. One-dimensional (1D): These materials are confined in two directions while one direction remains unrestricted or free. Nanowires and nanotubes are classic examples of 1D materials, exhibiting elongated structures with high aspect ratios.

3. Two-dimensional (2D): These materials are confined in one direction while being unrestricted in two directions, resembling a plane sheet. Graphene stands out as a prime example of a 2D material, renowned for its remarkable properties. Additionally, transition metal dichalcogenides (TMDs) like MoS_2 and WS_2 are notable examples of 2D materials, offering intriguing electronic and optical properties.

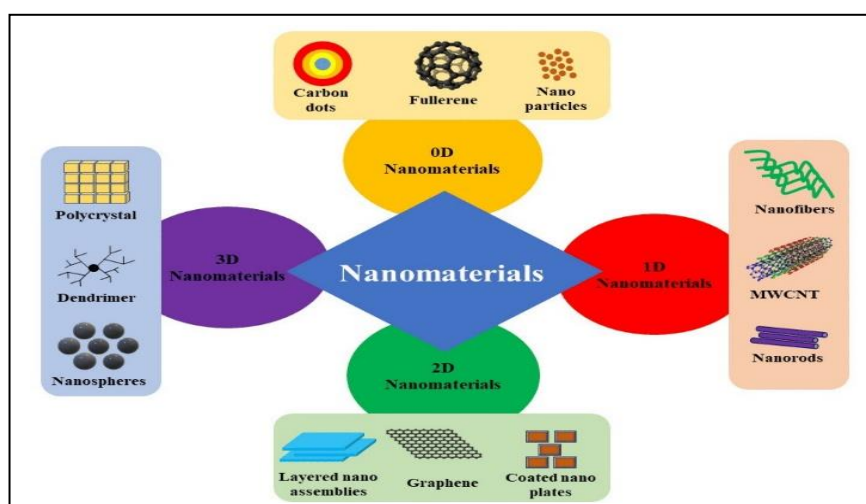


Figure 1.1: Classification of low dimensional Materials [Ref. 3]

1.1.1. Advantages of low dimensional materials over Bulk:

These low-dimensional materials exhibit unique electronic, optical, mechanical, and thermal properties due to quantum confinement effects, surface effects, and a high surface-to-volume ratio. One crucial property influenced by quantum confinement is the electronic density of states (DOS) which is defined as the number of different states that electron can occupy at particular energy level. The variation of electronic density of states with respect to energy can be expressed as follows: $D(E) \propto E^{\frac{n}{2}-1}$, where n can be 3, 2 or 1 depending on the dimensionality of the system. However, for 0D structures, DOS follows $\delta(E)$ function. In three-dimensional materials, the density of states (DOS) is continuous, meaning that energy levels are not quantized and electrons can occupy a range of energy states. However, in low-dimensional materials such as two-dimensional (2D) or one-dimensional (1D) materials, the density of states (DOS) exhibits discrete energy levels due to quantum confinement in one or more directions. This confinement leads to the quantization of energy levels, resulting in distinct energy states for electrons within the material. This difference in DOS behavior is a fundamental aspect of the electronic properties of low-dimensional materials and has important implications for their behavior and potential applications. The widespread adoption of low-dimensional materials across diverse fields such as optoelectronics, catalysis, and energy storage has been driven by their tunable electronic properties, achieved through modifications in size, shape, and dimensionality.

1.1.2. Challenges in working with low dimensional materials:

Despite their promising potential, dealing with low-dimensional materials poses several challenges, as elaborated below [4-10]:

- (i) **Synthesis and production:** Fabricating low-dimensional materials with high quality and scalability remains a challenge. Many synthesis methods are complex and expensive, limiting their widespread adoption. Techniques including chemical vapor deposition, sol-gel synthesis, and bottom-up assembly are commonly employed to fabricate these materials with tailored characteristics for specific applications. Controlling the size, shape, and orientation of these materials during synthesis is crucial for their properties and applications.
- (ii) **Characterization:** Characterizing low-dimensional materials demands the utilization of cutting-edge techniques such as X-ray photoelectron spectroscopy

(XPS), transmission electron microscopy (TEM), scanning electron microscopy (SEM), and others. These advanced methods allow scientists to delve deeply into the structural, electronic, and optical properties of these materials with utmost precision. By employing these techniques, researchers can unravel the intricate details of low-dimensional materials, paving the way for novel discoveries and advancements in various scientific disciplines.

- (iii) **Stability and environmental sensitivity:** Many low-dimensional materials are sensitive to environmental conditions, such as humidity, oxygen, and temperature variations, which can degrade their properties. Developing methods to stabilize these materials under various conditions without affecting their properties is essential.
- (iv) **Integration and device fabrication:** Integrating low-dimensional materials into devices while preserving their unique properties is challenging. Developing compatible fabrication processes and interfaces with existing materials and technologies is crucial for practical applications.
- (v) **Scalability and reproducibility:** Scaling up the production of low-dimensional materials to industrial levels while maintaining quality and reproducibility is a significant challenge. Ensuring uniformity and consistency in large-scale production is essential for commercial viability.
- (vi) **Manipulation and functionalization:** Precise manipulation and functionalization of low-dimensional materials are necessary for tailoring their properties and enabling specific applications. Developing methods for controlled doping, surface modification, and functionalization without introducing defects is crucial.
- (vii) **Understanding fundamental properties:** Despite significant progress, many fundamental properties and behaviors of low-dimensional materials are still not fully understood. Further research is needed to elucidate the underlying mechanisms governing their unique properties and behaviors. Addressing these challenges requires interdisciplinary efforts combining materials science, chemistry, physics, engineering, and nanotechnology. Collaborative research efforts involving academia, industry, and government institutions are essential for overcoming these hurdles and unlocking the full potential of low-dimensional materials for various applications.

1.1.3. Advantages of 2D materials compared to other low dimensional structures:

Although all low-dimensional materials, encompassing 1D structures like nanowires and nanotubes as well as zero-dimensional entities such as quantum dots and nanoparticles, present unique attributes and potential applications, 2D materials have garnered notable attention owing to several discernible advantages [10-17]:

- (a) **Versatility and tunability:** Unlike 1D and zero-dimensional materials, which typically exhibit limited properties dictated by their specific dimensions, 2D materials offer a broader range of tunability. Their properties can be modified by adjusting factors such as layer thickness, composition, strain, and doping, offering more versatility for tailoring material characteristics to specific applications.
- (b) **Large surface area:** 2D materials possess a large surface-to-volume ratio, providing abundant surface sites for interactions with other materials or environments. This characteristic is particularly advantageous for applications such as catalysis, sensing, and energy storage, where surface interactions play a crucial role.
- (c) **Mechanical strength:** Graphene, the most well-known 2D material, boasts exceptional mechanical properties, including high tensile strength and flexibility. These attributes make it suitable for various applications requiring robust and flexible materials, such as flexible electronics, wearable devices, and structural composites.
- (d) **High electrical conductivity:** Graphene exhibits remarkable electrical conductivity, surpassing that of many traditional materials like copper. This property, along with the inherent two-dimensional nature of graphene, enables the development of high-speed electronics, transparent conductive films, and efficient energy storage devices.
- (e) **Quantum confinement effects:** While quantum confinement effects are also present in 1D and zero-dimensional materials, they manifest uniquely in 2D materials due to their planar geometry. These effects can lead to novel electronic, optical, and quantum phenomena, offering opportunities for applications in quantum computing, optoelectronics, and spintronics.
- (f) **Layered heterostructures:** 2D materials can be stacked or combined with other 2D materials or bulk materials to form layered heterostructures with tailored properties and functionalities. This versatility enables the design of complex devices with multifunctionality and improved performance, surpassing the capabilities of individual materials.

- (g) Transparency and Flexibility:** Certain 2D materials, such as graphene and hexagonal boron nitride (h-BN), are transparent and flexible, making them suitable for applications in transparent electrodes, flexible displays, and optoelectronic devices.
- (h) Chemical Stability:** Some 2D materials exhibit excellent chemical stability, resisting degradation in harsh environments. This stability enhances the durability and longevity of devices and coatings, making them attractive for various applications, including corrosion protection and environmental sensing.

Overall, the unique combination of properties, tunability, and versatility offered by 2D materials makes them particularly promising for a wide range of applications across various fields, driving extensive research and technological advancements in this area.

1.1.4. Well known 2D materials:

The discovery of graphene in 2004 [18] marked a significant milestone in materials science and nanotechnology. Graphene, a single layer of carbon atoms arranged in a hexagonal lattice, exhibits remarkable properties such as high electrical conductivity, mechanical strength, and flexibility. Its discovery opened up new avenues for research and development in the field of 2D materials. Graphene was first isolated by Professors Andre Geim and Konstantin Novoselov at the University of Manchester through a groundbreaking method known as mechanical exfoliation or the "Scotch tape method" [19]. This involved repeatedly peeling layers of graphene from graphite using adhesive tape until a single layer of graphene remained. The researchers then characterized graphene's properties using various techniques, confirming its unique properties. The discovery of graphene sparked a surge of interest in 2D materials due to its exceptional properties and potential applications across a wide range of fields, including electronics, photonics, energy storage, and composites. This discovery induces researchers around the world for exploring other 2D materials, such as transition metal dichalcogenides (TMDs) [20], boron nitride [21], black phosphorus [22], Mxenes [23] and others. Transition metal dichalcogenides (TMDs) are a class of 2D materials composed of transition metal atoms (such as molybdenum, tungsten, or titanium) sandwiched between chalcogen atoms (such as sulfur, selenium, or tellurium). Some examples of TMDs include molybdenum disulfide (MoS_2) [24], tungsten diselenide (WSe_2) [25], and titanium disulfide (TiS_2) [26]. One of the most notable characteristics of TMDs is their tunable bandgap. Unlike graphene, which is a zero-bandgap material, TMDs exhibit a finite bandgap that can be manipulated by controlling factors such as layer thickness, strain, and doping. This property makes TMDs attractive for

applications in electronics, optoelectronics, and photonics, where a tunable bandgap is essential for device performance. TMDs often exhibit strong spin-orbit coupling, leading to intriguing spin-related phenomena. This property holds promise for spintronics applications, where manipulation of electron spin is exploited for novel functionalities. Similar to graphene, TMDs display layer-dependent properties. For instance, monolayer TMDs exhibit direct bandgaps, leading to enhanced light-matter interactions and optoelectronic device performance compared to their bulk counterparts. Some TMDs boast high carrier mobility, rivaling or even surpassing that of silicon. This high mobility, coupled with their semiconducting behavior, positions TMDs as attractive candidates for next-generation electronic devices with improved performance. TMDs exhibit strong light-matter interaction due to their direct bandgap in monolayer form. This property makes them ideal materials for applications in photodetection, photovoltaics, and light-emitting devices. TMDs generally exhibit good chemical stability, resisting degradation in various environments. This stability enhances their durability and longevity in practical applications, such as sensors and catalysts. The formation of heterostructures involving TMDs offers a versatile platform for tailoring material properties and exploring new functionalities. Heterostructures can be created by stacking TMD layers with other 2D materials, such as graphene or hexagonal boron nitride (h-BN), or by interfacing TMDs with bulk materials. One approach to heterostructure formation involves van der Waals (vdW) epitaxy, where TMD layers are grown on a substrate with a lattice mismatch, allowing for the formation of coherent interfaces between different materials. This technique enables the creation of atomically sharp interfaces and precise control over the heterostructure's properties. Another method involves mechanical transfer or direct synthesis of TMD layers onto pre-patterned substrates or other 2D materials. This approach allows for the integration of TMDs with existing device architectures and facilitates the fabrication of complex heterostructures with tailored functionalities. Heterostructures involving TMDs have been explored for a wide range of applications, including optoelectronics, spintronics, Catalysis etc [27, 28]. By combining TMDs with other materials, researchers can exploit synergistic effects, such as enhanced charge transport, efficient light absorption, and strong spin-orbit coupling, to develop novel devices with improved performance and functionality. In conclusion, transition metal dichalcogenides (TMDs) represent a versatile class of two-dimensional (2D) materials with unique properties and diverse applications. Their layer-dependent properties, semiconductor behavior, strong spin-orbit coupling, and optical properties make them promising candidates for a wide range of technological advancements. Additionally, the formation of heterostructures involving TMDs offers a versatile platform for tailoring material properties

and exploring new functionalities, further expanding their potential in various fields. Transition metal dichalcogenides (TMDs) exhibit a variety of fascinating phenomena beyond their intrinsic properties. Two notable phenomena observed in certain TMDs are charge density waves (CDWs) [29] and superconductivity, which have garnered considerable interest due to their potential applications and fundamental implications in condensed matter physics. CDWs are periodic modulations in the electron density of a material, resulting in a spatially periodic arrangement of charge. In TMDs, CDWs often arise from the nesting of the Fermi surface due to the strong electron-phonon coupling and the presence of an electronic instability. Below a certain critical temperature, the material undergoes a phase transition, forming a CDW state. Several TMDs have been found to exhibit CDW phenomena, including 1T TaS₂, 1T TiSe₂, and 2H NbSe₂ [30]. In these materials, the CDW phase transition can lead to dramatic changes in electronic and optical properties, such as the opening of a bandgap, the emergence of new electronic states, and alterations in the material's conductivity. The CDW state in TMDs has attracted attention for potential applications in electronic and optoelectronic devices, as well as for fundamental studies of correlated electron systems and quantum phenomena. Understanding the underlying mechanisms driving CDW formation and its interplay with other electronic phases is crucial for harnessing these materials for practical applications. Superconductivity is a phenomenon characterized by the loss of electrical resistance and the expulsion of magnetic fields below a critical temperature in certain materials. While TMDs are typically non-superconducting in their pristine form, superconductivity can be induced in these materials through various methods, such as chemical doping, intercalation, or applying external pressure. Among TMDs, 2H NbSe₂ is one of the most extensively studied materials exhibiting superconductivity. In its bulk form, 2H NbSe₂ undergoes a superconducting transition at temperatures below 7.2 K. However, recent studies have shown that thin layers of 2H NbSe₂ can exhibit enhanced superconducting properties, including higher critical temperatures and critical magnetic fields, making them promising candidates for applications in superconducting electronics and quantum computing [31]. Other TMDs, such as 2H TaS₂ and 2H TaSe₂, have also been investigated for their superconducting properties. These materials exhibit complex phase diagrams with multiple superconducting phases, unconventional pairing mechanisms, and competing electronic orders, providing rich opportunities for exploring new physics and applications in superconductivity [32]. In summary, charge density waves (CDWs) and superconductivity are intriguing phenomena observed in certain transition metal dichalcogenides (TMDs). These phenomena offer insights into the underlying physics of correlated electron systems and provide opportunities for developing novel electronic and

quantum devices. Further research into the mechanisms driving CDW formation and superconductivity in TMDs is essential for unlocking their full potential for future technologies. On the other hand, MXenes, another class of 2D materials, feature a hexagonally close-packed structure with interleaved layers of transition metals (M) and carbon or nitrogen (X). Surface terminations (-O, -OH, and -F) can be precisely controlled during synthesis or through subsequent treatments, significantly influencing material properties. These surface groups endow MXenes with high hydrophilicity and facilitate bonding to various species. MXenes have found applications in various fields, including energy storage devices (batteries, supercapacitors), electromagnetic shielding, wearable sensors, catalysis, optoelectronics, biomedicine etc [33, 34, 35, 36].

2D materials, including transition metal dichalcogenides (TMDs) exhibiting various phases such as 2H, 1T, and 1T' have garnered significant interest for catalytic applications, particularly in oxygen reduction reaction (ORR) [37, 38], hydrogen evolution reaction (HER) [39], and nitrogen reduction reaction (NRR) [40]. Their diverse properties ranging from semiconducting to metallic or semimetallic make them promising candidates for addressing challenges in these catalytic processes. TMDs offer tunable characteristics that enable precise control over their catalytic activity, thus propelling advancements in sustainable technologies for energy conversion and storage, environmental remediation, and chemical synthesis.

Before establishing a specific 2D material experimentally for particular applications, computational methods such as Density Functional Theory (DFT) can be utilized to predict their properties accurately. By employing DFT computationally, researchers can simulate the behavior of 2D materials at the atomic level, providing insights into their electronic structure, mechanical properties, and reactivity. This predictive approach enables the screening and optimization of 2D materials for various applications, guiding experimental efforts towards the synthesis of materials with desired properties. Additionally, computational simulations can expedite the discovery of novel 2D materials and facilitate the design of tailored materials for specific technological needs. Overall, computational methods like DFT play a crucial role in the rational design and development of 2D materials for diverse applications.

1.2. Understanding electrocatalytic activity and its implications in alternative energy:

Electrocatalytic activity [41] is a fundamental concept in electrochemistry, pivotal for accelerating electrochemical reactions crucial for various technological applications. Essentially, electrocatalysts function to lower the energy barrier required for a reaction to occur, thereby enhancing reaction rates and efficiency. Electrolysis of water is a process that involves the decomposition of water molecules (H_2O) into hydrogen gas (H_2) and oxygen gas (O_2) using electricity. This process occurs within an electrolytic cell, which consists of two electrodes submerged in an electrolyte solution, typically water with an added electrolyte to enhance conductivity, such as a salt or acid. This reaction naturally requires a certain amount of energy to proceed. An electrocatalyst facilitates this process by acting as a catalyst, reducing the activation energy needed for the water molecule to split. In simpler terms, it acts as a stepping stone, making the reaction happen faster and more efficiently.

The significance of electrocatalysts spans across various technological advancements, including fuel cells, electrolyzers, and batteries [42, 43, 44]:

- **Fuel Cells:** These devices convert chemical energy into electrical energy by facilitating reactions at the electrodes. Electrocatalysts play a crucial role in speeding up these reactions, enabling efficient fuel cell operation.
- **Electrolyzers:** These devices utilize electricity to produce clean hydrogen fuel from water. Electrocatalysts enhance the hydrogen evolution reaction, making the process more efficient.
- **Batteries:** Electrocatalysts can enhance the rate of charge and discharge cycles in batteries, resulting in faster charging times and extended battery life.

Key aspects of electrocatalytic activity include:

- **Electrochemical reactions:** These involve electron transfer between an electrode and a chemical species in a solution.
- **Activation energy:** The minimum energy required for a reaction to occur. Electrocatalysts reduce this energy barrier, facilitating faster reaction rates.

- **Electrode potential:** The electrical potential at which electrochemical reactions take place. Electrocatalysts can modify this potential to facilitate reactions.

Electrocatalysts come in different forms, including heterogeneous catalysts (solid materials like metals, alloys, or composites) and homogeneous catalysts (soluble molecules within the electrolyte solution). Researchers continually strive to develop novel electrocatalysts with improved properties such as high activity, selectivity, stability, and cost-effectiveness. The field of electrocatalytic activity is rapidly evolving, holding immense potential for advancing clean energy technologies and addressing global energy challenges. Continued research and innovation in this area are essential for driving the transition towards a sustainable energy future.

Throughout history, humanity has relied heavily on fossil fuels to meet its energy needs. From the onset of the industrial revolution to the present day, the demand for energy has steadily risen in tandem with advancements in technology and population growth. As the global population continues to expand at a rapid pace, the need for energy is expected to escalate even further. This increasing demand for energy has led to a significant dependence on the finite reserves of fossil fuels found within the Earth. These fossil fuel reserves, including coal, oil, and natural gas, have been the primary sources of energy for various sectors such as transportation, electricity generation, and industrial production. However, the finite nature of these reserves poses a significant challenge to meeting the growing energy demands of a rapidly expanding global population. Moreover, the widespread use of fossil fuels has resulted in numerous environmental challenges, including air and water pollution, habitat destruction, and greenhouse gas emissions. The combustion of fossil fuels releases carbon dioxide and other pollutants into the atmosphere, contributing to climate change and global warming.

As such, there is a pressing need to transition towards cleaner, renewable sources of energy to mitigate the environmental impact of energy generation and ensure sustainable development for future generations. Renewable energy sources such as solar, wind, hydroelectric, and geothermal power offer promising alternatives to fossil fuels, providing clean and abundant sources of energy that can help reduce greenhouse gas emissions and combat climate change. Investments in renewable energy technologies and infrastructure are essential for transitioning towards a more sustainable energy future. By harnessing the power of renewable energy sources, we can reduce our dependence on fossil fuels, mitigate environmental degradation, and pave the way for a more sustainable and resilient energy system for generations to come.

1.2.1. Diminishing fossil fuel reserves and escalating pollution levels:

As of 2022, fossil fuels account for 81.79% of global energy consumption, with renewable energy comprising 14.21% and nuclear energy making up 3.23% [45] [Figure 1.2]. This data highlights the predominant reliance on fossil fuels for meeting the world's energy needs, despite growing efforts to transition towards cleaner and more sustainable sources of energy. While renewable and nuclear energy sectors have seen modest growth, fossil fuels continue to dominate the global energy landscape. Efforts to increase the adoption of renewable and nuclear energy technologies are essential for reducing greenhouse gas emissions, mitigating climate change, and ensuring a more sustainable energy future.

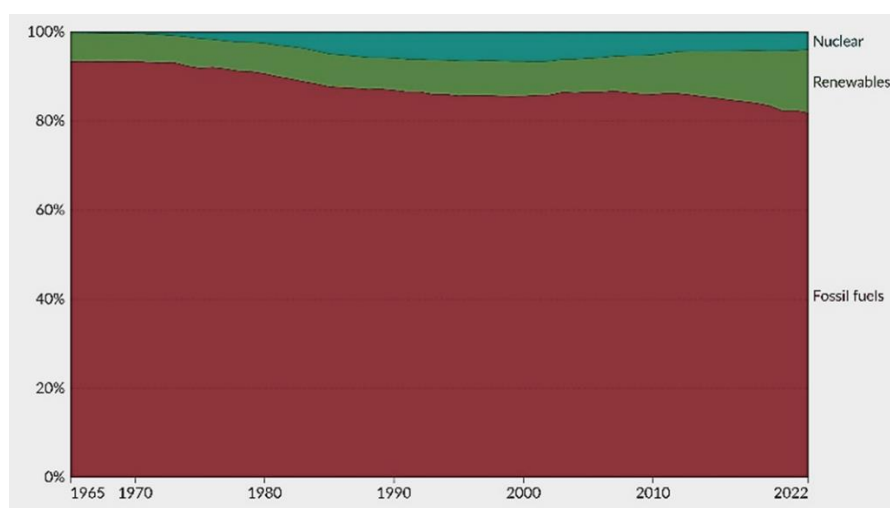


Figure 1.2: Global energy consumption data [Ref. 45]

Our world's insatiable need for energy is placing immense strain on the finite reservoirs of fossil fuels that our planet provides. Ever since the dawn of the Industrial Revolution, our reliance on fossil fuels like coal, oil, and natural gas has grown hand in hand with the expanding global population. Even in the year 2018, fossil fuels continued to dominate, accounting for a staggering 85% of the world's energy consumption. This includes electricity generation, which alone covers nearly 20% of the total energy needs globally, with demand showing a worrisome 4% increase in just that year [46].

The stark truth is that fossil fuels are not an endless supply – they're finite resources. While nature does slowly replenish these reserves over millions of years, our consumption far exceeds

this natural replenishment rate. As depicted in Figure 1.3, the current trends indicate projected timelines for the depletion of these resources.

To steer clear of an impending energy crisis, we must chart a course towards a sustainable future, one powered by renewable alternatives. Presently, these cleaner sources of energy meet only about 15% of the world's energy demand. However, with projections indicating a substantial 33% surge in global energy demand by the year 2040, driven by factors like population growth and economic expansion, making a significant shift towards renewables becomes not just desirable, but absolutely imperative [47].

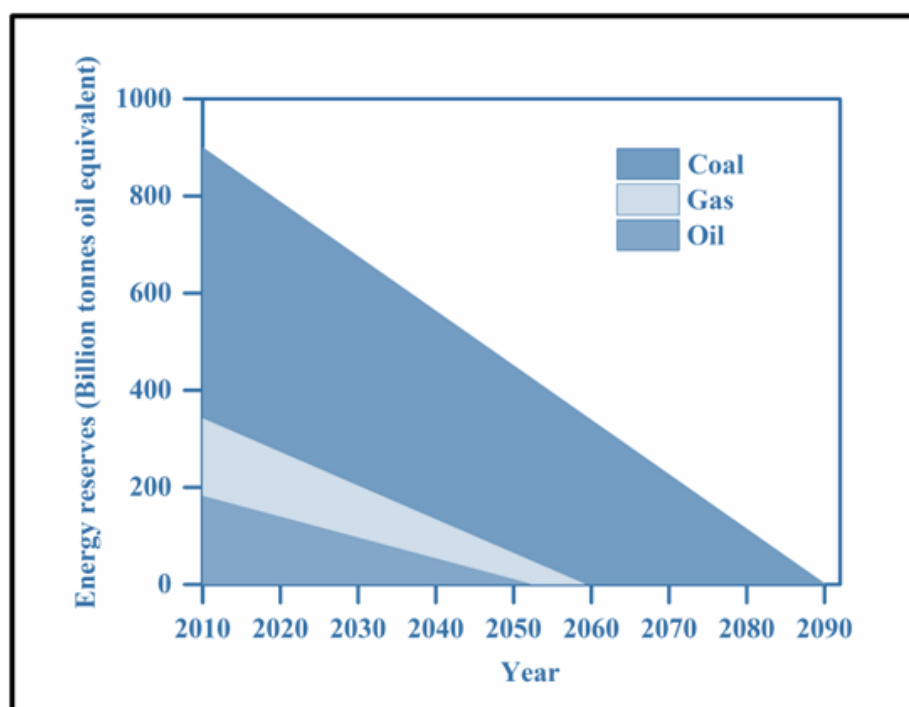


Figure 1.3: Depletion rate of fossil fuel.

The convenience of fossil fuels has long driven progress since the Industrial Revolution, but their usage exacts a significant environmental toll. Burning fossil fuels sets off a chain reaction of problems, with one of the most pressing being climate change. As fossil fuels combust, they release greenhouse gases, primarily carbon dioxide (CO₂), which trap heat in the atmosphere. As depicted in Figure 1.4, this has led to a troubling trend: a continual increase in CO₂ emissions as our dependence on fossil fuels grows. The warming effect of these emissions has extensive consequences. Climate change manifests in various disruptions, including the melting of glaciers and the rise of sea levels. These changes pose severe threats to ecosystems and coastal communities worldwide. Beyond just the encroaching waters, climate change

accelerates species extinction by altering habitats and depleting resources. This loss of biodiversity can disrupt food chains and jeopardize our ability to produce food.

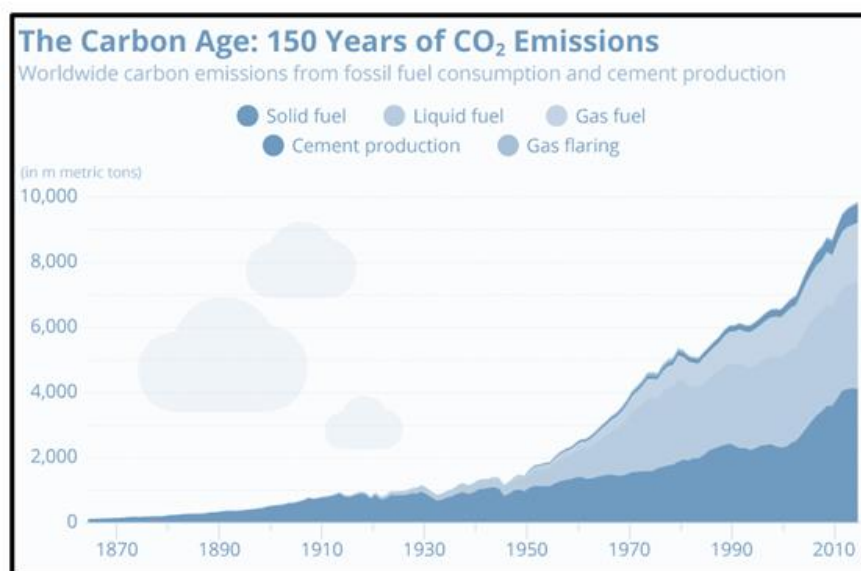


Figure 1.4: Carbon di-oxide emission rate [Ref. 48].

The environmental consequences of fossil fuel combustion extend beyond climate change. The burning of these fuels releases harmful pollutants like sulfur and nitrogen oxides, which combine with water vapor to form acid rain. This acid rain damages natural ecosystems and accelerates the erosion of buildings and monuments, especially those made from marble. Fossil fuels can also harbour radioactive elements. Coal combustion, for instance, releases trace amounts of thorium and uranium into the atmosphere [48]. While the immediate health risks are likely minimal, it's another factor to consider. Perhaps the most immediate threat is air pollution. Our growing reliance on fossil fuels for transportation has choked the skies of many major cities. This air pollution contributes to a range of health problems, including premature death, respiratory illnesses, and decreased lung function. Estimates suggest millions of deaths occur annually due to air pollution worldwide. The urgency of addressing these issues cannot be overstated. While resource depletion is a concern, the environmental and health impacts of fossil fuels demand immediate action. We must prioritize the development and adoption of clean, sustainable energy sources. The responsibility for a sustainable future is a shared one. Scientists must continue researching and developing efficient, cost-effective renewable energy

technologies. Governments and individuals alike need to prioritize these clean alternatives to meet our energy needs.

1.2.2. Alternative energies:

The quest for alternative green and renewable energy resources has become imperative in the face of escalating environmental concerns and the finite nature of fossil fuels. Renewable energy resources, characterized by their sustainability and low carbon emissions, are gaining traction globally. By 2026, the global capacity for renewable electricity is forecasted to experience a remarkable surge, exceeding 60% compared to the figures recorded in 2020 [49]. This surge is anticipated to surpass 4,800 GW, matching the total current global power capacity derived from fossil fuels and nuclear energy combined.

Solar energy: It sourced from the sun's radiation, fuels a variety of technologies including photovoltaic (PV) panels and solar thermal systems. PV panels directly convert sunlight into electricity, while solar thermal systems utilize it to heat fluids for electricity, hot water, and heating purposes. As a renewable and abundant resource, solar energy emits no greenhouse gases, providing a clean alternative to fossil fuels. It holds the potential to diminish reliance on non-renewable sources and address climate change concerns. Challenges such as intermittency and energy storage remain, but advancements in technology and declining costs are facilitating widespread adoption, leading towards a more sustainable future.

Wind energy: It is captured through wind turbines and offers a promising avenue for clean, renewable power generation. Turbines convert the kinetic energy of wind into electricity, providing a sustainable alternative to fossil fuels. While wind power holds immense potential, its viability depends on factors like wind speed and geographical location. Not every property is suitable for wind turbine installation, necessitating careful site selection. Despite these challenges, wind energy contributes significantly to reducing greenhouse gas emissions and mitigating climate change. Advancements in turbine technology and increasing investment in wind farms are driving down costs and improving efficiency, making wind energy an increasingly competitive option in the global energy landscape. With proper planning and investment, wind power has the capacity to play a crucial role in transitioning towards a cleaner and more sustainable energy future.

Hydro energy: Hydroelectric power, also referred to as hydro energy, utilizes the kinetic energy of moving water to produce electricity. This renewable energy source relies on the

gravitational force of water bodies such as rivers, dams, or reservoirs to turn turbines and produce electricity. Hydroelectric power is among the most established and reliable forms of renewable energy, offering a consistent and controllable source of electricity. It provides a clean alternative to fossil fuels, emitting minimal greenhouse gases during operation. Additionally, hydroelectric plants can store water, enabling them to adjust electricity production according to demand. While hydro energy has significant potential, its implementation depends on suitable geographical locations with access to sufficient water resources. Despite these limitations, hydroelectric power plays a crucial role in global energy generation and contributes to reducing carbon emissions and combating climate change.

Geothermal energy: It harnesses the natural heat stored beneath the Earth's surface to generate electricity and provide heating and cooling for residential and commercial buildings. This renewable energy source relies on the Earth's internal heat, which is continuously produced by radioactive decay and planetary formation processes. Geothermal power plants extract this heat by tapping into underground reservoirs of hot water or steam. The extracted heat is then used to drive turbines connected to generators, producing electricity. Geothermal energy offers several advantages, including low greenhouse gas emissions, high reliability, and minimal environmental impact compared to fossil fuels. It is particularly suitable for regions with abundant geothermal resources, such as geologically active areas with volcanic activity or hot springs. Despite its potential, geothermal energy currently accounts for a small fraction of global energy production, but ongoing advancements in technology and increased investment may help unlock its full potential in the future.

Biomass energy: Biomass energy refers to the energy derived from organic materials such as plants, agricultural and forestry residues, animal waste, and organic municipal solid waste. These organic materials, collectively known as biomass, can be converted into various forms of energy, including heat, electricity, and biofuels, through processes such as combustion, fermentation, and anaerobic digestion. One common method of utilizing biomass energy is through combustion, where organic materials are burned to produce heat. This heat can be used directly for heating purposes or to generate steam, which can then drive turbines to produce electricity. Biomass can also be converted into biofuels such as ethanol and biodiesel, which can be used as renewable alternatives to gasoline and diesel fuels in transportation. Biomass energy is considered renewable because the organic materials used to produce it can be replenished through natural processes, such as plant growth. Additionally, biomass energy production can help reduce greenhouse gas emissions and mitigate climate change by

displacing fossil fuel usage. However, sustainable biomass management practices are essential to ensure that biomass resources are harvested and utilized in an environmentally responsible manner, without causing deforestation or other negative environmental impacts.

Chemical energy: It holds significant promise as a renewable energy resource, offering environmentally friendly pathways for converting chemical energy into electricity. This energy transformation is facilitated by technologies like rechargeable batteries, hydrogen generators, and fuel cells. Fuel cells, in particular, stand out as a remarkable innovation in this field, capable of directly converting chemical energy into electrical energy [50-52]. In the process of electrocatalysis, chemical reactions occur at the electrodes, releasing electrons that flow through an external circuit, producing electricity. Fuel cells utilize reverse electrocatalysis to combine hydrogen with oxygen, generating electricity and producing water as a byproduct. Fuel cell technology, while currently employed in specialized applications such as automotive power, holds vast potential for broader implementation across various sectors. As advancements continue and scalability improves, fuel cells could revolutionize stationary power generation, portable electronics, and grid-scale energy storage, offering a cleaner and more sustainable alternative to traditional energy sources. While various renewable and green energy sources exist, their widespread adoption is hindered by the lack of efficient technologies and fuel materials. Figure 1.5 illustrates the contribution of different renewable energy resources to electrical power generation, with hydro energy making the largest contribution. However, for a future where renewable energy meets most of the global energy demands, we require other reliable energy resources to be scaled up. Fuel cells show promise in this regard, but their large-scale application faces limitations such as the absence of optimal cathode materials. In this thesis, we focus on developing efficient cathode materials based on 2D materials through theoretical calculations. The working principles, classifications, prospects, and limitations of fuel cells are discussed in the subsequent section.

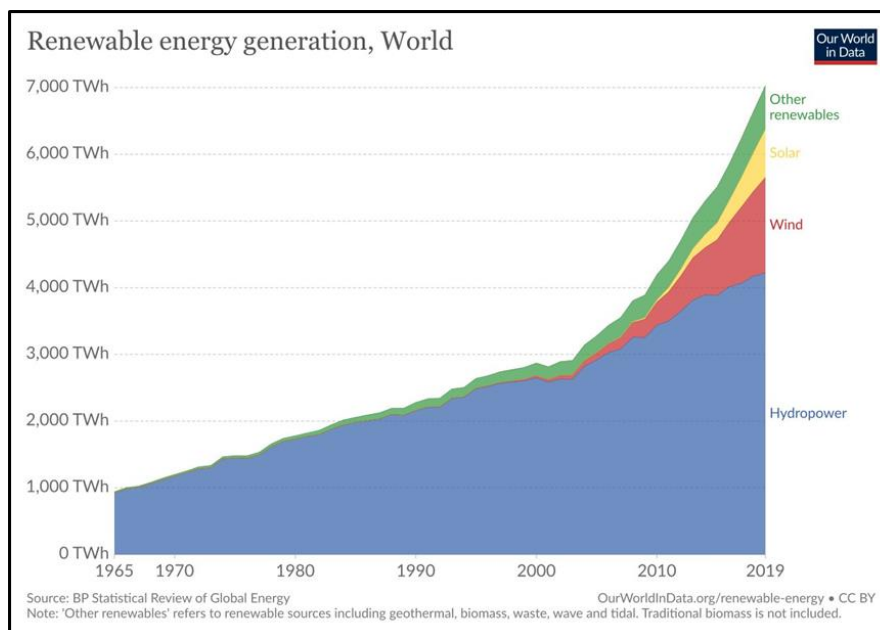


Figure 1.5: Energy generation from of renewable energy resources over the years (Ref. [49])

1.3. Understanding the fundamentals of fuel cells:

Fuel cells [50-52] represent a significant advancement in energy conversion technology, operating as galvanic cells that facilitate the direct conversion of chemical energy into electrical energy through the recombination of hydrogen and oxygen to produce water. This process involves the flow of electrons through the outer circuit of the cell, resulting in a clean and efficient energy conversion process. Compared to traditional heat engines, fuel cells boast higher theoretical efficiencies [53], making them a promising alternative for reducing our reliance on fossil fuels and mitigating harmful emissions into the atmosphere. While renewable energy sources like hydro, solar, and wind show great promise in the global energy landscape, their intermittent nature limits their capacity to meet the electrical base load consistently.

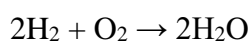
However, by integrating fuel cells with these renewable resources, we can create a more robust and reliable energy generation system. This hybrid approach offers the potential to harness the benefits of both clean energy sources and fuel cells, providing a sustainable solution for meeting our future power needs while minimizing environmental impact. Fuel cells are electrochemical devices that convert the free energy from chemical reactions into electrical energy through the flow of electrical current in an external circuit. The Gibbs free energy change associated with these reactions is directly related to the cell voltage, as expressed by the equation:

$$\Delta G = nF\Delta U_0$$

Here, n represents the number of electrons involved in the reaction, F is the Faraday constant, and ΔU_0 is the equilibrium cell voltage in the absence of external current.

Typically, hydrogen (H_2) and oxygen (O_2) gas serve as the primary fuel sources in fuel cells, although other ingredients may be used depending on the specific type of fuel cell. In the anode, hydrogen gas undergoes oxidation to produce H^+ ions, which then migrate through the electrolyte to the cathode. Meanwhile, oxygen molecules are adsorbed at the cathode and undergo reduction, facilitated by coupled electron and proton transfer processes, ultimately forming water.

The overall reaction in simple hydrogen/oxygen fuel cells can be represented succinctly as:



For the above reaction, the equilibrium cell voltage at standard conditions (25°C) is calculated as $\Delta U_0 = -\Delta G/nF = 1.23 \text{ V}$.

The equilibrium cell voltage for the same reaction can vary depending on the reaction environment, such as the type of electrolyte used (acidic or alkaline). While all fuel cells share a similar overall structure, each cell comprises two electrodes separated by an electrolyte and connected through an external circuit. These electrodes are exposed to gas or air flow to facilitate crucial adsorption and subsequent oxidation/reduction processes.

Following the oxidation process at the anode, the resulting ions participate in the reduction of O_2 to produce water. Electrons released at the anode during oxidation travel through the outer circuit to the cathode, where they aid in the reduction of O_2 alongside H^+ ions. The electrolyte must be impermeable to gas molecules to ensure efficient reactions. Typically, water is the product of the overall reaction, primarily generated at the cathode. However, in high-temperature fuel cells using oxygen ion-conducting electrolytes, water may also form at the anode.

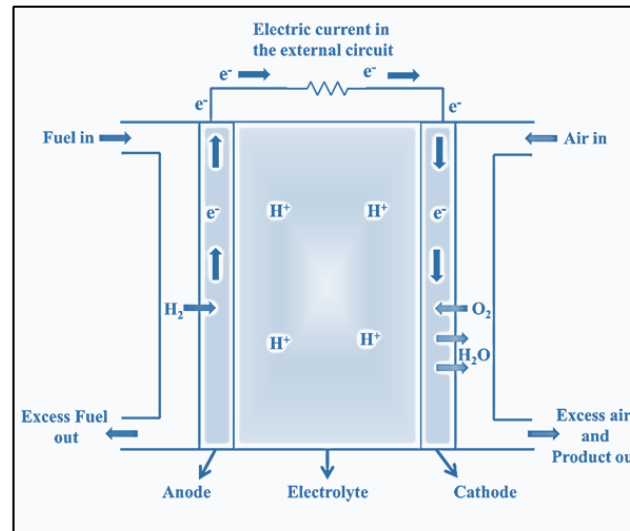


Figure 1.6: Working principles of a fuel cell.

1.3.1. Efficiency of fuel cells:

Fuel cells are renowned for their superior efficiency compared to traditional combustion engines. They typically boast a base efficiency ranging from 40% to 60%, indicating the ratio of electrical energy generated to the energy content of the fuel. Unlike combustion engines, which operate at efficiency levels below 20% and dissipate over 80% of the energy as heat, fuel cells employ an electrochemical process to directly convert the chemical energy from the fuel into electricity. This direct conversion minimizes energy losses, making fuel cells more efficient.

One crucial aspect affecting the performance of fuel cells is overpotential, represented by the Greek symbol η . Overpotential signifies the deviation of the cell potential from its equilibrium value when current flows through the cell. This deviation arises due to various factors, including limitations of the electrodes. While electrodes are pivotal in facilitating electron-related reactions, they can only operate at a finite rate due to constraints such as mass transport limitations and reaction kinetics. Consequently, the actual rate of electrochemical reactions at the electrodes may not suffice to maintain the cell potential at its equilibrium value, leading to overpotential.

To enhance fuel cell efficiency, reducing overpotential is imperative. Strategies for achieving this involve optimizing electrode materials, improving mass transport properties, and enhancing the kinetics of electrochemical reactions. Catalysts play a pivotal role in this regard

by facilitating reactions at the electrodes. They achieve this by lowering the activation energy required for reactions to occur, thereby increasing reaction rates and reducing overpotential.

Catalysts contribute to reducing overpotential in several ways. Firstly, they provide an alternative reaction pathway with lower activation energy compared to the uncatalyzed reaction, allowing reactions to proceed more readily. Secondly, catalysts enhance reaction kinetics by increasing the rate of electron transfer and reactant conversion at the electrode surface. Additionally, they improve selectivity, directing desired reaction pathways and minimizing side reactions that could contribute to overpotential. Furthermore, catalysts stabilize reaction intermediates, making them more available for further reaction steps and reducing energy barriers. Finally, catalysts can be structured or deposited to increase the active surface area, providing more sites for reaction and effectively reducing overpotential.

In summary, catalysts play a crucial role in reducing overpotential in fuel cells by improving reaction kinetics, lowering activation energies, and promoting selective and efficient reaction pathways. This contributes significantly to enhancing the efficiency and performance of fuel cells and other electrochemical devices.

The Butler-Volmer equation relates the current density at an electrode to the overpotential. It is expressed as:

$$j = j_0 \{ \exp(\alpha_A F \eta / RT) - \exp(\alpha_C F \eta / RT) \} \quad (1.1)$$

The exchange current density, denoted as j_0 represents the rate of electrochemical reactions occurring at the electrode interface under equilibrium conditions. Transfer coefficients α_A and α_C describe the kinetics of reactions at the anode and cathode, respectively. The overpotential η signifies the deviation from equilibrium potential due to various factors such as activation energy and charge transfer resistance. In addition to these factors, limitations like mass transport hindrance contribute to potential losses in the system. These losses affect the efficiency of the fuel cell by impeding the movement of reactants and products to and from the electrode surfaces. Experimental studies that examine the relationship between current density and overpotential provide crucial insights into the overall performance of the fuel cell. By analysing this relationship, researchers can understand how efficiently the cell converts chemical energy into electrical energy and identify areas for improvement, such as optimizing electrode materials or enhancing mass transport properties.

In theoretical calculations based on first principles, the spontaneity of reactions and intermediate steps is determined using Gibbs free energy change (ΔG). For reactions involving multiple electron transfers, overpotential is derived as the minimum ΔG value at any intermediate step. This is represented as:

$$\eta = \text{Min} [\Delta G_{ij}] \quad (1.2)$$

To compare a fuel cell's performance with other systems like internal combustion engines, we need to compute its thermodynamic efficiency. It's calculated using the equation:

$$\varepsilon^{\text{cell}} = \frac{W_e}{(-\Delta H)} = \frac{nF\Delta U_0}{(-\Delta H)} = \frac{\Delta G}{(-\Delta H)} = 1 - \frac{T\Delta S}{\Delta H} \quad (1.3)$$

Here, W_e is the electrical work done by the cell, ΔS is the entropy change at constant temperature, and $T\Delta S$ represents reversible heat exchange with the surroundings. ΔS depends on the reactants and products of the cell's chemical reaction.

Although electrochemical efficiency (ε_v) is a better measure of fuel cell performance, it's calculated as:

$$\varepsilon^v = \frac{\Delta U_{\text{cell}}}{\Delta U_0} = 1 - \frac{(|\eta_a(j)| + |\eta_c(j)| + R_e j)}{\Delta U_0} \quad (1.4)$$

In practical applications, other factors like Faradaic efficiency (ε_F), which measures actual current yield compared to theoretical maximum, and fuel utilization must be considered. Additionally, not all fuel is utilized to prevent depletion of electrode areas. The overall efficiency is expressed as:

$$\varepsilon = \varepsilon^{\text{cell}} * \varepsilon^v * \varepsilon^F * U * \varepsilon^H \quad (1.5)$$

Where U and ε_H represent fuel utilization and heating value efficiency respectively.

Despite these considerations, fuel cell efficiency surpasses that of heat engines. For instance, phosphoric acid fuel cells (PAFC) exhibit lower efficiency compared to other fuel cell types [52, 54]. Detailed discussions on various fuel cell types, their internal reactions, and applications follow in subsequent sections [50-56].

1.3.2. Types of fuel cell:

There are several types of fuel cells, each tailored for specific applications and featuring unique characteristics. Let's delve into some of the most common ones:

1. Proton exchange membrane fuel cell (PEMFC):

- PEMFCs function at relatively low temperatures, typically below 100°C, utilizing a solid polymer electrolyte membrane, such as Nafion, to conduct protons.
- They excel in applications requiring high power density and rapid startup times, like automotive vehicles, portable electronics, and backup power systems.
- Utilizing hydrogen as fuel and oxygen from the air as the oxidant, PEMFCs demonstrate high efficiency, low emissions, and quick response times, making them versatile for various uses.

2. Direct methanol fuel cell (DMFC):

- DMFCs, a variation of PEMFCs, directly utilize methanol as fuel instead of hydrogen.
- They offer ease of fuel handling, as methanol is simpler to transport and store compared to hydrogen.
- Primarily found in portable electronic devices like laptops, smartphones, and small generators, DMFCs, however, tend to have lower power densities and efficiencies than hydrogen-based PEMFCs.

3. Solid oxide fuel cell (SOFC):

- Operating at high temperatures ranging between 500°C and 1000°C, SOFCs employ a solid ceramic electrolyte, typically yttria-stabilized zirconia (YSZ), to conduct oxygen ions.
- With the capability to directly utilize various fuels including hydrogen, methane, and carbon monoxide, SOFCs offer flexibility in fuel options.
- Ideal for stationary power generation purposes such as residential and industrial combined heat and power (CHP) systems, as well as auxiliary power units (APUs) in transportation, SOFCs simplify fuel processing through internal hydrocarbon reforming.

4. Molten carbonate fuel cell (MCFC):

- Operating at temperatures between 650°C and 1000°C, MCFCs employ a molten carbonate salt mixture as the electrolyte.
- Versatile in fuel selection including natural gas, biogas, and hydrogen, MCFCs are well-suited for large-scale stationary power generation applications such as grid-connected power plants and industrial cogeneration facilities.
- The elevated operating temperatures facilitate internal hydrocarbon reforming, contributing to enhanced overall system efficiency.

5. Phosphoric acid fuel cell (PAFC):

- PAFCs operate at moderately high temperatures, typically between 150°C and 220°C. Operating a PAFC at 400K falls well within its optimal temperature range.
- At 400K, PAFCs can maintain efficient performance and high-power output. The elevated temperature facilitates the conductivity of the phosphoric acid electrolyte, enabling efficient ion transport and electrochemical reactions.
- PAFCs are known for their reliability and long-term stability, even at elevated temperatures. Operating at 400K allows for consistent performance and minimal degradation over time.
- These fuel cells are suitable for stationary power generation applications, such as cogeneration systems for residential, commercial, and industrial use.

6. Alkaline fuel cell (AFC):

- AFCs utilize an alkaline electrolyte, typically potassium hydroxide (KOH) solution, and operate at relatively lower temperatures.
- Historically employed in NASA's space missions due to their high efficiency and reliability, AFCs are undergoing continuous research and development for potential utilization in niche markets such as space exploration, stationary power generation, and specific military applications.

These various types of fuel cells offer distinct advantages and limitations, catering to diverse application requirements, operating conditions, and fuel availabilities. Continuous research and development endeavours are aimed at further enhancing the performance, durability, and cost-effectiveness of fuel cell technologies for widespread adoption across various sectors.

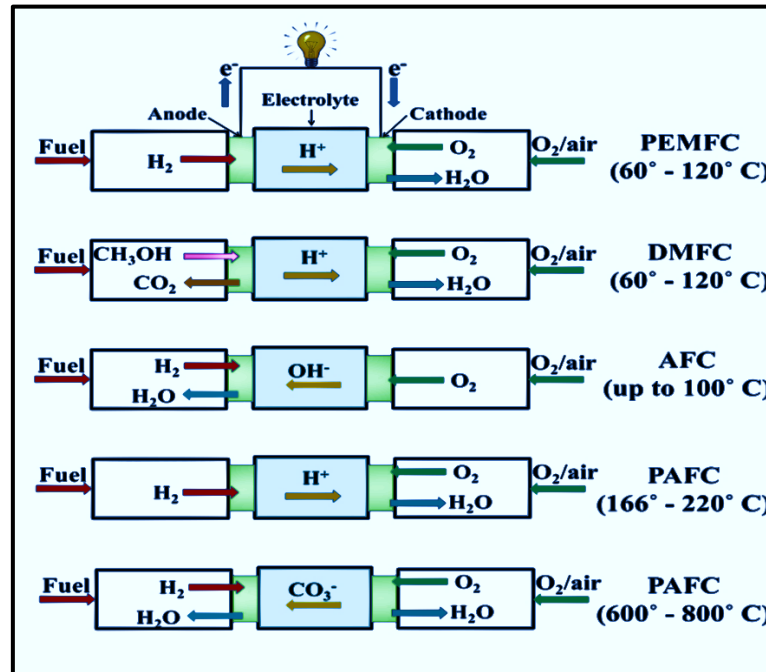


Figure 1.5: The operation of various types of fuel cells

Alkaline Fuel Cells (AFCs), Proton Exchange Membrane Fuel Cells (PEMFCs), and Phosphoric Acid Fuel Cells (PAFCs) have risen to prominence as the leading choices in fuel cell technology. AFCs boast the highest electrical efficiency among fuel cells [57-58]. However, they are limited to functioning effectively only with ultra-pure gas fuels, hindering their large-scale commercialization efforts. Despite this limitation, AFCs offer a distinct advantage over PAFCs with faster oxygen reduction rates at the cathode due to their alkaline electrolyte, making them appealing for specific applications. Notably, AFCs were among the first fuel cells deployed in space during the Apollo mission [59, 60].

PAFCs, on the other hand, have seen the most commercial development compared to other fuel cell types. Both PEMFCs and PAFCs share identical anodic and cathodic reactions. While PEMFCs find usage patterns akin to AFCs, PAFCs are predominantly employed in power plants ranging from dispersed to onsite generation facilities. PAFCs offer advantages such as simple configuration, high thermal and electrochemical stability, and non-volatility of the acid

electrolyte at operating temperatures, which have propelled their primary development for commercial use.

Despite the evident advantages of fuel cells in terms of energy generation efficiency and environmentally friendly energy production, widespread deployment to meet the energy demand across various sectors remains a distant reality. Major limitations hindering large-scale fuel cell production are discussed in subsequent sections.

1.3.3. Limitation of fuel cells:

Fuel cells hold immense promise as a green energy source with superior efficiency compared to heat engines, offering a wide range of power generation capabilities. However, the large-scale adoption of fuel cells for household and high-performance grid applications remains a challenge due to the absence of an optimal electrode material that balances efficiency and cost. The cathode, in particular, plays a critical role in fuel cell performance, and the lack of an efficient, stable, and low-cost cathode material is a major bottleneck in commercialization efforts.

The oxygen reduction reaction (ORR) at the cathode is complex and sluggish, leading to high overpotential and performance degradation. Efficient cathode materials must meet several key requirements:

- (a) **Activity:** The catalyst must adsorb oxygen molecules strongly enough to facilitate the ORR while allowing the product to desorb from the catalyst surface. The ideal interaction between the catalyst and adsorbate lies between weak physical adsorption and strong interaction to avoid blockage of active sites.
- (b) **Selectivity:** The catalyst should promote the ORR along the energetically efficient four-electron pathway, minimizing the formation of toxic by-products such as hydrogen peroxide. Maintaining selectivity is crucial for maximizing electrical power generation.
- (c) **Stability:** Cathode materials must withstand the harsh environment of fuel cells, including exposure to strong oxidants, reactive radicals, low pH, and temperature fluctuations. Stability is essential for long-term performance and durability.
- (d) **Poisoning resistance:** Resistance to poisoning from elements present in fuel cells and impurities in fuels, such as sulphur and carbon monoxide, is critical. These elements can block active sites on the electrode surface, reducing fuel cell efficiency significantly.

Traditionally, platinum group metals (PGMs) like Pt and Pd have been favoured as electrode materials due to their noble nature and moderate activity. However, challenges such as scarcity, high cost, and susceptibility to poisoning hinder their widespread use. Metals like Cu and Ni bind oxygen too strongly, leading to surface blockage [61-64], while metals like Ag and Au bind oxygen too weakly [65], resulting in slow reaction rates. Pt and Pd strike a balance, binding oxygen molecules with moderately strong interactions and following the dissociative adsorption manner, thereby increasing performance and reducing the production of undesirable by-products. Transition metals such as iron (Fe) and cobalt (Co) can indeed dissolve under certain conditions of low pH [66]. Despite their effectiveness, the scarcity and cost of PGMs, along with their susceptibility to poisoning [71-73], drive research efforts towards finding alternative cathode materials. The development of efficient, stable, and cost-effective cathode materials is crucial for overcoming the limitations hindering the large-scale commercialization of fuel cells.

1.3.4. The role of 2D materials in addressing fuel cell limitations:

2D materials offer significant promise due to their unique surface properties, mechanical stability, and electronic characteristics. These materials possess a high surface-to-volume ratio, excellent mechanical stability, and can be easily controlled in terms of thickness [78-87]. They also exhibit intrinsic properties that allow for manipulation of vacancies and creation of defects, all while being cost-effective to manufacture. These features make them excellent candidates for electrocatalysis in various important reactions, potentially replacing precious group metals (PGMs) as fuel cell cathode electrocatalysts in the near future. As these materials are thinned to single or few layers held together by weak Van der Waals forces, they expose more surface area compared to their 3D counterparts. This increased surface area leads to a higher number of active sites for chemical reactions, facilitating chemisorption and efficient interfacial charge transfer processes. Their ultra-high specific surface area, along with superior electrical conductivity and short charge transfer paths, makes them ideal for catalysis, electrocatalysis, and chemical reduction applications. Compared to other low-dimensional systems like nanotubes, nanowires, and nanoporous materials, 2D materials consistently offer larger specific surface areas, resulting in a greater number of electrocatalytic active sites at equivalent loading concentrations of the electrocatalyst. The ability to easily control the thickness of 2D materials is another advantageous characteristic that allows for modulation of their electronic and electrocatalytic properties. As the thickness decreases to a single layer or a few layers, the band gap widens due to quantum confinement effects, leading to a larger density of states

(DOS) at the surface compared to the bulk structure. This increased DOS at the surface enhances catalytic activities and facilitates smooth charge transfer processes. Moreover, reducing thickness can manipulate the electronic structure, such as lowering the work function, offering opportunities for band alignment in electrocatalyst design. Additionally, as 2D materials become thinner, they become more reactive due to increased bonding with other elements in the absence of interlayer Van der Waals interactions, further enhancing their chemical activities.

Cation and anion vacancies are fundamental modulators in 2D monolayered crystals (inherently due to their 3D crystal lattice origins) significantly impacting their electrocatalytic properties. These intrinsic defects, like oxygen vacancies in 2D In_2O_3 [88], create a higher density of states at the surface according to theoretical and experimental calculations. Vacancy defects lead to the formation of defect levels within the forbidden region, facilitating easier electron transfer from valence to conduction bands. This translates to higher carrier concentration and mobility, ultimately enhancing the electrocatalytic performance of these 2D materials [89].

2D layered structures, with their expansive surface area and increased accessibility, allow for easier introduction of external defects through doping and adsorption processes compared to bulk materials. This spontaneous defect creation offers exciting possibilities in terms of electronic, surface, and electrocatalytic properties. Doping these materials can redistribute electron density, increase the number of mobile electrons, and distort atomic arrangements. Additionally, the abundant exposed surface area provides a wealth of active sites readily available for chemical reactions [6, 90, 91]. By creating a surplus of active sites via doping or adsorption, we gain significant control over the electronic properties, allowing for fine-tuning of electrocatalytic performance.

In the context of utilizing 2D materials as cathode electrocatalysts in fuel cells, various phases of transition metal dichalcogenides (TMDs) such as MoS_2 [92], WS_2 [93], and WSe_2 [94] offer significant promise. These materials exhibit diverse properties across different phases, including 2H, 1T, and 1T', ranging from semiconducting to metallic or semi metallic behaviour [95]. Additionally, they demonstrate inherent resistance to sulphur and CO poisoning, crucial factors for maintaining catalytic activity in fuel cell environments. Moreover, 2D TMDs possess exceptional mechanical and chemical stability, further enhancing their suitability for long-term fuel cell applications. Moreover, these 2D TMDs offer the added advantage of cost-

effective manufacturing, making them highly attractive substitutes for replacing precious group metal (PGM)-based electrocatalysts. This affordability factor further strengthens their potential for the widespread commercialization of economic and efficient fuel cells.

While pure graphene remains inert towards the oxygen reduction reaction (ORR), transition metal dichalcogenides (TMDs) have emerged as promising alternatives for fuel cell cathode materials, particularly when doped with transition metals or exhibiting intrinsic defects. These modified versions of TMDs have demonstrated significant potential in enhancing ORR efficiency. However, much of the research has predominantly focused on doped and defected 2H-phase TMDs, with other phases such as 1T and 1T' remaining relatively unexplored both theoretically and experimentally. In my doctoral thesis, I aim to bridge this gap by investigating the electronic and catalytic properties of various TMD phases, including 2H, 1T, and 1T', while introducing doping and altering charge distribution to elucidate their potential in fuel cell applications. Moreover, the concept of Janus materials, inspired by the two-faced Roman god, involves structures with distinct properties or elemental compositions on opposing surfaces. In the realm of TMDs, Janus structures can exhibit different elements or surface terminations on each side. These Janus TMDs, although less studied compared to their uniform counterparts, offer exciting opportunities to explore a wide range of properties, including electronic, catalytic, phononic, and optical properties. My thesis work delves into the unique characteristics of Janus TMDs, aiming to unravel their full potential in various applications, including optoelectronics, solar energy, fuel cells, and more.

1.4. Phononic process:

In the fascinating world of condensed matter physics, phonons emerge as pivotal players. Unlike ordinary sound waves, they are quantized excitations, offering a quantum mechanical framework for describing vibrations within a crystal lattice of atoms or molecules. Imagine a lattice as a network of interconnected balls, and phonons represent the specific ways these balls vibrate together. Understanding phononic processes unravels insights into material properties and fuels innovative technologies [96].

Phonons: Unlike classical sound waves, phonons exist in discrete energy packets. Think of them as tiny packets of vibration energy moving through the lattice. The frequency of these packets determines the type of phonon – higher frequencies correspond to more energetic vibrations. Just like light is made of photons, sound in solids is made of phonons.

Types of Phononic processes: The world of phonons is a bustling one, filled with various interactions. Here are some key players:

Phonon-phonon scattering: As phonons travel, they can bump into each other, exchanging energy and momentum. This "scattering" can be further categorized based on how the phonon wavevectors (direction and magnitude of momentum) change during the interaction. Umklapp processes, where the total wavevector changes significantly, are particularly important at high temperatures and influence thermal conductivity.

Phonon-impurity scattering: When foreign atoms (impurities) sneak into the crystal lattice, they disrupt the smooth flow of vibrations. Phonons interact with these impurities, scattering and losing energy in the process. This scattering affects how efficiently heat travels through the material.

Phonon-electron scattering: The energetic interplay extends beyond just phonons. In certain materials, phonons engage in a dynamic interaction with electrons, facilitating the transfer of energy between them. This coupling is fundamental in superconductivity, where electrical resistance disappears at ultra-low temperatures.

Phonon-boundary scattering: When a phonon reaches the edge of the material, it encounters a boundary—a sharp departure from the familiar periodic lattice. This interaction can result in reflection, transmission, or even absorption of the phonon, which in turn impacts the material's thermal and acoustic characteristics.

Applications of Phononic processes: The knowledge of phononic processes empowers scientists and engineers to design materials with specific properties [97-100]:

- (i) **Thermal management:** By gaining insights into the mechanisms by which phonons transport heat, scientists can engineer materials with tailored thermal conductivity properties. This knowledge allows for the creation of materials with either high or low thermal conductivity. High thermal conductivity is highly desirable for applications such as heat sinks in electronics, where effective heat dissipation is critical for preventing overheating. Materials like diamond or certain ceramics exhibit high thermal conductivity because of the efficient transport of heat by phonons. This property allows them to efficiently transfer heat away from electronic components, thereby ensuring optimal performance and reliability. Low thermal conductivity is advantageous for applications requiring thermal insulation or for the development of

thermoelectric materials. Materials such as aerogels or certain polymers possess low thermal conductivity because phonons encounter significant obstacles in traveling through them. This property enables these materials to effectively inhibit the transfer of heat, making them suitable for insulation purposes or for enhancing the efficiency of thermoelectric devices. Researchers are actively involved in the development of materials with customized thermal conductivities using techniques like doping or nanostructuring. Their goal is to optimize thermal transport properties by understanding the intricate interactions between phonons and defects or interfaces within materials.

- (ii) **Phononic crystals:** By carefully engineering the crystal structure, scientists can create materials with periodic variations that manipulate phonons in specific ways. These phononic crystals have applications in sound filtering, acoustic waveguiding, and even thermal cloaking.
- (iii) **Superconducting materials:** Optimizing phonon-electron interactions is crucial for developing high-temperature superconductors, which would revolutionize power transmission and energy storage.

The world of phononic processes is vast and ever-evolving. Researchers are exploring the interaction of phonons with light (phonon-photon coupling) to create novel optoelectronic devices. Additionally, the study of nonlinear phononic processes, where multiple phonons interact in complex ways, opens doors to new possibilities in material manipulation. Phononic processes are the hidden language of vibrations within solids, dictating how heat flows, sound propagates, and electrons behave. By understanding this language, scientists can tailor materials to meet specific needs. In practical applications, the ability to control thermal conductivity offers significant potential. Engineers can employ materials with tailored thermal conductivities to create more efficient electronic devices, improve thermal management systems in buildings to enhance energy efficiency, and design advanced thermoelectric generators capable of converting waste heat into electricity with greater efficiency. These advancements have the potential to transform various industries, resulting in enhanced performance, energy conservation, and environmental sustainability.

1.5. The benefits of computational studies based on DFT:

This thesis aims to investigate the electrocatalytic properties of doped WS₂, primarily focusing on the 1T' and 2H phases, as potential cathode electrocatalysts in fuel cells. Additionally, this

study delves into less-explored Janus structures based on TaS₂ and TaSe₂, conducting a thorough investigation to comprehend their applicability in optoelectronic solar cells, catalysts, and other relevant areas. The exploration will be carried out through theoretical analysis using computer-based simulations, specifically leveraging density functional theory (DFT) [101, 102]. The utilization of DFT has proven to be invaluable, offering theoretical insights into material properties, applications, and providing experimental guidance while validating conceptual developments. Theoretical calculations based on DFT serve as a robust foundation for comprehending and developing potential electrocatalysts for heterogeneous catalysis [103]. The widespread implementation of DFT across various commercial and freely available software platforms such as VASP [104], PWscf [105], CASTEP [106], among others, coupled with advancements in computational efficiency and the computational power of high-performance computers (HPCs), has created an ideal environment for conducting extensive theoretical research. DFT has become indispensable in elucidating diverse material properties, making significant contributions to fields encompassing physics, chemistry, and materials science. This has led to a remarkable increase in the number of research papers utilizing DFT-based calculations in recent years, as depicted in Figure 1.6.

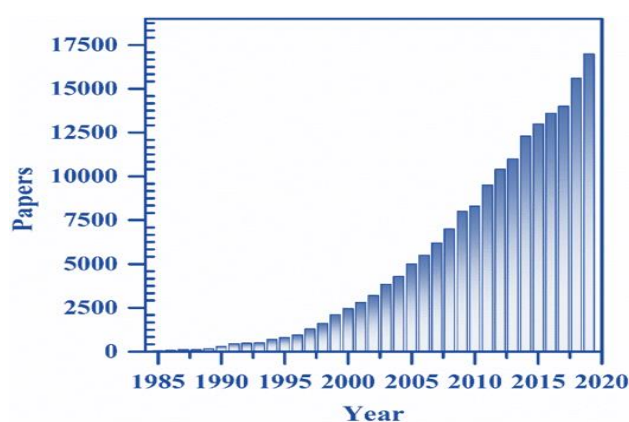


Figure 1.6: Number of papers published over the years using DFT

Computational methods based on Density Functional Theory (DFT) play a crucial role in designing efficient electrocatalytic systems. This approach provides valuable insights into the electronic interactions between dopant atoms and surrounding atoms, as well as between adsorbate molecules and surfaces [107, 108]. DFT calculations effectively reveal the band structures and density of states in doped or adsorbed systems. This information allows researchers to understand:

- Hybridization of orbitals

- Chemical bonding between foreign atoms/molecules and the base system
- Charge transfer processes
- Formation and adsorption energies
- Active site identification
- Selective adsorption behaviour

Furthermore, DFT demonstrates exceptional accuracy in predicting transition states and their corresponding energies during adsorption and reaction processes [109, 110]. The ability to model these transition states stems from their connection to the underlying electronic structure of the catalyst surface. In essence, DFT offers a powerful tool for understanding and optimizing electrocatalytic systems by providing detailed information on electronic interactions and reaction pathways. Kinetics of the chemical reaction is the central characteristic of the electrocatalyst which determines its prospects for practical implementation. The rate and selectivity of a reaction are the primary factors for designing an electrocatalyst. The chemical kinetics is closely related with microscopic properties such as adsorption energy, reaction barriers, free energy differences between intermediate steps etc. which are efficiently derived by DFT calculations. In principles, kinetics of a given electrochemical reaction can be derived from the free energy difference of the reaction (ΔG) and reaction barriers as a function of the surface structure of the catalyst. DFT calculations are able to provide the total enthalpy of the reactants and product of a reaction from which the free energy difference can be determined easily to predict the spontaneity of the reaction. In case of reactions involving gas phase molecules, such as ORR, HER etc., the inherent limitation of loss of degrees of freedom in a 0K DFT calculation can be swiftly overcome by incorporating the room temperature entropy-temperature terms of the respective gas molecules while deriving the free energy differences [65]. Also, the effect of electrolyte medium and electrode potential variation can be straightforwardly consolidated with the free energies derived from DFT calculations [65]. Moreover, DFT calculations play a pivotal role not only in revealing fundamental interactions but also in identifying key parameters that govern electrocatalyst performance. These parameters, crucial for tailoring catalysts to specific reactions, encompass adsorption energies of reaction intermediates and transition state energies. Even in seemingly simple reactions, a multitude of variables (ranging from 10 to 20) can influence reaction rates.

Fortunately, DFT calculations capitalize on the inherent correlations between these variables and the catalyst's electronic structure. This capability enables researchers to condense the myriad variables into one or two "descriptors" without sacrificing accuracy beyond the inherent limitations of DFT's exchange-correlation function. These descriptors encapsulate the essence of the reaction, facilitating prediction, comparison, and analysis of various electrocatalysts or active sites within a single catalyst.

Moreover, these descriptors serve as the foundation for establishing "volcano plots," a fundamental concept in catalysis. Volcano plots correlate the chosen descriptor with electrocatalyst performance, thereby unveiling the optimal catalyst residing at or near the peak of the curve. Remarkably, the optimal catalyst often remains independent of the specific descriptor employed.

In essence, DFT transcends the mere understanding of interactions to provide a crucial design framework. The identified descriptors act as a bridge between computational predictions and real-world catalyst development, steering experimentalists towards targeted laboratory efforts. As discussed earlier, the multitude of advantages offered by DFT proves invaluable in predicting the efficiency of an electrocatalyst for a specific reaction. Indeed, employing first-principles DFT-based calculations enables the determination of reaction kinetics and efficiencies of WS₂ phases towards oxygen reduction reaction (ORR) and hydrogen evolution reaction (HER). In this context, our study will utilize first-principles DFT methodologies to assess the electrocatalytic performance of pristine and doped 2H and 1T' phases of WS₂ for ORR and HER across various electrolyte mediums. The aim is to identify the most promising candidates by conducting a comprehensive comparison of their electrocatalytic performance using a common descriptor. Our objective is to provide a detailed roadmap for experimentalists, facilitating the utilization of doped 1T' WS₂ as the cathode material for fuel cells through systematic theoretical investigations into their electrocatalytic properties. Additionally, we validated the work on Zn-doped WS₂ through experimental validation. Furthermore, given the relatively unexplored nature of Janus forms of transition metal dichalcogenides (TMDs) and their limited synthesis in experimental settings, we have undertaken the development of Janus structures of TaS₂ and TaSe₂. These structures involve replacing sulfur or selenium sites with oxygen and pnictogen groups (such as N or P), followed by observation of their electronic and phononic properties analysis.

1.6. Aims and objectives:

The primary objective of this thesis is to conduct a theoretical investigation into the potential of 2H and 1T' phases of WS₂ materials as cathode electrocatalysts for fuel cells. The aim is to explore the possibility of enhancing their catalytic activity for oxygen reduction reaction (ORR) and hydrogen evolution reaction (HER) through the introduction of extrinsic defects via doping and subsequent oxygen adsorption processes. Additionally, the goal is to identify the most promising configurations that could serve as alternative cathode electrocatalysts for efficient energy production in fuel cells. In addition to studying the electrocatalytic activities of the WS₂ materials, another important objective is to analyze and depict significant changes in their electronic properties. This analysis will provide insights into how the introduction of defects and doping affects the electronic structure of transition metal dichalcogenides (TMDs) systems. Coinage metals are particularly promising candidates for doping in TMDs due to their chemical stability, reactive surface, and partially filled d-orbitals. These properties make them suitable for forming stable doped configurations with TMDs as catalysts. Additionally, zinc (Zn) plays a crucial role as a dopant in TMDs and will be explored in this thesis. Furthermore, comparatively less explored Janus forms of TMDs are investigated to discover their potential application in the field of optoelectronics.

Given these central themes, the major aims and objectives of this thesis can be summarized as follows:

- Investigate coinage metals (Cu, Ag, and Au) doping in 1T' WS₂ for ORR and HER in acidic conditions using first principles calculations, considering the most stable systems.
- Explore non-equivalent doping sites to identify the most stable configurations for 1T' WS₂ for doping and analyze electronic and electrocatalytic properties.
- The best electrocatalysts for ORR and HER on doped 1T' WS₂ in acidic medium are to be isolated through free energy analysis taking into account the effect of electrode potential variation and overpotential values.
- To compare and predict the coinage doped 1T' WS₂ ORR electrocatalyst in acidic medium in terms of the common descriptor.
- The activities and efficiencies of Zn doped WS₂ are to be analyzed to isolate potential descriptors for the activity of those systems towards ORR in alkaline medium.
- To extend the investigation of the ORR electrocatalytic properties to alkaline medium, associative O₂ adsorption process and evaluate the ORR activity of the doped WS₂

system subject to both types of adsorptions to find out the most feasible reaction mechanism using *ab-initio* calculations.

- For the hydrogen evolution reaction (HER) pathway, the aim is to calculate the activity barriers in terms of Gibbs free energy for hydrogen adsorption on each of the doped systems.
- To identify the ORR mechanism whether it is two or four electron pathways on active sites taking into account all crucial intermediates fork such as hydrogenation and desorption sites.
- Conduct d-band center calculations to evaluate chemical reactivity of doped systems.
- Crystal Orbital Hamiltonian Population (COHP) analysis was performed to evaluate chemical bonding in the compounds.
- Assess thermodynamic, mechanical, and dynamical stabilities of Janus TaXY (X= S, Se & Y= O, N, P) monolayers by replacing S or Se sites with Oxygen, Nitrogen, or Phosphorous.
- Determine lattice thermal conductivity and specific heats of Janus monolayers at various temperatures. Variation of specific heats of janus monolayers with temperatures.
- Analyze vibrational properties of Janus monolayers through Raman spectra.
- Study electronic band structures using GGA and HSE methods and examine optical properties for optoelectronic applications.

The works represented in the subsequent chapters of this thesis will be based on the aims and objectives as stated above.

References:

- [1] Baig, Nadeem, Irshad Kammakakam, and Wail Falath. "Nanomaterials: A review of synthesis methods, properties, recent progress, and challenges." *Materials Advances* 2.6 (2021): 1821-1871.
- [2] Panwar, Nishtha, et al. "Nanocarbons for biology and medicine: sensing, imaging, and drug delivery." *Chemical reviews* 119.16 (2019): 9559-9656.
- [3] Paras, et al. "A review on low-dimensional nanomaterials: nanofabrication, characterization and applications." *Nanomaterials* 13.1 (2022): 160.
- [4] Alam, Shahinoor, et al. "Synthesis of emerging two-dimensional (2D) materials—Advances, challenges and prospects." *FlatChem* 30 (2021): 100305.
- [5] Lin, Zhong, et al. "2D materials advances: from large scale synthesis and controlled heterostructures to improved characterization techniques, defects and applications." *2D Materials* 3.4 (2016): 042001.
- [6] Wang, Tiange, and Huaijie Cao. "Orientation control and characterization strategies towards developing 2D materials-based composite coatings for corrosion protection on metals: Progresses and challenges." *Progress in Organic Coatings* 182 (2023): 107715.
- [7] Castellanos-Gomez, Andres, et al. "Isolation and characterization of few-layer black phosphorus." *2D Materials* 1.2 (2014): 025001.
- [8] Jia, Linnan, et al. "Fabrication technologies for the on-chip integration of 2D materials." *Small Methods* 6.3 (2022): 2101435.
- [9] Stein, Frank, and Andreas Leineweber. "Laves phases: a review of their functional and structural applications and an improved fundamental understanding of stability and properties." *Journal of Materials Science* 56.9 (2021): 5321-5427.
- [10] Khan, Karim, et al. "Recent developments in emerging two-dimensional materials and their applications." *Journal of Materials Chemistry C* 8.2 (2020): 387-440.
- [11] Liu, Xiaolong, and Mark C. Hersam. "2D materials for quantum information science." *Nature Reviews Materials* 4.10 (2019): 669-684.
- [12] Yu, Shaoliang, et al. "2D materials for optical modulation: challenges and opportunities." *Advanced Materials* 29.14 (2017): 1606128.
- [13] Dong, Xinyue, et al. "Exploring the high dielectric performance of Bi₂SeO₅: from bulk to bilayer and monolayer." *Science China Materials* (2024): 1-8.
- [14] Dutta, Taposhree, et al. "Electronic properties of 2D materials and their junctions." *Nano Materials Science* (2023).

- [15] Selamneni, Venkatarao, and Parikshit Sahatiya. "Mixed dimensional transition metal dichalcogenides (TMDs) vdW heterostructure based photodetectors: A review." *Microelectronic Engineering* 269 (2023): 111926.
- [16] Javed, Muhammad Sufyan, et al. "The quest for negative electrode materials for Supercapacitors: 2D materials as a promising family." *Chemical Engineering Journal* 452 (2023): 139455.
- [17] Kim, Jongyoun, et al. "Ultrastable 2D material-wrapped copper nanowires for high-performance flexible and transparent energy devices." *Nano Energy* 106 (2023): 108067.
- [18] Novoselov, Kostya S., et al. "Electric field effect in atomically thin carbon films." *science* 306.5696 (2004): 666-669.
- [19] Mbayachi, Vestince B., et al. "Graphene synthesis, characterization and its applications: A review." *Results in Chemistry* 3 (2021): 100163.
- [20] Lamiel, Charmaine, et al. "Metal-organic framework-derived transition metal chalcogenides (S, Se, and Te): Challenges, recent progress, and future directions in electrochemical energy storage and conversion systems." *Coordination chemistry reviews* 480 (2023): 215030.
- [21] Zhang, Kailiang, et al. "Two-dimensional hexagonal boron nitride (2D-hBN): synthesis, properties and applications." *Journal of Materials Chemistry C* 5.46 (2017): 11992-12022.
- [22] Luo, Miaomiao, et al. "2D black phosphorus-based biomedical applications." *Advanced Functional Materials* 29.13 (2019): 1808306.
- [23] Gogotsi, Yury, and Babak Anasori. "The rise of MXenes." *ACS nano* 13.8 (2019): 8491-8494.
- [24] Wang, Zhongying, and Baoxia Mi. "Environmental applications of 2D molybdenum disulfide (MoS₂) nanosheets." *Environmental science & technology* 51.15 (2017): 8229-8244.
- [25] Langer, Fabian, et al. "Lightwave valleytronics in a monolayer of tungsten diselenide." *Nature* 557.7703 (2018): 76-80.
- [26] Dai, Jun, and Xiao Cheng Zeng. "Titanium trisulfide monolayer: theoretical prediction of a new direct-gap semiconductor with high and anisotropic carrier mobility." *Angewandte Chemie International Edition* 54.26 (2015): 7572-7576.
- [27] Idrees, M., et al. "Computation insights of MoS₂-CrXY (X≠ YS, Se, Te) van der waals heterostructure for Spintronic and photocatalytic water Splitting applications." *International Journal of Hydrogen Energy* 51 (2024): 1217-1228.
- [28] Jyothirmmai, M. V., et al. "Machine-Learning-Driven High-Throughput Screening of Transition-Metal Atom Intercalated g-C₃N₄/MX₂ (M= Mo, W; X= S, Se, Te) Heterostructures for the Hydrogen Evolution Reaction." *ACS Applied Materials & Interfaces* (2024).

- [29] McMillan, W. L. "Microscopic model of charge-density waves in 2 H– Ta Se 2." *Physical Review B* 16.2 (1977): 643.
- [30] Garnaes, J., et al. "Atomic force microscopy of charge density waves and atoms on 1T– TaSe₂, 1T–TaS₂, 1T–TiSe₂, and 2H–NbSe₂." *Journal of Vacuum Science & Technology B: Microelectronics and Nanometer Structures Processing, Measurement, and Phenomena* 9.2 (1991): 1032-1035.
- [31] Silva-Guillén, José Ángel, et al. "Electronic structure of 2H-NbSe₂ single-layers in the CDW state." *2D Materials* 3.3 (2016): 035028.
- [32] Luckin, William RB, et al. "Controlling charge density order in 2 H– TaSe₂ using a van Hove singularity." *Physical Review Research* 6.1 (2024): 013088.
- [33] Hussain, Iftikhar, et al. "Mo-based MXenes: Synthesis, properties, and applications." *Advances in Colloid and Interface Science* (2024): 103077.
- [34] Reddy, M. Sai Bhargava, and Shampa Aich. "Recent progress in surface and heterointerface engineering of 2D MXenes for gas sensing applications." *Coordination Chemistry Reviews* 500 (2024): 215542.
- [35] Reddy, M. Sai Bhargava, and Shampa Aich. "Recent progress in surface and heterointerface engineering of 2D MXenes for gas sensing applications." *Coordination Chemistry Reviews* 500 (2024): 215542.
- [36] Tan, Adriel Yan Sheng, et al. "Recent advances in the use of MXenes for photoelectrochemical sensors." *Chemical Engineering Journal* (2024): 148774.
- [37] Fan, Lu, et al. "Carbon-based synergistic catalysis with transition metal dichalcogenides for electrocatalytic oxygen evolution/reduction." *Materials Chemistry and Physics* (2024): 129163.
- [38] Li, Zhengrui, et al. "Theoretical screening of transition metal atoms doped two-dimensional VSe₂ monolayers as single-atom catalysts for HER, OER and ORR." *Applied Surface Science* 646 (2024): 158959.
- [39] Sen, Prasenjit. "Computational screening of layered metal chalcogenide materials for HER electrocatalysts, and its synergy with experiments." *Journal of Physics: Condensed Matter* 36 (2024): 223002.
- [40] Ma, Liangyu, et al. "Two-dimensional transition metal dichalcogenides for electrocatalytic nitrogen fixation to ammonia: Advances, challenges and perspectives. A mini review." *Electrochemistry Communications* 125 (2021): 107002.
- [41] Poojita, et al. "Intrinsic Specific Activity Enhancement for Bifunctional Electrocatalytic Activity toward Oxygen and Hydrogen Evolution Reactions via Structural Modification of Nickel Organophosphonates." *Inorganic Chemistry* 63(8) (2024) :3795–3806.

- [42] Xiang, Haiyan, et al. "Rational design and application of electrocatalysts based on transition metal selenides for water splitting." *Materials Chemistry Frontiers* 8 (2024):1888-1926.
- [43] Han, Xiaotong, Xu Yu, and Ho Seok Park. "Recent advances in trifunctional electrocatalysts for Zn–air battery and water splitting." *Materials Chemistry Frontiers* 8 (2024):1536-1562.
- [44] Wang, Xiaoyan, et al. "Recent advances of bifunctional electrocatalysts and electrolyzers for overall seawater splitting." *Journal of Materials Chemistry A* 12 (2024) 634-656.
- [45] World Energy Outlook 2019, IEA. Online available at: <https://www.iea.org/reports/world-energy-outlook-2019>
- [46] "Fossil fuel". ScienceDaily. Archived from the original on 10 May 2012. Online available at: https://www.sciencedaily.com/terms/fossil_fuel.htm
- [47] "When Fossil Fuels Run Out, What Then?", Gioietta Kuo, MAHB, 2019. Online available at: <https://mahb.stanford.edu/library-item/fossil-fuels-run/>.
- [48] "The Carbon Age: 150 Years of CO₂ Emissions", Dyfed Loesche, statista. Online available at: <https://www.statista.com/chart/13584/worldwide-carbon-emissions-from-fossil-fuel-consumption-and-cement-production/>.
- [49]"Renewable Energy", Hannah Ritchie and Max Rose, Our World in Data, 2020. Online available at: <https://ourworldindata.org/renewable-energy>
- [50] Dyer, Christopher K. "Fuel cells for portable applications." *Journal of Power Sources* 106.1-2 (2002): 31-34.
- [51] Carrette, Linda, K. Andreas Friedrich, and Ulrich Stimming. "Fuel cells: principles, types, fuels, and applications." *ChemPhysChem* 1.4 (2000): 162-193.
- [52] Carrette, L., K. A. Friedrich, and U1 Stimming. "Fuel cells-fundamentals and applications." *Fuel cells* 1 (2001): 5-39.
- [53] Hou, Yongping, Mingxi Zhuang, and Gang Wan. "The analysis for the efficiency properties of the fuel cell engine." *Renewable Energy* 32.7 (2007): 1175-1186.
- [54] Farooque, Mohammad, and Hans C. Maru. "Fuel cells-the clean and efficient power generators." *Proceedings of the IEEE* 89.12 (2001): 1819-1829.
- [55] Tomczyk, Piotr. "MCFC versus other fuel cells—Characteristics, technologies and prospects." *Journal of Power sources* 160.2 (2006): 858-862.
- [56] Rostrup-Nielsen, Jens R. "Conversion of hydrocarbons and alcohols for fuel cells." *Physical Chemistry Chemical Physics* 3.3 (2001): 283-288.

- [57] Gülzow, Erich, and Mathias Schulze. "Alkaline fuel cells." *Materials for Fuel Cells*. Woodhead Publishing, 2008. 64-100.
- [58] Adzic, Radoslav, et al. "Electrochemical Energy Conversion in Fuel Cells." *Platinum Monolayer Electrocatalysts* (2020): 19-25.
- [59] Warshay, Marvin, and Paul R. Prokopius. "The fuel cell in space: yesterday, today and tomorrow." *Grove Anniversary (1839-1989) Fuel Cell Symposium*. No. E-5084. 1989.
- [60] Medford, Andrew J., et al. "From the Sabatier principle to a predictive theory of transition-metal heterogeneous catalysis." *Journal of Catalysis* 328 (2015): 36-42.
- [61] Mamlouk, M., et al. "Characterization and application of anion exchange polymer membranes with non-platinum group metals for fuel cells." *Proceedings of the Institution of Mechanical Engineers, Part A: Journal of Power and Energy* 225.2 (2011): 152-160.
- [62] Piana, Michele, Stefano Catanorchi, and H. A. Gasteiger. "Kinetics of non-platinum group metal catalysts for the oxygen reduction reaction in alkaline medium." *Ecs Transactions* 16.2 (2008): 2045.
- [63] Hammer, Bjørk, and Jens Kehlet Nørskov. "Theoretical surface science and catalysis—calculations and concepts." *Advances in catalysis*. Vol. 45. Academic Press, 2000. 71-129.
- [64] Nørskov, Jens K., et al. "The nature of the active site in heterogeneous metal catalysis." *Chemical Society Reviews* 37.10 (2008): 2163-2171.
- [65] Nørskov, Jens Kehlet, et al. "Origin of the overpotential for oxygen reduction at a fuel-cell cathode." *The Journal of Physical Chemistry B* 108.46 (2004): 17886-17892.
- [66] Holton, Oliver T., and Joseph W. Stevenson. "The role of platinum in proton exchange membrane fuel cells." *Platinum Metals Review* 57.4 (2013): 259-271.
- [67] Feng, Yongjun, and Nicolas Alonso-Vante. "Nonprecious metal catalysts for the molecular oxygen-reduction reaction." *physica status solidi (b)* 245.9 (2008): 1792-1806.
- [68] Xia, Zhonghong, et al. "Non-Pt nanostructured catalysts for oxygen reduction reaction: synthesis, catalytic activity and its key factors." *Advanced Energy Materials* 6.17 (2016): 1600458.
- [69] Gong, Kuanping, et al. "Nitrogen-doped carbon nanotube arrays with high electrocatalytic activity for oxygen reduction." *science* 323.5915 (2009): 760-764.
- [70] Sun, Xiujuan, et al. "A class of high-performance metal-free oxygen reduction electrocatalysts based on cheap carbon blacks." *Scientific reports* 3.1 (2013): 2505.
- [71] Liu, Yuxiu, et al. "Effects of catalyst carbon support on proton conduction and cathode performance in PEM fuel cells." *Journal of The Electrochemical Society* 158.6 (2011): B614.

[72] Liu, Zhiming, et al. "Pt alloy electrocatalysts for proton exchange membrane fuel cells: a review." *Catalysis Reviews* 55.3 (2013): 255-288.

[73] Wu, Qiuling, et al. "A novel octahedral MnO/RGO composite prepared by thermal decomposition as a noble-metal free electrocatalyst for ORR." *Journal of Materials Science* 52 (2017): 6656-6669.

[74] Jeon, In-Yup, et al. "Edge-selectively sulfurized graphene nanoplatelets as efficient metal-free electrocatalysts for oxygen reduction reaction: the electron spin effect." *Advanced Materials* 25.42 (2013): 6138-6145.

[75] Jeon, In-Yup, et al. "Antimony-doped graphene nanoplatelets." *Nature communications* 6.1 (2015): 7123.

[76] Wang, Shuangyin, et al. "Vertically aligned BCN nanotubes as efficient metal-free electrocatalysts for the oxygen reduction reaction: a synergetic effect by co-doping with boron and nitrogen." *Angewandte Chemie International Edition* 50.49 (2011): 11756-11760.

[78] Gupta, Ankur, Tamilselvan Sakthivel, and Sudipta Seal. "Recent development in 2D materials beyond graphene." *Progress in Materials Science* 73 (2015): 44-126.

[79] Malyi, Oleksandr I., Kostiantyn V. Sopiha, and Clas Persson. "Energy, phonon, and dynamic stability criteria of two-dimensional materials." *ACS applied materials & interfaces* 11.28 (2019): 24876-24884.

[80] Lanza, Mario, et al. "Yield, variability, reliability, and stability of two-dimensional materials based solid-state electronic devices." *Nature communications* 11.1 (2020): 5689.

[81] Tong, Xin, et al. "Low-dimensional catalysts for oxygen reduction reaction." *Progress in Natural Science: Materials International* 30.6 (2020): 787-795.

[82] Liu, Yucheng, et al. "Abnormal vibrational anisotropy and thermal properties of a two-dimensional GeAs semiconductor." *Physical Chemistry Chemical Physics* 25.5 (2023): 3745-3751.

[83] Khan, Karim, et al. "Recent advances in two-dimensional materials and their nanocomposites in sustainable energy conversion applications." *Nanoscale* 11.45 (2019): 21622-21678.

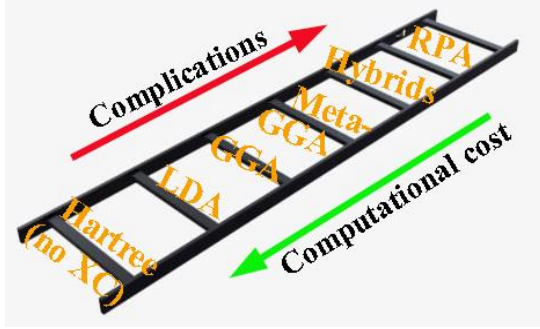
[84] Shanmughan, Bhavana, Amrita Nighojkar, and Balasubramanian Kandasubramanian. "Exploring the future of 2D catalysts for clean and sustainable hydrogen production." *International Journal of Hydrogen Energy* (2023): 28679-28693.

[85] Sen, D., R. Thapa, and K. K. Chattopadhyay. "Small Pd cluster adsorbed double vacancy defect graphene sheet for hydrogen storage: A first-principles study." *International journal of hydrogen energy* 38.7 (2013): 3041-3049.

- [86] Torrisi, Felice, and Jonathan N. Coleman. "Electrifying inks with 2D materials." *Nature nanotechnology* 9.10 (2014): 738-739.
- [87] Kostarelos, Kostas. "Translating graphene and 2D materials into medicine." *Nature Reviews Materials* 1.11 (2016): 1-2.
- [88] Wang, Yizhan, et al. "Two-dimensional nonlayered materials for electrocatalysis." *Energy & Environmental Science* 13.11 (2020): 3993-4016.
- [89] Jain, Ankit, Zhenbin Wang, and Jens K. Nørskov. "Stable two-dimensional materials for oxygen reduction and oxygen evolution reactions." *ACS Energy Letters* 4.6 (2019): 1410-1411.
- [90] Balasubramaniam, Bhuvaneshwari, et al. "Engineering of transition metal dichalcogenide-based 2D nanomaterials through doping for environmental applications." *Molecular Systems Design & Engineering* 4.4 (2019): 804-827.
- [91] Ruqia, Bibi, et al. "Catalyst activation: Surface doping effects of group VI transition metal dichalcogenides towards hydrogen evolution reaction in acidic media." *Journal of Energy Chemistry* 72 (2022): 217-240.
- [92] Li, Yanguang, et al. "MoS₂ nanoparticles grown on graphene: an advanced catalyst for the hydrogen evolution reaction." *Journal of the American Chemical Society* 133.19 (2011): 7296-7299.
- [93] Wu, Zhuangzhi, et al. "WS₂ nanosheets as a highly efficient electrocatalyst for hydrogen evolution reaction." *Applied Catalysis B: Environmental* 125 (2012): 59-66.
- [94] Hsu, Wei-Ting, et al. "Evidence of indirect gap in monolayer WSe₂." *Nature communications* 8.1 (2017): 929.
- [95] Mortazavi, Bohayra, et al. "Mechanical responses of two-dimensional MoTe₂; pristine 2H, 1T and 1T' and 1T'/2H heterostructure." *Extreme Mechanics Letters* 20 (2018): 65-72.
- [96] Gu, Xiaokun, et al. "Colloquium: Phononic thermal properties of two-dimensional materials." *Reviews of Modern Physics* 90.4 (2018): 041002.
- [97] Xie, Guofeng, et al. "Ultra-low thermal conductivity of two-dimensional phononic crystals in the incoherent regime." *npj Computational Materials* 4.1 (2018): 21.
- [98] Qian, Xin, Jiawei Zhou, and Gang Chen. "Phonon-engineered extreme thermal conductivity materials." *Nature Materials* 20.9 (2021): 1188-1202.
- [99] Sledzinska, Marianna, et al. "2D phononic crystals: Progress and prospects in hypersound and thermal transport engineering." *Advanced Functional Materials* 30.8 (2020): 1904434.
- [100] Vasileiadis, Thomas, et al. "Progress and perspectives on phononic crystals." *Journal of Applied Physics* 129.16 (2021).

- [101] Sholl, David S., and Janice A. Steckel. Density functional theory: a practical introduction. John Wiley & Sons, 2022.
- [102] Martin, Richard M. Electronic structure: basic theory and practical methods. Cambridge university press, 2020.
- [103] Nørskov, Jens K., et al. "Density functional theory in surface chemistry and catalysis." *Proceedings of the National Academy of Sciences* 108.3 (2011): 937-943.
- [104] Hafner, Jürgen. "Ab-initio simulations of materials using VASP: Density-functional theory and beyond." *Journal of computational chemistry* 29.13 (2008): 2044-2078.
- [105] Kokalj, Anton. "Computer graphics and graphical user interfaces as tools in simulations of matter at the atomic scale." *Computational Materials Science* 28.2 (2003): 155-168.
- [106] Clark, Stewart J., et al. "First principles methods using CASTEP." *Zeitschrift für kristallographie-crystalline materials* 220.5-6 (2005): 567-570.
- [107] Greeley, Jeff, Jens K. Nørskov, and Manos Mavrikakis. "Electronic structure and catalysis on metal surfaces." *Annual review of physical chemistry* 53.1 (2002): 319-348.
- [108] Gerosa, Matteo, et al. "Electronic structure and phase stability of oxide semiconductors: Performance of dielectric-dependent hybrid functional DFT, benchmarked against G W band structure calculations and experiments." *Physical Review B* 91.15 (2015): 155201.
- [109] Durant, Joseph L. "Evaluation of transition state properties by density functional theory." *Chemical physics letters* 256.6 (1996): 595-602.
- [110] Lever, Greg, et al. "Large-scale density functional theory transition state searching in enzymes." *The journal of physical chemistry letters* 5.21 (2014): 3614-361.

2. Theoretical Backgrounds:



2.1. Many-body problems & density functional theory:

In quantum mechanics, the behavior of a system with more than one electron is described by the many-body Schrödinger equation, which accounts for the interactions between all pairs of electrons. Solving this equation exactly for systems with even just a few electrons becomes computationally intractable due to the exponential growth in complexity with the number of particles. Density Functional Theory offers an elegant solution to this problem by focusing on the electron density rather than the many-electron wavefunction. Instead of directly solving the many-body Schrödinger equation, DFT reformulates the problem in terms of the electron density, which is a function of position. The central approximation in DFT is to describe the total energy of the system as a functional of the electron density alone, rather than the full many-body wavefunction.

The specific many-body problem addressed in this thesis revolves around a Hamiltonian involving electrons and nuclei, articulated by the following equation:

$$\hat{H} = -\frac{\hbar^2}{2m_e} \sum_i \nabla_i^2 - \sum_{i,I} \frac{Z_I e^2}{|\mathbf{r}_i - \mathbf{R}_I|} + \frac{1}{2} \sum_{i \neq j} \frac{e^2}{|\mathbf{r}_i - \mathbf{r}_j|} - \sum_I \frac{\hbar^2}{2M_I} \nabla_I^2 + \frac{1}{2} \sum_{I \neq J} \frac{Z_I Z_J e^2}{|\mathbf{R}_I - \mathbf{R}_J|} \quad (2.1)$$

The first term in the equation (2.1) accounts for the kinetic energy of the electrons, with lowercase letters such as 'i' representing the positions of individual electrons. This term encompasses contributions from each electron's kinetic energy, constituting a sum over single-electron terms. The second term captures the Coulomb potential generated by the nuclei, indicating that the electron's energy depends on the nuclei's coordinates denoted by uppercase letters (I, J) in the equation. At this stage, the electrons are considered independent of each other's positions. The third term corresponds to electron-electron interactions, necessitating the

consideration of multiple electrons simultaneously. Subsequently, the fourth and fifth terms describe the kinetic energy of the nuclei and the nucleus-nucleus interaction, respectively. Given the significantly larger mass of nuclei compared to electrons, the negligible nuclei kinetic energy term is often disregarded, employing the adiabatic Born-Oppenheimer approximation. Additionally, the fifth term introduces a constant to the Hamiltonian when considering the positions of the nuclei as a parameter, hence it can be neglected at this juncture. Consequently, the effective Hamiltonian simplifies to:

$$\hat{H} = -\frac{\hbar^2}{2m_e} \sum_i \nabla_i^2 - \sum_{i,I} \frac{Z_I e^2}{|\mathbf{r}_i - \mathbf{R}_I|} + \frac{1}{2} \sum_{i \neq j} \frac{e^2}{|\mathbf{r}_i - \mathbf{r}_j|} \quad (2.2)$$

Hence, the resultant Hamiltonian comprises the kinetic energy term of the electrons, along with the electron-nuclei and electron-electron Coulomb interaction terms. Additionally, any external potential exerted on the system from external sources can also be incorporated with the electron-nuclei term, denoted as the second term in equation (2.2).

However, despite this simplification, the problem remains challenging due to its high dimensionality. The arguments of the above equation can be written as

$$\hat{H}(\mathbf{r}_1, \mathbf{r}_2, \dots, \mathbf{r}_N) \Psi_\lambda(x_1, x_2, \dots, x_N) = E_\lambda \Psi_\lambda(x_1, x_2, \dots, x_N); \quad x_i \equiv (\mathbf{r}_i, \sigma_i) \quad (2.3)$$

In equation (2.3), the many-body Hamiltonian and wave function for each state λ depend on the three-dimensional spatial coordinates of each electron, denoted by $x_i = (\mathbf{r}_i, \sigma_i)$, as well as the electron spins σ_i . Even for systems with a small number of electrons, the dimension of the problem grows exponentially. This complexity arises from the fact that the electron coordinates cannot be isolated. To simplify the problem, one approach is to ignore the interactions between electrons entirely. This results in a many-body wave function represented as the product of single-particle wave functions:

$$\Psi_\lambda(x_1, x_2, \dots, x_N) = \psi_{n_1}(x_1) \psi_{n_2}(x_2) \dots \psi_{n_N}(x_N); \quad \lambda = \{n_1, \dots, n_N\} \quad (2.4)$$

While the independent electron approximation simplifies the problem by treating each electron as if it were acting alone in the external potential, it overlooks the complex interactions that give rise to collective phenomena and interesting effects. In this scenario, each electron would occupy the lowest energy level available, leading to a configuration where electrons behave independently without any interaction between them. This simplistic view fails to capture phenomena like electron correlation and electron-electron interactions, which are essential for understanding many-body systems. In reality, the Pauli exclusion principle dictates that

electrons with the same spin cannot occupy the same energy level, which introduces a level of complexity even in the independent electron model. Additionally, optimization of single-electron wave functions can refine the description of electron behaviour, but it still does not fully account for the intricate interactions between electrons. Despite these efforts, the many-body wave function remains extremely complex to deal with directly. To address this challenge, various simplifications and approximations are employed, such as mean-field theories and Density Functional Theory, which aim to capture the essential physics while reducing computational complexity. These methods seek to strike a balance between accuracy and computational feasibility, allowing researchers to explore the behaviour of many-body systems while retaining the essence of the physical problem at hand.

In the subsequent sections, we will delve into initial approaches to tackle this complex problem, focusing on the foundation and formalism of density functional theory in detail.

2.2. Early solutions to the many-body problem: the Hartree and Hartree-Fock models

In attempting to address the formidable challenge posed by the many-body problem, scientists encountered significant obstacles due to its complexity. As discussed previously, solving the Schrödinger equation for the many-body Hamiltonian, which involves approximately 10^{23} coupled differential equations, surpasses the capabilities of even the most advanced supercomputers. Moreover, even if it were feasible to solve the Schrödinger equation, storing the resulting many-body wave function would present another insurmountable hurdle. In 1928, Hartree proposed a pioneering solution to this conundrum, building upon the work of Schrödinger and others [1]. Hartree's approach involved considering a system of nearly non-interacting electrons, where each electron moves under the cumulative potential generated by all other electrons. Mathematically, this was expressed through an ansatz, assuming that the many-body wave function could be factorized into the product of normalized single-particle wave functions for each electron.

This factorization of the many-body wave function, represented as:

$$\Psi^H(\mathbf{r}_1, \mathbf{r}_2, \dots, \mathbf{r}_N) = \psi_{\alpha 1}(\mathbf{r}_1) \psi_{\alpha 2}(\mathbf{r}_2) \dots \psi_{\alpha N}(\mathbf{r}_N) \quad (2.5)$$

$$\text{and } \langle \psi_{\alpha i}(\mathbf{r}_i) | \psi_{\alpha i}(\mathbf{r}_i) \rangle = 1 \quad (2.6)$$

The indices α_i encompasses all quantum numbers. Hartree resolved the minimization of the expectation value of the Schrödinger equation, incorporating the Hamiltonian described in equation (2.2). This optimization was performed concerning the wave function as depicted in equation (2.5), while adhering to the normalization constraint outlined in equation (2.6). The methodology employed for this optimization involved the utilization of the Lagrange multipliers method as

$$\delta\langle\Psi^H|H|\Psi^H\rangle - \sum_i[\lambda_i \delta(\langle\psi_{\alpha i}(\mathbf{r}_i)|\psi_{\alpha i}(\mathbf{r}_i)\rangle - 1)] = 0 \quad (2.7)$$

This results in a Schrödinger-like equation for the i th electron:

$$\begin{aligned} & \left[-\frac{1}{2}\nabla^2 + V_{\text{ext}}(\mathbf{r}_i) + \sum_j' \int d\mathbf{r} \frac{n_{aj}(\mathbf{r})}{|\mathbf{r}_i - \mathbf{r}|} \right] \psi_{\alpha i}(\mathbf{r}_i) \\ & = \left[-\frac{1}{2}\nabla^2 + V_{\text{ext}}(\mathbf{r}_i) + V_H(\mathbf{r}_i) \right] \psi_{\alpha i}(\mathbf{r}_i) = \varepsilon_{\alpha i} \psi_{\alpha i}(\mathbf{r}_i) \end{aligned} \quad (2.8)$$

Here, $n_{aj}(\mathbf{r}) = |\psi_{\alpha j}(\mathbf{r})|^2$ represents the charge density of the electron j and the prime indicates that the term corresponding to $i=j$ is excluded. These equations can be solved iteratively, as the starting point is the very wave function that these single-particle equations are derived from. Typically, the atomic wave functions serve as the initial basis. However, the results from the Hartree approximation did not match well with observed results. This discrepancy arises from the neglect of electron-electron interactions in the Hartree approach. Additionally, the Hartree equation includes a "self-interaction" term when expressed in terms of electron density, wherein an electron feels the potential generated by itself.

To measure a quantum mechanical observable quantity of a many-body system, one integrates the corresponding quantum mechanical operator with the many-body wave function describing the system. However, integrals inherently perform an average, leading to a loss of some details. For instance, integrating a simple symmetric function with an asymmetric oscillation under symmetrical boundary conditions may fail to detect the oscillation in the result. This nature of integrals offers several possibilities. One approach is to simplify the many-body wave function by eliminating non-essential details for certain observables. This forms the basis of the Hartree-Fock approach, which incorporates the Pauli exclusion principle to account for electron spin interactions and approximates the many-body wave function as a Slater determinant, thereby fixing the symmetry of the wave function.

However, the Hartree-Fock method often yields worse results than the Hartree approach when applied to real systems. This limitation stems from its failure to consider correlation interactions, another crucial interaction that restricts the full effect of exchange interactions. Consequently, the Hartree-Fock method performs better for small molecules and clusters with fewer electrons, where the impact of correlation interaction is minimal compared to solids.

The Hartree-Fock method employs an iterative technique, the self-consistent field (SCF) minimization method, to determine the ground state many-body wave function. The SCF minimization iteratively constructs new orbitals based on the eigenfunctions of the Fock operator until the total electronic energy is minimized. This iterative process is depicted in Figure 2.1.

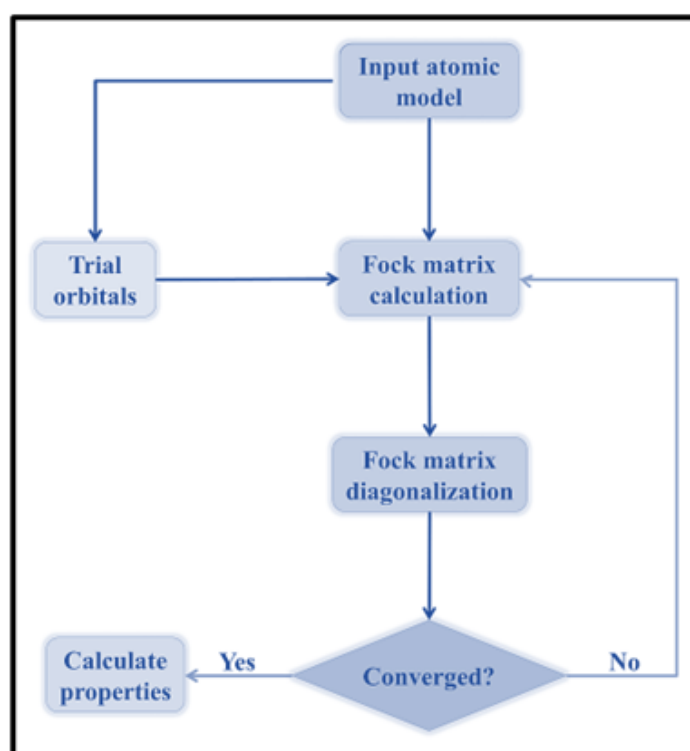


Figure 2.1: SCF iterative process of Hartee-Fock.

While both the Hartree and Hartree-Fock methods have shown success in specific cases, they fail to become universal methods for elucidating material properties due to their limitations in representing actual many-body interaction scenarios. Nonetheless, these approaches played a crucial role in the development of density functional theory (DFT) and self-consistent iterative calculations, highlighting the essential quantities that must be considered when describing a many-body system.

2.3. Density Functional Theory:

2.3.1. Observables in terms of electron density:

In the context of electron density, observables refer to quantities or properties that can be measured or calculated based on the distribution of electrons within a system. These observables are often expressed in terms of the electron density, which represents the spatial distribution of electrons in a given region of space. The primary goal of solving a many-body problem is to assess observables. While these observables can theoretically be derived from the true many-body wave function, the computational demands are prohibitive even for the most advanced supercomputers, making it impractical to store. In principle, observables solely depend on the external potential, but this dependence is too intricate to be practically useful. Therefore, the question arises: Is there another quantity in terms of which observables can be expressed?

If one is interested in a local one-body operator, the expectation value only involves the one-body operator and the one-body density 'n', due to the equivalent nature of all electrons, as shown by the equation:

$$O_1 = \int dx_1 O_1(x_1) n(x_1) \quad (2.9)$$

Thus, the density alone is sufficient to calculate the expectation value for a one-body operator. This concept can be extended to a two-body operator, such as the Coulomb interaction energy, for which the integral is reduced to a two-body density ' $n^{(2)}$ ':

$$V_{ee} = \int dx_1 dx_2 \frac{1}{2} \frac{e^2}{|r_1 - r_2|} n^{(2)}(x_1, x_2) \quad (2.10)$$

The Coulomb interaction energy expressed in this manner and the two-body densities are notably simpler than the full many-body wave function. Numerous examples demonstrate that the expectation value can be expressed in a much simpler form using quantities like electron density or other compact variables, which are easier to determine than the many-body wave function. Therefore, instead of directly solving for the many-body wave function, one can bypass the problem by evaluating the expectation value of observables directly in terms of these compact quantities, such as electron density or density matrix.

However, the challenge lies in determining these compact quantities themselves. One approach is to define various observables in terms of different compact quantities, while another is to

identify a general quantity that can express multiple observables. Density Functional Theory (DFT) follows the latter approach, expressing observables in terms of electron density. The expressions for the contribution of the external potential to the total energy (E_{ext}), the classical electrostatic term or the Hartree energy (E_{H}), and the electrons' kinetic energy from the Thomas-Fermi model (TTF) [2,3] as functionals of electron density are shown in the following equations:

$$E_{\text{ext}}[n] = \int dr n(r) V_{\text{ext}}(r) \quad (2.11)$$

$$E_{\text{H}}[n] = \frac{1}{2} \int dr dr' \frac{n(r)n(r')}{|r-r'|} \quad (2.12)$$

$$T^{\text{TF}}[n] = C \int dr n^{\frac{5}{3}}(r) \quad (2.13)$$

It is noteworthy that while E_{ext} is a local functional of the electron density, E_{H} is a non-local functional. Additionally, the Thomas-Fermi expression of the electrons' kinetic energy was one of the earliest developed functionals of electron density, predating Hartree theory, and played a significant role in the foundation of DFT.

2.3.2. The Hohenberg-Kohn theorem:

As discussed in the previous sub-section, one can evaluate the observable quantities by representing the observables as a functional of compact quantities such as electrons' density. This procedure bypasses the impossible task of calculating the many-body wave function. But a major question remains that whether electrons' density has the unique functional of the quantum mechanical observations.

If a non-relativistic Hamiltonian of the many electron systems is considered within the Born-Oppenheimer approximation as shown in equation (2.2), the ingredients of the Hamiltonian are the kinetic term that acts on each electron, the electron-electron interaction given by the Coulomb potential that acts on each couple of electrons and the external potential given by the positions of the nuclei that in turn acts on each electron. Among these terms, it is the external potential that defines the system. The first two terms are universal. For example, Nickel atom and bulk Silicon unit cell, both contains 28 electrons but their difference lies in the position and strength of the nuclei potential which is designated here as the external potential. In fact, if the external potential is given, the Hamiltonian can be formed readily which can be diagonalized and in principles, one can evaluate the eigenvectors, wave function and

eigenvalues from there. The external potential and the wave function of a system are related as bijective function. So, an one to one mapping exists between the external potential and many body wave function which notably indicates that every observable is a unique functional of the external potential. On the other hand, the wave function is in relation with the electron density. Given the wave function, there exists only one density obtained by the integration of its square modules over all but one special coordinate as shown below:

$$n(\mathbf{r}) = N \int d\mathbf{r}_2 \dots d\mathbf{r}_n |\Psi(\mathbf{r}, \mathbf{r}_2, \dots \mathbf{r}_n)|^2 \quad (2.14)$$

Where N represents the total number of electrons. This clearly indicates that the relation between the external potential and electron density is at least a surjective mapping. In their seminal paper in 1964 [4], Hohenberg and Kohn proved that given the one-to-one relationship between the external potential and wave function, the relation between external potential and electron density is also injective in nature. This demonstrates that there indeed exists a one-to-one relationship between the external potential and electron density, which constitutes the first part of the Hohenberg-Kohn theorem.

The ground state energy of a many-body system is the fundamental observable quantity used to determine other properties of the system. In this context, the operator of interest is simply the Hamiltonian. By employing the variational principle and exploring all possible wave functions of the system, the wave function that yields the lowest value, representing the ground state energy, is identified as the ground state wave function.

$$\Psi_{\min} \langle \Psi | \hat{H} | \Psi \rangle = \langle \Psi_0 | \hat{H} | \Psi_0 \rangle = E_0 \quad (2.15)$$

the one-to-one correspondence between the electron density and wave function established by the Hohenberg-Kohn theorem, the ground state density uniquely determines the ground state energy. In other words, by searching among all possible densities, the one that minimizes the energy functional represents the ground state density, denoted as $n(\mathbf{r})$, and corresponds to the ground state energy, denoted as E_0 . This relationship is expressed as:

$$n(\mathbf{r})_{\min} E[n] = E_0 \quad (2.16)$$

The Hohenberg-Kohn theorem offers a practical approach, akin to a variational procedure, for expressing observables as functionals of electron density. Rather than navigating through the vast realm of $3N$ -dimensional many-body wave functions, the theorem restricts the search to

the domain of densities, residing in a significantly smaller space, simplifying the search process considerably.

Although the significance of the Hohenberg-Kohn theorem, presented in their seminal paper of 1964, wasn't immediately recognized, it marked a breakthrough in addressing many-body problems. Its impact on modern-day research in this field is immeasurable. To this day, the paper remains the most cited work in the field of Physics, underscoring its enduring importance and influence.

Auxiliary system:

In the previous sections, it was highlighted that energy can be expressed as a functional solely dependent on electron density. However, electron density is essentially an integral of the many-body wave function, which poses a computational challenge in Density Functional Theory (DFT). The primary aim of DFT is to bypass the direct computation of the intricate many-body wave function.

In a system with multiple interacting electrons, the wave function becomes highly complex due to these interactions. Yet, if the electrons didn't interact, the many-electron wave function would simply be the product of single-particle wave functions. To simplify the analysis and avoid the complications arising from interactions, an effective non-interacting system, termed an auxiliary system, is devised. This system is tailored to reproduce the same electron density and certain observables as the real system, albeit for specific purposes.

However, it's crucial not to overburden the auxiliary system beyond its capacity, as this could lead to unreliable results. For instance, consider the scenario where calculating the energy levels of a one-dimensional harmonic oscillator is challenging, but feasible for a one-dimensional box potential. By adjusting parameters such as the position of the box potential to align with specific energy levels of the harmonic oscillator, it serves as a simpler auxiliary system for determining the harmonic oscillator's ground state energy.

If more stringent requirements are imposed, such as matching both the first and third energy levels of the harmonic oscillator, the auxiliary system must be granted additional flexibility. This might involve tuning both the position and width of the box potential. Consequently, the auxiliary system is designed specifically to replicate certain energy levels of the harmonic oscillator, while others may not align precisely as shown below:

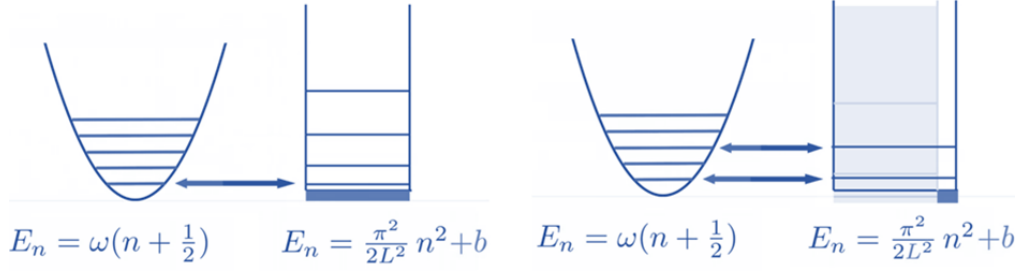


Figure 2.2: The depiction of one-dimensional infinite square well utilized as an auxiliary system to derive the energy levels of the one-dimensional harmonic oscillator.

The concept of employing an auxiliary system to derive specific observables, thereby avoiding the exhaustive calculation of the full problem, lies at the heart of Density Functional Theory (DFT). Within DFT, non-interacting electrons are utilized in an auxiliary system to determine the electron density and other observables. The external potential is adjusted accordingly to ensure consistency with the expected results. In DFT, the ground state density serves as the cornerstone for deriving other properties, including the ground state energy, as dictated by the Hohenberg-Kohn theorem. The auxiliary system of non-interacting electrons is fine-tuned to match the target density of the interacting system. Calculating the density of the auxiliary system is relatively straightforward since its wave function is merely the product of single-electron wave functions. However, achieving accuracy requires tuning the external potential to provide the effective potential necessary for solving the single-particle Schrödinger equation. This iterative process creates self-consistency within the problem, as adjustments are made until the computed density matches the desired target. Further insights into the application of the auxiliary system in DFT are elaborated upon in the subsequent subsection.

The Hohenberg-Kohn theorem established a one-to-one relationship between the energy of a many-body system and its density. In principle, if an energy functional exists, it can be derived from the electron density. However, not all components of the energy functional are known in terms of density. The unknown components are collectively referred to as the Hohenberg-Kohn functional, denoted as $F_{HK}[n]$. The total energy $E[n]$ of the system can be expressed as:

$$E[n] = T[n] + \int d\mathbf{r} n(\mathbf{r})V_{\text{ext}}(\mathbf{r}) + E_{\text{ee}}[n] \quad (2.17)$$

$$E[n]=F_{\text{HK}} [n]+\int d\mathbf{r} n(\mathbf{r}) V_{\text{ext}} (\mathbf{r}) \quad (2.18)$$

To simplify the energy functional and minimize the impact of the unknown terms, we can modify it as follows. By adding and subtracting the kinetic energy and interaction terms of a non-interacting electron system with density in the equation (2.17) and rearranging, we obtain:

$$E[n] = T_S[n] + \int d\mathbf{r} n(\mathbf{r})V_{\text{ext}}(\mathbf{r}) + \frac{1}{2} \int d\mathbf{r} d\mathbf{r}' \frac{n(\mathbf{r})n(\mathbf{r}')}{|\mathbf{r}-\mathbf{r}'|} + E_{\text{XC}}[n] \quad (2.19)$$

Here, $T_S[n]$ represents the kinetic energy of electrons in a non-interacting system, and the third term corresponds to the electron-electron interaction energy, equivalent to Hartree's approach. The term $E_{\text{XC}}[n]$, termed the exchange-correlation term, encapsulates all the unknown functionals and is defined as:

$$E_{\text{XC}}[n] = T[n] - T_S[n] + E_{\text{ee}}[n] - E_{\text{ee}}^{\text{H}}[n] \quad (2.20)$$

This reordering in equation (2.19) aims to minimize the contribution of the unknowns in the energy functional. After separating the known components such as the kinetic energy of the non-interacting system, the Hartree electron-electron interaction term, and the external potential, equation (2.19) is left with a smaller unknown part of the functional, which can be expressed as energy differences in equation (2.20). These energy differences are expected to be smaller than the values of the unknown full kinetic and electron-electron interaction functionals of the real interacting electron system.

In the Hartree approach, Hartree attempted to solve the many-body problem by considering the electrons as non-interacting. A system of N independent particles is factorized into N Schrödinger equations. Each equation contains a kinetic energy term and a term corresponding to the effective potential (V_{eff}), which is the same for all the electrons.

$$\left[-\frac{1}{2} \nabla^2 + V_{\text{eff}} \right] \psi_i(\mathbf{r}) = \lambda_i \psi_i(\mathbf{r}) \quad (2.21)$$

The electron density ($n(\mathbf{r})$) is also represented simply as the following

$$n(\mathbf{r}) = \sum_i^N |\psi_i(\mathbf{r})|^2 \quad (2.22)$$

From the Hohenberg-Kohn theorem, it is known that there is a unique correspondence between the electron density and the effective potential in the case of the independent particle system as well. Here, the external potential coincides with the effective potential. The total energy is also known in principle as it is a unique functional of the electron density. If the two scenarios of interacting and non-interacting electrons are put together, the question arises if the

two densities coincide. In other words, the question is whether a real system with interacting electrons of density n can have an auxiliary system of non-interacting electrons designed to have the same density n . This was exactly the idea of Walter Kohn and Lu Sham [5]. They assumed that for every real system with interacting electrons of density n , there exists an auxiliary system of non-interacting electrons having the same density. In order to determine the form of the single-particle Schrödinger-like equations and that of the effective potential, Kohn and Sham utilized the outcomes of the Hohenberg-Kohn theorem, which states that the total energy is a unique functional of the electron density even for the auxiliary system. As both the interacting and non-interacting auxiliary systems have the same density, the total energy functional of the interacting system will be stationary around the ground state density. Similarly, the best one-particle wave functions will be those that minimize the density and thus the total energy functional of the interacting system, as a consequence of the Hohenberg-Kohn theorem. To derive the one-particle equations, Kohn and Sham added the constraint of normalization on the single-particle wave functions and used the method of Lagrange multipliers to minimize the energy functional under constraints in terms of the single-particle wave functions. This can be expressed as:

$$\frac{\delta[E[n] - \lambda_i (\int d\mathbf{r} \psi_i^*(\mathbf{r}) \psi_i(\mathbf{r}) - 1)]}{\delta \psi_i^*(\mathbf{r})} = 0 \quad (2.23)$$

Where $E[n]$ has the form as represented in equation (2.19). Expressing the full form of $E[n]$ in equation (2.23) and taking the functional derivative leads to the following one-particle equation:

$$\left[-\frac{\nabla^2}{2} + V_{\text{ext}}(\mathbf{r}) + \int d\mathbf{r}' \frac{n(\mathbf{r}')}{|\mathbf{r} - \mathbf{r}'|} + \frac{\delta E_{\text{XC}}[n]}{\delta n(\mathbf{r})} \right] \psi_i(\mathbf{r}) = \lambda_i \psi_i(\mathbf{r}) \quad (2.24)$$

The third term is called the Hartree potential ($V_H[n]$), and the fourth term is called the exchange-correlation potential ($V_{\text{XC}}[n]$). The set of equations represented by equation (2.24) are called the Kohn-Sham equations, which are a set of one-particle equations of the auxiliary non-interacting system that reproduces the same density of the real interacting system 'n'. The effective potential to get the same density as the real system is called the Kohn-Sham potential and is represented as:

$$V_{\text{KS}}(\mathbf{r}) = V_{\text{ext}}(\mathbf{r}) + V_H([n], \mathbf{r}) + V_{\text{XC}}([n], \mathbf{r}) \quad (2.25)$$

The Kohn-Sham equations are exact equation in the sense that they provide the exact electron density. So one can obtain in principle, the exact density by solving simple one-particle

equations like the Hartree equations. The only problem in the beautiful formalism of Kohn and Sham is the exchange correlation potential which needs to be approximated. The approximation techniques will be discussed in the later sections. Once, the exact density is derived it can be utilized to evaluate the total energy of the interacting system using the Kohn-Sham eigenvalues via the following expression

$$E[n] = \sum_i \lambda_i - \frac{1}{2} \int d\mathbf{r} d\mathbf{r}' \frac{n(\mathbf{r})n(\mathbf{r}')}{|\mathbf{r}-\mathbf{r}'|} + E_{XC}[n] - \int d\mathbf{r} V_{XC}(\mathbf{r})n(\mathbf{r}) \quad (2.26)$$

and via the total energy, a large number of observables ranging from stability to equilibrium distance, from phonons to formation or adsorption energies, can be derived. Many other observables can also be tackled beyond the ground state energy. Notably, the density is not only the output of the Kohn-Sham equations; it is also the input to design the potentials. Therefore, the Kohn-Sham equations need to be solved iteratively, via the self-consistent minimization method introduced by Douglas Hartree in his approach to solving the many-body problem. Another major point to note is that the eigenvalues of the Kohn-Sham equation do not represent real electron energy levels as they correspond to the fictitious independent particles of the auxiliary system. There is no equivalent of Koopmans's theorem for the Kohn-Sham particles. However, in practice, this is not entirely the case, as the last occupied eigenvalue has a physical meaning; it represents the ionization energy, which is the energy required to ionize an atom or molecule by one electronic charge. For other eigenvalues, they have no physical interpretation.

2.3.3. The exchange-correlation functional and its approximations:

The total energy functional from Kohn-Sham formalism is given as

$$E[n] = T_S[n] + E_H[n] + E_{XC}[n] + \int d\mathbf{r} V_{ext}(\mathbf{r})n(\mathbf{r}) \quad (2.27)$$

The only unknown part in equation (2.27) is the exchange-correlation energy functional $E_{XC}[n]$. Typically, the exchange-correlation part contributes only a few percent in the total energy functional, and one can get away with approximations. However, the exchange-correlation interaction is very important in molecular bonding and is sometimes called the nature's glue. So, it is important to approximate it effectively. There are two general strategies to find approximate exchange-correlation functional, namely empirical and non-empirical methods. Generally, researchers in the field of quantum chemistry prefer the empirical method while Physicists prefer the non-empirical approach.

In the empirical method, the exchange-correlation functional involves free parameters that are adjusted to fit experimental data or high-level quantum mechanical calculations for a specific system. By fitting these parameters, the functional can accurately represent the system's behaviour and properties. Conversely, non-empirical functionals are designed to be more universally applicable as they are derived from fundamental principles and constraints that are believed to be universal across different systems. These functionals are not dependent on empirical input and can provide accurate descriptions of exchange and correlation effects across various systems. Both methodologies have demonstrated significant success in approximating the exchange-correlation functional. However, in this thesis, we will focus on utilizing exchange-correlation functionals derived from the non-empirical approach. Various types of non-empirical approximations will be discussed in subsequent sections.

2.3.4. The local density approximation and generalized gradient approximation:

In the discussion of exchange-correlation functionals, the local density approximation (LDA) and generalized gradient approximation (GGA) are two prominent methods. LDA represents a non-empirical approach to approximating the exchange-correlation functional. It relies on a reference system known as the homogeneous electron gas to establish the necessary constraints for constructing the functional. In the LDA, the primary variable is the uniform density of the homogeneous electron gas, denoted as \bar{n} . This density serves as the basis for formulating the exchange-correlation functional. The key requirement for LDA is knowledge of the energy per unit volume of the homogeneous electron gas, which is treated as a function of the density \bar{n} . By incorporating this information, LDA provides a means to approximate the exchange-correlation effects in density functional theory calculations.

$$\epsilon^{\text{Hom}}(\bar{n}) = \frac{E^{\text{Hom}}}{V} \quad (2.28)$$

The energy density in the local density approximation (LDA) can be expressed as a combination of the kinetic energy density ($\epsilon_{\text{kin}}^{\text{Hom}}$) and the densities of exchange ($\epsilon_{\text{X}}^{\text{Hom}}$) and correlation ($\epsilon_{\text{C}}^{\text{Hom}}$) interactions individually.

$$\epsilon^{\text{Hom}}(\bar{n}) = \epsilon_{\text{kin}}^{\text{Hom}} + \epsilon_{\text{X}}^{\text{Hom}} + \epsilon_{\text{C}}^{\text{Hom}} \quad (2.29)$$

The kinetic energy density $\epsilon_{\text{kin}}^{\text{Hom}}$ and the exchange energy density $\epsilon_{\text{X}}^{\text{Hom}}$ are precisely known, while for $\epsilon_{\text{C}}^{\text{Hom}}$, nearly exact formulas are available based on Quantum Monte-Carlo data [6,

7]. The exchange-correlation functional in LDA is expressed as an integral over the energy density of the homogeneous electron gas, determined from the density at each point \mathbf{r} .

$$E_{XC}^{LDA}[n] = \int d\mathbf{r} \epsilon_{XC}^{Hom}(n(\mathbf{r})) \quad (2.30)$$

In LDA, even a strongly inhomogeneous system is considered locally homogeneous within a small volume element around \mathbf{r} . This volume element is treated as a miniature homogeneous electron gas with the same density as the real system. Consequently, the system is treated locally as a homogeneous electron gas. LDA yields molecular ground state energies within 1%-5% of the exact energy and lattice constants within 1%-2%. However, lattice constants computed via LDA are typically too short, indicating that LDA overbinds the system. Despite its simplified nature, LDA remains useful and provides sufficiently accurate results because the LDA exchange-correlation hole density ($n_X^{LDA}(\mathbf{r}, \mathbf{r}')$) satisfies three important constraints expected for an accurate exchange-correlation hole density. Mathematically, these constraints satisfied by LDA are as follows:

$$n_X^{LDA}(\mathbf{r}, \mathbf{r}') \leq 0 \quad (2.31)$$

$$\int n_X^{LDA}(\mathbf{r}, \mathbf{r}') d\mathbf{r}' = -1 \quad (2.32)$$

$$\text{And } \int n_C^{LDA}(\mathbf{r}, \mathbf{r}') d\mathbf{r}' = 0 \quad (2.33)$$

The physical reason behind the success of LDA is that the reference system of the homogeneous electron gas satisfies certain constraints, which are then carried over to LDA.

The exchange-correlation hole at \mathbf{r} and \mathbf{r}' primarily depends on the density at the reference position \mathbf{r} . This implies that information about the density is only required in a small region around \mathbf{r} . Building upon this concept, the exchange-correlation functional can be enhanced from LDA by considering both the density and its gradient in a small neighbourhood around \mathbf{r} . This enhancement leads to the generalized gradient approximation (GGA) [8-12]. In GGA, the exchange-correlation energy can be expressed in a similar form to LDA, with an additional factor F_{XC} under the integral. This factor incorporates both the effects of local spin density and its gradients.

$$E_{XC}^{GGA}[n] = \int d\mathbf{r} \epsilon_{XC}^{Hom}(n(\mathbf{r})) F_{XC}(n^\sigma(\mathbf{r}), \nabla n^\sigma(\mathbf{r})) \quad (2.34)$$

GGA functionals are defined by their exchange-correlation term, F_{XC} , which is derived using exact constraints. Therefore, GGA is considered a non-empirical exchange-correlation

functional. It represents a notable advancement over LDA in computing lattice parameters, formation energies, and adsorption energies, all at a moderate computational cost. Consequently, GGA has become one of the most commonly utilized approaches for addressing exchange-correlation functionals in many-body problems. One well-known GGA example is the PBE functional, named after Perdew, Burke, and Ernzerhof, which has garnered over 120,000 citations on Google Scholar to date.

2.3.5. The Meta-GGAs and hybrid functionals:

Meta-GGA exchange-correlation functionals, similar to GGAs, are semi-local in nature. These functionals are represented as follows:

$$E_{XC}^{MGA}(n^\sigma) = \int d\mathbf{r} f(n^\sigma, \nabla n^\sigma, \tau^\sigma) \quad (2.35)$$

τ^σ is kinetic energy densities of spin σ which has the form

$$\tau^\sigma(\mathbf{r}) = \frac{1}{2} \sum_j^{occ} |\nabla \psi_j^\sigma(\mathbf{r})|^2 \quad (2.36)$$

Meta-GGA functionals offer distinct advantages, primarily due to the inclusion of the kinetic energy density τ^σ , which enhances sensitivity to electron localization. This feature enables Meta-GGAs to more effectively differentiate between covalent and metallic bonds. Moreover, τ^σ satisfies exact constraints related to one and two-electron densities, contributing to the accuracy of these functionals. It's noteworthy that τ^σ depends on the gradient of Kohn-Sham orbitals and cannot be explicitly expressed as a functional of density. Despite this, according to the Hohenberg-Kohn theorem, τ^σ must function as a density functional since Kohn-Sham orbitals are density-dependent. However, density only implicitly influences the expression of τ^σ via the Kohn-Sham equations. Consequently, the functional itself is semi-local as an orbital functional but non-local as a density functional. The benefits of Meta-GGAs extend to providing a clearer indication of bonding nature, more accurate enthalpy values, improved estimation of the band gap, and better dispersive force corrections compared to GGAs. Prominent examples of Meta-GGA functionals include TPSS [13] and SCAN [14] functionals. Generally, semi-local functionals like GGAs and Meta-GGAs demonstrate high accuracy and efficiency for systems where the exchange-correlation hole is sufficiently localized. However, they tend to falter in accurately predicting properties of weakly bonded systems, strongly correlated systems, and precise band gap measurements.

Hybrid functionals are non-local in nature. The key idea of forming hybrid functional is to mix semi-local exchange correlation functional with non-local exact exchange. They follow the form as given below

$$E_{XC}^{\text{Hybrid}} = aE_X^{\text{Exact}} + bE_{XC}^{\text{DFT}} \quad (2.37)$$

Where E_{XC}^{DFT} corresponds to the semi-local exchange-correlation functional from GGA or LDA. The exact exchange energy is represented by the Fock exchange term, which is expressed as:

$$E_X^{\text{Exact}}[n] = -\frac{1}{2} \sum_{\sigma=\uparrow\downarrow} \sum_{ij}^{\text{Occ}} \int d\mathbf{r} \int d\mathbf{r}' \frac{\psi_i^{\sigma*}(\mathbf{r}) \psi_i^{\sigma}(\mathbf{r}') \psi_j^{\sigma}(\mathbf{r}) \psi_j^{\sigma*}(\mathbf{r}')}{|\mathbf{r}-\mathbf{r}'|}$$

The exact exchange energy in hybrid functionals, such as B3LYP, is essentially the Hartree-Fock exchange energy computed using the Kohn-Sham orbitals. Since the Kohn-Sham orbitals are uniquely determined by the electron density, the exact exchange energy functions as an implicit density functional. However, its dependence on the orbitals is explicit and non-local. One of the most widely used hybrid functionals is B3LYP [10-15], which stands for Becke, 3-parameter, Lee-Yang-Parr. It combines the semi-local exchange-correlation functional with the exact exchange energy as follows:

$$E_{XC}^{\text{Hybrid}} = (1-a)E_X^{\text{LDA}} + aE_X^{\text{Exact}} + bE_X^{\text{b88}} + cE_C^{\text{LYP}} + (1-c)E_C^{\text{LDA}} \quad (2.38)$$

The hybrid functionals, characterized by coefficients a , b , and c with values of 0.20, 0.72, and 0.81 respectively, are derived by fitting to a molecular dataset. Unlike LDA and GGA, obtaining the functional derivative of hybrid functionals is challenging due to the implicit appearance of density in their expressions. To address this, the generalized Kohn-Sham approach (GKS) is often employed, where the energy variation is carried out with respect to the orbitals. This simplifies the computation of functional derivatives, facilitating the determination of the exchange-correlation potential. However, this process renders the generalized Kohn-Sham equations non-local. Hybrid functionals exhibit remarkable accuracy in predicting formation enthalpies, lattice constants, and cohesive energies for molecules. However, for solids, GGAs and Meta-GGAs tend to outperform hybrid functionals. Additionally, the computational expense associated with calculating the Hartree-Fock exchange can vary depending on the method used. Nonetheless, the primary advantage of hybrid functionals lies in their exceptional ability to predict band gaps with superior accuracy compared to other discussed functionals. The classification of exchange-correlation functionals is often depicted in Figure 2.3, commonly referred to as the "Jacob's ladder" of DFT, inspired

by the Biblical story where Jacob dreams of a ladder connecting earth to heaven. In the context of DFT, the lowest part of the ladder symbolizes the Hartree world, where no exchange-correlation effects are considered, akin to the earthly realm. Conversely, heaven represents the exact exchange-correlation functional, which is unattainable in practice. The rungs between these extremes signify the various approximations used in DFT, with higher rungs indicating better approximations that bring us closer to the ideal of heaven. At the base of the ladder lies LDA, followed by GGA, Meta-GGAs, and hybrid functionals successively above it. The highest rung of the Jacob's ladder encompasses the most advanced functionals, such as the RPA-like functionals [16, 17]. As one ascends the ladder, both the complexity and computational cost increase. However, the accuracy and overall performance of the functionals also improve, leading us closer to achieving more accurate descriptions of electronic properties.

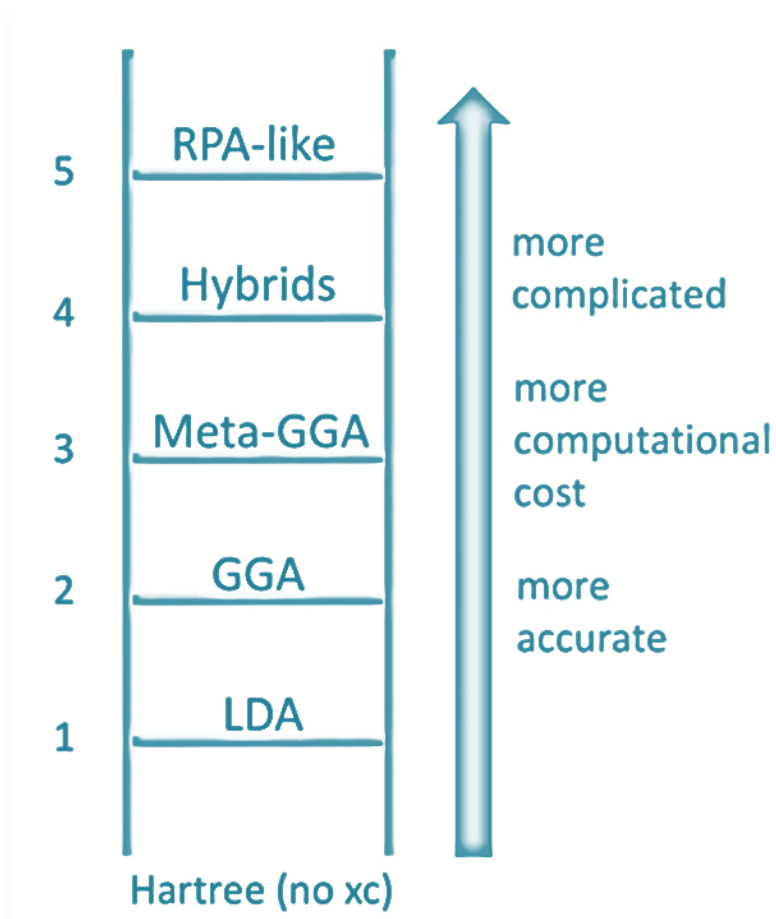


Figure 2.3: Jacob's ladder of the DFT exchange-correlation functionals.

2.3.6. Plane wave basis sets and energy cut-off:

Thus far, we have explored how Density Functional Theory (DFT), grounded in the Hohenberg-Kohn theorem and Kohn-Sham equations, simplifies the daunting many-body problem into solving numerical solutions of single-particle Schrödinger-like equations. These equations correspond to an auxiliary system of free electrons navigating within an effective potential to reproduce the ground state density of the real many-body system. Various approximation schemes for the unknown exchange-correlation functional have been presented to address this challenge. However, solving the ground state density via the set of one-particle Kohn-Sham equations remain a computationally demanding task, requiring a series of numerical approximations, which will be discussed in subsequent sections. As a simplification strategy, the many-electron system is often conceptualized as an infinite crystalline solid, with atoms arranged in an infinite array of regular patterns. Assuming an absolute zero temperature, the nuclei in such a system are positioned in space in a periodic manner. When solving the Schrödinger equation for such a system, it must adhere to the fundamental properties outlined in Bloch's theorem. According to Bloch's theorem, the effective potential in such a system must exhibit the same periodicity as the periodic arrangement of the nuclei. In other words, if the dimension of the unit cell is then the effective potential possesses periodicity as follows:

$$V_{\text{eff}}(\mathbf{r} + \mathbf{l}) = V(\mathbf{r}) \quad (2.39)$$

In the context of Bloch's theorem, where $\mathbf{l} = \sum_{i=1}^3 n_i \mathbf{a}_i$ and n_i is an integer, the theorem effectively reduces the dimensionality of the problem to the realm of one-electron wave functions corresponding to the number of electrons in the unit cell. This reduction in complexity, achieved through assuming an infinite periodic solid system and applying Bloch's theorem, significantly diminishes both the scale and computational cost of the problem.

In a periodic solid, the one-electron wave functions can be expressed using Bloch's theorem as

$$\psi_i = e^{i\mathbf{k} \cdot \mathbf{r}} u_i(\mathbf{r}) \quad (2.40)$$

Here, \mathbf{r} represents the position vector, and \mathbf{k} is the wave vector, constrained to certain values based on the dimensions of the unit cell. The exponential component signifies the plane-wave characteristics of the Bloch wave functions, while $u_i(\mathbf{r})$ denotes the periodicity of the unit cell.

The second part of the Bloch wave function can be expanded into a finite number of plane waves using a special group of wave vectors \mathbf{G} , expressed as:

$$u_{i,G}(\mathbf{r}) = \sum_{\mathbf{G}} c_{i,G} e^{i\mathbf{k} \cdot \mathbf{r}} \quad (2.41)$$

The special set of wave vectors \mathbf{G} comprises reciprocal space wave vectors of the unit cell, satisfying the condition that for any lattice vector \mathbf{a}_i in the real space, $\mathbf{G} \cdot \mathbf{a}_i = 2\pi m_i$, where m_i is integer.

Combination of equation (2.40) and (2.41) gives

$$\psi_i = \sum_{\mathbf{G}} c_{i,\mathbf{k}+\mathbf{G}} e^{i(\mathbf{k}+\mathbf{G}) \cdot \mathbf{r}} \quad (2.42)$$

The Bloch wave function's form enables solving the Schrödinger equation for each independent \mathbf{k} corresponding to the unit cell, rather than the entire solid. This characteristic also facilitates the use of plane waves as the basis set due to the plane wave nature of ψ_i . The vector \mathbf{k} spans the space termed reciprocal space, where most DFT problems are more easily solved compared to real space spanned by \mathbf{r} . Substituting the Bloch plane waves, as expressed by equation (2.43), into the Kohn-Sham equations leads to a reciprocal space representation of the Kohn-Sham equations:

$$\sum_{\mathbf{G}'} \left\{ \frac{\hbar^2}{2m_e} |\mathbf{k} + \mathbf{G}| \delta_{\mathbf{G}\mathbf{G}'} + V_{\text{ext}}(\mathbf{G} - \mathbf{G}') + V_H(\mathbf{G} - \mathbf{G}') + V_{XC}(\mathbf{G} - \mathbf{G}') \right\} \times c_{i,\mathbf{k}+\mathbf{G}'} = c_{i,\mathbf{k}+\mathbf{G}} \quad (2.43)$$

These equations are computationally more affordable to solve. However, it's noteworthy that for systems with defects or randomly ordered materials, the periodicity of the unit cell is disrupted. In such cases, a portion of interest of the supercell must be selected, which is then subjected to periodic boundary conditions expressed in terms of plane waves. The supercell must be chosen carefully to ensure that there is no interaction between the original defects and their periodic images. This approach allows for effectively modeling systems with defects or disorder within the framework of DFT. As indicated by equation (2.43), every single \mathbf{k} -point of interest in reciprocal space involves a sum over an infinite number of possible reciprocal lattice vectors \mathbf{G} . Fortunately, the coefficients of the plane in equation (2.43) have a straightforward interpretation, as they include the term corresponding to the kinetic energy $\frac{\hbar^2}{2m_e} |\mathbf{k} + \mathbf{G}|^2$. Consequently, plane waves with smaller kinetic energy values are anticipated to have a more significant impact than those with higher kinetic energies. This presents an opportunity to truncate the infinite sum in equation (2.43) above a certain value, depending on

the characteristics of the system under study. By considering only the plane waves with lower kinetic energy values, one can effectively manage computational resources while preserving the accuracy of the calculation. This approach is commonly employed in practical implementations of DFT calculations to strike a balance between computational efficiency and accuracy.

$$E_{\text{Cut}} = \frac{\hbar^2}{2m_e} G_{\text{Cut}}^2 \quad (2.44)$$

$$\psi_i = \sum_{\mathbf{G}+\mathbf{k} < G_{\text{Cut}}} c_{i,\mathbf{k}+\mathbf{G}} e^{i(\mathbf{k}+\mathbf{G})\cdot\mathbf{r}} \quad (2.45)$$

The discussion above highlights a crucial parameter in DFT calculations: the cut-off energy for the plane wave basis set, denoted as E_{Cut} . If E_{Cut} is not specified manually, most commercially available DFT codes utilize a default value equal to the E_{Cut} of the element present in the system with the highest cut-off value. However, this approach can introduce a systematic error in the calculation of total energy. To mitigate this error, it's advisable to manually set a sufficiently high value for E_{Cut} during calculations. When performing DFT calculations for determining relative energies or free energy differences between different systems, it's crucial to use a common E_{Cut} value for all calculations to ensure better accuracy. This practice helps maintain consistency across calculations and minimizes discrepancies arising from varying cut-off energies.

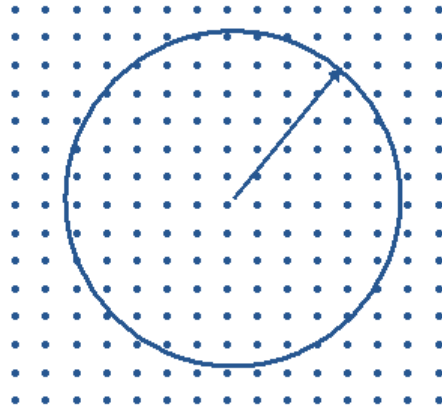


Figure 2.4: Illustration of the plane wave energy cut-off

loch's theorem simplifies the calculation by reducing the infinite number of wave functions to a finite number due to the presence of a finite number of electrons in the unit cell. However, for improved accuracy, an infinite number of discrete \mathbf{k} -points must be considered, and the total energy of the unit cell is computed as an integral over all these discrete \mathbf{k} -points.

Fortunately, the wave functions at neighbouring \mathbf{k} -points often exhibit similarities, allowing for the use of an interpolation scheme in typical DFT calculations with a finite number of \mathbf{k} -points. This interpolation effectively converts the integral into a sum over the discrete \mathbf{k} -points, weighted appropriately to account for the finite number of points. Nevertheless, a systematic error can arise when \mathbf{k} -points are not sufficiently dense. Therefore, it's essential to perform convergence tests before conducting detailed DFT calculations, considering \mathbf{k} -point grids of varying densities. These tests ensure that the chosen \mathbf{k} -point sampling is adequate for obtaining accurate results.

2.3.7. The pseudopotential method:

For plane waves oscillating on short length scales, a high energy cut-off is necessary. This poses a significant challenge because the highly localized core electrons of an atom also exhibit these oscillations [18]. Consequently, a large number of plane waves with high kinetic energies are required to accurately describe them, leading to increased computational costs. However, the core electrons do not significantly influence the physical properties of the element. Instead, it's the loosely bound valence electrons that play a crucial role in determining the system's physical properties. Therefore, approximating the core wave functions can substantially reduce the computational burden without compromising the accuracy of DFT calculations. The pseudopotential approximation method leverages this concept by separating the effects of core electrons and nuclei from the valence electrons. It substitutes the effect of core electrons with a pseudopotential acting on pseudo wave functions, rather than the true valence wave function. This substitution is designed such that outside a cut-off radius, the pseudopotential and the corresponding pseudo wave functions become identical to the all-electron potential and wave functions. The schematic representation of the variation of a pseudopotential and wave function compared to their all-electron counterparts inside and outside the cut-off radius is depicted in Figure 2.5. This method effectively reduces computational costs while preserving the accuracy of DFT calculations.

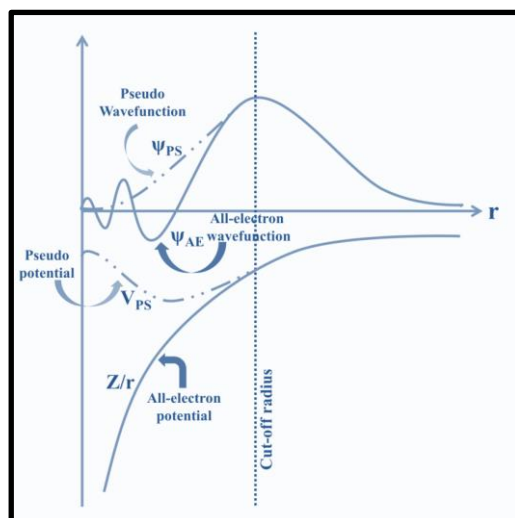


Figure 2.5: Representation of the pseudo and all electron wave function and pseudo and all electron potential

Following the aforementioned method, pseudo wave functions are prepared and then supplied to the inverse Kohn-Sham equations to construct the pseudopotential. Ideally, pseudopotentials are constructed for isolated atoms of elements but can be reliably utilized even when these atoms are placed in different chemical environments without requiring modifications to the pseudopotential. This property is known as the transferability of pseudopotentials. Most current DFT codes provide a library of pseudopotentials for all elements in the periodic table, including pseudopotentials for different valence electron configurations for selected elements. There are primarily two types of pseudopotentials: norm-conserving pseudopotentials and ultrasoft pseudopotentials. In norm-conserving pseudopotentials, the amount of charge enclosed by the pseudopotential in a certain space is equivalent to the charge enclosed by an all-electron potential in the same region. Conversely, ultrasoft pseudopotentials relax this condition and employ charge augmentation functions to compensate for the difference. Ultrasoft pseudopotentials were initially proposed by David Vanderbilt in 1990 [19]. As the name suggests, ultrasoft pseudopotentials require fewer plane waves for expansion, and the need for a high plane wave energy cut-off is alleviated when utilizing this type of pseudopotential. However, one drawback of ultrasoft pseudopotentials is the requirement for specifying empirical parameters for each element. While current DFT codes typically include carefully developed pseudopotentials, they may also incorporate ultrasoft pseudopotentials with varying degrees of softness for specific elements in special cases.

2.3.8. The projector augmented wave (PAW) method:

The projector augmented wave (PAW) method [20] integrates the pseudopotential method with the linear augmented plane wave method, significantly enhancing the efficiency of DFT calculations. It has emerged as one of the most widely used techniques in current DFT codes. Valence electronic wave functions exhibit rapid oscillations on short length scales near the core region to satisfy orthogonality conditions between valence and core electron wave functions, necessitating very fine k-point grids for accurate description. The PAW approach addresses this challenge by transforming the rapidly oscillating wave functions into smooth auxiliary wave functions, reducing computational costs and enabling the calculation of all-electron properties—a feat not achievable through the pseudopotential method alone. Most contemporary DFT codes employ either partial (e.g., CASTEP) or full implementation (e.g., VASP [22-25]) of the PAW method. In the PAW approach, the primary objective is to replace the rapidly oscillating electronic wave functions with auxiliary smooth wave functions within an augmented region through a linear transformation operator \mathbf{T} , which transforms the smooth wave functions $|\tilde{\psi}\rangle$ into all-electron wave functions $|\psi\rangle$.

$$|\psi\rangle = \mathbf{T}|\tilde{\psi}\rangle \quad (2.46)$$

An augmentation sphere ($|\mathbf{r} - \mathbf{R}^a| < r_c^a$) is constructed around each atom 'a'. Where r_c^a is the cut-off radius, \mathbf{a} is the atom index and \mathbf{R}^a is the atom position. The linear transformation operator can be written as

$$\mathbf{T} = 1 + \sum_a \mathbf{T}^a \quad (2.47)$$

\mathbf{T}^a only acts within the augmentation sphere. So $|\psi\rangle$ and $|\tilde{\psi}\rangle$ are different only within the augmentation sphere. Within the augmented region, a complete basis set of partial waves $|\phi_i^a\rangle$ is defined to expand the all-electron wave functions which are the solution to all electron Kohn-Sham equations. Smooth partial wave functions can be obtained using the transformation operator \mathbf{T} as

$$|\phi_i^a\rangle = \mathbf{T}|\tilde{\phi}_i^a\rangle = (1 + \sum_{a'} \mathbf{T}^{a'})|\tilde{\phi}_i^a\rangle = (1 + \mathbf{T}^a)|\tilde{\phi}_i^a\rangle \quad (2.48)$$

Outside the augmentation sphere, *i.e.* for $\mathbf{r} > r_c^a$, the smooth and all electron partial wave functions become identical, $|\phi_i^a\rangle = |\tilde{\phi}_i^a\rangle$, for $\mathbf{r} > r_c^a$. Inside the cut-off radius, the smooth wave functions can be expanded in terms of the above defined smooth partial wave functions as

$$|\widetilde{\psi}\rangle = \sum_i P_i^a |\widetilde{\phi}_i^a\rangle \quad (2.49)$$

Multiplying equation (2.49) by the transformation operator T, one can obtain the all-electron wave functions inside the augmented sphere as

$$|\psi\rangle = \sum_i P_i^a |\phi_i^a\rangle \quad (2.50)$$

Thus, both the smooth and all electron wave function have the same expansion coefficients P_i^a . To determine the coefficients, a set of smooth projection functions $|\widetilde{p}_i^a\rangle$ are defined that satisfy the orthogonality and completeness criterion within the augmented sphere, *i.e.*

$$\langle \widetilde{p}_i^a | \widetilde{\phi}_j^a \rangle = \delta_{ij} \quad (2.51)$$

And

$$\sum_i |\widetilde{\phi}_i^a\rangle \langle \widetilde{p}_i^a| = 1 \quad (2.52)$$

There is no restriction of the projection function outside the sphere. Multiplying equation (2.51) with $\langle \widetilde{p}_i^a |$ and using equation (2.52), the expansion coefficients are determined as the following:

$$\langle \widetilde{p}_i^a | \psi \rangle = \sum_j P_j^a \langle \widetilde{p}_i^a | \widetilde{\phi}_j^a \rangle = \sum_j P_j^a \delta_{ij} = P_i^a \quad (2.53)$$

The linear transformation operator can also be expressed in terms of $|\phi_i^a\rangle$, $|\widetilde{\phi}_i^a\rangle$ and $|\widetilde{p}_i^a\rangle$ as

$$T = 1 + \sum_a \sum_i (|\phi_i^a\rangle - |\widetilde{\phi}_i^a\rangle) \langle \widetilde{p}_i^a| \quad (2.54)$$

The PAW approach as described above ensure the pseudopotential wave functions to have the same form as the whole electron one outside the augmentation region whereas inside the augmented region the wave function continues as a smooth one. Just like the Hartree or Hartree-Fock scheme the projector augmented wave method based DFT calculations also use an iterative method to minimize the total energy. A simplified mechanism of the SCF scheme as utilized in DFT frameworks is illustrated in Figure 2.6.

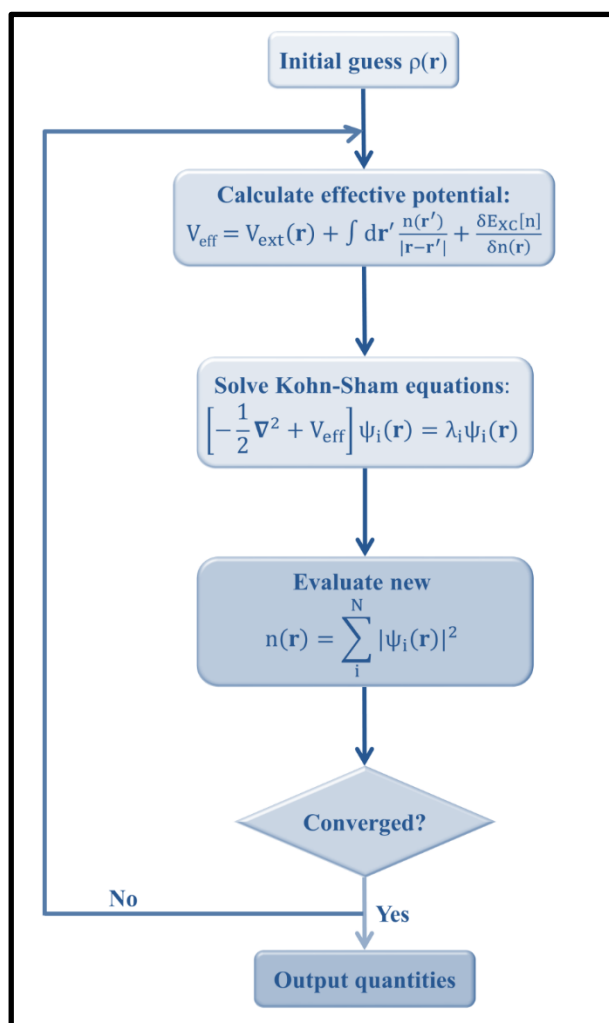


Figure 2.6: Simplified illustration of the SCF minimization process within DFT level of theory

References:

- [1] Hartree, Douglas R. "The wave mechanics of an atom with a non-Coulomb central field. Part I. Theory and methods." *Mathematical Proceedings of the Cambridge Philosophical Society*. Vol. 24. No. 1. Cambridge university press, 1928.
- [2] Thomas, Llewellyn Hilleth. "I. The kinematics of an electron with an axis." *The London, Edinburgh, and Dublin Philosophical Magazine and Journal of Science* 3.13 (1927): 1-22.
- [3] Parr, R. G., and W. Yang. "Horizons of quantum chemistry." *Horizons of Quantum Chemistry*. Springer. <https://doi.org/10.1007/978-94-009-9027-2> (1980).
- [4] Hohenberg, Pierre, and Walter Kohn. "Inhomogeneous electron gas." *Physical review* 136.3B (1964): B864.
- [5] Kohn, Walter, and Lu Jeu Sham. "Self-consistent equations including exchange and correlation effects." *Physical review* 140.4A (1965): A1133.
- [6] Perdew, John P., and Alex Zunger. "Self-interaction correction to density-functional approximations for many-electron systems." *Physical review B* 23.10 (1981): 5048.
- [7] Ceperley, David M., and Berni J. Alder. "Ground state of the electron gas by a stochastic method." *Physical review letters* 45.7 (1980): 566.
- [8] Perdew, John P., and Wang Yue. "Accurate and simple density functional for the electronic exchange energy: Generalized gradient approximation." *Physical review B* 33.12 (1986): 8800.
- [9] Langreth, David C., and M. J. Mehl. "Beyond the local-density approximation in calculations of ground-state electronic properties." *Physical Review B* 28.4 (1983): 1809.
- [10] Lee, Chengteh, Weitao Yang, and Robert G. Parr. "Development of the Colle-Salvetti correlation-energy formula into a functional of the electron density." *Physical review B* 37.2 (1988): 785.
- [11] Becke, Axel D. "Density-functional exchange-energy approximation with correct asymptotic behavior." *Physical review A* 38.6 (1988): 3098.
- [12] Perdew, John P., Kieron Burke, and Matthias Ernzerhof. "Generalized gradient approximation made simple." *Physical review letters* 77.18 (1996): 3865.
- [13] Tao, Jianmin, et al. "Climbing the density functional ladder: Nonempirical meta-generalized gradient approximation designed for molecules and solids." *Physical review letters* 91.14 (2003): 146401.
- [14] Sun, Jianwei, Adrienn Ruzsinszky, and John P. Perdew. "Strongly constrained and appropriately normed semilocal density functional." *Physical review letters* 115.3 (2015): 036402.
- [15] Becke, Axel D. "A new mixing of Hartree–Fock and local density-functional theories." *The Journal of chemical physics* 98.2 (1993): 1372-1377.
- [16] Harl, Judith, and Georg Kresse. "Cohesive energy curves for noble gas solids calculated by adiabatic connection fluctuation-dissipation theory." *Physical Review B* 77.4 (2008): 045136.

- [17] Grüneis, Andreas, et al. "Making the random phase approximation to electronic correlation accurate." *The Journal of chemical physics* 131.15 (2009).
- [18] Hamann, D. R., M. Schlüter, and C. Chiang. "Norm-conserving pseudopotentials." *Physical review letters* 43.20 (1979): 1494.
- [19] Vanderbilt, David. "Soft self-consistent pseudopotentials in a generalized eigenvalue formalism." *Physical review B* 41.11 (1990): 7892.
- [20] Blöchl, Peter E. "Projector augmented-wave method." *Physical review B* 50.24 (1994): 17953.
- [21] Clark, Stewart J., et al. "First principles methods using CASTEP." *Zeitschrift für kristallographie-crystalline materials* 220.5-6 (2005): 567-570.
- [22] Kresse, Georg, and Jürgen Hafner. "Ab initio molecular dynamics for liquid metals." *Physical review B* 47.1 (1993): 558.
- [23] Kresse, Georg, and Jürgen Hafner. "Ab initio molecular-dynamics simulation of the liquid-metal–amorphous-semiconductor transition in germanium." *Physical Review B* 49.20 (1994): 14251.
- [24] Kresse, Georg, and Jürgen Furthmüller. "Efficiency of ab-initio total energy calculations for metals and semiconductors using a plane-wave basis set." *Computational materials science* 6.1 (1996): 15-50.
- [25] Kresse, Georg, and Jürgen Furthmüller. "Efficient iterative schemes for ab initio total-energy calculations using a plane-wave basis set." *Physical review B* 54.16 (1996): 1116.

3. Review of past works:

3.1. Introduction:

The discovery of graphene in 2004 sparked a revolution in 2D materials research [1]. This class of ultra-thin materials, with their exceptional electronic, surface, and catalytic properties, holds immense potential across scientific disciplines. Beyond graphene, researchers have unveiled a diverse range of 2D materials including graphynes [2], transition metal dichalcogenides [3], and MXenes [4]. Each type boasts unique characteristics, making them prime candidates for applications in electronics, energy storage, catalysis, and even medicine. 2D materials are revolutionizing electrocatalysis. Their unique combination of excellent electronic properties, high stability, and tailorable surfaces makes them ideal for driving critical reactions in electrochemical cells, including oxygen reduction (ORR), oxygen evolution (OER), and hydrogen evolution (HER). While graphene, the first discovered 2D carbon material, initially shows limited efficiency in its original form, strategic modifications can unlock its true potential. This is where transition metal dichalcogenides (TMDs) come into play. The extensive variety of transition metals and chalcogenides (sulfur, selenium, tellurium) combined with the diverse structural phases (such as 2H, 1T, and 1T') present in TMDs provides scientists with a broad spectrum for designing and optimizing electrocatalysts. In all structural phases of transition metal dichalcogenides (MX_2), transition metal atoms are positioned between two layers of chalcogenide atoms (X-M-X). These TMDs exhibit multiple structural phases arising from distinct coordination geometries of the transition metal atoms, with 2H featuring a trigonal prismatic configuration, 1T showcasing an octahedral geometry, and 1T' displaying a distorted octahedral structure (Figure 3.1) [5]. The stacking orders of the atomic planes (X-M-X) also vary among these phases, with 2H-TMDs demonstrating Bernal (ABA) stacking and 1T-TMDs featuring rhombohedral ABC stacking [6]. This diversity in structural phases results in various electronic properties. For example, while 2H MoS_2 displays semiconducting attributes, 1T and 1T' MoS_2 exhibit metallic and semimetallic characteristics respectively [7]. The pristine 2H MoS_2 monolayer exhibits limited activity for electrocatalytic processes like hydrogen evolution reaction (HER) and oxygen reduction reaction (ORR). This limitation stems from a high energy barrier associated with the reactions on its surface. However, by strategically introducing defects or doping with other elements (metals or non-metals), the chemical reactivity of the MoS_2 monolayer can be significantly enhanced. These modifications create additional active sites on the material's surface, facilitating the adsorption and

conversion of reactant molecules. This ultimately leads to improved electrocatalytic performance, characterized by lower overpotentials (the extra voltage required to drive the reaction). Additionally, these adjustments can improve conductivity, providing further support for efficient electrocatalysis. The 1T phase of MoS₂, despite its dynamic instability, possesses metallic conductivity and an abundance of active sites. This distinctive combination positions it as a promising candidate for electrocatalysis applications. Motivated by the promising electrocatalytic activity of the 1T phase, researchers have actively pursued strategies to transform the more stable 2H MoS₂ into 1T MoS₂. These strategies include doping the material with specific elements or utilizing single-atom catalysts to facilitate the phase transition [8]. Another phase of MoS₂, known as 1T', has recently garnered attention from researchers due to its remarkable properties. Unlike the dynamically unstable 1T phase, 1T' is dynamically stable [9]. Its semimetallic nature and stability have drawn interest for electrocatalysis applications. Beyond MoS₂, other transition metal dichalcogenides (TMDs) like WS₂ are attracting increasing interest. Theoretical and experimental studies have revealed diverse structural phases in WS₂, similar to those observed in MoS₂. This growing understanding of WS₂ phases paves the way for in-depth exploration of its electrocatalytic activity. Indeed, the electrocatalytic performance of WS₂ has been relatively less explored compared to MoS₂, highlighting a significant research opportunity. To address this gap, it is imperative to review previous work on the different phases of WS₂. By comprehensively examining the existing literature on WS₂ phases, including structural characteristics, electronic properties, and electrochemical behavior, researchers can gain valuable insights into its potential as an electrocatalyst. This review would not only enhance our understanding of WS₂-based electrocatalysis but also provide valuable guidance for future research directions, potentially unlocking new avenues for the development of efficient and sustainable energy conversion technologies.

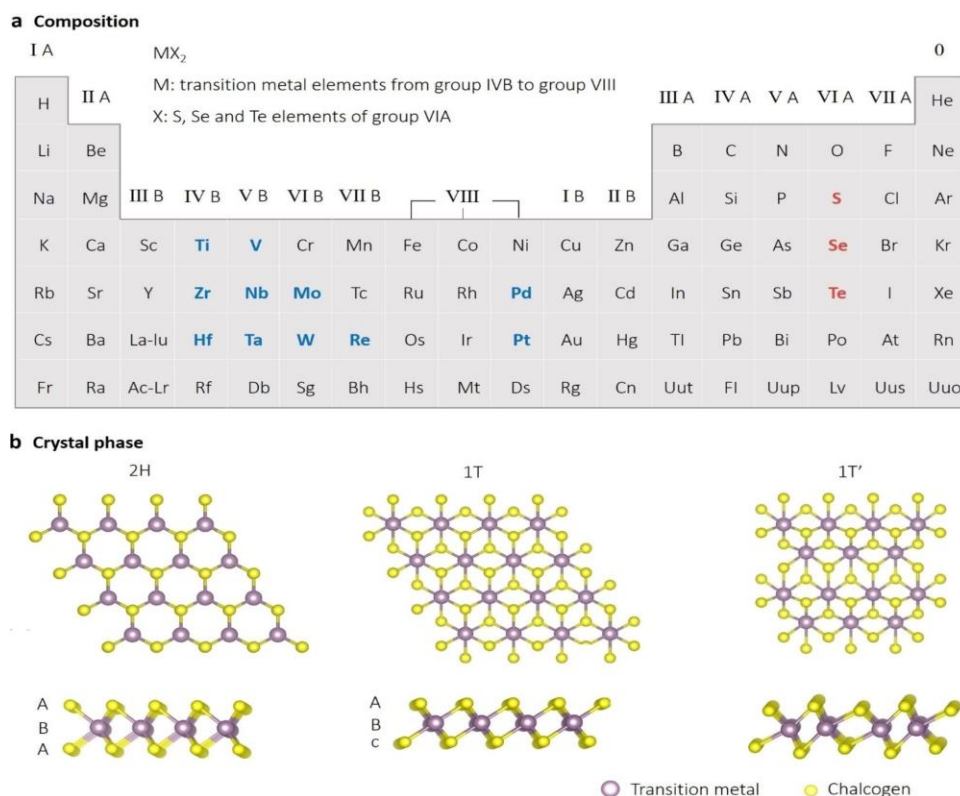


Figure 3.1: 2H, 1T and 1T' phases of Transition metal dichalcogenides [Ref. 5].

Moreover, Low-dimensional Janus transition metal dichalcogenides (TMDs) have emerged as a captivating class of materials, captivating researchers with their unique and exploitable properties. Inspired by the Roman god Janus, depicted with two faces symbolizing beginnings and endings, Janus TMDs possess a fascinating duality [10]. Unlike their conventional counterparts, these materials exhibit distinct characteristics on opposing surfaces. This remarkable property, often manifested as contrasting wettability, unlocks a treasure trove of potential applications across diverse scientific and technological frontiers. Beyond their intriguing surface duality, Janus TMDs boast another layer of exceptional qualities. They possess the remarkable ability to exhibit tuneable electronic band gaps. This characteristic allows scientists to precisely control their electrical properties, paving the way for their integration into advanced devices. Additionally, Janus TMDs exhibit a unique coexistence of several fascinating physical effects, including the Rashba effect, excitonic effects, and piezoelectricity [11]. These effects are rarely observed together in traditional TMDs, making Janus TMDs a truly unique and versatile material platform. Recent scientific investigations have shed light on the origin of these extraordinary properties in Janus TMDs. The key lies in the material's broken mirror symmetry. This asymmetry within the crystal structure disrupts the inherent balance, leading to the formation of an intrinsic dipole moment perpendicular to

the material's layers. This intrinsic dipole moment is believed to be the driving force behind the observed surface duality and the coexistence of various physical effects. The potential applications of Janus TMDs are as diverse as their properties. In the realm of water purification and desalination, their contrasting wettability offers a distinct advantage. One surface can be engineered to be highly hydrophilic (water-loving), facilitating efficient water transport through the membrane. Simultaneously, the opposing surface can be designed to be hydrophobic (water-repelling), effectively blocking the passage of salt ions and other contaminants. This opens doors for the development of next-generation filtration technologies with superior efficiency and selectivity [12]. Janus TMDs also hold immense promise for revolutionizing the field of energy conversion and storage [13]. Their tunable electronic band gaps make them ideal candidates for applications in solar cells and photocatalysis, where light is harnessed to drive chemical reactions [14]. By strategically designing the band gap of a Janus TMD, scientists can optimize light absorption for efficient solar energy conversion or tailor the material to act as a highly effective electrode in a battery. The unique properties of Janus TMDs also position them favourably for advancements in sensing technologies. The coexistence of the Rashba effect and piezoelectricity can be exploited to develop highly sensitive sensors capable of detecting a wide range of chemicals and biological molecules. Such sensors have the potential to revolutionize various fields, from environmental monitoring and healthcare diagnostics to drug discovery. The realm of spintronics, a field that explores the spin of electrons for information processing and devices, could also benefit from Janus TMDs [15]. The broken mirror symmetry inherent to their structure can lead to intriguing spin-related phenomena that could be harnessed for the development of novel spintronic devices with superior performance. Catalysis, a cornerstone of numerous chemical processes, presents another exciting avenue for Janus TMD exploration. Janus transition metal dichalcogenides (TMDs) exhibit a remarkable duality: tunable electronic band gaps and contrasting surface properties. This translates to a significant increase in active sites for gas molecule adsorption due to the differing wettability of each surface. This inherent property opens exciting avenues for catalysis research. By strategically engineering the band gap, scientists can finely tune the adsorption and activation of reactant molecules on each Janus TMD surface. Furthermore, the contrasting wettability enable selective interaction with reaction components. This targeted control over reaction behaviour has the potential to revolutionize numerous chemical processes, promoting sustainability and efficiency across various industries. Janus TMDs, therefore, offer a promising platform for advancing catalysis research and paving the way for innovative solutions to real-world challenges. Additionally, their tuneable properties make

them well-suited for photocatalytic water splitting applications [16]. While the potential applications of Janus TMDs are vast and enticing, it's crucial to remember that this field is still in its early stages. Extensive research efforts, encompassing both experimental and computational studies, are ongoing to fully understand and exploit the potential of these remarkable materials. As research progresses, we can confidently expect to witness the emergence of even more innovative and groundbreaking applications of Janus TMDs, propelling technological advancements across a multitude of fields.

3.2. Previous computational and experimental reports on the structural, electronic and electrocatalytic properties of pure/ doped TMDs and their Janus Structures:

Linus Pauling's pioneering work in 1923 laid the foundation for our understanding of the structure of transition metal dichalcogenides (TMDs) [17]. Following this, Robert Frindt's groundbreaking work in 1963 pioneered the use of adhesive tapes for producing ultrathin layers of MoS₂[18]. Frindt's technique laid the groundwork for the exfoliation method, which later played a critical role in isolating single-layer materials like graphene and MoS₂. Subsequently, in 1986, the production of monolayer MoS₂ suspensions marked a significant milestone in the exploration of two-dimensional materials [19]. This achievement opened doors for investigating the unique properties of single-layer MoS₂, leading to potential applications in diverse fields such as electronics, optoelectronics, and catalysis. Following the groundbreaking discovery of graphene in 2004, the search for ultrathin monolayers like Transition Metal Dichalcogenides (TMDs) has intensified [20]. The abundance of semiconducting MoS₂ among Transition Metal Dichalcogenides (TMDs), coupled with its tunable band gap, has garnered significant attention for research, particularly in electrocatalytic properties [21].

Computer simulations have become a powerful tool for understanding how a material's electronic structure influences its ability to act as a catalyst. These simulations can even guide the design of better catalysts. However, accurately creating the desired atomic configurations in real-world experiments can be difficult, making it challenging to directly compare theoretical predictions with practical results. For molybdenum disulfide (MoS₂), past research has shown that its molybdenum (Mo) edges are active for the hydrogen evolution reaction (HER) while the sulphur (S) edges are inactive [22]. In early 2015, Haotian Wang et. al. utilized a computational approach based on descriptors to predict that incorporating transition metals like iron (Fe), cobalt (Co), nickel (Ni), or copper (Cu) could activate the S-edges for HER [23].

Vertically aligned MoS₂ nanofilms with well-defined edges were chosen as a model system to test these predictions experimentally. The results showed that doping the MoS₂ nanofilms with transition metals increased the exchange current densities by at least a factor of two, confirming the theoretical calculations. This work highlights the potential of strategically adding promoter atoms to specific atomic sites for improving electrocatalysts. Additionally, it demonstrates the value of well-defined systems in understanding how these promoters enhance catalytic activity.

Electrochemical water splitting is a promising method for clean hydrogen production. Two-dimensional molybdenum disulfide (MoS₂) has emerged as a potential alternative to expensive platinum catalysts for the hydrogen evolution reaction (HER). However, MoS₂'s catalytic activity is primarily limited to its edge sites, leaving a significant portion of the material inactive. In 2015, Jiao Deng et. al. introduces a novel approach to activate the underutilized in-plane sulfur (S) atoms in MoS₂ for HER [24]. The researchers demonstrate, for the first time, that doping MoS₂ with single metal atoms can significantly enhance its catalytic activity. Experiments using single platinum (Pt) atoms doped onto few-layered MoS₂ nanosheets (Pt-MoS₂) showed a remarkable improvement in HER performance compared to undoped MoS₂. Density functional theory (DFT) calculations revealed that the enhanced activity stems from the influence of doped Pt atoms on the adsorption behavior of hydrogen (H) atoms on neighboring in-plane S sites. The researchers further screened the HER activity of MoS₂ doped with various transition metals using DFT calculations. They observed a volcano-shaped relationship between the H atom adsorption free energy and HER activity, which was experimentally validated by doping MoS₂ with non-precious metals like cobalt (Co) and nickel (Ni).

B.B. Xiao et al. in 2015 [25] found that Density functional theory (DFT) simulations were employed to explore the viability of cobalt (Co) and nickel (Ni) doped molybdenum disulfide (MoS₂) as electrocatalysts for the oxygen reduction reaction (ORR). The investigation unveiled that the rate-determining step (RDS) in the ORR process is contingent upon both the type of dopant and the electrolyte. For Co/MoS₂: In acidic conditions, the RDS entails the formation of the second water molecule with an energy barrier of 1.49 eV. Under alkaline conditions, the RDS shifts to the formation of hydroxyl ions (OH⁻) with a reduced barrier of 0.94 eV. Regarding Ni/MoS₂: In acidic environments, the RDS mirrors that of Co/MoS₂, albeit with a slightly diminished barrier of 0.87 eV. Conversely, in alkaline settings, the RDS for Ni/MoS₂ becomes the formation of oxygen atoms (O) with a barrier of 0.92 eV. Furthermore, the strong adsorption of HOOH intermediates suggests a predominant 2-electron ORR pathway for

Ni/MoS₂, potentially leading to lower activity compared to Co/MoS₂. These findings underscore the potential of employing DFT to enhance conventionally inactive materials for effective ORR catalysis. This presents an avenue for the development of economical, platinum-free catalysts for fuel cell applications.

Cuicui Du et. al. [26] observed that Sn-MoS₂ nanosheets exhibit exceptional HER performance. They achieve a low overpotential (28 mV) at a specific current density (10 mA cm²) and a small Tafel slope (37.2 mV dec⁻¹), demonstrating impressive stability as well. This significant improvement compared to pure MoS₂ nanosheets is attributed to several factors: increased availability of active edge sites, enhanced inherent catalytic activity of each active site, and faster electron transfer due to Sn doping.

Mn-MoS₂/rGO hybrid exhibits improved catalytic activity for HER with a low overpotential (around 110 mV). This enhanced performance is attributed to two key factors. First, the reduced graphene oxide component provides high conductivity, facilitating efficient electron transport. Second, doping MoS₂ with manganese ions (Mn) at its sulfur edges (S-edge) appears to directly enhance its intrinsic catalytic activity. These findings suggest that Mn-doping plays a positive role in boosting HER activity. Overall, the Mn-MoS₂/rGO hybrid developed in this study demonstrates potential as a viable alternative to expensive noble metal catalysts for HER, paving the way for more sustainable and cost-effective hydrogen production [27].

Developing efficient, affordable, and durable alternatives to platinum-based catalysts for the oxygen reduction reaction (ORR) is critical for the widespread adoption of fuel cells. Zhongxu Wang et. al. [28] utilizes density functional theory (DFT) calculations to systematically explore the ORR activity of MoS₂ monolayers substitutionally doped with various transition metals (TM). The computations reveal that these TM atoms interact strongly with sulfur vacancies (S-vacancies) within the MoS₂ structure, leading to significant changes in its electronic and magnetic properties. By analyzing the calculated free energies, the study identifies Cu doped MoS₂ monolayers as exhibiting the best ORR performance due to their optimal interaction with ORR-related molecules. This research suggests that strategically substituting MoS₂ with suitable transition metals is a promising approach to enhance its ORR catalytic activity. This finding paves the way for the development of novel 2D electrocatalysts for efficient ORR in fuel cells.

Molybdenum disulfide (MoS₂) with sulphur vacancies (MoS_{2-x}) has recently shown promise for the hydrogen evolution reaction (HER). However, the activity is sensitive to the number of

vacancies, creating a trade-off between maximizing activity per site and the total number of active sites. Sangwook Park [29] used computer modelling (density functional theory, DFT) and experiments to address this challenge. Their work demonstrates that decorating the basal plane of MoS_{2-x} with cobalt (Co) clusters significantly enhances HER activity. DFT calculations reveal that the optimal configuration involves Co clusters anchored on the sulfur vacancies, with the Co-Mo interface acting as the most effective active site. Experimental results confirm that adding Co not only boosts the activity per active site but also increases the overall electrochemically active surface area. These findings demonstrate that strategically placing transition metal clusters on sulphur vacancies can activate the basal plane of MoS_{2-x} for improved HER performance.

In a recent study by Zhang et al., the focus was on activating the typically inert basal plane of 2H MoS_2 for catalysing the oxygen reduction reaction (ORR) [30]. They accomplished this activation by substituting nitrogen (N) and phosphorus (P) atoms at the sulphur sites within the MoS_2 structure. This doping strategy induced significant spin polarization, thereby creating conducive conditions for oxygen (O_2) adsorption. Their investigation unveiled a notable contrast in catalytic performance between N-doped and P-doped MoS_2 monolayers. N-doped MoS_2 exhibited superior ORR efficiency, demonstrating a lower overpotential (0.67 V) compared to P-doped MoS_2 . The researchers attributed the inferior performance of P-doped MoS_2 to its strong affinity towards intermediate reaction products such as oxygen (O) and hydroperoxyl (OOH) species. This robust binding impeded the overall reaction pathway, resulting in diminished catalytic activity.

Introducing metal atom intercalation into the interlayer positions of 1T MoS_2 leads to a significant decrease in overpotential for the hydrogen evolution reaction (HER). The onset potential in acidic conditions for pristine 1T MoS_2 is 180 mV, but with the introduction of cations such as Na^+ , Ca^{2+} , Ni^{2+} , and Co^{2+} , this value decreases substantially to 60 mV. Research findings indicate that Na^+ intercalation notably reduces the Gibbs free energy of hydrogen adsorption (ΔG_{H}), approaching nearly zero. Experimental results further corroborate that Na^+ intercalation yields the most favourable outcomes among the tested cations, resulting in significantly lower overpotential for the HER [31].

Electrolysis, particularly the hydrogen evolution reaction (HER), offers a promising path towards clean energy production using water-splitting devices. However, widespread adoption relies on developing affordable and highly efficient catalysts to replace expensive platinum.

Building on these findings, this study proposes a strategy to enhance MoS₂'s HER performance by directly doping it with transition metals and influencing its energy levels. In 2017, Yi Shi et. al. observed that zinc-doped MoS₂ (Zn-MoS₂) exhibits exceptional electrochemical activity for HER [32]. This is evident by the significantly improved onset potential (the voltage needed to initiate the reaction), reaching -0.13 V vs RHE (reversible hydrogen electrode). Additionally, Zn-MoS₂ achieves a remarkable turnover rate (molecules converted per active site per second) of 15.44 s⁻¹ at a low overpotential of 300 mV, surpassing previously reported MoS₂ catalysts by a significant margin. This dramatic improvement can be attributed to a combined effect: electronic modification (better energy level alignment) and morphological changes (increased active sites). These factors work together to accelerate the HER process thermodynamically and kinetically, respectively. This research paves the way for further exploration of incorporating promoters (dopants) to create improved electrocatalysts. It also deepens our understanding of how to optimize the electrocatalytic activity of these unique materials.

Metal-organic frameworks (MOFs) and metal dichalcogenides (MDs) are highly promising materials owing to their versatility, expansive surface area, intricate pore structures, and inherent catalytic capabilities [33]. This study presents an innovative electrocatalyst: vertically aligned molybdenum disulfide (MoS₂) nanosheets incorporated within a molybdenum-nitrogen-carbon (Mo-N/C) framework. This distinctive architecture demonstrates outstanding multifunctional electrocatalytic performance and durability across three pivotal reactions: hydrogen evolution (HER), oxygen evolution (OER), and oxygen reduction (ORR).

The research conducted by Haoran Guo et al. in 2019 sheds light on the potential of single transition metal atoms decorating defective molybdenum disulfide (MoS₂) sheets as catalysts for the conversion of nitrogen gas (N₂) into ammonia (NH₃) through an electrocatalytic process, known as the Nitrogen Reduction Reaction (NRR) [34]. Their study utilized computer simulations based on Density Functional Theory (DFT) to investigate the catalytic properties of various transition metals anchored onto MoS₂ sheets. They observed that incorporating single transition metals weakens the strong nitrogen-nitrogen triple bond, thereby facilitating the activation of inert nitrogen gas. Among the transition metals tested (Scandium, Titanium, Copper, Hafnium, Platinum, and Zirconium), titanium (Ti) decorated MoS₂ exhibited the most favorable energy change for the rate-limiting step of ammonia production. This highlights the potential of Ti-decorated MoS₂ as an efficient catalyst for the NRR. To gain further insights into the catalytic role of transition metals, the researchers developed a new descriptor (ϕ) that combines the number of valence electrons with the electronegativity of the decorating metal

atom. This descriptor revealed a correlation between the position of the metal's d-orbitals (d-band center) and its binding strength to nitrogen atoms. However, metals with less than half-filled d-orbitals exhibited deviations from this trend, indicating the potential for promoting unwanted side reactions. Interestingly, MoS₂ sheets decorated with Sc, Ti, Zr, and Hf showed promising NRR efficiency and selectivity, suggesting their potential for sustainable ammonia production. Moreover, the insights gained from this study can potentially extend to other catalytic processes such as Oxygen Reduction Reaction (ORR), Hydrogen Evolution Reaction (HER), etc., facilitating the development of improved electrocatalysts for various sustainable energy applications.

Much of the research on electrocatalysis using two-dimensional transition metal dichalcogenides (TMDs) has predominantly centered on molybdenum disulfide (MoS₂). Consequently, the potential of numerous other TMDs remains largely untapped and underexplored in this field. In 2021 Shufang Tian et. al. [35] investigates the oxygen reduction reaction (ORR) activity of various sulfur-based TMDs with different crystal structures. The findings reveal that pristine (undoped) TMDs exhibit no ORR activity. However, strategic doping with single atoms offers a powerful method to activate these materials. Doping with transition metals (like Ni or Co) or substituting certain elements within the TMD structure significantly modifies their properties. Particularly exciting are the results for Ni or Co-doped TMDs in specific crystal phases (1T-TiS₂, 2H-TiS₂, 1T-ZrS₂, 1T-TaS₂, 1T-NbS₂, and 2H-TaS₂). These doped TMDs display ORR activity with overpotentials (a measure of efficiency) ranging from 0.32 to 0.55 volts, comparable to the performance of top-tier platinum (Pt) based catalysts. For other TMDs (2H-WS₂, 2H-TaS₂, 2H-TiS₂, and 1T'-WS₂), nitrogen doping proves to be an effective activation method. These N-doped TMDs achieve overpotentials between 0.3 and 0.75 volts. The study's key takeaway is that single-atom doping can dramatically alter the ORR activity of TMDs. This finding should spark further experimental exploration of these materials for potential use in ORR applications.

In 2012 Zhuangzhi Wu et al. [36] developed a new and efficient method for producing tungsten disulfide (WS₂) nanosheets (NSs) as electrocatalysts for the hydrogen evolution reaction (HER). This simple and reliable approach, called a mechanical activation strategy, uses tungsten trioxide (WO₃) and sulfur (S) as starting materials. The resulting WS₂ NSs exhibit a unique structure of individual nanosheets less than 10 nanometers thick. By analyzing the effects of different synthesis conditions on the material, the researchers proposed a plausible

reaction pathway and formation mechanism. They believe a critical step involves ball milling pretreatment, which facilitates the formation of the WS₂ NSs. These WS₂ NSs possess a large number of active sites due to their unique structural characteristics. The loosely stacked layers provide highly exposed edges and rims, ideal for HER. Consequently, the WS₂ NSs demonstrate exceptional electrocatalytic activity for HER, significantly surpassing the performance of commonly used molybdenum disulfide (MoS₂) catalysts.

In 2013 Damien Voiry [37] explored the potential of chemically exfoliated tungsten disulfide (WS₂) nanosheets for hydrogen evolution. molybdenum or tungsten disulfide nanoparticles with high concentrations of metallic edges have shown promising results. However, a key challenge remains: increasing the number and activity of these catalytic sites. Their findings indicate that monolayered WS₂ nanosheets, obtained through chemical exfoliation, exhibit excellent electrocatalytic activity for hydrogen evolution with very low energy overpotentials. Analysis suggests this enhanced performance is linked to the high concentration of a strained metallic phase (1T) present in these newly formed nanosheets. These results highlight the potential of chemically exfoliated WS₂ nanosheets as promising and cost-effective catalysts for clean hydrogen production.

In 2015, Darwin Barayang Putungan et al. [38] pioneered the use of computer simulations, specifically density functional theory, to delve into a class of two-dimensional materials denoted as 1T' MX₂, where M represents molybdenum or tungsten, and X denotes sulfur, selenium, or tellurium, for potential catalytic applications in the hydrogen evolution reaction (HER). The study centered on a particular crystal structure within this material class known as 1T'. Their simulations revealed that 1T' structures generally exhibit greater stability compared to their closely related 1T counterparts, hinting at their potential relevance in explaining past experimental findings and practical applications. Moreover, the research identified trends in HER activity across various materials. Among these, sulfide-based materials, particularly those with sulfur (X = sulfur), showcased the most promising catalytic performance for HER, followed by selenides and tellurides. Notably, molybdenum disulfide (1T' MoS₂) and tungsten disulfide (1T' WS₂) demonstrated exceptional HER efficiency within the sulfide category. The team introduced a novel mechanism for understanding HER activity, rooted in the calculated electronic properties, specifically the density of states, of these materials, diverging from the conventional assumption of metallicity used in prior studies. Furthermore, the study highlighted the substantial impact of the atomic arrangement within the 1T' structure, where

stretched or compressed X sites exerted contrasting effects on HER activity—stretched sites promoting HER while compressed ones impeding it. Leveraging these insights, the researchers explored the potential enhancement of HER performance by subjecting the material to external strain. Overall, this research furnishes crucial insights into comprehending previous experimental observations and pinpointing promising materials for clean energy applications, particularly those revolving around HER.

In 2016 Ping Xiao et. al. introduces a new catalyst for HER: palladium nanoparticles (Pd NPs) supported on inorganic fullerene-like tungsten disulfide (WS_2) [39]. Notably, the Pd loading in this catalyst is just 0.76 wt%, making it potentially more cost-effective than existing options. Tests conducted in a sulfuric acid solution (0.5 M H_2SO_4) revealed that the Pd/ WS_2 catalyst exhibits impressive HER activity. It achieves a low overpotential (around 130 mV) at a specific current density (10 mA cm^{-2}) and a small Tafel slope (82.4 mV dec^{-1}), comparable to the performance of more expensive platinum catalysts loaded on WS_2 (Pt/ WS_2) with a higher Pt content (0.88 wt%). Further analysis showed the presence of tungsten trioxide (WO_3) impurities formed on the WS_2 surface during catalyst preparation. Additionally, the Pd NPs were found to be primarily located within the WS_2 nanocages. Based on these observations and contrasting experiments, the researchers propose a reaction mechanism. They suggest that the WO_3 impurities play a key role in generating a critical intermediate (Hads), while the Pd NPs act as the active sites for hydrogen (H_2) production. The Pd/ WS_2 catalyst also demonstrates remarkable long-term stability due to the protected location of the Pd NPs inside the WS_2 cages. This combination of high HER activity, lower cost compared to Pt catalysts, and good stability makes the Pd/ WS_2 catalyst a promising alternative for future hydrogen production.

Jin's work in 2017, have shown promise in using earth-abundant transition metal phosphides, particularly cobalt phosphide (CoP), for hydrogen production via the hydrogen evolution reaction (HER) [40]. However, researchers are actively seeking ways to further enhance their catalytic activity. This research explores combining CoP nanoparticles with tungsten disulfide (WS_2) nanosheets to create a more effective HER catalyst. By experimenting with different ratios of CoP to WS_2 , the scientists aimed to identify the optimal combination for peak performance. A straightforward method using ultrasound was employed to prepare the CoP/ WS_2 composites. Notably, all the composite materials exhibited improved HER activity compared to pure CoP nanoparticles or WS_2 nanosheets alone. The most effective CoP/ WS_2 composite achieved impressive results. It displayed a very low starting energy requirement (50

mV overpotential), a high current density (78 mA/cm² at 300 mV overpotential), and a small Tafel slope (64.63 mV/decade). These characteristics all point towards exceptional HER catalytic activity.

A computational approach (first-principles method) was used to study the magnetic properties of single and double nickel (Ni) atoms doped into a single layer of tungsten disulfide (WS₂) in 2016 [41]. The results showed that both configurations exhibit magnetism. The magnetism arises from interactions between the Ni atom's electrons (p orbitals) and the electrons in neighbouring sulphur (S) atoms (d orbitals). This interaction is referred to as p-d hybridization and leads to ferromagnetism (magnetism where neighbouring atomic moments align) in the Ni-doped WS₂ monolayer. However, as the distance between the Ni atoms increases, the magnetic coupling weakens and becomes antiferromagnetic (magnetism where neighbouring atomic moments point in opposite directions). This behaviour can be explained by the two-impurity Haldane-Anderson model, which was simulated using a quantum Monte Carlo method. These findings suggest that WS₂ monolayers doped with two closely spaced Ni atoms could be promising candidates for a new class of two-dimensional magnetic materials called transition-metal nanosheets. The study also investigated the energy required to incorporate Ni atoms under different conditions (tungsten-rich or sulfur-rich environments). The results predict that incorporating Ni atoms would be easier in a sulfur-rich WS₂ monolayer during experiments.

Doping tungsten disulfide (WS₂) with exotic atoms has been a strategy to improve its ability to generate hydrogen through the hydrogen evolution reaction (HER). This approach aims to create more active sites on the base plane of the material and narrow its bandgap for better performance. However, most existing catalysts use dopants with similar electronegativity (electron-attracting tendency) to the atoms already present in WS₂. This limits the ability to significantly adjust the bandgap and reduce the free energy required for hydrogen adsorption (ΔG_H). In 2020 Yaping Pan et. al. explored tellurium (Te) as a dopant for WS₂ due to its ability to drastically alter the bandgap and its significantly lower electronegativity compared to sulfur (S) atoms in WS₂ [42]. They created vertically aligned WS₂ nanoelectrodes doped with Te. Experimental results and computer simulations (density functional theory, DFT) confirmed successful bandgap narrowing after Te doping. This narrowing reduces the Schottky barrier, which is the energy barrier hindering electron transfer. Consequently, it improves the overall electrocatalytic performance of the material. Additionally, the lower electronegativity of Te atoms increases the electron density in surrounding regions. This activates both the sulfur edges

of the basal plane near the Te atoms and the hollow sites within the WS₂ nanosheets for HER. DFT calculations showed a decrease in ΔG_H for both types of active sites: basal plane S edges (from 2.27 eV to 2.08 eV) and hollow sites (from 2.28 eV to 1.85 eV) after Te doping. The Te-doped WS₂ nanosheets demonstrated excellent HER performance, requiring an overpotential of only 213 mV to achieve a current density of 10 mA/cm² and exhibiting a low Tafel slope of 94 mV/dec. Additionally, they displayed remarkable stability when used in acidic environments.

In 2021 Xiaofeng Pu et al. focuses on iron-doped tungsten disulfide (Fe-doped WS₂) nanosheet arrays grown on carbon cloth using a solvothermal method. Both experimental results and computer simulations (first principles calculations) confirm that iron doping offers several benefits [43]. It increases the rate of charge transfer within the material, reduces resistance at the interface between the catalyst and the electrolyte, and expands the usable surface area. More importantly, iron doping activates previously inert sites within the plane of the WS₂ nanosheets, leading to a significant improvement in HER activity. The optimized sample achieved a low overpotential of 166 mV to drive a current density of 10 mA/cm² and a small Tafel slope of 82.2 mV/dec when tested in a 0.5 M sulfuric acid solution (H₂SO₄). These findings demonstrate that strategically introducing dopant atoms is a versatile approach for fine-tuning the electronic structure of WS₂, ultimately leading to enhanced electrocatalytic performance for HER.

Recent research (2021) by Zhuangchai Lai and colleagues has highlighted the growing interest in metastable 1T' phase transition metal dichalcogenides (1T' TMDs). These materials possess unique distorted structures and fascinating properties that depend on their specific phase [44]. However, producing high-quality crystals of 1T' TMDs, especially for group VIB elements (tungsten, molybdenum, selenium), has remained a significant challenge. This study presents a novel, general method for large-scale synthesis of metastable 1T' phase group VIB TMDs. This includes materials like tungsten disulfide (WS₂), tungsten diselenide (WSe₂), molybdenum disulfide (MoS₂), molybdenum diselenide (MoSe₂), and various alloys combining these elements (WS₂xSe₂(1-x) and MoS₂xSe₂(1-x)). We successfully determined the crystal structures of 1T' WS₂, WSe₂, MoS₂, and MoSe₂ using single-crystal X-ray diffraction. The newly synthesized 1T'-WS₂ displays a fascinating property – its intrinsic superconductivity depends on its thickness. Samples with a thickness of 90.1 nm exhibit a critical transition temperature (the temperature at which superconductivity occurs) of 8.6 K. This value drops to 5.7 K for single-layer 1T' WS₂. We attribute this behaviour to the high

concentration of intrinsic charge carriers and the semi-metallic nature of this specific TMD phase. This novel synthesis method paves the way for more systematic studies of the inherent properties within metastable TMDs, potentially leading to exciting discoveries in future research.

TMD based Janus monolayers:

Scientists have developed a new way to create a special type of two-dimensional material called a Janus monolayer. Unlike typical materials where the atoms are arranged symmetrically, Janus monolayers have a unique asymmetry. In this case, the researchers specifically broke the symmetry in the out-of-plane direction (up and down). Traditionally, scientists have tried to break the in-plane symmetry (across the plane of the material) of graphene using electric fields or by stacking different materials. Transition metal dichalcogenides, on the other hand, already have some natural in-plane asymmetry, making them useful for optoelectronics. This new approach focuses on breaking the out-of-plane symmetry. In 2017 Ang-Yu Lu et. al. developed Janus monolayers by taking a single layer of molybdenum disulfide (MoS_2) and completely replacing the top layer of sulphur atoms with selenium atoms [45]. They then used special techniques to confirm the structure and the presence of an asymmetry. This new method for creating Janus monolayers paves the way for further exploration of these unique materials and their potential applications in spintronics and other fields.

In 2017 Zhuangchai Lai et al. [46] successfully also created and analyzed a new material called Janus S MoSe monolayer. This material has a unique structure where a molybdenum atom is sandwiched between layers of sulfur and selenium atoms. They achieved this by carefully converting a single layer of molybdenum diselenide (MoSe_2) into Janus S MoSe through a process called controlled sulfurization. This involved replacing the top layer of selenium atoms with sulfur atoms, leaving the bottom selenium layer untouched. The researchers then used various techniques to examine the structure of Janus S MoSe monolayer. These techniques included Raman spectroscopy, photoluminescence, transmission electron microscopy, X-ray photoelectron spectroscopy, and time-of-flight secondary ion mass spectrometry. Additionally, they employed density functional theory (DFT) calculations to gain a deeper understanding of the material's vibrational modes and electronic structure. The results from the DFT calculations closely matched the experimental observations. Finally, the study revealed that Janus S MoSe monolayer exhibits high activity for the hydrogen evolution reaction (HER) on its basal plane.

DFT calculations suggest that this activity is due to a combined effect of inherent defects within the Janus structure and the strain caused by its unique configuration.

In 2018, San-Dong Guo reported understanding heat transport within MoSSe monolayers. Researchers used advanced computational methods to analyze the movement of vibrations (phonons) and how efficiently they carry heat (lattice thermal conductivity, κ_L) [47]. The results show that MoSSe monolayers have a significantly lower κ_L compared to MoS₂ monolayers but higher than MoSe₂ monolayers. This translates to a moderate thermal sheet conductance for MoSSe, around 342.50 W K⁻¹ at room temperature. He delved deeper by examining the speed (group velocity) and lifespan (lifetime) of these vibrations. Compared to MoS₂, MoSSe's lower κ_L can be attributed to slower-moving vibrations with shorter lifespans. Conversely, MoSSe's higher κ_L compared to MoSe₂ is primarily due to faster-moving vibrations within the material. The study also explored the elastic properties (resistance to deformation) of these materials, finding a correlation between the Young's modulus (a measure of elasticity) and κ_L . Additionally, they considered how substituting certain atoms with isotopes (atoms with the same number of protons but different numbers of neutrons) slightly reduces κ_L (by about 5.8%). Finally, the research investigated how the size of the MoSSe monolayer affects its heat transport properties. They discovered that when the size shrinks to around 110 nanometers, the κ_L is reduced by half. These findings offer valuable insights for managing heat flow in MoSSe monolayers, which could be beneficial for applications in thermoelectric devices (converting heat to electricity), thermal circuits (managing heat in electronic devices), and nanoelectronics (miniaturized electronic devices). The study highlights the potential of Janus TMDs and may encourage further research on their thermal transport properties, both through theoretical and experimental approaches.

In 2018, Whenhu Shi et al. employed computational techniques such as density functional theory (DFT) to explore the mechanical and electronic characteristics of a novel category of 2D materials termed Janus monolayer transition metal dichalcogenides (MXY) [48]. These materials feature distinct elements (X and Y) positioned on opposite sides, with M representing various metals. Their research revealed that manipulating this structural asymmetry, particularly by disrupting the out-of-plane symmetry, can lead to significant modifications in the electronic and mechanical properties of these monolayers. Of particular note, for tungsten-based (WXY) and molybdenum-based (MoXY) monolayers, the band gap could be finely adjusted within specific ranges (0.16-1.91 eV and 0.94-1.69 eV, respectively). Intriguingly, certain materials (M = Ti, Zr, Hf) underwent a transition from semiconductor to metal behavior

upon adopting the Janus structure. Additionally, the intrinsic characteristics of the metal atom (M) were found to exert a crucial influence, with vanadium, niobium, tantalum, and chromium-based monolayers (MXY) displaying metallic traits regardless of structural symmetry. Regarding mechanical properties, a range of behaviors was observed based on composition. Molybdenum, titanium, zirconium, hafnium, and tungsten-based monolayers (MXY) were characterized as brittle, while chromium and vanadium-based monolayers (CrXY and VXY) exhibited ductility, allowing deformation under stress. Stiffness values varied between 22 and 158 N/m across these materials. Overall, this study underscores the potential of Janus monolayer transition metal dichalcogenides due to their adaptable electronic and mechanical attributes. These versatile properties hold promise for advancements in various fields, including ultra-sensitive detectors, nanogenerators, low-power electronics, and electromechanical systems for energy harvesting and signal conversion.

In 2018 Yan-Ni Wen et al. [49] explored how missing atoms (vacancies) in Janus MoSSe monolayers, a new type of two-dimensional material, can be used to control their properties. These vacancies can be single points or lines of missing atoms. Using a powerful computational method called density functional theory, researchers studied how vacancies form in these monolayers. Interestingly, they found that vacancies are more likely to occur in the selenium (Se) layer compared to the sulfur (S) layer. For point defects (multiple missing atoms close together), the study revealed that arrangements resembling zigzag lines have the lowest energy state, making them the most favourable configuration. In the case of linear defects (continuous lines of missing atoms), the research suggests that these lines tend to stay far apart from each other for reasons of stability. The study also explored how vacancies affect the bandgap, a crucial property for electronic and optical devices. The bandgap of a perfect Janus MoSSe monolayer was measured to be 1.080 electron volts (eV). When point vacancies were introduced, the bandgap decreased significantly, reaching 0.675 eV with a higher number of vacancies. For linear vacancies, the bandgap exhibited a different behavior. It initially decreased but then started oscillating around 0.530 eV as the distance between the vacancy lines increased. These findings offer valuable insights for manipulating the bandgap of Janus MoSSe monolayers through vacancy engineering. This control over the bandgap paves the way for developing advanced optical and electronic devices based on MoS₂ materials.

In 2019 Wenzhe Zhou recently created new Janus transition metal dichalcogenides (MXY, where M is molybdenum or tungsten, X and Y are different chalcogen atoms like sulfur,

selenium, or tellurium) [50]. These materials have unique properties due to a broken mirror symmetry in their atomic structure. This asymmetry leads to an intrinsic Rashba spin splitting (a way to split electron energy levels) and an out-of-plane dipole moment (separation of positive and negative electrical charges). The study used a computational technique (first-principles calculations) to investigate the stability and electronic properties of these materials in single, double, and multiple layers (mono-, bi-, and multilayer MXY) using tungsten selenide (WSSe) as an example. The research revealed that sulfur atoms contribute more to the energy state at a specific point (Gamma point) in the material compared to selenium atoms. Interestingly, interactions between layers significantly affect this contribution. While a specific stacking pattern (AA') remains the most stable configuration, the order of chalcogen atoms within each layer can vary. The study identified two preferred arrangements for neighboring layers: S-Se-Se-S and Se-S-Se-S. The scientists discovered that the Se-S-Se-S stacked WSSe bilayer exhibits a significant separation between layers due to the built-in electric field. This separation holds promise for applications in solar cells. Additionally, the study found that the Rashba splitting (a measure of spin-orbit interaction) depends on the layer arrangement and can be tuned by adjusting the distance between layers. This tunability originates from controlling the electrostatic interactions between the layers. However, symmetrically stacked WSSe bilayers don't exhibit layer separation, and the Rashba splitting has opposite effects on the two layers when the interlayer distance is large enough. Overall, the study demonstrates that by controlling the order of chalcogen atoms within layers, scientists can manipulate the electronic structure and spin splitting of these Janus materials. This control allows researchers to tailor mono-, bi-, and multilayer MXY for specific applications.

Vuong Van Thanh et al. conducted simulations to explore the properties of a new class of materials called Janus monolayers in 2020 [51]. These monolayers are a specific type of transition metal dichalcogenide (TMD) where the two chalcogen atoms (like sulfur or selenium) on either side of the metal atom are different elements. The simulations showed that among these Janus TMDs, WSSe (tungsten with selenium on one side and sulfur on the other) is particularly strong and stiff due to the strong ionic bonds between its atoms. In terms of electrical properties, some Janus TMDs were found to be direct-gap semiconductors, meaning they conduct electricity more easily, while others were indirect-gap semiconductors. Applying stretching forces (tensile strain) to the Janus TMDs affected both their electrical and light absorption properties. The simulations predict that this strain narrows the band gap (energy difference between conducting and insulating states) due to interactions between the atoms.

This strain can also significantly increase the material's light absorption at certain energy levels. Overall, the study suggests that Janus TMDs have unique properties that make them promising for applications in tiny mechanical devices, optoelectronic devices that involve both light and electricity, and even photocatalysts, which are materials that use light to drive chemical reactions.

In 2020 Dipesh B. Trivedi et al. reports a method to create various Janus crystals at room temperature. This method uses special molecules that can gently remove the top layer of atoms on a single layer of material and replace it with a different type of atom [52]. This allows scientists to transform regular transition metal dichalcogenides (TMDs) into Janus crystals. The resulting Janus crystals have properties that combine the characteristics of their top and bottom layers. Importantly, the room-temperature technique allows researchers to create the first Janus crystal heterojunctions, where two different Janus crystals are connected vertically or laterally. This research is a significant advancement in the field of 2D materials. It opens the door for creating a wider range of Janus crystals and complex structures made from them, paving the way for future applications in areas like electronics and optoelectronics.

In 2020 M. Yagmurcukardes et al. used computer simulations based on density functional theory to design a new material: a single layer of Janus MoSO. This material has a unique structure with sulfur, molybdenum, and oxygen atoms arranged in a specific way (S-Mo-O) [53]. The simulations predict that Janus MoSO is a stable semiconductor with a band gap (energy difference between conducting and insulating states). This material also has a strong electric polarization because of the uneven distribution of charge across its two surfaces. Interestingly, Janus MoSO is different from similar materials (MoS_2 and MoO_2) because it has four unique vibrational modes and a strong piezoelectric effect (ability to generate electricity when squeezed). They also investigated how stretching or compressing the material affects its properties. They found that stretching Janus MoSO can even cause an electronic transition, while both stretching and compressing it shift the energy levels involved in conduction. Despite these changes, the simulations show that Janus MoSO is quite stable even under moderate strain. This stability makes it a promising candidate for applications in nanotechnology that involve tiny, flexible devices. Based on the predicted stability and strong piezoelectric effect, the researchers believe this material could be fabricated in a practical way.

Abhishek Patel et. al. investigated the potential of Janus monolayers, specifically WSSe and WSTe, for thermoelectric applications using a combination of advanced computational

methods in 2020 [54]. These materials possess a unique structure with different elements on opposing sides (Janus). The study revealed that both Janus WSSe and WSTe monolayers exhibit a direct band gap, with values of 1.72 eV and 1.84 eV respectively. Additionally, they demonstrate exceptional electrical conductivity and a remarkably high Seebeck coefficient (a measure of voltage generated due to temperature differences). This combination translates to a significantly large power factor, a crucial parameter for thermoelectric devices. Another key finding is the relatively low lattice thermal conductivity in these Janus monolayers compared to traditional WS₂ monolayers. This low thermal conductivity contributes to a high thermoelectric figure of merit (ZT), a measure of thermoelectric efficiency. Notably, the ZT value for Janus WSTe reaches an impressive 2.56 at higher temperatures. Based on these results, the study proposes Janus WSTe monolayers as promising candidates for thermoelectric materials due to their exceptional thermoelectric performance. The research suggests that Janus monolayers hold significant potential for advancing thermoelectric conversion technology.

In 2021, Xi Wan et al. successfully synthesized a Janus monolayer of MoSH through plasma treatment [55]. The electronic properties of this material were thoroughly investigated to assess its intrinsic characteristics and carrier concentration. The metallic nature of MoSH was found to be advantageous for facilitating plasmonic behavior, particularly in the mid-infrared range.

In 2021 M. Jahangirzadeh Varjovi et. al. explored a new class of two-dimensional materials called Janus WXO monolayers, where W represents tungsten, X can be sulfur (S), selenium (Se), or tellurium (Te), and the material has a unique asymmetrical structure [56]. The study used computer simulations to predict the properties of three potential atomic arrangements (1H, 1T, and 1T') for these monolayers. The simulations showed that the 1H arrangement is stable, while the 1T form is unstable and transforms into a slightly distorted version (1T'). Further simulations confirmed that both the 1H and the stable 1T' structures are robust even at high temperatures. Interestingly, these Janus monolayers have unique fingerprint vibrations (Raman modes) compared to similar materials with symmetrical structures. The mechanical properties of the 1H monolayers were found to be the same in all directions, but the 1T' monolayers showed variations depending on the direction of force applied. In terms of electrical properties, the 1H monolayers were predicted to be semiconductors with an indirect band gap that gets smaller as the element X changes from sulfur to tellurium. The 1T' monolayers (except for WSO) also have narrow band gaps due to a specific distortion within their structure. Including the effects of spin-orbit coupling in the simulations slightly modified the band gaps. Overall,

the study suggests that Janus WXO monolayers have a combination of interesting mechanical and electronic properties, along with a strong piezoelectric response. These characteristics make them promising candidates for future applications in nanoelectronics.

In 2021, Surinder Pal Kaur et. al. Janus transition metal dichalcogenide materials have unique properties due to their inherent strain and electric field, making them promising for various nanodevice applications [58]. However, their usefulness in gas sensing devices is limited because pristine (undoped) Janus monolayers don't interact strongly with gas molecules. They explored a solution: introducing foreign atoms (N, P, and As) into the lattice structure of Janus WSSe monolayers. This process, called doping, modifies the material's electronic and structural properties. Scientists used a computational method called spin-polarized density functional theory to study how doping affects gas sensing performance for CO, NO, and HF gases. Their analysis showed that incorporating a small amount (3.12%) of N, P, or As atoms at specific sites (replacing sulfur or selenium) releases energy, making it a favourable process. Doping also introduced new energy states near the Fermi level (the energy at which adding an electron neither adds nor removes energy). Simulations revealed that doping significantly improves gas sensing by strengthening the interaction between the gas molecules and the doped Janus WSSe monolayers. They further investigated this interaction by analysing the density of states, which provides information about the available energy levels for electrons. The study also found that applying a slight uni-axial tensile strain (stretching the material in one direction) can further enhance the adsorption of CO gas molecules on nitrogen-doped WSSe. In conclusion, this research demonstrates that doping Janus WSSe monolayers with just 3.12% of N, P, or As atoms significantly improves their gas sensing ability for CO, NO, and HF gases, even without applying external strain. This paves the way for developing more efficient gas sensing devices using Janus materials.

References:

- [1] Novoselov, Kostya S., et al. "Electric field effect in atomically thin carbon films." *science* 306.5696 (2004): 666-669.
- [2] Qiu, Hu, et al. "Graphynes for water desalination and gas separation." *Advanced Materials* 31.42 (2019): 1803772.
- [3] Choi, Wonbong, et al. "Recent development of two-dimensional transition metal dichalcogenides and their applications." *Materials Today* 20.3 (2017): 116-130.
- [4] Gogotsi, Yury, and Babak Anasori. "The rise of MXenes." *ACS nano* 13.8 (2019): 8491-8494.
- [5] Qian, Xiaofeng, et al. "Quantum spin Hall effect in two-dimensional transition metal dichalcogenides." *Science* 346.6215 (2014): 1344-1347.
- [6] Chen, Ye, et al. "Phase engineering of nanomaterials." *Nature Reviews Chemistry* 4.5 (2020): 243-256.
- [7] Liang, Zhangqian, et al. "Rationalizing and controlling the phase transformation of semi-metallic 1T'-phase and semi-conductive 2H-phase MoS₂ as cocatalysts for photocatalytic hydrogen evolution." *Chemical Engineering Journal* 396 (2020): 125344.
- [8] Shi, Shangli, Zhuxing Sun, and Yun Hang Hu. "Synthesis, stabilization and applications of 2-dimensional 1T metallic MoS₂." *Journal of Materials Chemistry A* 6.47 (2018): 23932-23977.
- [9] Yang, Ruijie, et al. "2D transition metal dichalcogenides for photocatalysis." *Angewandte Chemie* 135.13 (2023): e202218016.
- [10] Zhang, Jing, et al. "Janus monolayer transition-metal dichalcogenides." *ACS nano* 11.8 (2017): 8192-8198.
- [11] Chen, Shaobo, et al. "Large tunable Rashba spin splitting and piezoelectric response in Janus chromium dichalcogenide monolayers." *Physical Review B* 106.11 (2022): 115307.
- [12] Yu, Xiantong, et al. "2D van der Waals heterojunction nanophotonic devices: from fabrication to performance." *Advanced Functional Materials* 31.42 (2021): 2104260.

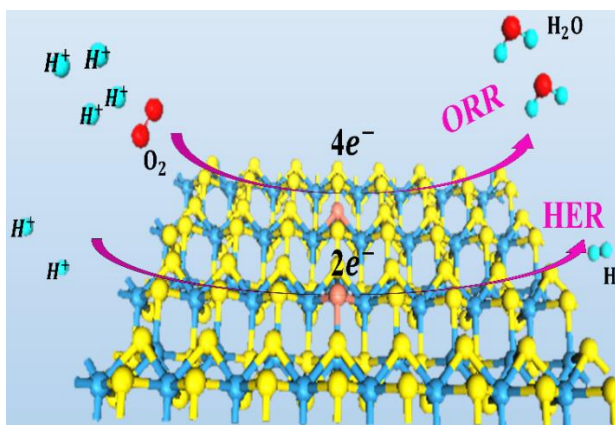
- [13] Chen, Wenzhou, et al. "Two-dimensional Janus transition metal oxides and chalcogenides: multifunctional properties for photocatalysts, electronics, and energy conversion." *ACS applied materials & interfaces* 10.41 (2018): 35289-35295.
- [14] Zhu, Qiaohong, et al. "Recent progress of metal sulfide photocatalysts for solar energy conversion." *Advanced Materials* 34.45 (2022): 2202929.
- [15] Nguyen, Duy Khanh, J. Guerrero-Sanchez, and D. M. Hoat. "HfXO (X= S and Se) Janus monolayers as promising two-dimensional platforms for optoelectronic and spintronic applications." *Journal of Materials Research* 38.9 (2023): 2600-2612.
- [16] Ji, Yujin, et al. "Janus structures of transition metal dichalcogenides as the heterojunction photocatalysts for water splitting." *The Journal of Physical Chemistry C* 122.5 (2018): 3123-3129.
- [17] Dickinson, Roscoe G., and Linus Pauling. "The crystal structure of molybdenite." *Journal of the American Chemical Society* 45.6 (1923): 1466-1471.
- [18] Frindt, R. F., and A. D. Yoffe. "Physical properties of layer structures: optical properties and photoconductivity of thin crystals of molybdenum disulphide." *Proceedings of the Royal Society of London. Series A. Mathematical and Physical Sciences* 273.1352 (1963): 69-83.
- [19] Joensen, Per, R. F. Frindt, and S. Roy Morrison. "Single-layer mos₂." *Materials research bulletin* 21.4 (1986): 457-461.
- [20] Chhowalla, Manish, et al. "The chemistry of two-dimensional layered transition metal dichalcogenide nanosheets." *Nature chemistry* 5.4 (2013): 263-275.
- [21] Lu, Qipeng, et al. "2D transition-metal-dichalcogenide-nanosheet-based composites for photocatalytic and electrocatalytic hydrogen evolution reactions." *Advanced Materials* 28.10 (2016): 1917-1933.
- [22] Benck, Jesse D., et al. "Catalyzing the hydrogen evolution reaction (HER) with molybdenum sulfide nanomaterials." *Acs Catalysis* 4.11 (2014): 3957-3971.
- [23] Wang, Haotian, et al. "Transition-metal doped edge sites in vertically aligned MoS₂ catalysts for enhanced hydrogen evolution." *Nano Research* 8 (2015): 566-575.

- [24] Deng, Jiao, et al. "Triggering the electrocatalytic hydrogen evolution activity of the inert two-dimensional MoS₂ surface via single-atom metal doping." *Energy & environmental science* 8.5 (2015): 1594-1601.
- [25] Xiao, B. B., et al. "Functional MoS₂ by the Co/Ni doping as the catalyst for oxygen reduction reaction." *Applied Surface Science* 354 (2015): 221-228.
- [26] Du, Cuicui, et al. "Enhanced electrocatalytic hydrogen evolution performance of MoS₂ ultrathin nanosheets via Sn doping." *Applied Catalysis A: General* 538 (2017): 1-8.
- [27] Wu, Liqian, et al. "Mn doped MoS₂/reduced graphene oxide hybrid for enhanced hydrogen evolution." *Applied Surface Science* 425 (2017): 470-477.
- [28] Wang, Zhongxu, et al. "Computational screening for high-activity MoS₂ monolayer-based catalysts for the oxygen reduction reaction via substitutional doping with transition metal." *Journal of materials chemistry A* 5.20 (2017): 9842-9851.
- [29] Park, Sangwook, et al. "Enhancing catalytic activity of MoS₂ basal plane S-vacancy by Co cluster addition." *ACS Energy Letters* 3.11 (2018): 2685-2693.
- [30] Zhang, Xiaoming, et al. "The catalytic activity and mechanism of oxygen reduction reaction on P-doped MoS₂." *Physical Chemistry Chemical Physics* 20.27 (2018): 18184-18191.
- [31] Attanayake, Nuwan H., et al. "Effect of intercalated metals on the electrocatalytic activity of 1T-MoS₂ for the hydrogen evolution reaction." *ACS Energy Letters* 3.1 (2017): 7-13.
- [32] Shi, Yi, et al. "Energy level engineering of MoS₂ by transition-metal doping for accelerating hydrogen evolution reaction." *Journal of the American Chemical Society* 139.43 (2017): 15479-15485.
- [33] Amiin, Ibrahim Saana, et al. "Multifunctional Mo–N/C@ MoS₂ electrocatalysts for HER, OER, ORR, and Zn–air batteries." *Advanced Functional Materials* 27.44 (2017): 1702300.
- [34] Guo, Haoran, et al. "Theoretical investigation on the single transition-metal atom-decorated defective MoS₂ for electrocatalytic ammonia synthesis." *ACS applied materials & interfaces* 11.40 (2019): 36506-36514.

- [35] Tian, Shufang, and Qing Tang. "Activating transition metal dichalcogenide monolayers as efficient electrocatalysts for the oxygen reduction reaction via single atom doping." *Journal of Materials Chemistry C* 9.18 (2021): 6040-6050.
- [36] Wu, Zhuangzhi, et al. "WS₂ nanosheets as a highly efficient electrocatalyst for hydrogen evolution reaction." *Applied Catalysis B: Environmental* 125 (2012): 59-66.
- [37] Voiry, Damien, et al. "Enhanced catalytic activity in strained chemically exfoliated WS₂ nanosheets for hydrogen evolution." *Nature materials* 12.9 (2013): 850-855.
- [38] Putungan, Darwin Barayang, Shi-Hsin Lin, and Jer-Lai Kuo. "A first-principles examination of conducting monolayer 1T'-MX₂ (M= Mo, W; X= S, Se, Te): promising catalysts for hydrogen evolution reaction and its enhancement by strain." *Physical Chemistry Chemical Physics* 17.33 (2015): 21702-21708.
- [39] Xiao, Ping, et al. "Fullerene-like WS₂ supported Pd catalyst for hydrogen evolution reaction." *Journal of Catalysis* 380 (2019): 215-223.
- [40] Jin, Jialei, et al. "CoP nanoparticles combined with WS₂ nanosheets as efficient electrocatalytic hydrogen evolution reaction catalyst." *International Journal of Hydrogen Energy* 42.7 (2017): 3947-3954.
- [41] Luo, Min, Shen Yu Hao, and Yin Tai Ling. "Ab initio study of electronic and magnetic properties in Ni-doped WS₂ monolayer." *AIP Advances* 6.8 (2016).
- [42] Pan, Yaping, et al. "Enhanced electrochemical hydrogen evolution performance of WS₂ nanosheets by Te doping." *Journal of catalysis* 382 (2020): 204-211.
- [43] Pu, Xiaofeng, et al. "Adjusting the electronic structure of WS₂ nanosheets by iron doping to promote hydrogen evolution reaction." *FlatChem* 29 (2021): 100278.
- [44] Lai, Zhuangchai, et al. "Metastable 1T'-phase group VIB transition metal dichalcogenide crystals." *Nature Materials* 20.8 (2021): 1113-1120.
- [45] Lu, Ang-Yu, et al. "Janus monolayers of transition metal dichalcogenides." *Nature nanotechnology* 12.8 (2017): 744-749.
- [46] Zhang, Jing, et al. "Janus monolayer transition-metal dichalcogenides." *ACS nano* 11.8 (2017): 8192-8198.

- [47] Guo, San-Dong. "Phonon transport in Janus monolayer MoSSe: a first-principles study." *Physical Chemistry Chemical Physics* 20.10 (2018): 7236-7242.
- [48] Shi, Wenwu, and Zhiguo Wang. "Mechanical and electronic properties of Janus monolayer transition metal dichalcogenides." *Journal of Physics: Condensed Matter* 30.21 (2018): 215301.
- [49] Wen, Yan-Ni, Ming-Gang Xia, and Sheng-Li Zhang. "Bandgap engineering of Janus MoSSe monolayer implemented by Se vacancy." *Computational Materials Science* 152 (2018): 20-27.
- [50] Zhou, Wenzhe, et al. "Geometry and electronic structure of monolayer, bilayer, and multilayer Janus WSSe." *Physical Review B* 99.7 (2019): 075160.
- [51] Van Thanh, Vuong, et al. "First-principles study of mechanical, electronic and optical properties of Janus structure in transition metal dichalcogenides." *Applied Surface Science* 526 (2020): 146730.
- [52] Trivedi, Dipesh B., et al. "Room-temperature synthesis of 2D Janus crystals and their heterostructures." *Advanced materials* 32.50 (2020): 2006320.
- [53] Yagmurcukardes, M., and F. M. Peeters. "Stable single layer of Janus MoSO: Strong out-of-plane piezoelectricity." *Physical Review B* 101.15 (2020): 155205.
- [54] Patel, Abhishek, et al. "High thermoelectric performance in two-dimensional Janus monolayer material WS-X (X= Se and Te)." *ACS applied materials & interfaces* 12.41 (2020): 46212-46219.
- [55] Wan, Xi, et al. "Synthesis and characterization of metallic Janus MoSH monolayer." *ACS nano* 15.12 (2021): 20319-20331.
- [56] Varjovi, M. Jahangirzadeh, et al. "Janus two-dimensional transition metal dichalcogenide oxides: first-principles investigation of W X O monolayers with X= S, Se, and Te." *Physical Review B* 103.19 (2021): 195438.
- [57] Pal Kaur, Surinder, Tanveer Hussain, and T. J. Dhilip Kumar. "Substituted 2D Janus WSSe monolayers as efficient nanosensor toward toxic gases." *Journal of Applied Physics* 130.1 (2021).

4. Coinage metals doped 1T' WS₂ as efficient bifunctional electrocatalyst towards ORR and HER: a first principles study



4.1. Introduction:

Stock fossil fuels have been the main source of energy since the dawn of the industrial revolution. The ever-increasing demand of fuels is threatening towards the depletion of stock fossil reserves. On the other hand, worldwide increase in environmental pollution with increasing consumption of fossil fuels has become a major concern that draws the global attention to find alternative pollution free and economic energy resources. Fuel cells [1,2] are one of the environmentally friendly alternative energy resources in this regard, as they produce electrical energy by simple chemical combination of hydrogen and oxygen leaving only water as product. Fuel cells also possess highly anticipated traits like high theoretical efficiencies [3] and high-energy densities [4] that make them a promising candidate for application in the field of green energy production. However, a major drawback towards the full-scale commercialization of fuel cells is the absence of an optimum cathode electrocatalyst to carry out the necessary oxygen reduction reaction (ORR). To date, platinum (Pt) has been the most celebrated cathode material for fuel cells [5-8]. However, its high cost, sluggish ORR kinetics and proclivity towards CO poisoning have barred the use of Pt for large-scale production of fuel cells [9-10]. Therefore, search for efficient cathode electrocatalysts for fuel cells has become one of the major focal points of cutting-edge research.

Since the discovery of graphene [11], the world of stable two-dimensional materials has expanded to a vast domain. This induced an increasing interest to apply those two-dimensional layered materials as cathode electrocatalysts for ORR due to their exotic surface characteristics [12-15] and high surface to volume ratio [16]. B/ N doped graphene [17], g-C₃N₄ [18], graphynes [19,20], pure/ doped transition metal di-chalcogenides (TMDs) [21-23] etc. have

shown promising activity towards ORR. Among them, two-dimensional materials based on non-precious and abundant transition metals especially attracted attention of researchers worldwide as an alternative electrocatalysts for fuel cell owing to their vast domain of different stable phases [24], high surface area [25], resistivity towards CO poisoning [26] and high efficiency towards electrocatalysis [27]. However, TMDs in their pristine state hold uniform distribution of surface charge that mostly render them inactive towards O_2 adsorption [28-30]. Hence, most of the prior reports in their pristine state involve improving the adsorption efficiency by introducing defects through doping or adsorption to produce a non-uniform surface charge distribution. In one of the recent works, Chen et al. [29] reported that with the addition of dopants in the pristine MoS_2 , its catalytic activity is enhanced in the ORR application. Wang et al. [31] showed substitutional doping with transition metals at the Sulphur sites of MoS_2 improves its catalytic performance for ORR. In another work, Zhang et al. [32] reported the enhancement of ORR activity by the N and P doping at Sulphur sites of MoS_2 . Prominently, most of these works span around the 2H phase of the TMDs. TMDs can also frequently form other two-dimensional phases like 1T, 1T' etc. The stability of the most celebrated 1T, 1T' phase of TMDs like MoS_2 , WS_2 , $MoSe_2$, WSe_2 etc. are already confirmed through rigorous theoretical or experimental validation [33, 34, 35, 36]. Once formed, TMDs in 1T' phase are able to maintain their structural integrity and possess a high transition energy barrier (1eV per formula unit) towards their transformation into the 2H phase [37]. Hence, it is highly unlikely for a TMD in 1T' phase to transform into 2H phase easily. However, to the authors' knowledge only a few studies have been carried out till date to shed light on the electrocatalytic activities of the TMDs towards Oxygen reduction reaction and hydrogen evolution reaction (ORR and HER) in those phases. Tian et al. [38] showed that transition metal doped 1T' MoS_2 exhibit ORR activity and interesting electrochemical performance with comparatively low overpotential value. It is evidenced by some reports that TMDs could also act as a bi-functional electrocatalytic material [39, 40]. Zengming Qin et al. [41] showed that the 1T MoS_2 supported Pd cluster acts as a highly efficient bi-functional catalyst for ORR and OER. Nevertheless, to the best of the authors' knowledge, the electrocatalytic activities of one of the most stable 1T' phase of TMDs, that is 1T' WS_2 , has remained unexplored and with the current work the authors' aim is to fill up that void.

1T' WS_2 also has an intrinsic uniform surface charge distribution like its 2H counterpart. Hence, it is necessary to incorporate extrinsic defects within the system to enhance its O_2 adsorption capability. As discussed in the previous paragraph, substitution of the S atom

through metals like Cu, Au and Ag has been proven to be highly beneficial to improve the electrocatalytic activities of 2H MoS₂ [31]. In the current work, the authors have applied similar doping criteria to improve the electrocatalytic activities of 1T' WS₂ towards ORR and doped it substitutionally with Cu, Ag and Au respectively at the S atom site to study ORR mechanism in terms of thorough free energy analysis. The Cu, Ag, Au substituted 1T' WS₂ systems are thoroughly relaxed to obtain the ground state geometry of the doped systems. Electronic properties of these doped structures are critically investigated. Subsequently, initial step of ORR, i.e. oxygen molecule (O₂) adsorption, is studied for each non-equivalent adsorption site linked with dopant for each system and the most favorable O₂ adsorbed configurations isolated in terms of adsorption energy are considered to analyze the subsequent ORR steps. The most feasible reaction routes on each of the doped systems are pointed out in terms of their respective free energy profile and the study of the effect of electrode potential variation on the free energy profiles is further carried out to identify the rate limiting steps and overpotential values. The activity of Cu, Ag and Au doped 1T' WS₂ towards HER are further studied in terms of Gibbs free energy and the active sites for the reaction on each electrocatalyst's surface are identified using first principles methodologies.

4.2. Theoretical Methods:

Vienna Ab initio simulation packages (VASP) [42-45] with Projector-augmented-wave (PAW) [46] approach was used to perform the first principles calculations. Exchange and Correlation contributions were taken into account via the Perdew-Burke-Ernzerhof (PBE) functional [47] within the GGA approximation. Energy cut off for plane wave basis was taken as 500 eV for all the calculations. 3×3×1 k-points grid was implemented during the geometry optimizations of the sufficiently large doped systems. Total energies of the structures were converged up to 1×10^{-6} eV per atom. A (4×2) supercell of 1T' WS₂ was deployed to study metal doping, O₂ adsorption and subsequent ORR/ HER kinematics. A vacuum slab of length of 22 Å was employed along the perpendicular direction of all the layers to cancel the false interaction between the periodic images along the normal direction to the two-dimensional layers. Bader charge analysis [48] is performed to estimate charge transfer values among the elements of the doped systems. PBE+D2 forcefield (Grimme's) [49] method was used during the adsorption studies to include van der Waal's interaction. Formation energies of different doped structures were calculated to compare their stabilities using following equation:

$$E_{\text{for}} = E_{\text{doped}} - E_{\text{pris}} + n_{\text{S}}\mu_{\text{S}} - n_{\text{d}}\mu_{\text{d}} \quad (4.1)$$

where E_{for} is the formation energy of the doped structure, E_{doped} is the computed total ground state energy of the doped system, E_{pris} is the computed total ground state energy of the pristine system, n_s is the number of sulfur atoms replaced through doping, μ_s is the chemical potential of sulfur atom (calculated with respect to orthorhombic S_{32} system as reference), n_d is the number of dopant atom, and μ_d chemical potential of dopant atom (calculated with respect to metallic FCC phases of Cu, Ag and Au). Lower value of formation energy calculated from the equation (4.1) represents better stability to the system under consideration.

Gibbs free energy of each step of ORR/ HER reactions was studied using following equation:

$$\Delta G = \Delta E + \Delta ZPE - T\Delta S + \Delta G_U \quad (4.2)$$

where ΔE is the change in enthalpy, ΔZPE is the correction due to zero-point energy and ΔS is the change in entropy. $\Delta G_U = -eU$ (e = electronic charge and U = electrode potential with respect to standard hydrogen electrode (SHE))

All the computations are performed in an acidic medium ($\text{pH} = 0$) at $T=0\text{K}$ (standard DFT protocol) to study ORR on different structures. Here ΔE values are obtained from DFT calculations and the values of $T\Delta S$ for the gas phase molecules are adopted from standard table [50]. The free energy of the reaction ($\text{H}^+ + e$) is calculated using the free energy value of $\frac{1}{2} \text{H}_2$ as suggested by Srinivasu et al. [51] under standard conditions $U = 0$ and $\text{pH} = 0$.

Oxygen molecule adsorption capacity of different doped structures of 1T' WS_2 was calculated using the following equation:

$$E_{\text{ads}}^{\text{do}} = E_{\text{tot}}^{\text{do}} - E_P - E^{\text{do}} \quad (4.3)$$

where, $E_{\text{ads}}^{\text{do}}$ is the adsorption energy of oxygen molecule on a host, $E_{\text{tot}}^{\text{do}}$ is total energy of the oxygen molecule adsorbed host system, E_P is the energy of the host adsorbent and E^{do} is the computed energy of one oxygen molecule in the gas phase. Lower value of adsorption energy of dioxygen as obtained from the above equation indicates stronger adsorption of oxygen molecules. The overpotential value for each doped system was calculated by using the following equation

$$\eta_{\text{over}} = 1.23\text{V} - \eta_{\text{onset}} \quad (4.4)$$

where η_{over} and η_{onset} represent the overpotential value and onset potential of the particular doped system respectively. η_{onset} is defined as the value of the electrode potential up to which the reaction remains spontaneous in terms of free energy as the electrode potential is increased from 0 V. The interaction between the adsorbed hydrogen atom and the adsorbent atom during HER was further analyzed in terms of crystal orbital Hamilton population analysis using the LOBSTER code^[52, 53]. Dynamical stabilities of Cu, Ag and Au doped 1T' WS₂ structures were inspected using ab initio finite temperature molecular dynamics (MD) simulations at 400 K for 5000 steps with the time interval of 1fs using Nose'-Hoover Thermostat heat bath scheme as implemented in VASP.

4.3. Results and Discussions:

4.3.1. Doping in 1T' WS₂:

In this work, the implications of substitutional Cu, Ag and Au doping on the electrocatalytic activities of 1T' WS₂ towards oxygen reduction reaction (ORR) in acidic medium are thoroughly investigated by the means of density functional theory-based calculations. In the first place, a complete geometry relaxation of the pristine 1T' WS₂ system was carried out. The lattice parameters of pristine 1T' WS₂ unit cells were calculated to be 3.19 Å and 5.72 Å. Subsequent doping was performed by considering a (4×2) supercell of 1T' WS₂ unit cell and substituting the S atom by Cu, Ag and Au respectively. Two non-equivalent S atoms sites are present in 1T' WS₂. S atoms are distributed in wider and narrower strips subject to the distance between the S atoms in 1T' WS₂ resulting in two non-equivalent S atoms (Figure 4.1) sites for coinage metal doping. Both of those S atom sites were considered for substitutional doping via Cu, Ag and Au at a fixed dopant concentration of 3.12 %.

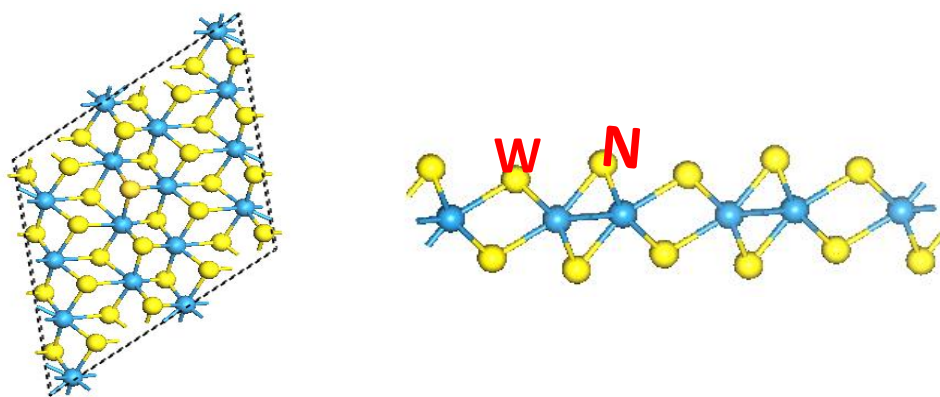


Figure 4.1: (a) Top view & (b) side view with wider (W) and narrower (N) sulphur position of 1T' WS₂

The formation energies for doping were calculated using equation (4.1). The formation energies for Cu, Ag and Au doping for S substitution in wider and narrower strips as shown in Figure 4.2(a) and Figure 4.2(b) are 1.20 eV, 0.96 eV, -0.53 eV, 1.31 eV, 1.10 eV and -0.28 eV respectively. The lower value of the formation energies as obtained for S substitution in wider strip for all three coinage metals, indicate that the metal atoms prefer to replace S atoms in a less dense region or in the wider strip. The negative value of the formation energy represents an exothermic process and vice versa. Although the formation energy values show that substitution of S via Au to be predominantly favorable, the small positive value of the formation energies for other two elements also denote that substitutional doping of 1T' WS₂ via those elements could be achieved very easily. It is crucial to note that, S plays the role of anion in the pristine WS₂ system. We replaced the S atom via metallic elements like Cu, Ag and Au that typically play the role of a cation. Thus, substitution of S via those elements could introduce instability in the WS₂ system if significant disturbance is incurred in the charge distribution upon substitution. In this regard, we carried out the Bader charge analysis of the doped systems to investigate the role played by the dopant elements. The amount of charge transferred to or from dopant and its nearby atoms are listed in Table 4.1. It is evident from Table 4.1 that each of the dopant elements acts as a recipient of electronic charge from the nearest W atoms, hence stabilizing the doped system. A total of 0.06e, 0.08e and 0.42e amount of charge was transferred to Cu, Ag and Au upon doping from the nearest W atoms (Figure 4.3). The maximum amount of charge acquired by the dopant Au amount clearly dictates the highest stability of the Au doped 1T' WS₂ system confirming the conclusions drawn from the formation energy values.

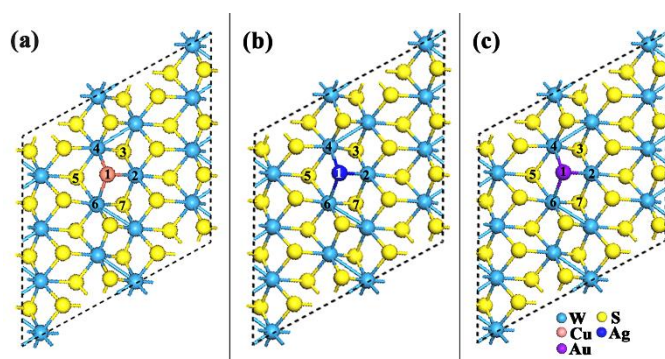


Figure 4.2(a): Optimized geometry of the (a)Cu doped 1T' WS₂ (b) Ag doped 1T' WS₂ and (c) Au doped 1T' WS₂ systems. Numbers over the dopant and its nearest atoms are utilized to discuss the charge transfer mechanism in the manuscript.

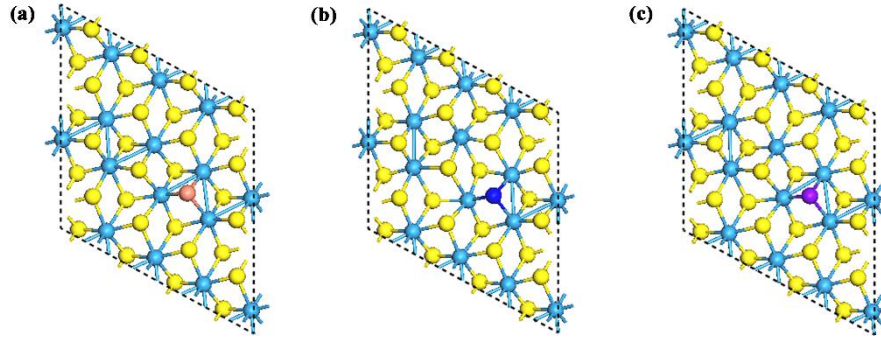


Figure 4.2(b): Narrower sulphur sites of (a) Cu doped 1T' WS₂ (b) Ag doped 1T' WS₂ (c) Au doped 1T' WS₂

Table 4.1: Amount of charge transfer to or from the dopant and its nearest atoms.

Dopant	Atom no as denoted in Figure 4.1	Charge Transfer (e)
Cu	1	-0.06
	2	1.99
	3	-1.06
	4	2.54
	5	-1.12
	6	2.59
	7	-1.05
Ag	1	-0.08
	2	2.59
	3	-1.12
	4	2.54
	5	-1.06
	6	2.34
	7	-1.05
Au	1	-0.42
	2	2.09
	3	-1.03
	4	1.96
	5	-1.02
	6	2.04
	7	-1.03

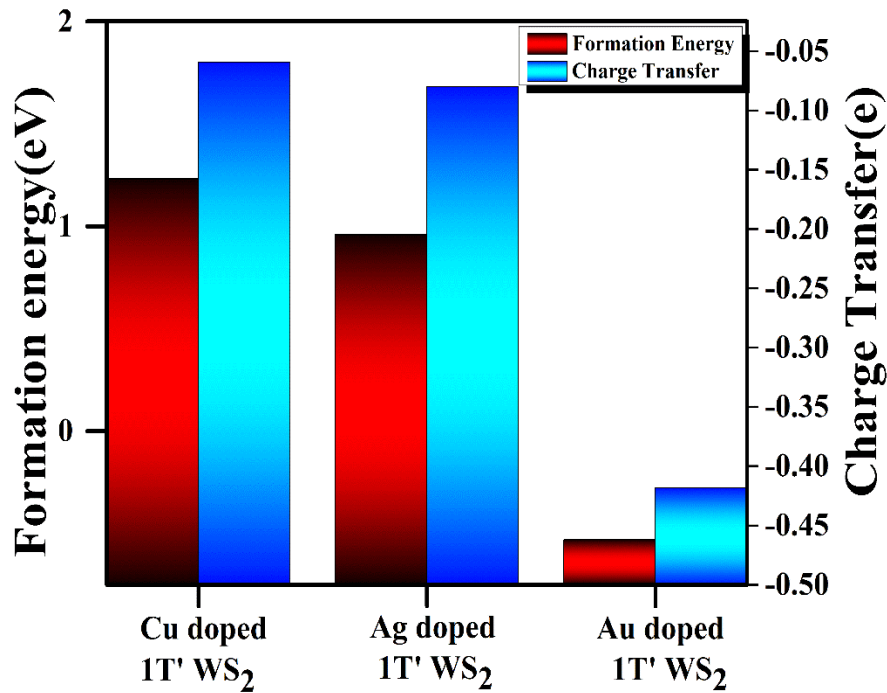


Figure 4.3: Formation energy and the amount of charge transfer to the dopant for Cu, Ag and Au doped 1T' WS₂.

The electronic properties of the three doped systems are analyzed in terms of the total density of states (TDOS) (Figure 4.4). Pristine 1T' WS₂, which is a low band gap semiconductor in its pristine form (Figure 4.6), turns into a metallic system upon doping via any of the considered metal elements. From the TDOS plot we have calculated spin polarization using the formula: $P(E_F) = (((D(E_F, \uparrow) - D(E_F, \downarrow)) / (D(E_F, \uparrow) + D(E_F, \downarrow))) \times 100$, where $D(E_F, \uparrow)$ and $D(E_F, \downarrow)$ represent the values of TDOS of up and down spin respectively at the Fermi level. All the doped systems were found to possess very small spin polarization at the Fermi level with Cu, Ag and Au doped 1T' WS₂ having $P(E_F)$ equal to 0.15%, 0.15% and 0.09% respectively. We also plotted the partial contribution of the most prominent orbitals for the region just above and below the Fermi level for each of the doped systems (Figure 4.4(d) – 4.4(f)). As prominent from the Partial density of states (PDOS) plots, the W atoms bonded to the dopant and the nearest S atoms contribute the most near and at the Fermi level corresponding to the metallic nature of the material and spin polarization the Fermi level. The contribution from the W_d orbitals was found to be maximum in the region near Fermi level. In addition, the hybridization between the W_d and S_p orbitals remained intact upon doping as prominent from Figure 4.4(d)

– (f). Contribution of s, p and d orbitals of the dopant near/ at the Fermi level are shown in the Figure 4.5 shows that for all the doped 1T' WS₂ systems, the dopant atom contributes to the spin polarization near/ at the Fermi energy, albeit by a smaller proportion, in a fashion similar to W and S atoms.

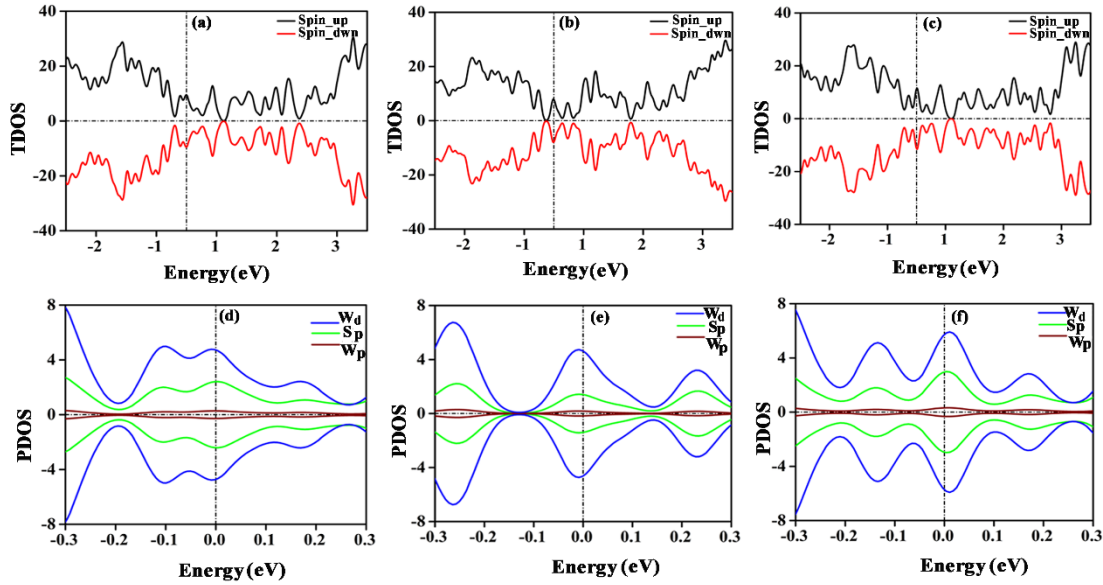


Figure 4.4: TDOS for (a) Cu doped (b) Ag doped (c) Au doped 1T' WS₂. PDOS for (d) Cu doped (e) Ag doped (f) Au doped 1T' WS₂.

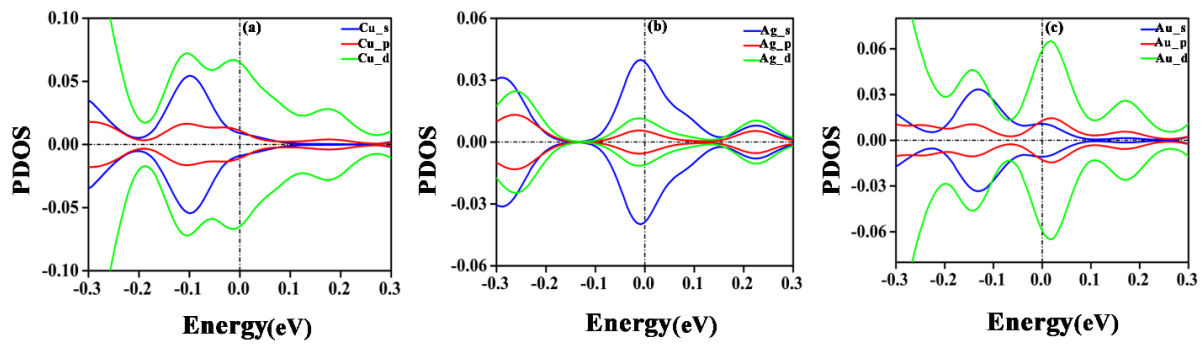


Figure 4.5: (a) PDOS of Cu site of Cu doped 1T' WS₂ (b) PDOS of Ag site of Ag doped 1T' WS₂ (c) PDOS of Au site of Au doped 1T' WS₂.

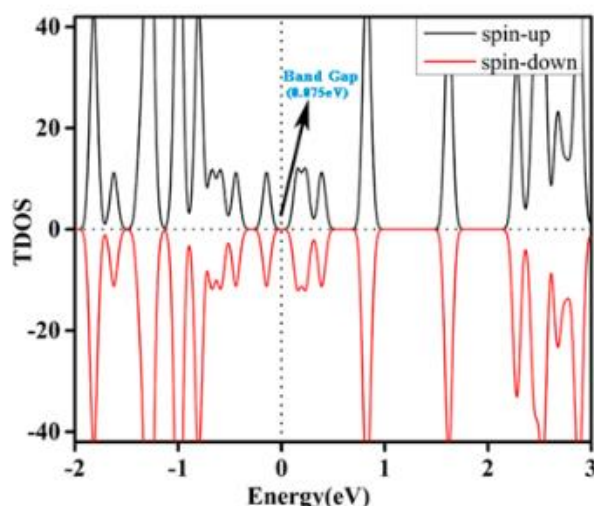


Figure 4.6: TDOS of 1T' WS₂ (Pristine Form)

Molecular Dynamics Simulation at 400K with the time duration of 5000fs was analyzed to observe the dynamical stabilities of Cu, Ag and Au doped 1T' WS₂ systems. Final structures of these doped systems (Figure 4.7(a)-(c)) were found to be stable without any significant distortion after the simulation was over. Beside this, Total free energy of Cu, Ag and Au doped 1T' WS₂ systems (Figure 4.8(d)-(f)) was remained approximately constant during the simulation indicating the well incorporation of dopants (Cu, Ag and Au) into the 1T' WS₂ system. Variation in the temperature during the molecular dynamics simulations are shown in Figure 4.7(a)-(c) which shows almost identical fluctuation of the simulation temperature above and below the 400 K value over the simulation time. RMSD values for the dopants and its nearest atoms bonded with the dopants fluctuated below the value of 0.7Å^o indicates that the stable bonding between the dopant and its nearest neighboring atoms can be formed keeping the overall structural integrity of 1T' WS₂ (Figure 4.8(d)-(f)).

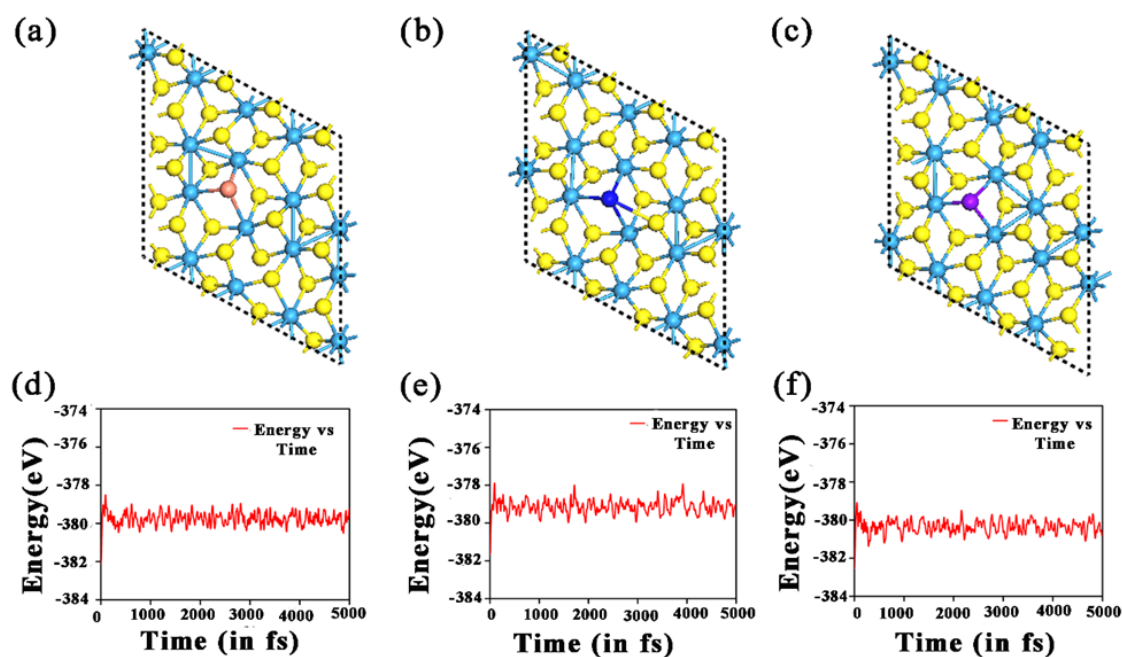


Figure 4.7: Final structures of (a) Cu doped 1T'WS₂ (b) Ag doped 1T'WS₂ and (c) Au doped 1T'WS₂ after Molecular Dynamics Simulation. Total energy of (d) Cu doped 1T'WS₂ (e) Ag doped 1T'WS₂ and (f) Au doped 1T'WS₂ during the simulation in the time duration of 5000fs.

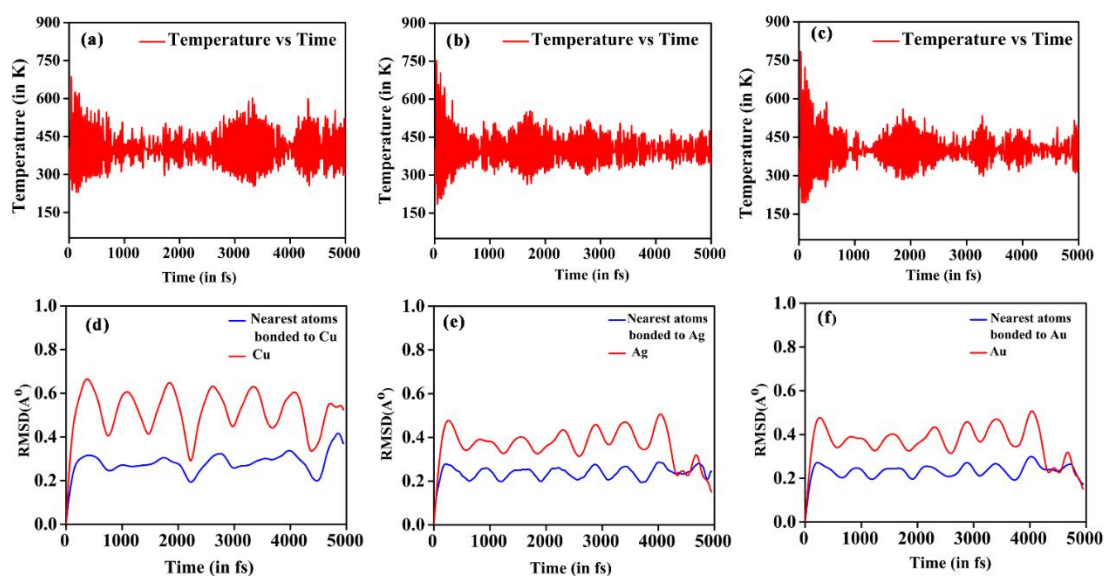


Figure 4.8: Temperature variation with time during Molecular dynamics simulation for (a) Cu doped (b) Ag doped (c) Au doped 1T' WS₂. RMSD (Å) values variation with time for (d) Cu doped (e) Ag doped (f) Au doped 1T' WS₂.

4.3.2. Oxygen reduction reaction mechanism:

In this section, the electrocatalytic activities of Cu/Ag/Au doped 1T' WS₂ as the cathode electrocatalyst to carry out ORR in acidic medium are discussed in detail. To this font, the adsorption of di-oxygen molecule (O₂) on the doped 1T' WS₂ systems is studied at first as it is the rudimentary step of ORR in any kind of electrolyte. The O₂ adsorption process was found to be exothermic in nature on all the doped systems irrespective of the dopant. Starting with different initial positions of the O₂ molecule, two different O₂ adsorbed configurations were found on the Cu doped 1T' WS₂. In one of the O₂ adsorbed configurations on Cu doped 1T' WS₂, O atoms of oxygen molecule bonded to Cu and a nearby S atom (Figure 4.9(a)) with large amount of O-O bond stretching (18.8%) which will be denoted as WS(x) throughout the rest of this paper. In the other O₂ adsorbed configuration, one of the oxygen atoms of the adsorbed O₂ molecule bonded with Cu site keeping the oxygen atom in the other end free (Figure 4.9(b)) and this O₂ adsorbed configuration will be denoted as WS(y) henceforth. The amount of stretching in the O-O bond was found to be only 4.9%. The adsorption energy for O₂ adsorption in WS(x) and WS(y) was calculated to be -0.23 eV and -0.54 eV respectively using equation (4.3). In contrast to the Cu doped 1T' WS₂ system, different initial configurations always led to one final O₂ adsorbed configuration on Ag and Au doped 1T' WS₂. On both the systems the adsorption of O₂ was found to be associative in nature with configurations being similar to the WS(y) configuration (Figure 4.9(c) & 4.9(d)). The adsorption energy values for O₂ adsorption on Ag and Au doped 1T' WS₂ were calculated to be -0.25 eV and -0.19 eV respectively. The amount of stretching in the di-oxygen bond for adsorption on each system is given in Table 4.2. The Bader charge analysis was carried out for the O₂ adsorbed configurations and the charge transfer values are represented in Table 4.2 that shows a significant amount of charge is transferred to the adsorbed O₂ molecule in all the adsorbed configurations. The O-O bond stretching (for associated configurations)/ the distance between the O atoms (for dissociated configurations) was found to be proportional to the amount of charge transfer to the O₂ molecule upon adsorption. The linear relationship between the distance between the O atoms and the charge transfer to the O₂ molecule is represented in Figure 4.10.

Table 4.2. Percentage of O-O bond stretching after adsorption to Cu, Ag and Au doped 1T' WS₂ surface and the amount of charge transfer to the oxygen atoms.

System	Bond stretching (%)	Charge transfer to oxygen atom bonded to metal dopant(e)	Charge transfer to non-bonded/attached elsewhere oxygen atom(e)
WS _(x)	18.8%	-0.43	-0.42
WS _(y)	4.9%	-0.27	-0.12
Ag doped 1T' WS ₂	3.21%	-0.20	-0.10
Au doped 1T' WS ₂	3.62%	-0.22	-0.09

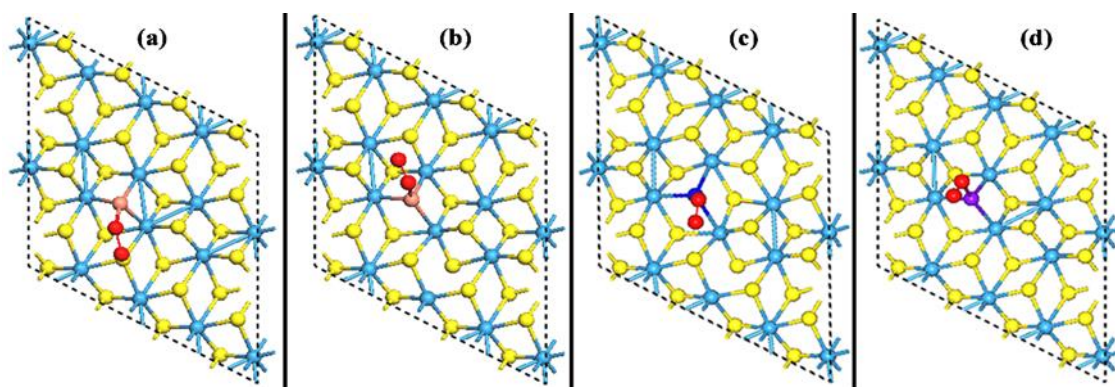


Figure 4.9: Optimized geometry of the energetically most favorable O₂ adsorbed configuration for (a) WS(x), (b) WS(y), (c) Ag doped 1T'WS₂ and (d) Au doped 1T'WS₂.

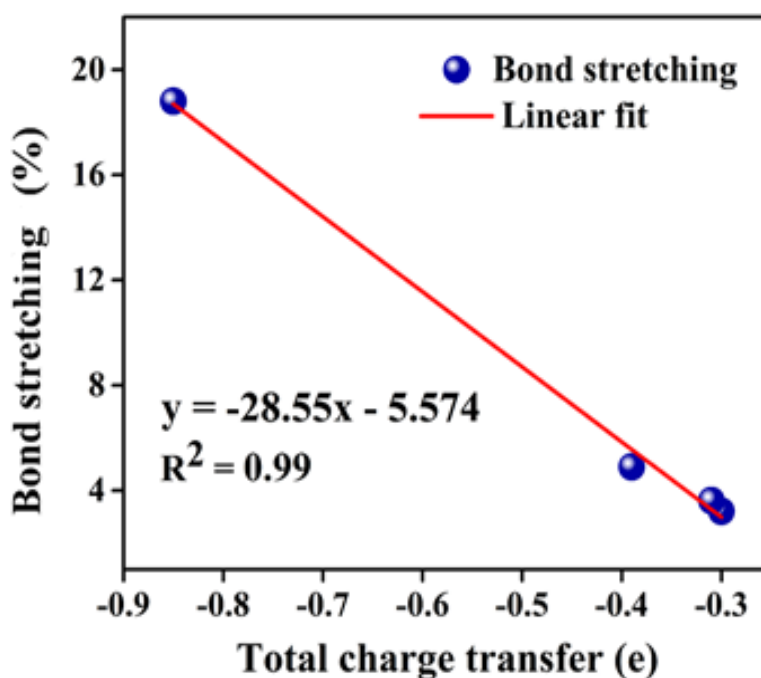


Figure 4.10: Percentage of O-O bond stretching after adsorption to Cu, Ag and Au doped 1T' WS₂ surface and the amount of charge transfer to the oxygen atoms.

ORR in acidic medium can proceed via two distinct pathways, namely the two-electron pathway and the four-electron pathway, depending on the number of electrons transferred through the outer circuit in one complete cycle and the end products. The two-electron pathway, as the name suggests, is mediated by two coupled electrons and proton transfer with the end product being hydrogen peroxide (H₂O₂). On the other hand, the four-electron pathway is energetically more efficient as it is mediated via four coupled proton and electron transfer processes in a complete reaction cycle and is much more anticipated to be carried out by the electrocatalyst as the end product in this process is water (H₂O). The detail mechanisms of both the reaction pathways are as follows:

Two electron pathway: (1) $O_2 + 2(H^+ + e^-) \rightarrow (2) *O_2 + 2(H^+ + e^-) \rightarrow (3) *OOH + (H^+ + e^-) \rightarrow (4) H_2O_2$; in summary : $O_2 + 2(H^+ + e^-) \rightarrow H_2O_2$

And four electron pathway: (1) $O_2 + 4(H^+ + e^-) \rightarrow (2) *O_2 + 4(H^+ + e^-) \rightarrow (3a) *OOH + 3(H^+ + e^-)$ or (3b) $*O + *OH + 3(H^+ + e^-) \rightarrow (4a) 2*OH + 2(H^+ + e^-)$ or (4b) $*O + H_2O + 2(H^+ + e^-) \rightarrow (5) *OH + H_2O + (H^+ + e^-) \rightarrow (6) 2H_2O$; In summary: $O_2 + 4(H^+ + e^-) \rightarrow 2H_2O$

where * refers to a chemisorption site on the catalyst surface.

The feasibility of ORR proceeding through both the mechanisms was tested thoroughly for all the systems in terms of the free energy of the ORR intermediates. The free energy difference values of the system at each reaction coordinate were calculated using equation (4.2), considering the free energy of the final product as reference. In the first reaction coordinate, the O₂ molecule is present outside the interaction range of the catalytic surface. The values of the free energy difference (ΔG_1) at this phase of the reaction, i.e. at reaction coordinate (1), were calculated to be 4.93 eV which is a universal value for ORR in acidic medium irrespective of the electrocatalyst. At the second reaction coordinate, the O₂ molecule is adsorbed on the electrocatalyst's surface with a considerable amount of stretching thus weakening the O-O bond strength. ΔG_2 for the Cu doped 1T' WS₂ was found to be 5.35 eV, 1.30 eV and the same for Ag and Au doped 1T' WS₂ was calculated to be 5.33 eV, 5.38 eV respectively. In terms of adsorption energy, O₂ adsorption on all the doped 1T' WS₂ systems is spontaneous in nature as asserted earlier but a small free energy barrier exists in case of O₂ adsorption on Cu, Ag and Au doped systems. Those small free energy barriers are expected to be overcome by external stimulation easily and subsequent ORR steps were studied on all the three doped systems. In the following step, i.e. in the first coupled electron and proton transfer process (reaction coordinate (3)), the H⁺ ion can get adsorbed onto either of the O atoms of the adsorbed O₂ molecule. As stated earlier that in the case of WS(x), O atoms of O-O bond adsorbed in two different nearest locations (one is attached with dopant (O_{Cu}) and other with neighboring sulfur atom (O_S)) and in the other structure WS(y), one of oxygen atoms of O-O bond is adsorbed only on the Cu site keeping other oxygen atom free. In the case of WS₂(x), H⁺ ion prefers to get attached to the O_{Cu} than to O_S and the O-O bond was observed to be dissociated in the process facilitating intermediate reaction route 3(b) in terms of free energy (ΔG_3) which was calculated to be 2.90 eV. First protonation occurred in WS₂(x) at Cu site (O_{Cu}) of di-oxygen bond. In contrast, H⁺ ion adsorption happened on WS₂(y) at the free end of adsorbed oxygen molecule with ΔG_3 value obtained as 0.62 eV. While for Ag and Au doped systems, H⁺ ion prefers to be attached to the free end of adsorbed O₂ molecule keeping the O-O bond associated following the path (3a) in terms of free energy (ΔG_3 values were calculated to be 4.91 eV and 4.81 eV respectively for Ag and Au doped 1T' WS₂).

The next reaction step, i.e. the second coupled proton and electron transfer process, is a crucial one as it determines whether the reaction will proceed through the two-electron pathway or the four-electron pathway. Due to the dissociation of the O-O bond after first protonation, WS(x) would most certainly follow the four-electron pathway. On WS(x), this step can occur in two

possible ways: the 2nd H atom could either be attached to the O_s atom which was unused during the 1st protonation process and form 2*OH configuration on the catalyst's surface (reaction intermediate (4a)) or it could get attached to the O_{Cu} atom releasing one water molecule and forming *O configuration on the catalyst's surface (reaction intermediate (4b)). The possibility of the formation of both the reaction intermediates (4(a) and 4(b)) was considered. It was found that in case of WS(x), the second protonation occurs on the H atom bonded O_{Cu} following the reaction pathway 4(b) with lower ΔG_4 value. For WS(y) and other doped systems, this step determines the proclivity of electrocatalyst towards two or four electron pathways due to the associative nature of O₂ adsorption. WS(y) follows the two-electron reaction pathway (4) producing H₂O₂ as the end product in terms of free energy. In contrast, for the Au and Ag doped systems, formation of both H₂O₂ (reaction coordinate 4 for the two-electron pathway) and *O (reaction coordinate 4(b) for the four-electron pathway) configurations on the electrocatalyst's surface are almost equally probable as the difference between the free energy values of the intermediates were found to be very low. Overall, the free energy difference values for the second coupled proton and electron transfer process were calculated to be in the range 0.62 eV to 3.89 eV. Although, as per the free energy difference values (ΔG_4) at reaction coordinate 4, the two-electron pathway, i.e. formation of H₂O₂, was found to be slightly more spontaneous (Figure 4.12), the marginal difference between the ΔG_4 values of the two different types of intermediates clearly indicates that both Ag and Au doped 1T' WS₂ will produce both H₂O₂ and H₂O competitively as the end product. Hence, rest of the ORR steps via the four-electron pathway was studied on both Ag and Au doped 1T' WS₂ along with WS(x). For all the doped systems, following the four-electron pathway, the first water molecule was released during the second coupled proton and electron transfer process and the catalyst surface had one O atom adsorbed on it i.e. the *O configuration at reaction coordinate 4(b). During the third protonation process (reaction coordinate 5), H⁺ was attached with *O structures and transformed into *OH configuration spontaneously for all the systems with ΔG_5 values between 1.93 and 3.89 eV. The second water molecule was released upon the final protonation process spontaneously for all with the free energy difference values within the range 1.58 to 1.80 eV.

From the above results, it is prominent that WS(x) produces the most efficient electrocatalyst for ORR among the considered systems as the monotonically exothermic free energy profile represents a spontaneous reduction of O₂ following only the four-electron pathway. WS(y) follows only two electron pathway produces H₂O₂ as a result. On the other hand, for the Ag and Au doped 1T' WS₂ systems, both the two and four electron pathways would carry out the

reduction process competitively on the catalyst's surface. To gain further insight of the mechanism of the reduction process on those doped systems, the free energy profiles were evaluated varying the electrode potential (U) following the four-electron reduction route for all. For WS(x), the monotonically exothermic nature of the free energy profile persists up to the electrode potential value of 0.38 V denoting that the overpotential of ORR on WS(x) in acidic medium is 0.85 V (using equation (4.4)). The substantially low value of overpotential for ORR on WS(x) clearly indicates that Cu doped 1T' WS₂ could be a very promising cathode material for acidic medium fuel cells. The free energy profile of Cu doped 1T' WS₂ for WS(x) at different electrode potential values is represented in the Figure (4.11(a)). The third coupled proton and electron transfer process was found to be the rate limiting step of ORR on WS(x). For Ag and Au doped 1T' WS₂, the spontaneous nature of the ORR along the four-electron pathway (Figure 4.11(b) & 11(c)) persisted up to the electrode potential value of 0.43 V and 0.57 V respectively. The overpotential values for ORR along the four-electron pathway on Ag and Au doped 1T' WS₂ was calculated to be 0.80 V and 0.66 V respectively using the equation (4.4). Detailed structures of the reaction intermediates for ORR on Cu, Ag, Au doped 1T' WS₂ via the four-electron pathway are shown in the Figure 4.13, 4.14 and 4.15 respectively. The first protonation step of Ag and Au doped 1T' WS₂ was found to be the rate limiting step of ORR. The exceptionally low value of overpotential on Au doped 1T' WS₂ corresponds to the shift of the adsorption energies of the ORR intermediates along the four-electron pathway by almost a constant value. As a result, the free energy of each ORR intermediate decreases by almost identical amounts following each coupled proton and electron transfer process. Although the low overpotential value of ORR on Au doped 1T' WS₂ is very promising, the competition between the two and four electron ORR pathway would remain a concern towards its practical application. Hence, we conclude that among the three considered doped systems Cu doped 1T' WS₂ is undoubtedly the best electrocatalyst for ORR in acidic medium fuel cells and it holds great potential to replace Pt group-based metals as the cathode material in acidic medium fuel cells.

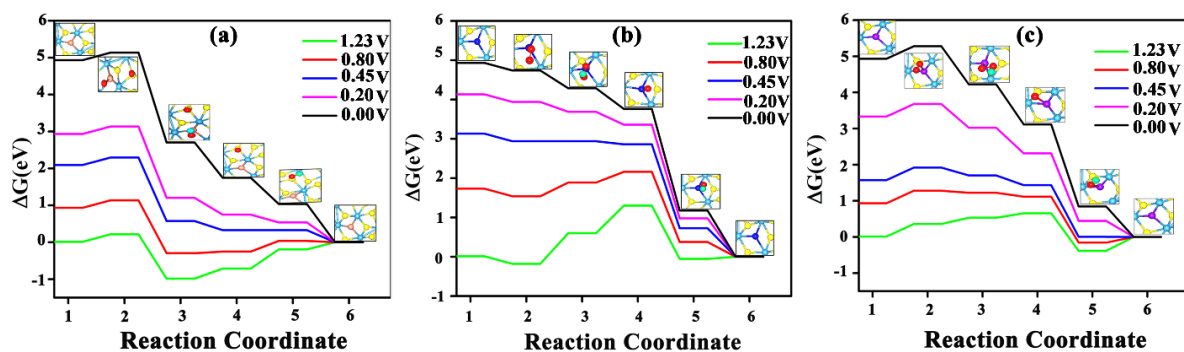


Figure 4.11: Free energy diagram of ORR at different values of the electrode potential for (a) WS₂ (b) Ag doped 1T' WS₂ (c) Au doped 1T' WS₂ via the four-electron pathway.

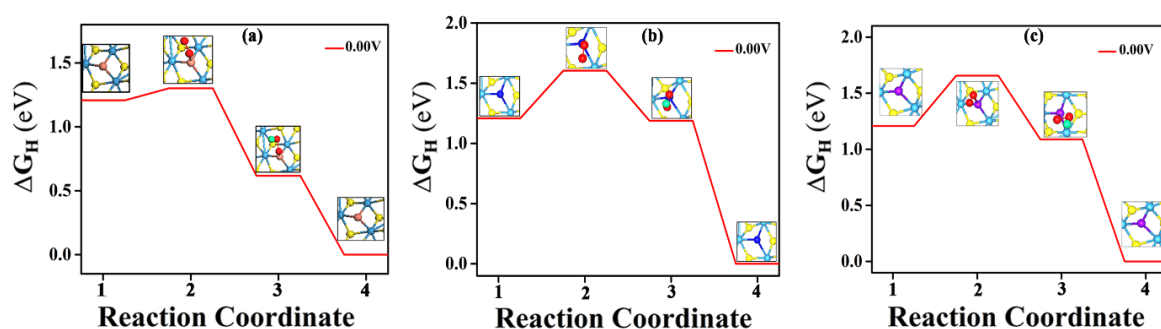


Figure 4.12: Free energy diagram at zero electrode potential (U) - (a) Cu_1T' WS₂-O₂(y), (b) Ag doped 1T' WS₂, (c) Au doped 1T' WS₂.

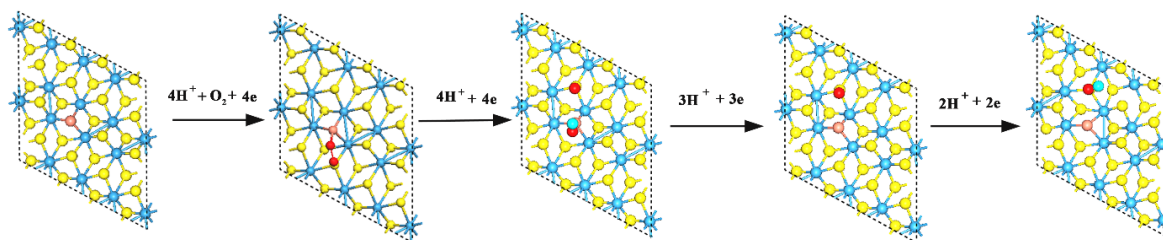


Figure 4.13: Intermediate steps of four electron pathways of Cu doped 1T' WS₂.

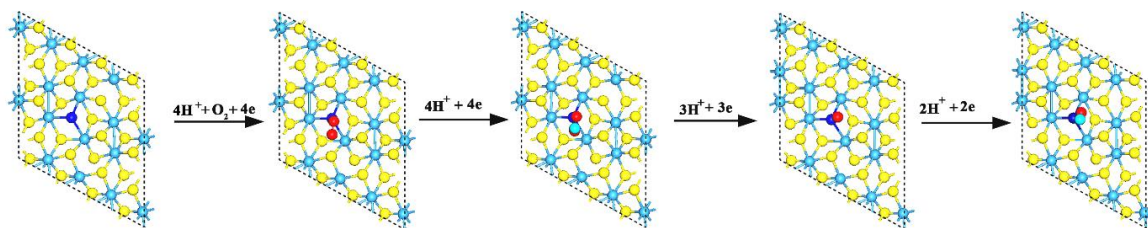


Figure 4.14: Intermediate steps of four electron pathways of Ag doped 1T' WS₂.

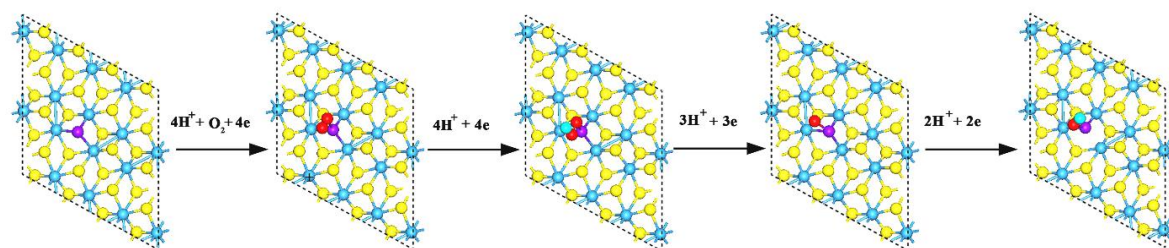
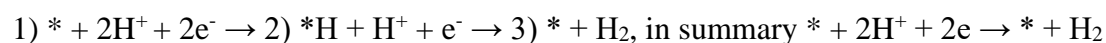


Figure 4.15: Intermediate steps of four electron pathways of Au doped 1T' WS₂.

4.3.3. Hydrogen evolution reaction:

The electrocatalytic activity of the metal doped 1T' WS₂ towards hydrogen evolution reaction (HER) is elaborated in this section. HER in acidic electrolyte occurs via the following two step process:



* represents the active site of the system for H adsorption. One H⁺ gets attached to the active site on the electrocatalyst's surface forming a *H configuration. Subsequently, another H⁺ interacts with the *H liberating the H₂ molecule.

Adsorption of H⁺ was studied on the dopant and its nearest W and S sites for each metal doped 1T' WS₂ system. Each active site for H⁺ on the electrocatalysts surface is represented as X_Y WS₂ in rest of this manuscript for the doped systems. X represents the dopant atom (Cu, Ag, Au) and Y represents adsorbent atom (dopant/W/S). Similarly, W site and S site of pristine 1T' WS₂ are represented as WS₂(W) and WS₂(S). It was found that on pristine 1T' WS₂, H⁺ gets adsorbed only on the S atom site. The H⁺ ion migrates and gets adsorbed to the S atom (WS₂(S)) site upon optimization even when it was initially placed near the W atom site. We will use the name of the adsorption site to indicate a particular *H configuration in the rest of the

manuscript. The free energy change of H^+ adsorption (ΔG_H) on $WS_2(S)$ was calculated to be 1.02 eV representing a relatively weak adsorption process (Figure (4.16)). In case of the doped systems, the H^+ adsorption was found to take place only on the S and dopant (Cu, Ag, Au) sites. The H^+ ion, initially placed near W site, migrated and formed the $*H$ configuration on the dopant atom for all the doped 1T' WS_2 systems. Hence, for each metal doped 1T' WS_2 systems, two different $*H$ configurations were found (namely $(Cu_{Cu} WS_2$ and $Cu_S WS_2$ for Cu doped 1T' WS_2 , $Ag_{Ag} WS_2$ and $Ag_S WS_2$ for Ag doped 1T' WS_2 , $Au_{Au} WS_2$ and $Au_S WS_2$ for Au doped 1T' WS_2). Gibbs free energy change for the H^+ adsorption (ΔG_H) on electrocatalyst's surface determines the HER activity of that system. Optimal value of Gibbs free energy should be equal to zero. Positive value of free energy ΔG_H indicates weaker adsorption and negative value of ΔG_H indicates stronger adsorption of H^+ . The value of ΔG_H close to zero signifies that Hydrogen adsorption on the catalytic surface is neither too strong nor too weak, which is advantageous for releasing Hydrogen molecule from the catalytic surface and improved HER performance. ΔG_H value of $WS_2(S)$ is 1.02 eV indicating poor HER activity of pristine 1T' WS_2 system. The free energy plots for HER on each active site on every metal doped 1T' WS_2 system is represented in Figure (4.16). Then ΔG_H values for $Cu_{Cu} WS_2$, $Cu_S WS_2$, $Ag_{Ag} WS_2$, $Ag_S WS_2$, $Au_{Au} WS_2$ and $Au_S WS_2$ was calculated to be -0.14 eV, 0.95 eV -0.17 eV, 0.52 eV, 0.18 eV and 0.40 eV respectively. For all the metal doped 1T' WS_2 systems, the metal dopant ($Cu_{Cu} WS_2$, $Ag_{Ag} WS_2$ and $Au_{Au} WS_2$) universally plays the role of most active site for HER with lower value of ΔG_H compared to HER on S site. Overall, $Cu_{Cu} WS_2$ showed the best electrocatalytic activities towards HER with the lowest ΔG_H value (-0.14 eV). The free energy diagrams for HER on pristine and metal doped 1T' WS_2 are represented in Figure (4.16) and the optimized structure of the $*H$ configurations are shown in Figure (4.17). Interaction between adsorbent atom and the adsorbed H was further probed using crystal orbital Hamilton population (COHP) analysis to shed light into the HER activity of different active sites in each metal doped 1T' WS_2 system. The COHP plots of the interaction between adsorbent atom and adsorbed H atom for different $*H$ configurations are shown in Figure (4.18). For all the $*H$ configurations, small occupied antibonding states are found just below or/ and at the Fermi energy (E_F). Notably, for $*H$ configurations with S being the adsorbent atom, a large energy gap is observed between occupied bonding and antibonding states (Figure (4.18b), (4.18d) and (4.18f)). On the contrary, for the $*H$ configurations with the metal dopant being the adsorbent, no such energy gap was observed between the occupied bonding and antibonding states (Figure (4.18a), (4.18c) and (4.18e)). The absence of energy gap between occupied bonding and antibonding states for $Cu_{Cu} WS_2$, $Ag_{Ag} WS_2$ and $Au_{Au} WS_2$ might have played the pivotal role

in facilitating the smooth transition of electrons between the bonding and antibonding states and hence rendering the bond between the metal dopant and H atom more activated compared to the S-H bonds. The activated Cu-H /Ag-H/ Au-H bonds becomes prone to further reaction which results in the reduced free energy barrier for HER on $\text{Cu}_{\text{Cu}}\text{WS}_2$, $\text{Ag}_{\text{Ag}}\text{WS}_2$ and $\text{Au}_{\text{Au}}\text{WS}_2$ systems. Furthermore, the Ag-H and Au-H bonds might have been the most activated ones among all with relatively larger antibonding peaks right at the Fermi energy level which paved the way for further hydrogenation and formation of H_2 on the $\text{Ag}_{\text{Ag}}\text{WS}_2$, $\text{Au}_{\text{Au}}\text{WS}_2$ systems with the lowest free energy barrier. The COHP plot of the S-H interaction in the $^*\text{H}$ configuration on the pristine system ($\text{WS}_2(\text{S})$) is shown in Fig. (4.19). Similar to the doped systems, a large energy gap between the occupied bonding and antibonding states was observed indicating poor HER activity.

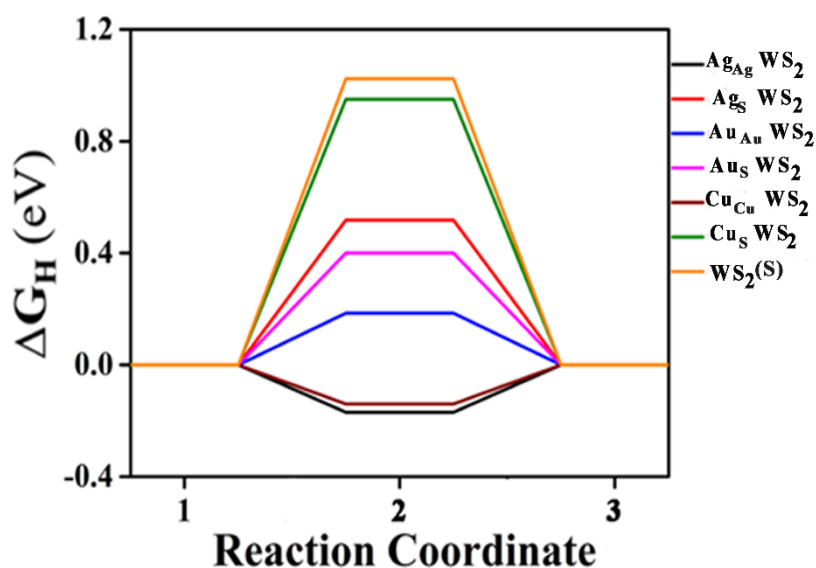


Figure 4.16: Free energy diagram of HER on $\text{Cu}_{\text{Cu}}\text{WS}_2$, $\text{Cu}_{\text{S}}\text{WS}_2$, $\text{Ag}_{\text{Ag}}\text{WS}_2$, $\text{Ag}_{\text{S}}\text{WS}_2$, $\text{Au}_{\text{Au}}\text{WS}_2$, $\text{Au}_{\text{S}}\text{WS}_2$ and $\text{WS}_2(\text{S})$.

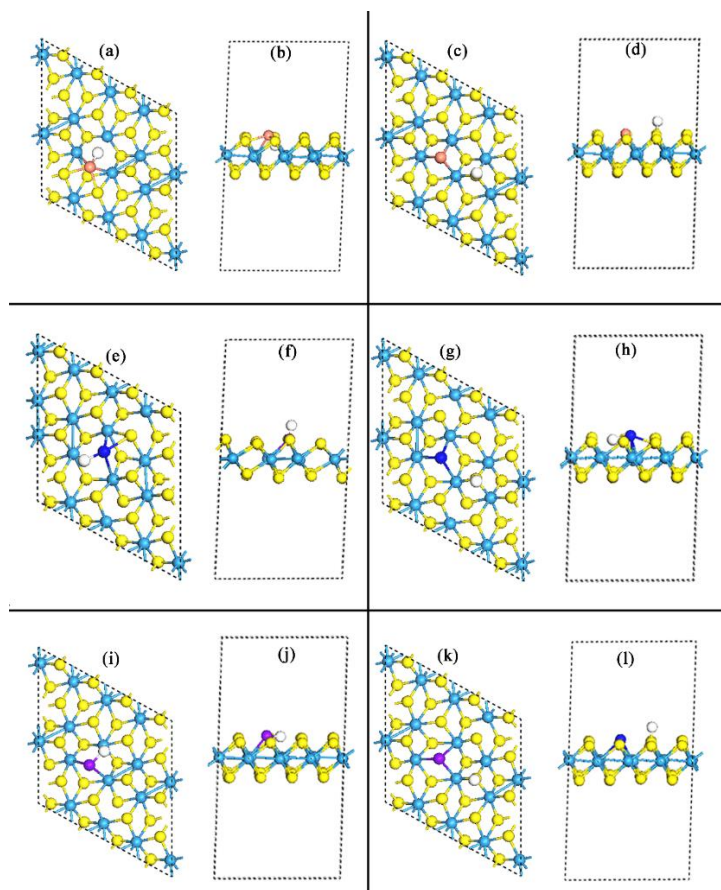


Figure 4.17: Top view and Side view of H^+ ion adsorbed on (a), (b): Cu_{Cu} WS_2 ; (c), (d): CuS WS_2 ; (e), (f): Ag_{Ag} WS_2 ; (g), (h): AgS WS_2 ; (i), (j): Au_{Au} WS_2 ; (k), (l): AuS WS_2 respectively.

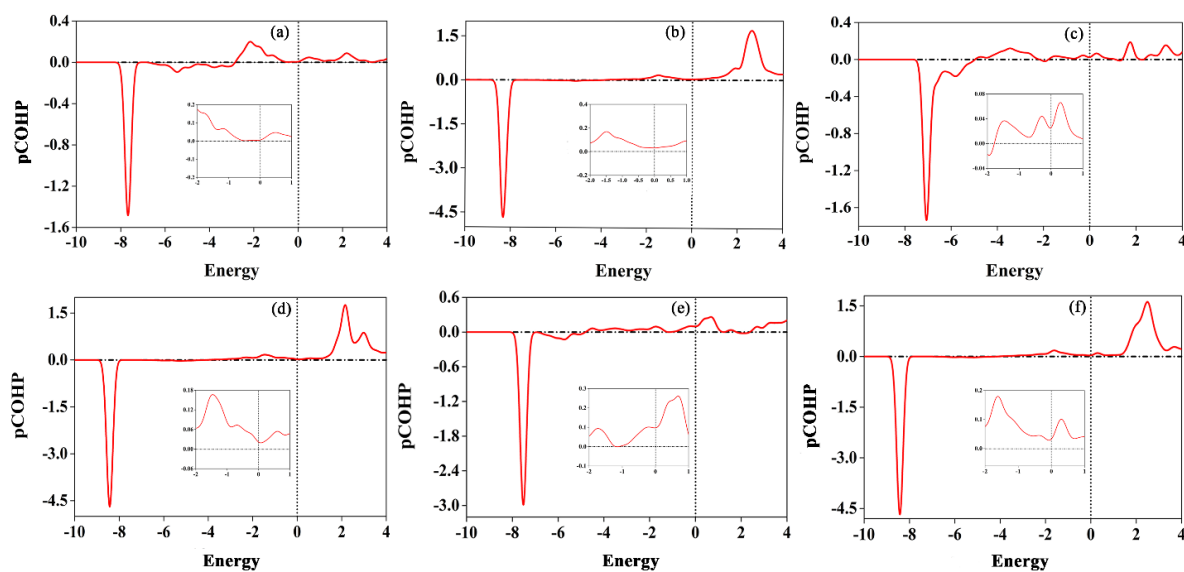


Figure 4.18: (a), (b), (c), (d), (e) and (f) represents the COHP plot of H^+ ion adsorbed on (Cu)-Cu-1T' WS_2 , (S)-Cu-1T' WS_2 , (Ag)-Ag-1T' WS_2 , (S)-Ag-1T' WS_2 , (Au)-Au-1T' WS_2 and (S)-Au-1T' WS_2 respectively.

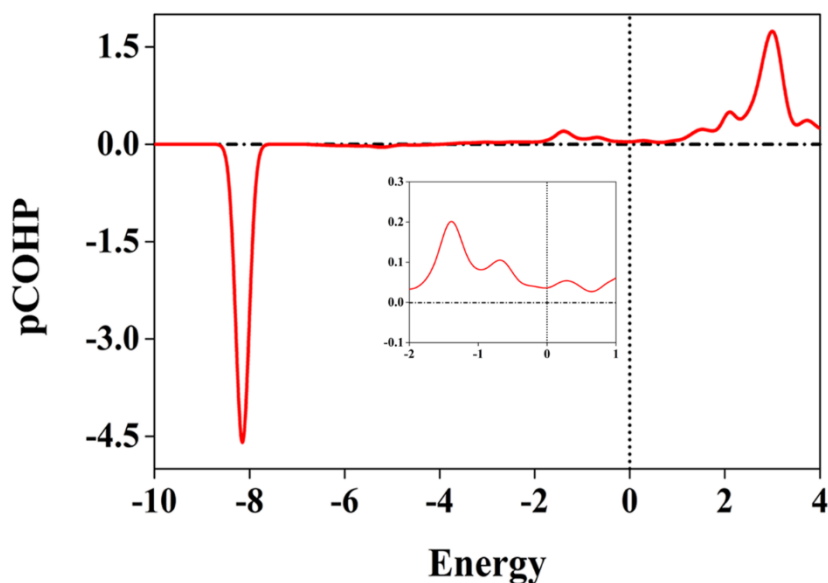


Figure 4.19: COHP plot of Pristine 1T' WS₂.

4.4. Conclusion:

Dispersive force corrected density functional theory is implemented to explore the electronic properties and electrocatalytic performance of Cu, Ag and Au doped 1T' WS₂ as bifunctional electrocatalysts towards ORR and HER. Charge is universally found to be transferred to the dopant atom in all doping scenarios maintaining the stabilities of the doped configurations. The observed results of AIMD simulation at 400K demonstrated the dynamical stabilities of Cu, Ag and Au doped 1T' WS₂ and support their potential application as catalysts in fuel cells. O₂ adsorption on all the doped systems is found to be associative in nature. In terms of adsorption energy, two different O₂ adsorbed configuration is isolated to be stable on Cu doped 1T' WS₂. On the other hand, only one O₂ adsorbed structure is obtained for other doped systems. The adsorption process is exothermic on all the systems with adsorption energy values within the range -0.19 eV to -0.54 eV. Significant amounts of charge transfers from the catalyst surface to oxygen atoms are also noticed.

ORR kinetics of all the doped 1T' WS₂ structures are systemically investigated in terms of free energy to observe spontaneity of the reaction process. WS(x) configuration follows only four electron pathways involuntarily because of O-O bond breaking after first protonation but WS(y) configuration attends two electron pathways only. ORR on Ag and Au doped 1T' WS₂ is expected to proceed via both two and four electron pathways competitively due to the very

low free energy difference between the intermediates formed after the 2nd protonation step following either pathway. Variation of the electrode potential value reveals substantially low overpotential value of 0.66 V for Au doped 1T' WS₂ along the four-electron pathway and a moderate overpotential value of 0.85 V and 0.80V for Cu and Ag doped 1T' WS₂. First protonation step is found to be rate limiting step for Ag and Au doped 1T' WS₂. For the Cu doped 1T' WS₂, third protonation step was observed to be the rate limiting step. We conclude that among the considered doped systems, Cu doped 1T' WS₂ is the most efficient and promising cathode material for acidic medium fuel cells with overpotential of value 0.85 V because of its proclivity towards only the four-electron pathway.

The electrocatalytic activities of Cu, Ag and Au doped 1T' WS₂ towards HER is further investigated. The active sites for HER on each doped system are isolated in terms of free energy analysis. The free energy difference of H⁺ adsorption (ΔG_H) was calculated to be 1.02 eV for the sole active S site in pristine 1T' WS₂ indicating its poor performance towards HER. In the case of the doped system, two active sites (S site and dopant site) were isolated for H⁺ ion adsorption. ΔG_H values obtained for Cu_{Cu} WS₂, Cu_S WS₂, Ag_{Ag} WS₂, Ag_S WS₂, Au_{Au} WS₂ and Au_S WS₂ are -0.14 eV, 0.95 eV -0.17 eV, 0.52 eV, 0.18 eV and 0.40 eV respectively. Cu_{Cu} WS₂ are found to be the most efficient electrocatalyst for HER among the considered systems with ΔG_H value close to zero.

References:

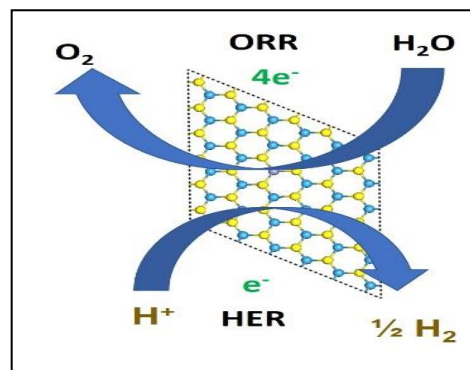
- [1] S. Kakac, A. Pramuanjaroenkij, X.Y. Zhou, A review of numerical modeling of solid oxide fuel cells, *International journal of hydrogen energy*, 32 (2007) 761-786.
- [2] G. Merle, M. Wessling, K. Nijmeijer, Anion exchange membranes for alkaline fuel cells: A review, *Journal of Membrane Science*, 377 (2011) 1-35.
- [3] B. Peng, J. Chen, Functional materials with high-efficiency energy storage and conversion for batteries and fuel cells, *Coordination Chemistry Reviews*, 253 (2009) 2805-2813.
- [4] C.K. Dyer, Fuel cells for portable applications, *Journal of Power Sources*, 106 (2002) 31-34.
- [5] M. Oezaslan, F. Hasche, P. Strasser, Pt-based core-shell catalyst architectures for oxygen fuel cell electrodes, *The Journal of Physical Chemistry Letters*, 4 (2013) 3273-3291.
- [6] N. Jung, D.Y. Chung, J. Ryu, S.J. Yoo, Y.-E. Sung, Pt-based nanoarchitecture and catalyst design for fuel cell applications, *Nano Today*, 9 (2014) 433-456.
- [7] D.Y. Chung, J.M. Yoo, Y.E. Sung, Highly durable and active Pt-based nanoscale design for fuel-cell oxygen-reduction electrocatalysts, *Advanced materials*, 30 (2018) 1704123.
- [8] R.-Q. Zhang, T.-H. Lee, B.-D. Yu, C. Stampfl, A. Soon, The role of titanium nitride supports for single-atom platinum-based catalysts in fuel cell technology, *Physical Chemistry Chemical Physics*, 14 (2012) 16552-16557.
- [9] C.-H. Chen, K.E. Meadows, A. Cuharuc, S.C. Lai, P.R. Unwin, High resolution mapping of oxygen reduction reaction kinetics at polycrystalline platinum electrodes, *Physical chemistry chemical physics*, 16 (2014) 18545-18552.
- [10] Z. Cai, Z. Lu, Y. Bi, Y. Li, Y. Kuang, X. Sun, Superior anti-CO poisoning capability: Au-decorated PtFe nanocatalysts for high-performance methanol oxidation, *Chemical Communications*, 52 (2016) 3903-3906.
- [11] A.K. Geim, K.S. Novoselov, The rise of graphene, *Nanoscience and technology: a collection of reviews from nature journals*, World Scientific 2010, pp. 11-19.
- [12] H. Wan, F. Chen, W. Ma, X. Liu, R. Ma, Advanced electrocatalysts based on two-dimensional transition metal hydroxides and their composites for alkaline oxygen reduction reaction, *Nanoscale*, 12 (2020) 21479-21496.
- [13] A. Kumar, Q. Xu, Two-Dimensional Layered Materials as Catalyst Supports, *ChemNanoMat*, 4 (2018) 28-40.
- [14] Y. Xiao, L. Tang, High-throughput approach exploitation: Two-dimensional double-metal sulfide (M₂S₂) of efficient electrocatalysts for oxygen reduction reaction in fuel cells, *Energy & Fuels*, 34 (2020) 5006-5015.

- [15] S. Jayabal, G. Saranya, J. Wu, Y. Liu, D. Geng, X. Meng, Understanding the high-electrocatalytic performance of two-dimensional MoS₂ nanosheets and their composite materials, *Journal of Materials Chemistry A*, 5 (2017) 24540-24563.
- [16] B.K. Das, D. Sen, K. Chattopadhyay, Nitrogen doping in acetylene bonded two-dimensional carbon crystals: Ab-initio forecast of electrocatalytic activities vis-à-vis boron doping, *Carbon*, 105 (2016) 330-339.
- [17] Y. Xue, D. Yu, L. Dai, R. Wang, D. Li, A. Roy, F. Lu, H. Chen, Y. Liu, J. Qu, Three-dimensional B, N-doped graphene foam as a metal-free catalyst for oxygen reduction reaction, *Physical Chemistry Chemical Physics*, 15 (2013) 12220-12226.
- [18] X. Chen, R. Hu, DFT-based study of single transition metal atom doped g-C₃N₄ as alternative oxygen reduction reaction catalysts, *International Journal of Hydrogen Energy*, 44 (2019) 15409-15416.
- [19] B.K. Das, D. Sen, K.K. Chattopadhyay, Implications of boron doping on electrocatalytic activities of graphyne and graphdiyne families: a first principles study, *Physical Chemistry Chemical Physics*, 18 (2016) 2949-2958.
- [20] B.K. Das, D. Sen, K.K. Chattopadhyay, Mechanism of Oxygen Reduction Reaction in Alkaline Medium on Nitrogen-Doped Graphyne and Graphdiyne Families: A First Principles Study, *ChemPhysChem*, 23 (2022) e202100900.
- [21] Y. Singh, S. Back, Y. Jung, Activating Transition Metal Dichalcogenides by Substitutional Nitrogen-Doping for Potential ORR Electrocatalysts, *ChemElectroChem*, 5 (2018) 4029-4035.
- [22] D. Chen, Y. Zou, S. Wang, Surface chemical-functionalization of ultrathin two-dimensional nanomaterials for electrocatalysis, *Materials Today Energy*, 12 (2019) 250-268.
- [23] J. Deng, H. Li, J. Xiao, Y. Tu, D. Deng, H. Yang, H. Tian, J. Li, P. Ren, X. Bao, Triggering the electrocatalytic hydrogen evolution activity of the inert two-dimensional MoS₂ surface via single-atom metal doping, *Energy & Environmental Science*, 8 (2015) 1594-1601.
- [24] W. Choi, N. Choudhary, G.H. Han, J. Park, D. Akinwande, Y.H. Lee, Recent development of two-dimensional transition metal dichalcogenides and their applications, *Materials Today*, 20 (2017) 116-130.
- [25] K. Cho, J. Pak, S. Chung, T. Lee, Recent advances in interface engineering of transition-metal dichalcogenides with organic molecules and polymers, *ACS nano*, 13 (2019) 9713-9734.
- [26] X. Zhang, S.Y. Teng, A.C.M. Loy, B.S. How, W.D. Leong, X. Tao, Transition metal dichalcogenides for the application of pollution reduction: A review, *Nanomaterials*, 10 (2020) 1012.
- [27] C.R. Zhu, D. Gao, J. Ding, D. Chao, J. Wang, TMD-based highly efficient electrocatalysts developed by combined computational and experimental approaches, *Chemical Society Reviews*, 47 (2018) 4332-4356.

- [28] S. Kc, R.C. Longo, R.M. Wallace, K. Cho, Surface oxidation energetics and kinetics on MoS₂ monolayer, *Journal of Applied Physics*, 117 (2015) 135301.
- [29] J. Chen, J. Cao, J. Zhou, W. Wang, Y. Zhang, J. Liu, X. Liu, A computational evaluation of MoS₂-based materials for the electrocatalytic oxygen reduction reaction, *New Journal of Chemistry*, 44 (2020) 14189-14197.
- [30] H. Liu, N. Han, J. Zhao, Atomistic insight into the oxidation of monolayer transition metal dichalcogenides: from structures to electronic properties, *Rsc Advances*, 5 (2015) 17572-17581.
- [31] Z. Wang, J. Zhao, Q. Cai, F. Li, Computational screening for high-activity MoS₂ monolayer-based catalysts for the oxygen reduction reaction via substitutional doping with transition metal, *Journal of Materials Chemistry A*, 5 (2017) 9842-9851.
- [32] H. Zhang, Y. Tian, J. Zhao, Q. Cai, Z. Chen, Small dopants make big differences: Enhanced electrocatalytic performance of MoS₂ monolayer for oxygen reduction reaction (ORR) by N- and P-doping, *Electrochimica Acta*, 225 (2017) 543-550.
- [33] D.B. Putungan, S.-H. Lin, J.-L. Kuo, A first-principles examination of conducting monolayer 1T'-MX₂ (M= Mo, W; X= S, Se, Te): promising catalysts for hydrogen evolution reaction and its enhancement by strain, *Physical Chemistry Chemical Physics*, 17 (2015) 21702-21708.
- [34] Q. Tang, D.-e. Jiang, Stabilization and band-gap tuning of the 1T-MoS₂ monolayer by covalent functionalization, *Chemistry of Materials*, 27 (2015) 3743-3748.
- [35] Q. Tang, D.-e. Jiang, Mechanism of hydrogen evolution reaction on 1T-MoS₂ from first principles, *Acs Catalysis*, 6 (2016) 4953-4961.
- [36] S.J. Tan, I. Abdelwahab, Z. Ding, X. Zhao, T. Yang, G.Z. Loke, H. Lin, I. Verzhbitskiy, S.M. Poh, H. Xu, Chemical stabilization of 1T' phase transition metal dichalcogenides with giant optical Kerr nonlinearity, *Journal of the American Chemical Society*, 139 (2017) 2504-2511.
- [37] W. Li, J. Li, Ferroelasticity and domain physics in two-dimensional transition metal dichalcogenide monolayers, *Nature communications*, 7 (2016) 1-8.
- [38] S. Tian, C. Deng, Y. Tang, Q. Tang, Effect of Adatom Doping on the Electrochemical Performance of 1T' MoS₂ for Oxygen Reduction Reactions, *The Journal of Physical Chemistry C*, 124 (2020) 24899-24907.
- [39] J. Hwang, S.H. Noh, B. Han, Design of active bifunctional electrocatalysts using single atom doped transition metal dichalcogenides, *Applied Surface Science*, 471 (2019) 545-552.
- [40] U. De Silva, J. Masud, N. Zhang, Y. Hong, W.P. Liyanage, M.A. Zaeem, M. Nath, Nickel telluride as a bifunctional electrocatalyst for efficient water splitting in alkaline medium, *Journal of Materials Chemistry A*, 6 (2018) 7608-7622.

- [41] Z. Qin, J. Zhao, 1T MoSe₂ monolayer supported single Pd atom as a highly-efficient bifunctional catalyst for ORR/OER, *Journal of Colloid and Interface Science*, 605 (2022) 155-162.
- [42] G. Kresse, J. Furthmüller, J. Hafner, Theory of the crystal structures of selenium and tellurium: the effect of generalized-gradient corrections to the local-density approximation, *Physical Review B*, 50 (1994) 13181.
- [43] G. Kresse, J. Furthmüller, Efficiency of ab-initio total energy calculations for metals and semiconductors using a plane-wave basis set, *Computational materials science*, 6 (1996) 15-50.
- [44] G. Kresse, J. Furthmüller, Efficient iterative schemes for ab initio total-energy calculations using a plane-wave basis set, *Physical review B*, 54 (1996) 11169.
- [45] G. Kresse, J. Hafner, Ab initio molecular dynamics for liquid metals, *Physical Review B*, 47 (1993) 558.
- [46] Y. Du, C. Ouyang, S. Shi, M. Lei, Ab initio studies on atomic and electronic structures of black phosphorus, *Journal of Applied Physics*, 107 (2010) 093718.
- [47] J.P. Perdew, K. Burke, M. Ernzerhof, Generalized gradient approximation made simple, *Physical review letters*, 77 (1996) 3865.
- [48] R.F. Bader, A quantum theory of molecular structure and its applications, *Chemical Reviews*, 91 (1991) 893-928.
- [49] S. Grimme, Semiempirical GGA-type density functional constructed with a long-range dispersion correction, *Journal of computational chemistry*, 27 (2006) 1787-1799.
- [50] J.K. Nørskov, J. Rossmeisl, A. Logadottir, L. Lindqvist, J.R. Kitchin, T. Bligaard, H. Jonsson, Origin of the overpotential for oxygen reduction at a fuel-cell cathode, *The Journal of Physical Chemistry B*, 108 (2004) 17886-17892.
- [51] K. Srinivasu, S.K. Ghosh, Transition metal decorated graphyne: an efficient catalyst for oxygen reduction reaction, *The Journal of Physical Chemistry C*, 117 (2013) 26021-26028.
- [52] R. Dronskowski, P.E. Bloechl, Crystal orbital Hamilton populations (COHP): energy-resolved visualization of chemical bonding in solids based on density-functional calculations, *The Journal of Physical Chemistry*, 97 (1993) 8617-8624.
- [53] V.L. Deringer, A.L. Tchougréeff, R. Dronskowski, Crystal orbital Hamilton population (COHP) analysis as projected from plane-wave basis sets, *The journal of physical chemistry A*, 115 (2011) 5461-5466.

5. Zinc doping induced WS₂ accelerating the HER and ORR kinetics: A theoretical and Experimental Validation



5.1. Introduction:

As the environmental and energy crisis increase due to unreasonable development, there is a need for clean, renewable hydrogen energy and fuel cells, which are alternatives to natural energy that lead to their environment-friendly, abundant supply, and high energy density [1-3]. Since then, green energy has been classified into three types, including sustainable energy, the optimization of traditional energy sources, and fuel cells, in which hydrogen and oxygen fuel is considered to be the most promising green energy sources because of their better combustion performance, superior thermal conductivity, and higher energy density [4]. The production of hydrogen by electrolyzing water in acidic media (hydrogen evolution reaction (HER)) has been demonstrated to be more environmentally friendly in comparison with the steam reforming of fuels (such as methane and ethanol), which is observed to be the primary and efficient pathway [5-7]. However, this procedure depends on the betterment of HER electrocatalysts, where inexpensive, plentiful, and highly stable electrocatalysts can be used to replace noble metals [8]. Thus, developing high-efficiency catalysts with fast kinetics and low overpotential is vital for the HER and oxygen reduction reaction (ORR) process [9,10]. To accelerate the HER process, Pt-based metals or Pd-group alloys have been assumed to be the most efficient catalysts in the long run. Still, due to the extremely high cost of these extremely high-cost precious metals, they have not been mostly used in electrocatalytic HER and ORR [11-14]. Recently, many transition metal compounds have emerged as promising HER electrocatalysts, which include sulphides [15-16], selenides [17], phosphides [18], nitrides [19], carbides [20]. Among these compounds, two-dimensional transition-metal dichalcogenides (2D-TMDCs) have captured great attention due to their excessive capabilities for the production of clean energy via photocatalysis [21], photovoltaic activities [22], and electrochemical water splitting [23]. In particular, transition-metal (TM) disulfides such as WS₂ and MoS₂ have been detected as catalysts for efficient HER and ORR in virtue-of better environmental and chemical

inertness for longer time intervals [24,25]. Since then, it has been known that the TMDCs edge sites are predominating for the electrochemical reactions, whereas the basal planes are proven inert [26]. Apart from that, as only chalcogen atoms take part in the reaction, while TM atoms are expected to be inert, the theoretical analysis of the HER of 2D-TMDCs has proven that the unstrained materials show poor HER activity [27-29]. Using this observation, the best technique to tune HER activity is substitutional doping in TMDCs or alloy engineering in ternary alloys of TMDCs [30,31]. Due to the mismatch in the atomic size of atoms of host and dopant elements, the substitutional /atomic doping can lead to the generation of additional strain in the crystal structure [32]. Using this technique, HER activity can be significantly improved and easily employed for effective energy generation [33]. In this case, various works were dedicated to modulation the electronic structure by various means, such as doping and interface or defect engineering, to improve HER activity. It can be proven that the metallic element doping in TMSs can change the electronic configurations of catalysts and optimize hydrogen adsorption energy. Therefore, it is considered an effective method for obtaining excellent TMS electrocatalysts.

Therefore, a number of approaches have been adopted to improve the HER and ORR properties of WS₂ electrocatalysts and unremitting efforts in recent years have led to several achievements, including doping with certain heteroatoms, phase transition, combining with conductive substrates (e.g., carbon nanotubes (CNTs), reduced graphene oxides.) and control of the morphology or structures to add more available active sites [34]. Among them, the strategy of suitable metal doping, which can effectively facilitate the HER activity of transition-metal dichalcogenides via simultaneously increasing the active sites and conductivity, deserves special mention. With these critical points of conductivity and active sites, metal-doped WS₂ will be a promising system to explore further how to efficiently promote the HER and ORR processes. In particular, Zn dopant can activate the catalytic activity of S atoms in the basal plane and be the active site itself. Furthermore, Zn dopant can also enhance the conductivity of pure WS₂, resulting in excellent HER and ORR performance. We also provide experimental and theoretical proof that synthesized Zn-doped WS₂ catalysts show enhanced electrochemical activity compared with pure WS₂.

5.2. Theoretical Method:

All the First Principles calculations are performed using Vienna Ab-initio Simulation Packages (VASP) with Projector-augmented-wave (PAW) approach [35-39]. The Perdew-Burke-Ernzerhof (PBE) functional was taken into account within the GGA approximation to consider Exchange and Correlation contributions [40]. Energy cut off for plane wave basis was set as 500 eV for all the calculations and total energies of the structures were converged up to 1×10^{-6} eV per atom. Zinc doping, O₂ adsorption and subsequent ORR/ HER kinematics were studied on (6×6) supercell of 2H phase of WS₂. Due to sufficiently large doped systems Γ centered (1×1×1) k-points grid was deployed during the geometry optimizations. To minimize all factious interaction between the recurrent images along the normal direction to the two-dimensional layers, a vacuum slab of length of 23 Å was considered along the perpendicular direction. Van der Waal's interaction was included using PBE+D2 forcefield (Grimme's) method as implemented in VASP [41]. Formation energy of doped structures was calculated to compare their stabilities using following equation:

$$E_{\text{for}} = E_{\text{doped}} - E_{\text{pris}} + n_W \mu_W - n_d \mu_d \quad (5.1)$$

where E_{for} is the formation energy of the doped structure, E_{doped} is the computed total ground state energy of the doped system, E_{pris} is the computed total ground state energy of the pristine system, n_W is the number of Tungsten atoms replaced through doping, μ_W is the chemical potential of Tungsten atom (calculated with respect to BCC Tungsten structure as reference), n_d is the number of dopant atom, and μ_d chemical potential of Zn atom (calculated from Hexagonal Structure). Gibbs free energy change from one reaction step to another of ORR kinematics was studied using following equation:

$$G = \Delta E + \Delta \text{ZPE} + T\Delta S + G_U \quad (5.2)$$

where ΔE is the change in enthalpy, ΔZPE is the correction due to zero-point energy (neglected in our present calculations) and ΔS is the change in entropy. For the n number of electrons transfer involved in each reaction step was calculated as $\Delta G_U = -neU$ (e = electronic charge and U = electrode potential with respect to standard hydrogen electrode (SHE)). $T\Delta S$ values are calculated at room temperature using standard physical chemistry table [42]. All the free energy calculations were done at the absolute alkaline medium i.e pH = 14. Overpotential value for ORR in alkaline medium of a particular structure was calculated using the following equation:

$$\eta_{\text{over}} = 0.4\text{V} - \eta_{\text{onset}} \quad (5.3)$$

Oxygen molecule adsorption capacity of different percentages of Zn doped WS₂ structures were calculated using the following equation:

$$E_{\text{ads}} = E_{\text{tot}}^{\text{do}} - E_P - E^{\text{do}} \quad (5.4)$$

where, E_{ads} is the adsorption energy of oxygen molecule on a particular system, $E_{\text{tot}}^{\text{do}}$ is total energy of the oxygen molecule adsorbed that system, E_P is the energy of the adsorbent and E^{do} is the computed energy of one oxygen molecule in the gas phase.

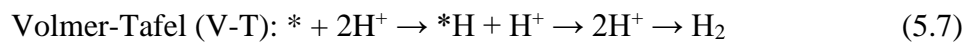
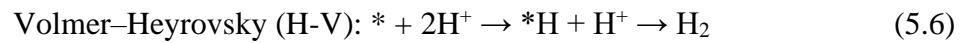
The center of d-projected DOS was calculated using the following equation

$$E_d = \frac{\int_{-\infty}^0 n(E)E dE}{\int_{-\infty}^0 n(E) dE} \quad (5.5)$$

where $n(E)$ is the total density of states (TDOS), E is the energy corresponding to TDOS plot. The Fermi energy was scaled to the value of 0 eV for all the systems.

5.3. Results and discussions on HER and ORR:

HER on the electrocatalyst surface can proceed via two distinct mechanisms, namely the Volmer–Heyrovsky and Volmer-Tafel mechanisms. The Zn doping percentage in the study was considered at three different concentrations i.e. 2.77 %, 4%, and 8.33%. The reaction mechanism along those two pathways is as follows:



where ‘*’ indicates a chemisorption site. The possibility of both those mechanisms on the Zn doped WS₂ system was investigated. The energetically most favorable H adsorbed configurations (H-V pathway) are shown in Figure 5.1(a). Those two active sites were named site_1 and site_2 respectively. The free energy profiles of HER following the Volmer–Heyrovsky mechanism for site_1 and site_2 is shown in Figure 5.1(b). As prominent from Figure (HV pathway), the limiting potential for HER is 0.22 eV and 0.13 eV respectively for HER on site_1 and site_2. The H⁺ is found to be more strongly adsorbed on site_1. So, the reaction along the Volmer-Tafel mechanism was studied only for the *H configuration at site_1. The free energy profile of HER along the Volmer-Tafel (V-T) mechanism is shown in Figure 5.1(c). Large free energy barrier of 1.14 eV was observed towards the formation of 2*H configuration on the electrocatalyst’s surface. This indicates that the Volmer–Heyrovsky mechanism of HER is more favored on Zn doped WS₂ than the Volmer-Tafel mechanism. The

2*H configuration of the Volmer-Tafel mechanism is shown in Figure 5.1(d). The results discussed above indicate that 4% Zn doped WS₂ is an efficient electrocatalyst to carry out HER via the Volmer–Heyrovsky mechanism with substantially low overpotential value.

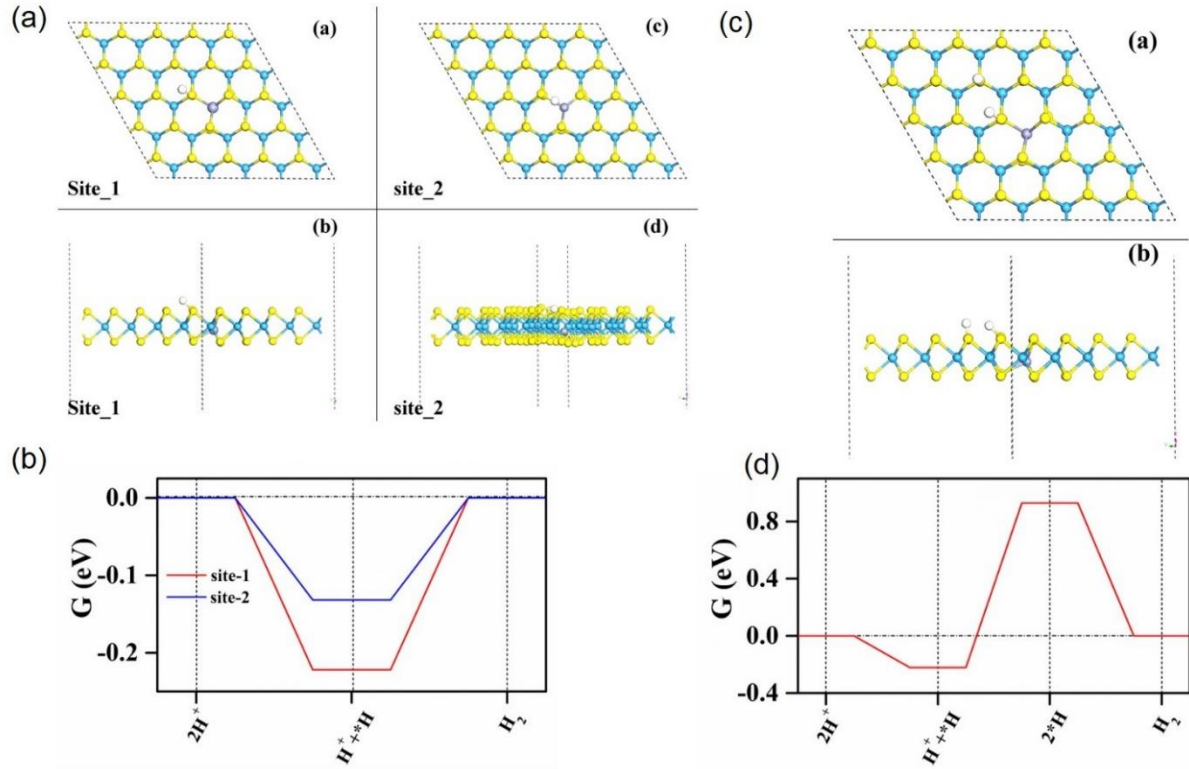


Figure 5.1: (a,b) HER Volmer–Heyrovsky (H-V) site 1 and site 2 of Zn doped-WS₂ and corresponding free energy diagram (c,d) HER Volmer–Tafel (V-T) site 1 and site 2 of Zn doped-WS₂ and corresponding free energy diagram. (W: Cyan; Zn: Violet, S: yellow, H: White).

In addition, Zn doped 2H WS₂ as the cathode electrocatalyst to carry out ORR in alkaline medium through the associative pathway is investigated thoroughly. ORR, in the associative pathway, for alkaline medium fuel cells proceeds via the following steps:





* stands for chemisorption site on the catalyst.

A (6x6) supercell of WS_2 was considered to study ORR with three different Zn percentages as 2.70%, 5.50% and 8.30%. The optimized structure of Zn doped WS_2 with 2.7% Zn doping with one active site A1 is represented in Figure 5.2(a). As for 5.5% and 8.30% Zn doping, Zn substitutes two and three W atoms within the WS_2 supercell respectively, Zn doped WS_2 has two and three possible structures depending on Zn doping position for those cases. The configurations associated with Figure 5.2(b) & 5.2(e) are energetically most stable for 5.5% & 8.3% Zn doped system respectively with two active sulfur sites A1 & A2. Formation energies along with the total optimized energies of 2.70%, 5.50% and 8.30% of Zn doped WS_2 are also represented in Figure 5.2. Formation energy calculations suggest that sulfur-rich conditions are more energetically favorable for doping compared to tungsten-rich conditions in experimental synthesis. This is supported by the lower observed formation energy in sulfur-rich conditions compared to tungsten-rich conditions.

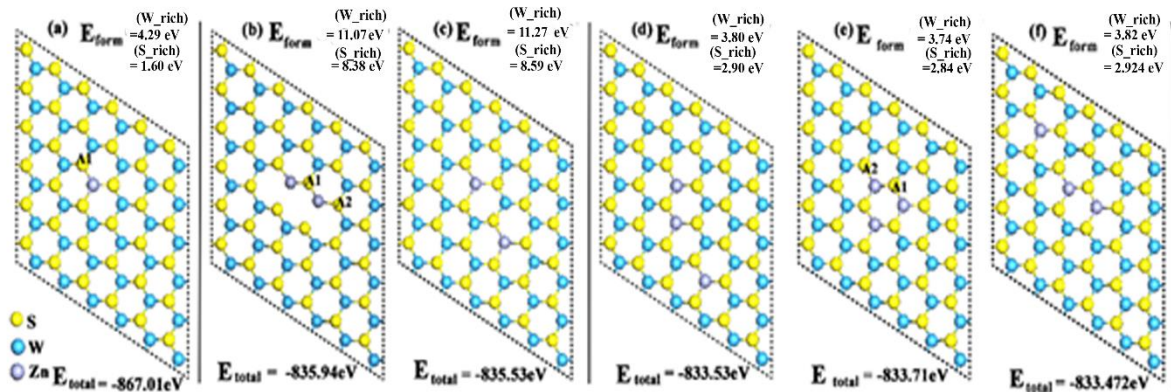


Figure 5.2: (a) 2.7% Zn doped WS_2 with only active sulfur site A1, (b) & (c) 5.5% Zn doped WS_2 with three active sites A1, A2, A3 mentioned in fig (b); (d), (e) & (f) 8.3% Zn doped WS_2 with two active sites A1 and A2 mentioned in the fig (e). Here E_{form} and E_{total} represent formation energy and total optimized energy respectively. (W: Cyan; Zn: Violet; S: yellow)

In the pristine state, WS_2 is semiconducting in nature [43] and hinders the oxygen adsorption in side-on and end-on modes both on its surface (Figure 5.6). The electronic properties of these three Zn doped structures are investigated in terms of the total density of states (TDOS) (Figure 5.4(a-c)) and partial density of states PDOS (Figure 5.4(d-f)). As WS_2 is substitutionally doped with Zn, its semiconducting nature (Figure 5.5) is converted into metallic nature that facilitates

oxygen adsorption on its surface. Spin polarization of these three systems was calculated using the formula: $P(E_F) = (((D(E_F, \uparrow) - D(E_F, \downarrow)) / (D(E_F, \uparrow) + D(E_F, \downarrow))) \times 100$, where $D(E_F, \uparrow)$ and $D(E_F, \downarrow)$ represent the values of TDOS of up and down spin respectively, at the Fermi level. Spin polarization values are 8.6%, 6.8% and 0.15% at the Fermi level for 2.7%, 5.5% and 8.3% Zn doped WS_2 structures respectively. The highest value of spin polarization obtained for 2.7% Zn doped WS_2 structure advocates better oxygen adsorption on its surface than other two Zn doped structures [44]. We also plotted the partial contribution of the most prominent orbitals for the region just above and below the Fermi level for each doped system (Figure 5.4(d-f)). The contributions of p orbitals of S (S_p) bonded to Zn and d orbitals of nearby W (W_d) atoms are most prominent at and adjacent to the Fermi level. Besides this, smaller contribution from d orbitals of Zn (Zn_d) was also found near the Fermi level. The d-band centers of the pristine WS_2 and three above mentioned doped structures were calculated and shown in TDOS plots (Figure 5.4(a-c)) to find out surface activity of these Zn doped systems. The position of d-band center for up spin and down spin of 2.7%, 5.50%, 8.30% percentages of Zn doped WS_2 and pristine WS_2 as calculated using the equation (5.5) were obtained to be -3.63 eV, -3.62 eV; -3.37 eV, -3.36 eV; -3.75 eV, -3.75 eV and -3.26 eV, -3.26 eV respectively. Initial step ORR in alkaline medium fuel cell is Oxygen molecule adsorption which occurred in side-on mode with 2.70% of Zn doped WS_2 and end-on mode with 5.50% and 8.30% of Zn doped WS_2 . All the energetically favorable oxygen adsorbed configurations are shown in Fig (5.7).

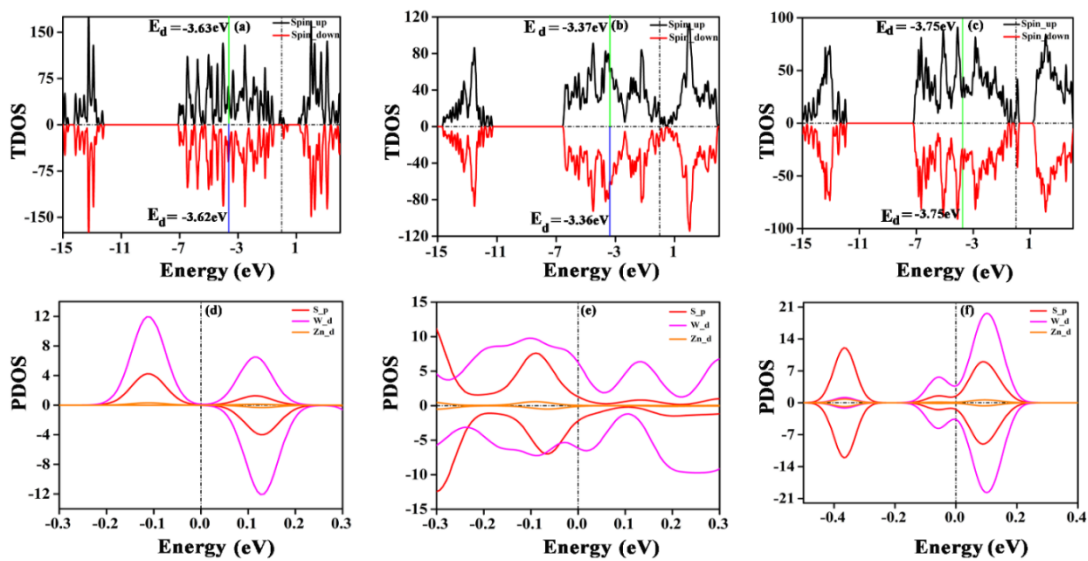


Figure 5.4: Oxygen molecule adsorbed configurations with bader charge values associated with oxygen atoms for (a) 2.7% Zn doped (b) 5.5% Zn doped (c) 8.3% Zn doped WS_2 system

respectively (W: Cyan; O: Red; Zn: Violet, S: yellow, H: White) (d)Volcano plot of Oxygen Adsorption Energy with respect to Average d-band center; Gibbs free energy profile for (e) 2.7% Zn doped (f) 5.5% Zn doped (g) 8.3% Zn doped WS₂ system respectively.

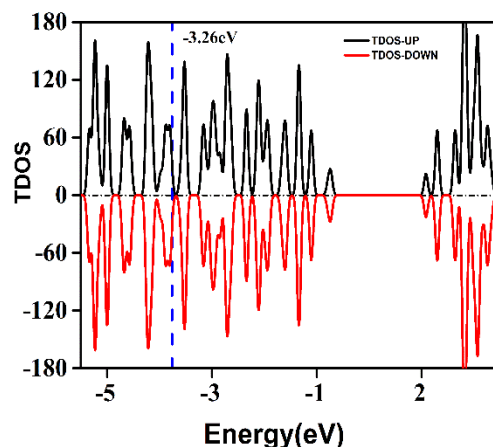


Figure 5.5: d-band center of pristine WS₂ (-3.26 eV).

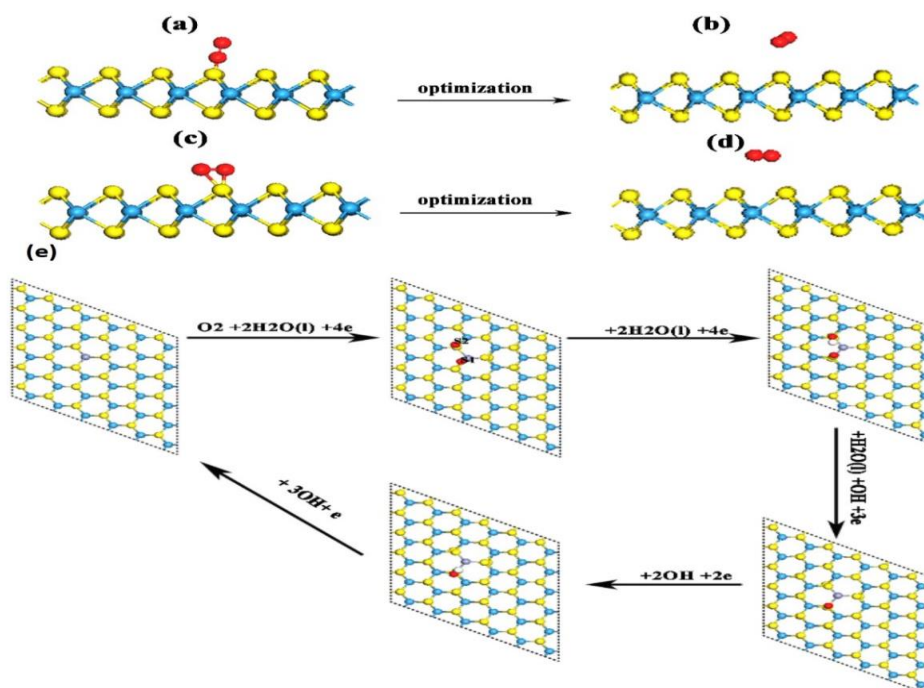


Figure 5.6: Oxygen molecule placed WS₂ in end-on mode (a) before optimization, (b) after optimization and side-on mode (c) before optimization, (d) after optimization; (W: Cyan; O: Red; Zn: Violet, S: yellow, H: White) (e) ORR pathways in alkaline medium for 2.7% Zn doped WS₂.

In 2.7% Zn doped WS₂, oxygen molecule was adsorbed following the O-O bond dissociation and two oxygen atoms were attached with two different nearby S atoms (S1 & S2 mentioned

in Figure 5.7(a)). In systems with a higher concentration of Zn doping, oxygen molecule adsorption was associative in nature with a significant amount of bond stretching (7.4%, 7.7% for 5.50% and 8.30% Zn doped WS₂ respectively) and one oxygen atom was attached with S atom remaining another oxygen atom site free. Oxygen adsorption energies of 2.70%, 5.50% and 8.30% of Zn doped WS₂ obtained from the equation (5.4) are -1.256eV, -1.186eV, -1.156eV respectively. To observe the surface activity in terms of oxygen adsorption capability, we plotted oxygen adsorption energy (essentially exothermic in nature due to negative energy values) against the averaged energies of d-band centers values which followed a volcanic nature (Figure 5.7(d)). The indicated doped structures' inclination towards Oxygen adsorption was investigated through the Bader charge analysis. Maximum Bader charge values (-1.048e and -1.0734e) observed for the oxygen atoms attached with S1 and S2 positions of 2.7% Zn doped WS₂ supports the stronger adsorption of oxygen on its surface through the O-O bond dissociation (Figure 5.7(a)). Bader charges associated with the oxygen atom attached to sulfur atom (O1) and oxygen atom (O2) at the free end of adsorbed oxygen molecule are -0.3025e, -0.1963e and -0.3074e, -0.2049e for 5.5% and 8.3 % Zn doped WS₂ structures respectively ((Figure 5.7(b-c). Lower values of Bader charges associated with the oxygen atoms of adsorbed oxygen molecules of these doped structures indicate the weaker adsorption of oxygen molecules, i.e., lower values of oxygen adsorption energies in comparison to 2.7% Zn doped WS₂.

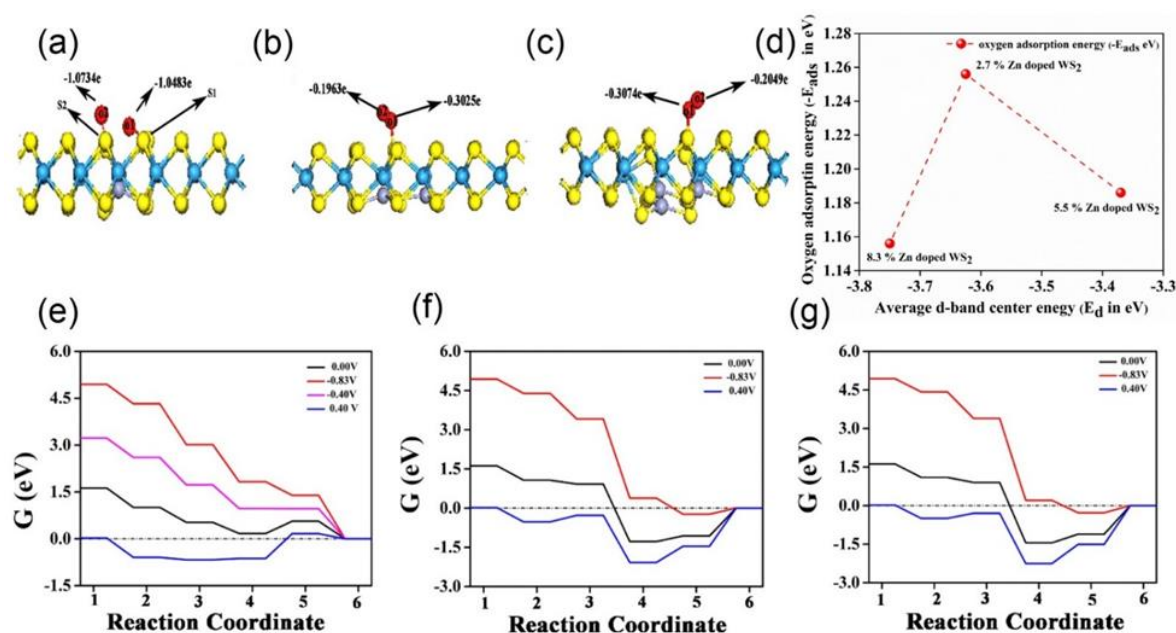


Figure 5.7: Oxygen molecule adsorbed configurations with bader charge values associated with oxygen atoms for (a) 2.7% Zn doped (b) 5.5% Zn doped (c) 8.3% Zn doped WS₂ system

respectively (W: Cyan; O: Red; Zn: Violet, S: yellow, H: White) (d) Volcano plot of Oxygen Adsorption Energy with respect to Average d-band center; Gibbs free energy profile for (e) 2.7% Zn doped (f) 5.5% Zn doped (g) 8.3% Zn doped WS₂ system respectively.

After the oxygen adsorption step, we studied the next steps of ORR in alkaline medium for the three mentioned Zn doped systems. All the calculations were carried out at electrode potential of -0.83V (0V) vs. SHE(RHE). An energetically downward trend of four electron pathways of ORR in alkaline medium was obtained for 2.7% Zn doped WS₂ at electrode potential -0.83V (0V) vs. SHE (RHE). In order to study the effect of higher concentration of Zn doping on ORR, the 5.5% and 8.3% Zn doped WS₂ configurations were also considered to investigate ORR activity. The ORR activities of all the systems are analyzed in terms of free energy values calculated with respect to the final reaction coordinate as reference. The Free energy value (G_1) corresponding to reaction coordinate 1 was found to be 4.94 eV for all the doping percentage of Zn as the initial and final products are same for all the systems. The primary and most significant step of ORR is oxygen adsorption and it was found to be energetically exothermic in nature for all the doped systems varied from 4.32 eV to 4.42 eV (Reaction coordinate 2). In the next step H₂O dissociates into H⁺ and OH⁻ ion in alkaline medium and this H⁺ ion prefers to be attached with the oxygen atom site of adsorbed O₂ molecule to form *OOH (*O+*OH) configuration. For 2.7% Zn doped WS₂, O-O bond of O₂ molecule dissociates after adsorption and gets attached to the nearby two S atoms namely S1 & S2. Now, the oxygen atom (O1) adsorbed at site S1 is energetically more favorable for H⁺ ion adsorption than the oxygen atom attached to S2 site. But, for the other two doped systems, one atom of the oxygen molecule prefers to be adsorbed on most energetically acceptable Sulfur atom site (S1), keeping another oxygen atom site free (S2). H⁺ ion gets adsorbed on this free oxygen atom site (S2). This first coupled proton electron transfer process occurred exothermically and this energy (G_3) ranges from 3.01 eV to 3.41 eV.

In the following step (Reaction coordinate 4), OH⁻ ion is released from the electrocatalyst surface to produce *O configuration. In this step, desorption of first OH⁻ ion is spontaneous for all the system and their energies (G_4) lay between 0.38eV to 1.82eV. In the next step (i.e., reaction coordinate 5), another H₂O molecule dissociates like reaction coordinate 3 and produces H⁺ and OH⁻ ions. This H⁺ ion prefers to be attached with *O and produces *OH configuration. The energy in this step (G_5) varies from -0.23 to 0.56 eV. In the last and final step (reaction coordinate 6), an electron is transferred to the adsorbate *OH to release final OH⁻ ion. Here the spontaneous nature of ORR steps was discontinued due to uplifted free energy

values found for 5.5% and 8.3 % Zn doped WS₂. But, continuous downward trend of free energy profile was only followed by a 2.7 % Zn doped system. We further varied electrode potential for 2.7 % Zn doped WS₂ to find the onset potential below which energetically spontaneous downward nature of the free energy profile of ORR discontinued (Fig. 5.7(e)). As the Onset potential value observed for this structure was -0.4V, overpotential value was calculated to be 0.8V from the equation (5.3). Reaction steps of ORR in alkaline medium are represented in Figure 5.6(e) for 2.7% Zn doped WS₂. We conclude that increase in doping percentage of Zn in WS₂ declines the ORR performance in alkaline medium.

5.4. Conclusion:

Combining theoretical calculations and electrochemical measurements, we demonstrate that Zn doped WS₂ has a superior electrochemical activity for HER and ORR compared with pure WS₂. The remarkable enhancement can be attributed to the more significant number of active sites and better conductivity. First, Zn dopant can activate the electrocatalytic activity of the S sites in the basal plane, and Zn site itself can also be the new active site; second, better conductivity for Zn-doped WS₂ can facilitate the transfer of electrons between the active sites and electrode. Therefore, this work provides a reliable strategy for designing other low-cost and high-powered transition-metal dichalcogenide electrocatalysts to exhibit four-electron ORR pathways rather than toxic H₂O₂ production at the intermediate. This work offers a feasible method to modulate the electronic structure of electrocatalysts for effective hydrogen production and oxygen reduction and provides an experience to design highly efficient earth abundant electrocatalysts for future energy applications.

References:

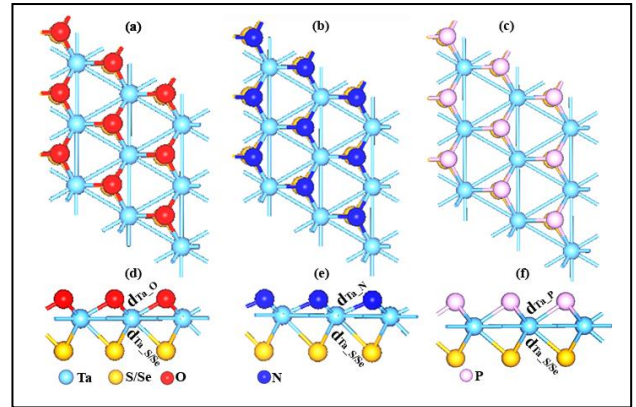
1. J. Alper Water splitting goes au nature (2003) 1686-1687.
2. Q. Liu, J. Tian, J. W. Cui, , P. Jiang, N. Cheng, A.M. Asiri, and X. Sun, , Carbon nanotubes decorated with CoP nanocrystals: a highly active non-noble-metal nanohybrid electrocatalyst for hydrogen evolution. *Angew. Chem. Int. Ed.* 53 (2014) 6710-6714.
3. L. Cheng, W. Huang, Q. Gong, C. Liu, Z. Liu, Y. Li, and H. Dai. Ultrathin WS₂ nanoflakes as a high-performance electrocatalyst for the hydrogen evolution reaction. *Angew. Chem. Int. Ed.* 126 (2014) 7994-7997.
4. B. Wolter, M.G. Pullen, M. Baudisch, M. Sclafani, M. Hemmer, A. Senftleben, C.D. Schröter, J. Ullrich, R. Moshhammer, and J. Biegert, Strong-field physics with mid-IR fields. *Phys. Rev. X.* 5 (2015) 021034.
5. N. Laosiripojana, and S. Assabumrungrat, Catalytic steam reforming of methane, methanol, and ethanol over Ni/YSZ: The possible use of these fuels in internal reforming SOFC. *J. Power Sources* 163 (2007) 943-951.
6. V. ed. Dusastre, *Materials for sustainable energy: a collection of peer-reviewed research and review articles from Nature Publishing Group.* World Scientific (2011) 171-179.
7. M. De Rosa, C. Nardini, C. Piccolo, C. Corsi, and F. D amato, Pressure broadening and shift of transitions of the first overtone of HCl. *Appl. Phys. B* 72 (2001) 245-248.
8. J. Kibsgaard, T.R. Hellstern, S.J. Choi, B.N. Reinecke, and T.F. Jaramillo, Mesoporous ruthenium/ruthenium oxide thin films: active electrocatalysts for the oxygen evolution reaction. *ChemElectroChem* 4 (2017) 2480-2485.
9. D. Kong, J.J. Cha, H. Wang, H.R. Lee, and Y. Cui, First-row transition metal dichalcogenide catalysts for hydrogen evolution reaction. *Energy Environ. Sci.* 6 (2013) 3553-3558.
10. M.S. Faber, R. Dziedzic, M.A. Lukowski, N.S. Kaiser, Q. Ding, and S. Jin, High-performance electrocatalysis using metallic cobalt pyrite (CoS₂) micro-and nanostructures. *J. Am. Chem. Soc.* 136 (2014) 10053-10061.
11. Y.H. Li, P.F. Liu, L.F. Pan, H.F. Wang, Z.Z. Yang, L.R. Zheng, P. Hu, H.J. Zhao, L. Gu, and H.G. Yang, Local atomic structure modulations activate metal oxide as electrocatalyst for hydrogen evolution in acidic water. *Nat. Commun* 6 (2015) 1-7.
12. C.G. Morales-Guio, L.A. Stern, and X Hu, Nanostructured hydrotreating catalysts for electrochemical hydrogen evolution. *Chem. Soc. Rev.* 43 (18) (2014) 6555-6569.
13. L. Liao, S. Wang, J. Xiao, X. Bian, Y. Zhang, M.D. Scanlon, X. Hu, Y. Tang, B. Liu, and H.H. Girault, *Energy Environ. Sci.* 7 (2014) 387–392

14. K. Fominykh, G.C. Tok, P. Zeller, H. Hajiyani, T. Miller, M. Döblinger, R. Pentcheva, T. Bein, and D. Fattakhova-Rohlfing, Rock salt Ni/Co oxides with unusual nanoscale-stabilized composition as water splitting electrocatalysts. *Adv. Funct. Mater* 27 (2017) 1605121.
15. J. Yin, J. Jin, H. Zhang, M. Lu, Y. Peng, B. Huang, P. Xi, and C.H. Yan, Atomic Arrangement in Metal-Doped NiS₂ Boosts the Hydrogen Evolution Reaction in Alkaline Media. *Angew. Chem. Int. Ed.* 131 (2019) 18849-18855.
16. M.A. Lukowski, A.S. Daniel, F. Meng, A. Forticaux, L. Li, and S. Jin, et al. "Enhanced hydrogen evolution catalysis from chemically exfoliated. *J. Am. Chem. Soc.* 135 (2013) 10274.
17. K. Jiang, B. Liu, M. Luo, , S. Ning, M. Peng, Y. Zhao, Y.R. Lu, T.S. Chan, F.M. de Groot, and Y. Tan, Single platinum atoms embedded in nanoporous cobalt selenide as electrocatalyst for accelerating hydrogen evolution reaction *Nat. Commun* 10. (2019) 1-9.
18. C. Liu, T. Gong, J. Zhang, X. Zheng, J. Mao, H. Liu, Y. Li, and Q. Hao, Engineering Ni₂P-NiSe₂ heterostructure interface for highly efficient alkaline hydrogen evolution. *Appl. Catal. B* 262 (2020) 118245.
19. D. Gao, J. Zhang, T. Wang, W. Xiao, K. Tao, D. Xue, and J. Ding, Metallic Ni₃N nanosheets with exposed active surface sites for efficient hydrogen evolution. *J. Mater. Chem. A*. 4 (2016) 17363-17369.
20. Q. Hao, S. Li, H. Liu, J. Mao, Y. Li, C. Liu, J. Zhang, and C. Tang, Dual tuning of nickel sulfide nanoflake array electrocatalyst through nitrogen doping and carbon coating for efficient and stable water splitting. *Catal. Sci. Technol.* 9 (2019) 3099-3108.
21. Y. Jing, X. Mu, C. Xie, H. Liu, R. Yan, H. Dai, C. Liu, and X.D. Zhang, Enhanced hydrogen evolution reaction of WS₂-CoS₂ heterostructure by synergistic effect. *Int. J. Hydrog. Energy* 44(2019) 809-818.
22. H. Tian, C. Fan, G. Liu, S. Yuan, Y. Zhang, M. Wang, and E. Li, Ultrafast broadband photodetector based on SnS synthesized by hydrothermal method. *Appl. Surf. Sci* 487 (2019) 1043-1048.
23. P.M. Pataniya, M. Tannarana, C.K. Zankat, S.A. Bhakhar, S. Narayan, G.K. Solanki, K.D. Patel, P.K. Jha, and V.M. Pathak, Low-temperature Raman investigations and photoresponse of a detector based on high-quality WSe₂ crystals. *J. Phys. Chem. C* 124 (2020) 2251-2257.
24. H. Tian, C. Fan, G. Liu, S. Yuan, Y. Zhang, M. Wang, and E. Li, Ultrafast broadband photodetector based on SnS synthesized by hydrothermal method. *Appl. Surf. Sci* 487 (2019) 1043-1048.
25. R. Roy, R. Thapa, S. Biswas, S., Saha, U.K. Ghorai, D. Sen, E.M. Kumar, G.S. Kumar, N. Mazumder, D. Roy and K.K. Chattopadhyay, Resonant energy transfer in a van der Waals stacked MoS₂-functionalized graphene quantum dot composite with ab initio validation. *Nanoscale*, 10(35) (2018) 16822-16829.

26. J.Y. Xue, F.L. Li, Z.Y. Zhao, C. Li, C.Y. Ni, H.W. Gu, D.J. Young, and J.P. Lang, In situ generation of bifunctional Fe-doped MoS₂ nanocanopies for efficient electrocatalytic water splitting. *Inorg. Chem.* 58 (2019) 11202-11209.
27. B. Hinnemann, P.G. Moses, J. Bonde, K.P. Jørgensen, J.H. Nielsen, S. Horch, I. Chorkendorff, and J.K. Nørskov, Biomimetic hydrogen evolution: MoS₂ nanoparticles as catalysts for hydrogen evolution. *J. Am. Chem. Soc.* 127 (2005) 5308-5309.
28. D. Roy, S. Sarkar, K. Bhattacharjee, K.; Panigrahi, B.K. Das, K. Sardar, S. Sarkar, K.K. Chattopadhyay, Site specific nitrogen incorporation in reduced graphene oxide using imidazole as a novel reducing agent for efficient oxygen reduction reaction and improved supercapacitive performance. *carbon* 166 (2020) 361-373.
29. D. Roy, K. Panigrahi, B.K. Das, U.K. Ghorui, S. Bhattacharjee, M. Samanta, S. Sarkar, K.K. Chattopadhyay, Boron vacancy: a strategy to boost the oxygen reduction reaction of hexagonal boron nitride nanosheet in hBN–MoS₂ heterostructure. *Nanoscale Adv.* 3 (2021) 4739-4749.
30. L. Zeng, K. Sun, X. Wang, Y. Liu, Y. Pan, Z. Liu, D. Cao, Y. Song, S. Liu, and C. Liu, Three-dimensional-networked Ni₂P/Ni₃S₂ heteronanoflake arrays for highly enhanced electrochemical overall-water-splitting activity. *Nano Energy* 51 (2018) 26-36.
31. S.R. Kadam, A.N. Enyashin, L. Houben, R. Bar-Ziv, and M. Bar-Sadan, Ni–WSe₂ nanostructures as efficient catalysts for electrochemical hydrogen evolution reaction (HER) in acidic and alkaline media. *J. Mater. Chem. A.* 8.3 (2020) 1403-1416.
32. D. Escalera-López, Y. Niu, J. Yin, K. Cooke, N.V. Rees, and R.E. Palmer, Enhancement of the hydrogen evolution reaction from Ni–MoS₂ hybrid nanoclusters. *ACS Catal* 6 (2016) 6008-6017.
33. S.R. Kadam, A.N. Enyashin, L. Houben, R. Bar-Ziv, and M. Bar-Sadan, Ni–WSe₂ nanostructures as efficient catalysts for electrochemical hydrogen evolution reaction (HER) in acidic and alkaline media. *J. Mater. Chem. A.* 8 (2020) 1403-1416.
34. P. Hu, G. Long, A. Chaturvedi, S. Wang, K. Tan, Y. He, L. Zheng, G. Liu, Y. Ke, Y. Zhou, and H. Jiang, Agent-assisted VSSe ternary alloy single crystals as an efficient stable electrocatalyst for the hydrogen evolution reaction. *J. Mater. Chem. A.* 7 (2019) 15714-15721.
35. G. Kresse, J. Hafner, Ab initio molecular dynamics for liquid metals, *Phys. Rev. B.*, 47 (1993) 558.
36. G. Kresse, J. Furthmüller, J. Hafner, Theory of the crystal structures of selenium and tellurium: the effect of generalized-gradient corrections to the local-density approximation, *Phys. Rev. B.* 50 (1994) 13181.
37. G. Kresse, J. Furthmüller, Efficiency of ab-initio total energy calculations for metals and semiconductors using a plane-wave basis set, *Comput. Mater. Sci.* 6 (1996) 15-50.

38. G. Kresse, J. Furthmüller, Efficient iterative schemes for ab initio total-energy calculations using a plane-wave basis set, *Phys. Rev. B.* 54 (1996) 11169.
39. J.J. Mortensen, L.B. Hansen, K.W. Jacobsen, Real-space grid implementation of the projector augmented wave method, *Phys. Rev. B.* 71 (2005) 035109.
40. J.P. Perdew, K. Burke, M. Ernzerhof, Generalized gradient approximation made simple, *Phys. Rev. Lett.*, 77 (1996) 3865.
41. S. Grimme, Semiempirical GGA-type density functional constructed with a long-range dispersion correction, *J. Comput. Chem.* 27 (2006) 1787-1799.
42. K. Mathew, R. Sundararaman, K. Letchworth-Weaver, T. Arias, R.G. Hennig, Implicit solvation model for density-functional study of nanocrystal surfaces and reaction pathways, *Chem. Phys.* 140 (2014) 084106.
43. J.F. Felix, A.F. Da Silva, S.W. Da Silva, F. Qu, B. Qiu, J. Ren, W.M. De Azevedo, M. Henini, C.-C. Huang, A comprehensive study on the effects of gamma radiation on the physical properties of a two-dimensional WS₂ monolayer semiconductor, *Nanoscale Horiz.* 5 (2020) 259-267.
44. H. Li, J. Wang, R. Qi, Y. Hu, J. Zhang, H. Zhao, J. Zhang, Y. Zhao, Enhanced Fe 3d delocalization and moderate spin polarization in FeNi atomic pairs for bifunctional ORR and OER electrocatalysis, *Appl. Catal. B* , 285 (2021) 119778.
45. C. Lee, B.G. Jeong, S.J. Yun, Y.H. Lee, S.M. Lee, M.S. Jeong, Unveiling defect-related Raman mode of monolayer WS₂ via tip-enhanced resonance Raman scattering. *ACS nano* 12 (2018) 9982-9990.
46. R. Bhandavat, I. David, L. and G. Singh, Synthesis of surface-functionalized WS₂ nanosheets and performance as Li-ion battery anodes *J. Phys. Chem. Lett.*, 3(11) (2012) 1523-1530.

6. Vibrational, thermal, electronic and optical properties of TaXY Janus monolayers (X= S, Se; Y= O, N, P): A First-principles Study



6.1. Introduction:

In the realm of nanomaterials, two-dimensional (2D) structures have emerged as exceptional candidates for revolutionary technological applications. The groundbreaking discovery of single-layer graphene and its extraordinary properties [1] ignited a surge of interest in exploring ultrathin two-dimensional (2D) materials. Despite possessing numerous exceptional physical, mechanical, and physicochemical properties, graphene faces drawbacks due to its lack of an intrinsic band gap, limiting its application in optoelectronic devices [2] [3]. In efforts to overcome these limitations, researchers have consistently sought alternative graphene-like structures, resulting in the discovery of various 2D nanostructures such as Silicene [4], Germanene [5], Stanene [6], MXenes [7], 2D binary monolayers [8] and Transition Metal Dichalcogenides (TMDs) [9]. In this context, two-dimensional transition metal chalcogenides play a vital role, showcasing a range of electronic properties from semiconducting and semi-metallic to superconducting [10] [11] [12]. This electronic versatility arises from the distinctive characteristics of well-known TMD phases, such as 2H [13], 1T [14], and 1T' [15] each with unique electronic properties and configurations. In transition metal dichalcogenides (MX_2), the transition metal (M) is positioned between two identical chalcogenide atoms (X). However, when one of the chalcogenide atoms (X) in a layer is replaced with another element (Y), it results in the formation of MXY with distinct faces on both the top and bottom sides of the transition metal. This configuration is termed a Janus material, reflecting its characteristic of having dissimilar faces on either side [16] [17]. The Janus structure introduces an asymmetry that can lead to unique and tunable properties, making it of particular interest for various applications in materials science and nanotechnology [18] [19]. Among the TMDs MoS_2 ,

MoSe₂, WS₂, WSe₂ are very well known due to their tuning electronic, optical, catalytic properties by external atoms doping, creating hetero structure, defect and strain engineering [20] [21] [22] [23]. Y C cheng et al. breaks the symmetry of these Mo and W based dichalcogenides by replacing one of the chalcogenide layers by another chalcocogen and observed enhanced Rashba splitting that has potential application in Spintronics [24]. Dipesh B. Trivedi et. al. successfully synthesized WSSe and MoSSe monolayers and their hetero structures in room temperature [25]. Yin Qin et. al. also tried to synthesize SWSe, SNbSe and SMoSe by in situ Deterministic growth [26]. This recent advancements in Janus structure synthesis have brought optimism and promise to experimental research, sparking a heightened interest in utilizing computational methods for predicting future Janus materials. Despite the extensive studies on TaS₂ and TaSe₂, particularly concerning charge density wave (CDW) [27] [28] and superconductivity [29], the exploration of their Janus forms has been comparatively limited. Z. Kharaman et al. successfully predicted the stability of Janus material in TaSe₂ by surface functionalization using Hydrogen and Fluorine [30]. Wenwu Shi et. al studied mechanical and electronic properties of large range Transition metal dichalcogenide based janus monolayers including TaSSe, TaSTe, TaSeTe using first-principles calculations using DFT [31]. Similarly, Kiana Falahati et. al. predicted WSC, WSN, WSP, WSAs, WSO monolayers and compared with WS₂, WSSe and WSTe monolayers to observe light matter interaction [32]. M. Jahangirzadeh Varjovi et al. also investigated vibrational, thermal and electronics properties of 2H, 1T and 1T' phases of WSO, WSeO and WTeO monolayers using First-principles investigation [33]. These comprehensive studies provide inspiration for our research, where we aim to explore the mechanical stability, vibrational, thermal, electronic, and optical properties of Janus materials based on tantalum, specifically TaSN, TaSO, TaSP, TaSeN, TaSeO, and TaSeP.

6.2. Computational Methods:

Our first-principles computations utilized the Cambridge Sequential Total Energy Package (CASTEP) code [34], employing a supercell methodology within the framework of density functional theory. For the exchange and correlation terms, the Perdew–Burke–Ernzerhof (PBE) functional [35] under the generalized gradient approximation (GGA) was applied. Vanderbilt norm-conserving pseudopotentials [36] accurately represented tantalum, sulphur, selenium, oxygen, nitrogen and phosphorus. The calculation utilized plane waves with an energy cutoff set at 500 eV, ensuring a comprehensive representation of the electronic structure. Geometrical

optimization was facilitated by allowing the system to fully relax through the BFGS (Broyden–Fletcher–Goldfarb–Shanno) scheme [37]. The optimization process continued until the total energy converged to less than 2×10^{-5} eV/atom, the maximum force converged to lower than 0.05 eV/Å, and the maximum displacement was constrained to 0.002 Å. Brillouin zone integrations were performed using the Monkhorst Pack scheme [38], employing a $20 \times 20 \times 1$ k-point mesh for the fine structure optimization, while the rest of the calculations utilized a $5 \times 5 \times 1$ k-point mesh for all the unit cells of Janus structures. To avoid any artificial interactions between adjacent images, a vacuum spacing of approximately 20 Å was established in the nonperiodic direction. It is noteworthy that all calculations were carried out in a spin-unrestricted manner, allowing for a comprehensive exploration of electronic properties in the system. The strength of atomic binding in the Janus structures is characterized by the cohesive energy (E_C), which is computed using the following equation [33]:

$$E_C = \frac{N_{Ta}E_T(Ta) + N_XE_T(X) + N_YE_T(Y) - E_T(TaXY)}{(N_{Ta} + N_X + N_Y)} \quad (6.1)$$

Here, $E_T(Ta)$ total energy of isolated Ta atom, $E_T(X)$ total energy of X atom (where X can be S, Se atoms) and $E_T(Y)$ total energy of Y atom (where Y can be O, N or P). Similarly, N_{Ta} , N_X and N_Y represent total no of Ta, X and Y atom respectively in a particular Janus structure. $E_T(TaXY)$ represents the total energy of the Janus structure composed of Ta, X, and Y atoms. The mechanical stability and elastic coefficients of these materials were assessed using the VASPKIT software [39], which is built upon VASP [40, 41, 42, 43] utilizing the PAW [44] approach and incorporating the PBE functional [35] within the GGA approximation. The elastic strain energy per unit area can be represented using the strain-energy method as follows [45]:

$$\Delta E(S, \{\varepsilon_i\}) = S_0(C_{11}\varepsilon_1^2 + C_{22}\varepsilon_2^2 + 2C_{12}\varepsilon_1\varepsilon_2 + 2C_{16}\varepsilon_1\varepsilon_6 + 2C_{26}\varepsilon_2\varepsilon_6 + C_{66}\varepsilon_6^2) \quad (6.2)$$

The expression for C_{ij} , which represents the second partial derivative of the strain energy E with respect to strain ε , is given by:

$$C_{ij} = \frac{1}{S_0} \frac{\partial^2 E}{\partial \varepsilon_i \partial \varepsilon_j} \quad (6.3)$$

where S_0 is the equilibrium area of 2D material. Seven strain structures were considered for calculating elastic coefficients.

6.3. Result and discussion:

6.3.1. Atomic Structure and stability:

To develop monolayers of TaXY, with X denoting S or Se and Y representing O, N, or P, the process commences by optimizing the 2H phase of TaS₂ and TaSe₂ monolayers. Following this optimization, the next step involves substituting the top layer of S and Se atoms with O, N, and P atoms. This substitution results in the formation of distinct monolayer configurations, namely TaSO, TaSN, TaSP, TaSeO, TaSeN, and TaSeP, each tailored to specific compositions and exhibiting unique properties. This systematic approach ensures the successful generation of versatile TaXY monolayers with targeted elemental combinations.

Table 6.1: Lattice Parameters (a, b), Bond lengths ($d_{\text{Ta-X/Y}}$), Cohesive energy (E_C), Elastic constants (C_{11} , C_{12} , C_{66}) of TaXY monolayers are presented.

Crystal Structure	a (Å)	b (Å)	$d_{\text{Ta-X}}$ (Å)	$d_{\text{Ta-Y}}$ (Å)	E_C (eV/atom)	C_{11} (N/m)	C_{12} (N/m)	C_{66} (N/m)
TaSO	3.04	3.04	2.42	2.03	6.71	65.00	204.00	-70.00
TaSN	3.11	3.11	2.49	1.99	7.60	177.25	61.77	115.48
TaSP	3.39	3.39	2.52	2.40	6.78	86.98	26.15	60.83
TaSeO	3.10	3.10	2.49	2.04	6.39	13.92	229.71	-107.92
TaSeN	3.17	3.17	2.59	2.00	6.21	170.36	58.73	55.18
TaSeP	3.45	3.45	2.63	2.39	5.43	84.61	20.78	31.93

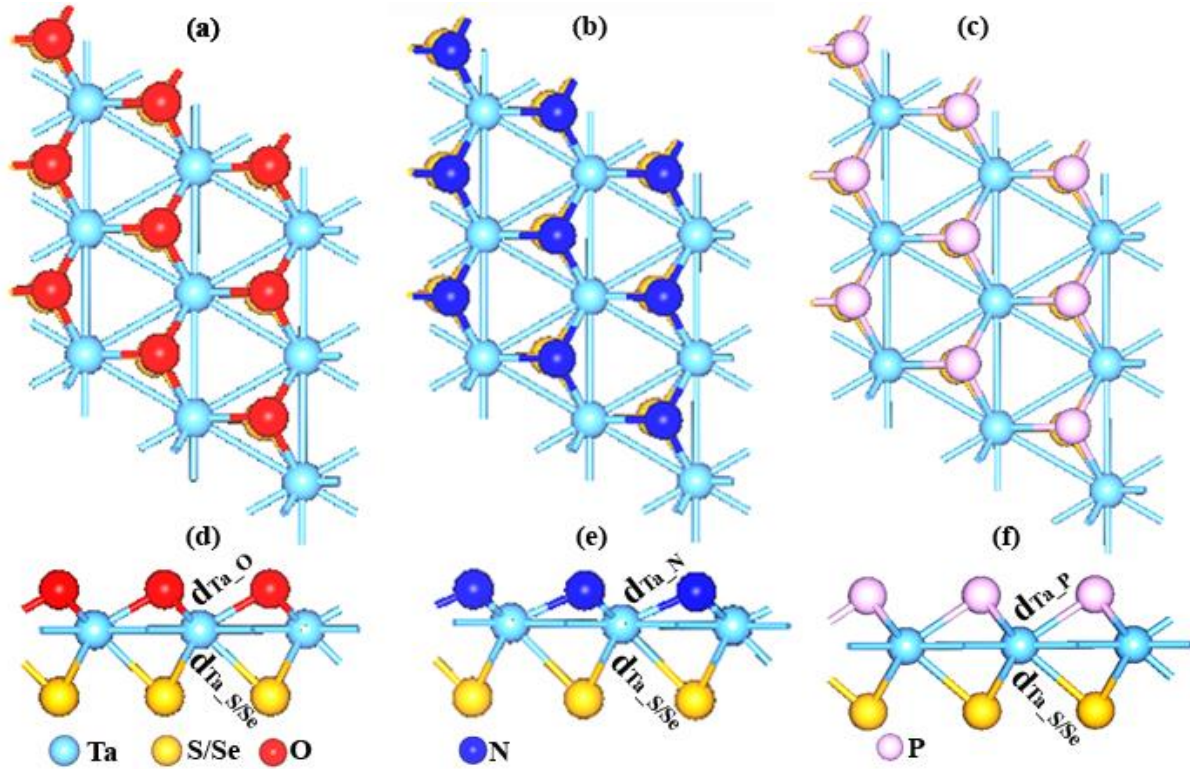


Figure 6.1: Top (a, b, c) and Side (d, e, f) views of TaXY monolayers (where X= S/Se and Y = O, N, P)

The top view and side views of these six Janus monolayers are depicted in figure (6.1). The lattice parameters of TaXY monolayers (where $a = b$ in Å) increase when the Y atom (O, N, P) changes, corresponding to a particular X atom (S/Se) as observed from the Table 6.1. Bond lengths between Ta and X ($d_{\text{Ta-X}}$) as well as Ta and Y atoms ($d_{\text{Ta-Y}}$) are summarized in Table 6.1. The cohesive energy per atom for all the Janus structures is calculated using Equation (6.1) to investigate strength of the atomic binding and thermodynamic stability. Notably, TaSN exhibits the highest cohesive energy at around 7.60 eV/atom, while TaSeP has the lowest cohesive energy at nearly 5.43 eV/atom, as indicated in Table 6.1. All the Janus materials are thermodynamically stable due to their high cohesive energy values.

Furthermore, the elastic constants of TaXY monolayers are evaluated to examine structural mechanical stability. The second-order elastic constants (SOECs) play a crucial role in determining the mechanical and dynamical properties of materials, particularly their stability and stiffness. The calculated elastic constants using Equation (6.2) are listed in Table 6.1. For the 2D hexagonal structure, there are two independent elastic constants C_{11} and C_{12} , while the non-independent elastic constant is determined as $C_{66} = \frac{C_{11} - C_{12}}{2}$. All the elastic constants must

satisfy all the equilibrium conditions $C_{11}C_{12} - C_{12}^2 > 0$ and $C_{11}, C_{22}, C_{12} > 0$ to confirm mechanical stability of 2D hexagonal structure. However, TaSO and TaSeO do not satisfy these conditions, indicating mechanical instability. On the other hand, TaSN, TaSP, TaSeN, and TaSeP are identified as mechanically stable as they fulfill all of these equilibrium conditions.

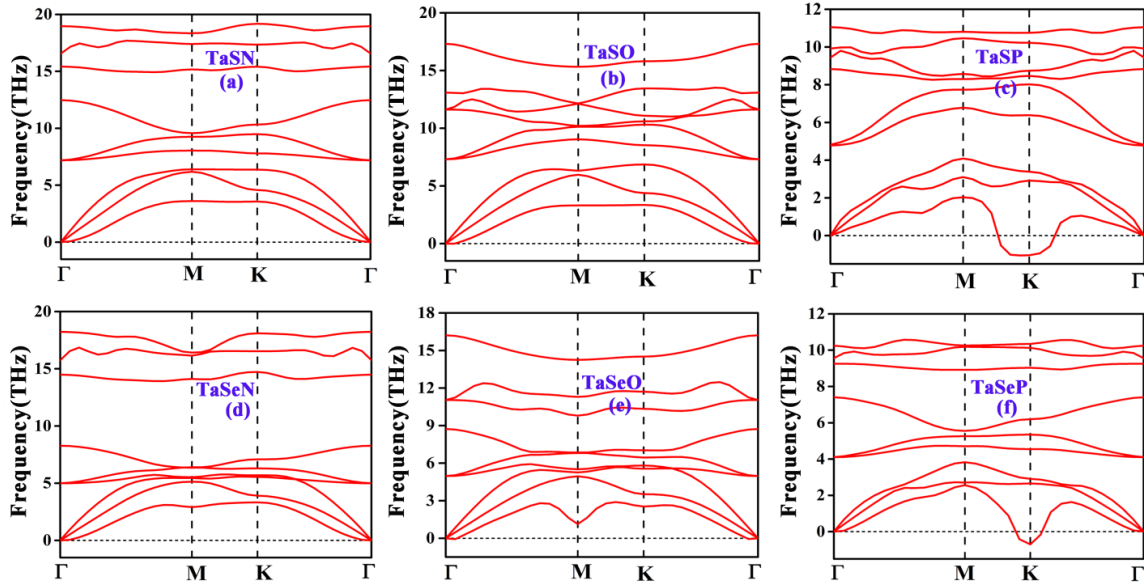


Figure 6.2: (a), (b), (c), (d), (e) & (f) representing Phonon dispersion curves of TaSN, TaSO, TaSP, TaSeN, TaSeO & TaSeP respectively.

To further evaluate dynamical stability, the phonon dispersion curves of the mentioned Janus structures are illustrated in the figure (6.2), arranged in ascending order of the average mass of the crystals ($\text{TaSN} < \text{TaSO} < \text{TaSP} < \text{TaSeN} < \text{TaSeO} < \text{TaSeP}$). As the mass of the systems increases, the highest frequency of vibrations of phonons decreases, resulting in TaSN exhibiting the highest frequency of vibration, while TaSeP demonstrates the lowest frequency of vibrations. Each Janus system comprises three atoms in the unit cell, contributing to three acoustical modes and six optical modes in each phonon dispersion curve. Remarkably, among the Janus structures, TaSP and TaSeP display imaginary frequencies near the K point in the figure (6.2(c) & 6.2(f)), suggesting dynamic instability in their structures. However, TaSeP demonstrates a comparatively lower imaginary frequency than TaSP, indicating better stability in its structure. All other Janus structures are dynamically stable, showing no negative frequencies of vibration. The observed forbidden gap between the acoustical and optical branches is influenced by the mass difference between the constituent atoms. TaSeN and TaSeO have a smaller mass difference among constituent atoms than TaSN and TaSO, mainly because the Se atom is heavier than the S atom. Consequently, this leads to the convergence of

acoustical and optical branches of phonons in TaSeN and TaSeO without a distinct forbidden gap.

In summary, the above analyses indicate that TaSO and TaSeO are mechanically stable but dynamically unstable, suggesting a metastable phase and the possibility for synthesis in a free-standing mode [46]. TaSN and TaSeN are both mechanically and dynamically stable, while TaSP and TaSeP are mechanically stable but dynamically unstable in nature.

6.3.2. Thermal conductivity:

The inherent elastic and dynamic stability observed in TaSN and TaSeN prompted us to evaluate their potential for thermal device applications. Consequently, we applied the Slack model and the Debye-Callaway model to calculate and compare their thermal conductivity. Lattice thermal conductivity according to Slack equation [47] is given by

$$k_l = A \frac{M_a \Theta_D^3 N^{1/3} \delta}{\gamma^2 T} \quad (6.4)$$

where M_a is the average mass of the atoms, Θ_D is the Debye temperature, N is the no of atoms in the cell, δ^2 is the unit-cell area per atom, γ is the Grüneisen parameter, T is the temperature in Kelvin and greater than Θ_D . Debye temperature in two dimensional materials [48] can be expressed like this

$$\Theta_D = \frac{h v_s}{2\pi k_B} \frac{(4\pi N)^{1/2}}{S^{1/2}} \quad (6.5)$$

where h , v_s , k_B , N and S represent plank constant, sound velocity, Boltzman constant, no of atoms per unit cell, S area of 2D material.

The velocity of sound can be calculated as

$$v_s = \left[\frac{1}{3} \left(\frac{1}{v_l^3} + \frac{2}{v_t^3} \right) \right]^{1/3} \quad (6.6)$$

After obtaining the Bulk Modulus (B) as the in-plane stiffness coefficient of 2D materials, expressed in units of N/m [48], the Shear Modulus (G) in N/m, and Poisson's ratio (ν) using VASPKIT software, we can calculate the sound velocities along the longitudinal acoustical direction (v_l) and transverse acoustical direction (v_t) [48]. Additionally, Grüneisen parameter (γ) [49] can be evaluated using the following equation:

$$v_l = \sqrt{\frac{B+G}{\rho}} \quad (6.7)$$

$$v_t = \sqrt{\frac{G}{\rho}} \quad (6.8)$$

where ρ represents areal mass density of the 2D material

$$\gamma = \frac{3(1+\nu)}{2(2-3\nu)} \quad (6.9)$$

In accordance with Slack's theory, Debye temperature plays a crucial role in comprehending and predicting the thermal conductivity of materials. A lower Debye temperature implies diminished efficiency in thermal transport, signifying a reduced capacity for the material to conduct heat effectively. Conversely, higher Debye temperatures signal enhanced conductivity. As per Table 6.2, the Debye temperatures for TaSN and TaSeN are 426.57K and 382.19K respectively. The observed higher Debye temperature for TaSN, suggests that the thermal conductivity of TaSN surpasses that of TaSeN. The thermal conductivity values for TaSN and TaSeN, derived from Equation (6.4), are approximately 23 W/mK and 21 W/mK, respectively, at a temperature of 450 K. This specific temperature was chosen as it exceeds the Debye temperature for both materials.

Table 6.2: Bulk Modulus (B), Shear Modulus (G), Poisson's ratio (ν), areal mass density (ρ), longitudinal velocity (v_l), transverse velocity (v_t), Debye temperature (Θ_D), Grüneisen parameter (γ) for TaSN and TaSeN monolayers are presented.

Material	B (N/m)	G (N/m)	ν	ρ (kg/m ²)	v_l (km/s)	v_t (km/s)	Θ_D (K)	γ
TaSN	119.51	57.74	0.35	2.15×10^{-6}	9.07	5.17	426.57	2.13
TaSeN	114.55	55.82	0.34	2.5×10^{-6}	8.25	4.72	382.19	2.05

The thermal conductivities of TaSN and TaSeN were further determined using Modified Debye–Callaway (MDC) model, as formulated by Asen-Palmer [50, 51] and integrated into the AICON code [52]. This model involves the calculation of thermal conductivity by considering the average contributions from acoustic and optical branches based on their specific heat. In the AICON2 code [53], modifications were made to the contributions from optical phonon branches in the calculation of lattice thermal conductivity. This adjustment was implemented to enhance the accuracy of predictions, particularly for materials characterized

by low thermal conductivity. The thermal conductivity of penta-graphene at room temperature, estimated using this code, is approximately 568 W/mK, which closely matches the value calculated using the highly accurate approach implemented in the ShengBTE code [54]. Additionally, another report using the AICON code estimated the lattice thermal conductivity for penta-BCN as 98 W/mK [55]. Notably, the AICON code offers low computational cost compared to ShengBTE while still providing reliable and accurate results. In employing the MDC approach, the final value of lattice thermal conductivity (k_l) is evaluated using AICON2 after determining the necessary parameters such as the Debye temperature (θ_D), phonon velocity (v), and Grüneisen parameter (γ) through quasiharmonic approximation [53] with the assistance of the PHONOPY code [56]. Furthermore, this software package has the capability to compute phonon-phonon relaxation times associated with various scattering mechanisms, including the Normal process (N), Umklapp process (U), and Isotope (ISO) scattering for two transverse acoustical branches (TA, TA'), one longitudinal acoustical branch (LA), and one pseudo-optic branch (O) – an average of all optical branches. The alterations in contributions from the TA, TA', LA, and O mode phonon branches in both N-process and U-process scattering are illustrated against temperature in figure 3((a)-(d)). Relaxation times corresponding to Isotope scattering effect for different phonon branches (TA, TA', LA and O) of TaSN and TaSeN are independent of temperature. This relaxation time functionality is crucial for a more in-depth exploration of heat transfer phenomena. The total relaxation time, as depicted in figure (6.3) for TaSN, is higher than for TaSeN, implying that TaSeN attributes more scattering effect compared to TaSN. This enhancement of scattering effect in TaSeN hinders the propagation of heat through this material, resulting in lower thermal conductivity. The thermal conductivity decreases with an increase in temperature for both TaSN and TaSeN, as illustrated in figure (6.4). The room temperature thermal conductivities for TaSN and TaSeN, determined through the specified method, are 29.71 W/mK and 0.38 W/mK, respectively. Nevertheless, for the purpose of comparison with Slack's model, the thermal conductivities of TaSN and TaSeN assessed at 450K in Debye-Callyway method are reported as 18 W/mK and 0.23 W/mK respectively. The noticeable deviation observed in the Slack model and Debye-Callyway model for TaSeN, compared to TaSN, can be attributed to the amalgamation of optical and acoustical branches. These merging results in an augmented scattering effect, a factor not accounted for in the Slack model, which exclusively considers acoustical modes. In systems where a forbidden gap exists, thermal conductivity mainly relies on the characteristics of low-frequency acoustical branches due to less scattering of phonons in higher wavelengths. Conversely, when acoustical and optical branches merge, it leads to

increased scattering and reduced thermal conductivity [57, 58]. Therefore, TaSeN, with its merged branches and the absence of a forbidden gap, is expected to have relatively lower thermal conductivity due to increased scattering effects. On the other hand, TaSN demonstrates relatively better thermal conductivity due to the presence of a forbidden band gap, which enhances its thermal conductivity.

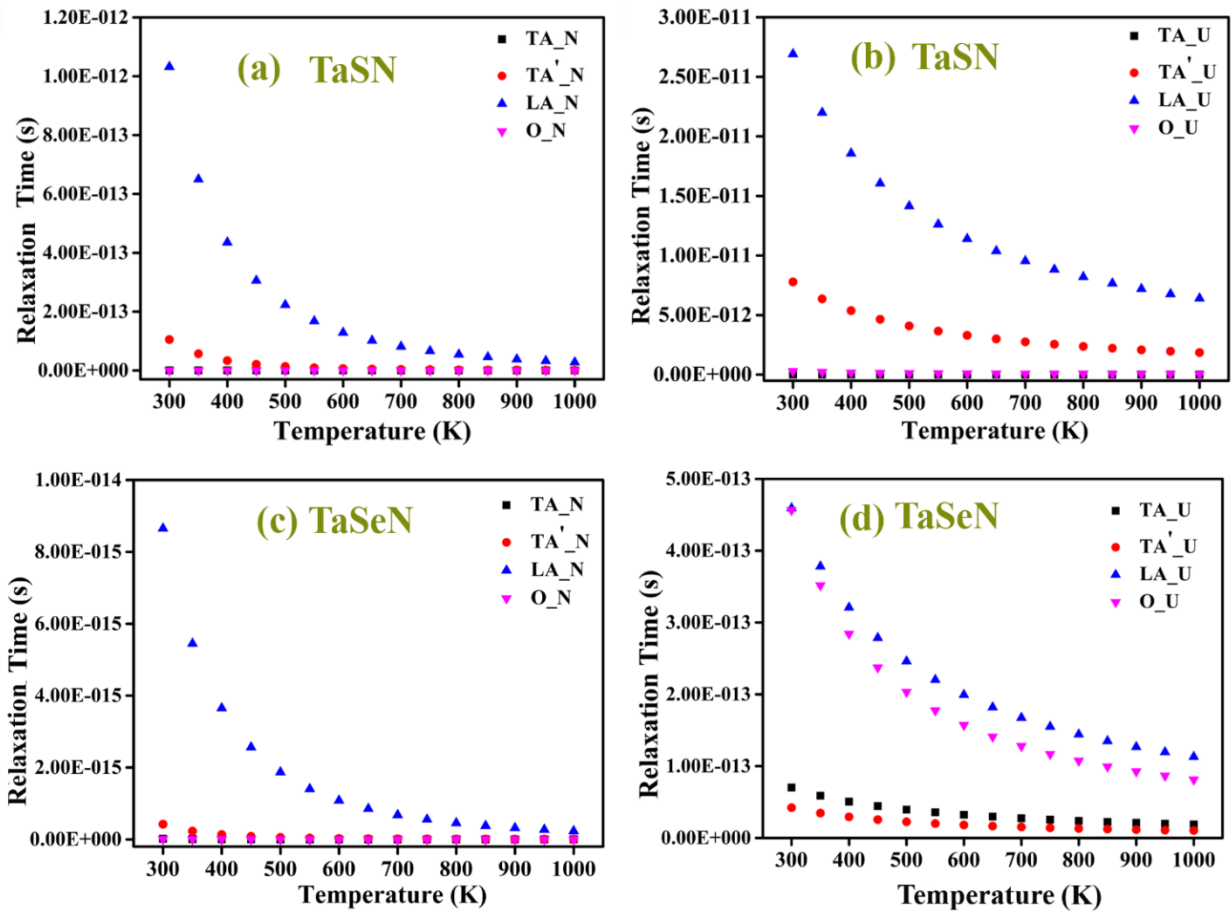


Figure 6.3: (a), (c) representing variations of Relaxation time with temperature for N- process scattering of TaSN and TaSeN respectively; (b), (d) representing variation of phonon relaxation time with temperature for U- process scattering of TaSN and TaSeN respectively.

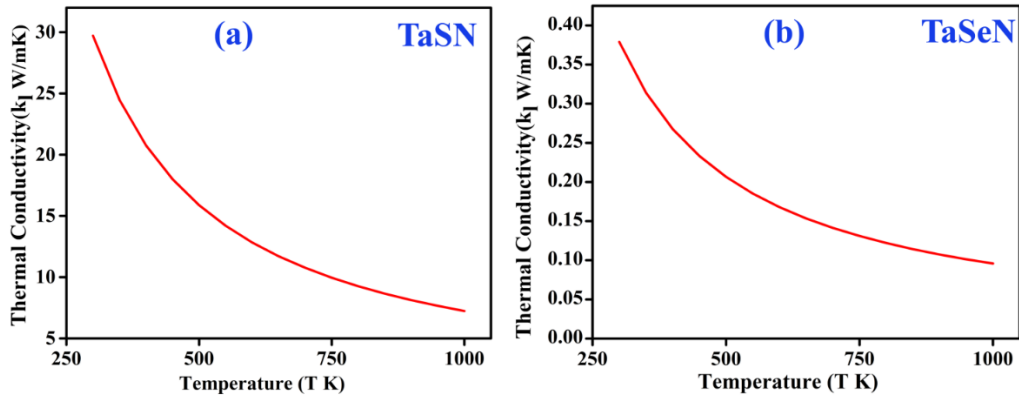


Figure 6.4: Variation of lattice thermal conductivity of TaSN ((a)) and TaSeN ((b)) respectively.

6.3.3. Electronic Properties:

The electronic band structure, calculated using the GGA-PBE method, is illustrated in figure (5). Upon scrutinizing these band structures, it is observed that TaSO and TaSeO exhibit metallic characteristics. In contrast, TaSN and TaSeN are identified as both direct and indirect band gap semiconductors, with band gap values of 0.64 eV and 0.07 eV, respectively. On the other hand, TaSP and TaSeP are classified as indirect band gap semiconductors, with band gap values of 0.45 eV and 0.77 eV, respectively. As the generalized gradient approximation (GGA) tends to underestimate the band gap, we opted to compute the electronic band structures of these six Janus structures using the HSE method (figure 6.6). Our analysis revealed no alteration in the metallic character of the TaSO and TaSeO band structures. However, TaSN and TaSeN exhibited a transition to indirect band gap semiconductors, with band gaps of 1.42 eV and 0.63 eV, respectively. Similarly, TaSP and TaSeP displayed direct band gaps, measuring 1.00 eV and 1.21 eV, respectively.

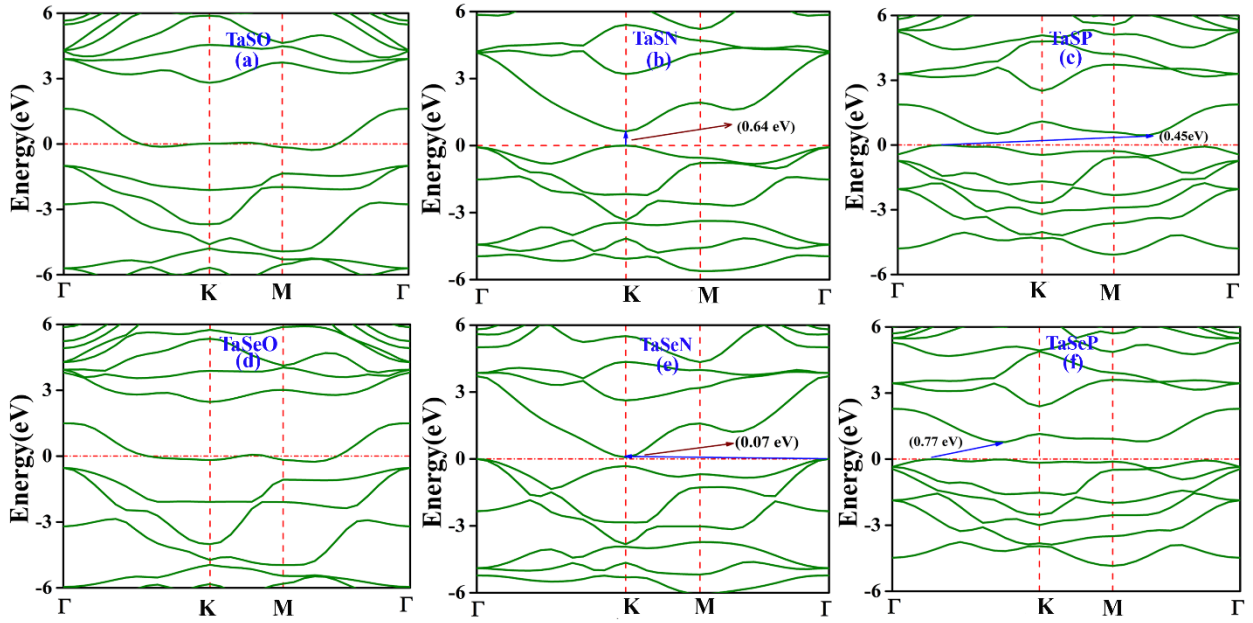


Figure 6.5: (a), (b), (c), (d), (e) & (f) representing Band Structures of TaSO, TaSN, TaSP, TaSeO, TaSeN & TaSeP obtained using GGA method.

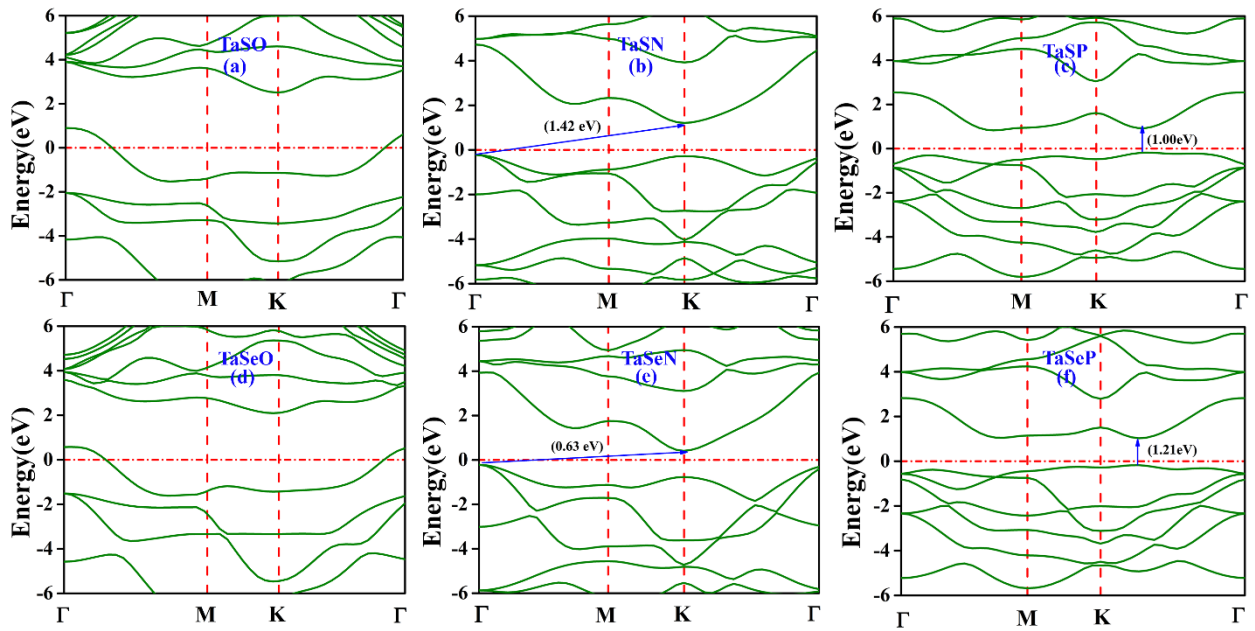


Figure 6.6: (a), (b), (c), (d), (e) & (f) representing Band Structures of TaSO, TaSN, TaSP, TaSeO, TaSeN & TaSeP obtained using HSE method.

6.3.4. Vibrational Properties:

Raman spectroscopy serves as a valuable tool in the exploration of lattice symmetries and phase-dependent properties in crystals at the Γ point. TaSO and TaSeO showcase metallic properties, suspending any discernible Raman Effect. In contrast, the remaining four Janus structures derived from nitrogen and phosphorus (TaSN, TaSeN, TaSP, and TaSeP), exhibit semiconducting behavior and present distinctive Raman spectra. Group theoretical calculations outlined in S2 indicate that these four Janus monolayers share C_{3v} symmetry. In their phonon spectra, the irreducible representation is expressed as $\Gamma = 2A_1 + 2E$. The non-degenerate A_1 eigenmodes are linked to vibrations along the z-direction, while the doubly degenerate E phonon modes correspond to in-plane vibrations. As a result, each of these Janus monolayers exhibits four active Raman modes. The wave number corresponding to a specific Raman peak can be calculated using the equation [59]:

$$\omega = \frac{1}{2\pi c} \sqrt{\frac{k}{\mu}} \quad (6.10)$$

where c is the speed of light, k is force constant, and μ represents the reduced mass.

The equation presented above clearly indicates that an increase in reduced mass results in a shift of Raman modes towards lower wave numbers, facilitating the assignment of specific Raman modes. Drawing insights from previously reported Raman spectra of TaS₂ and TaSe₂ [60, 61] it is evident that the E mode exhibits lower energy than the A mode. This observation assists in categorizing the Raman peaks as E and A modes, contingent on the Ta-X/Y bond, where X=S, Se, and Y= N, P (figure 6.7). In the case of TaSN and TaSeN, sharing a common Ta-N bond, the distinctive Raman shift is attributed to the presence of sulfur (S) with a lower mass than selenium (Se), as depicted in figure 6.7(a-b). A similar effect is evident in TaSP and TaSeP (figure (6.7(c-d)) sharing common Ta-P bond, where the differing masses of sulfur and selenium contribute to the observed Raman shift in their respective spectra. Two E modes, characterized by lower and higher wave numbers, and two A_{1g} modes, also exhibiting lower and higher wave numbers, were observed. The lower wave numbers (indicating lower energy) corresponding to the E and A modes are attributed to the Ta-X bond, whereas the higher wave numbers (indicating higher energy) corresponding to E and A modes are attributed to the Ta-Y bonds. The distinct Raman spectra modes associated specific wave numbers, as illustrated in figure 6.7(a-d) for these structures, are provided in Table 6.3. These findings are consistent with previously reported results on WS₂ based Janus monolayers [33].

Table 6.3: Raman Spectra corresponding to two E_g modes (lower energy and higher energy) and two A_{1g} modes (lower energy and higher energy) are presented.

Structures	E_g (lower energy) cm^{-1} (Ta-X)	A_{1g} (lower energy) cm^{-1} (Ta-X)	E_g (higher energy) cm^{-1} (Ta-Y)	A_{1g} (higher energy) cm^{-1} (Ta-Y)
TaSN	239.01	415.08	514.26	632.79
TaSeN	167.04	176.00	483.77	609.34
TaSP	159.28	292.96	331.52	368.93
TaSeP	136.78	246.83	308.91	341.28

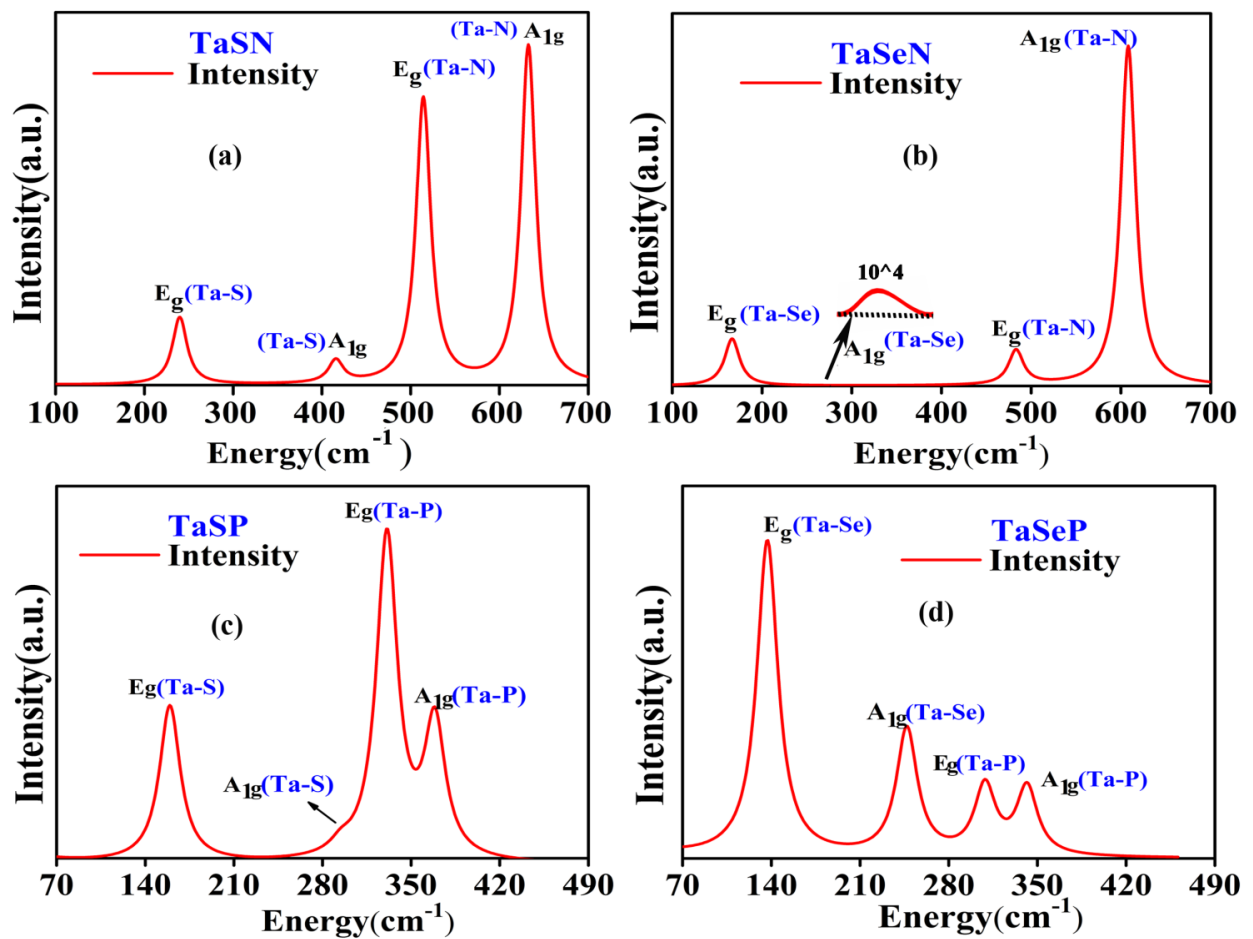


Figure 6.7: (a), (b), (c) & (d) depicting Raman Spectra of TaSN, TaSeN, TaSP & TaSeP respectively.

6.3.5. Thermal Properties:

After conducting phonon spectrum calculations, we observed a rapid variation in the specific heat capacity at constant volume (C_v) with temperature for TaSN, TaSeN, TaSO, TaSeO, TaSP, and TaSeP at low temperatures (below 300 K) (figure 6.8). As the temperature increases, C_v tends to stabilize and approaches a constant value around 600 K, consistent with the Dulong-Petit law observed in bulk structures. In this regime, C_v approximates $3Nk_B$, where N represents the number of atoms in the unit cell, and k_B is the Boltzmann constant. Remarkably, in all nitride, oxide, and phosphide-based Janus materials (TaSN, TaSeN, TaSO, TaSeO, TaSP, TaSeP), there is a conspicuous rise in the specific heat capacity at constant volume (C_v) as the transition occurs from sulfur to selenium, particularly below room temperature. This temperature-dependent pattern implies a unique and discernible behavior in the specific heat capacity of these Janus compounds. The substantial increase in C_v during this transition suggests that selenium plays a significant role in influencing the vibrational modes and thermal properties of these Janus compounds at lower temperatures. For the 2D material C_v is proportional to $T^{(2/n)}$ [33] at low temperatures. Here n values are 1.07, 1.01, 1.06, 1.05, 1.71, 1.29 for TaSN, TaSeN, TaSO, TaSeO, TaSP and TaSeP respectively below 50K (figure 6.8).

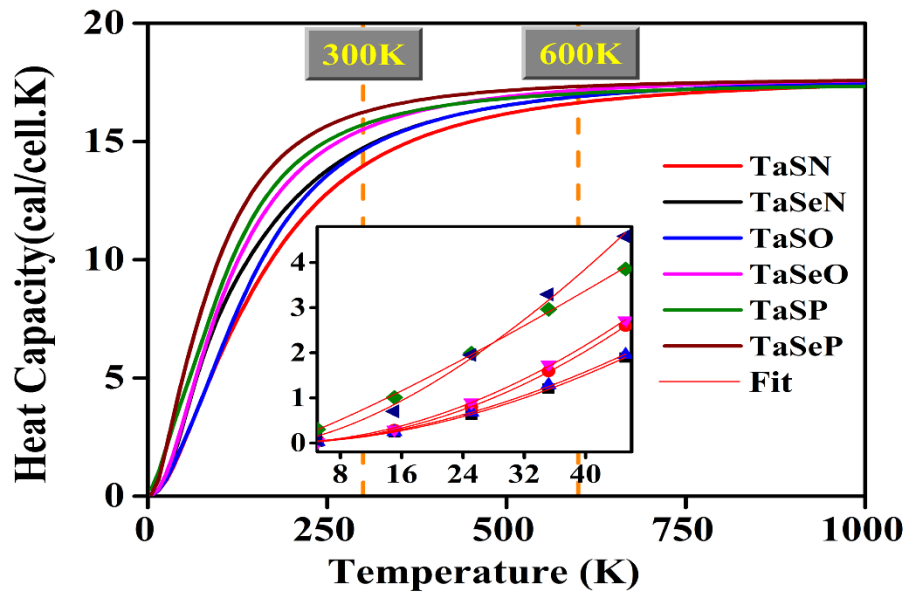


Figure 6.8: Variation of Specific heat capacities at constant volume (C_v) of TaXY monolayers.

6.3.6. Optical Properties:

Complex dielectric function signifies how the material behaves under oscillating electric field at specific frequency and defined by

$$\varepsilon(\omega) = \varepsilon_1(\omega) + i\varepsilon_2(\omega) \quad (6.11)$$

The real ($\varepsilon_1(\omega)$) and imaginary ($\varepsilon_2(\omega)$) components of the dielectric functions are connected through the widely recognized Kramer–Kronig relation [62], expressed as follows:

$$\varepsilon_2(\omega) = \frac{Ve^2}{2m^2\omega^2} \sum_{ij} \int k_i |p| k_j^2 f(k_i) (1 - f(k_j)) \delta(E_{k_i} - E_{k_j} - \omega) d^3k \quad (6.12)$$

$$\varepsilon_1(\omega) = 1 + \frac{2}{\pi} P \int_0^\infty \frac{\omega' \varepsilon_2(\omega')}{\omega'^2 - \omega^2} d\omega' \quad (6.13)$$

The real ($n(\omega)$) and imaginary ($k(\omega)$) part of refractive index, Conductivity($\sigma(\omega)$) absorption($\alpha(\omega)$), reflectivity ($R(\omega)$) and loss function($L(\omega)$) [62] were calculated using following equations

$$n(\omega) = \sqrt{\frac{\sqrt{\varepsilon_1^2(\omega) + \varepsilon_2^2(\omega)} + \varepsilon_1(\omega)}{2}} \quad (6.14)$$

$$k(\omega) = \sqrt{\frac{\sqrt{\varepsilon_1^2(\omega) + \varepsilon_2^2(\omega)} - \varepsilon_1(\omega)}{2}} \quad (6.15)$$

$$\sigma(\omega) = \sigma_r(\omega) + \sigma_i(\omega) = -i \frac{\omega}{4\pi} (\varepsilon(\omega) - 1) \quad (6.16)$$

$$\alpha(\omega) = \frac{\omega}{c} \sqrt{2(\sqrt{\varepsilon_1^2(\omega) + \varepsilon_2^2(\omega)} - \varepsilon_1(\omega))} \quad (6.17)$$

$$R(\omega) = \frac{\sqrt{\varepsilon(\omega)} + 1}{\sqrt{\varepsilon(\omega)} - 1} \quad (6.18)$$

$$L(\omega) = \frac{\varepsilon_2(\omega)}{\varepsilon_1(\omega) + \varepsilon_2(\omega)} \quad (6.19)$$

Imaginary part $\varepsilon_2(\omega)$ is related to absorption phenomena. It signifies the extent to which the material absorbs and dissipates energy in the form of heat during exposure to the oscillating electric field. The real part, $\varepsilon_1(\omega)$, characterizes the material's polarization behavior. It reflects the ability of the material to store electrical energy as a result of charge displacement in response to the applied electric field. Static dielectric constant $\varepsilon(0)$ can be obtained when $\omega \rightarrow$

0. Static dielectric constant obtained for TaSO, TaSN, TaSP, TaSeO, TaSeN and TaSeP are 3.53, 6.24, 15.29, 4.10, 8.54 and 12.46 respectively (figure 6.9(a)). The higher static dielectric constant values for TaSP (15.29) and TaSeP (12.46) suggest that these compounds have a greater ability to store electrical energy in comparison to the others listed. This could make TaSP and TaSeP potentially suitable for capacitor applications, where a high dielectric constant is desirable to increase the capacitance of the capacitor. $\epsilon_2(\omega)$ becomes zero when the incident photon energy less than 0.7eV for TaSO and TaSeO. Furthermore, it is noteworthy that the imaginary part of the dielectric constant, $\epsilon_2(\omega)$, approaches zero around 20 eV of incident photon energy for all six Janus materials (figure 6.9(b)). This characteristic indicates low absorption in this energy range, rendering these materials transparent. Refractive index of above six janus material is described by $n(\omega) = n_r(\omega) + n_i(\omega)$, where $n_r(\omega)$ and $n_i(\omega)$ is the real part and the imaginary part of refractive index respectively. Static refractive index $n_r(\omega)$ for TaSO, TaSN, TaSP, TaSeO, TaSeN and TaSeP are 1.88, 2.49, 3.91, 2.04, 2.92, 3.52 respectively (figure 6.9(e) & 6.9(f)). Imaginary part is basically attenuation or absorption of the electromagnetic wave. The optical conductivity, denoted as $\sigma(\omega) = \sigma_r(\omega) + \sigma_i(\omega)$, comprises a real part ($\sigma_r(\omega)$) and an imaginary part ($\sigma_i(\omega)$) (figure 6.9(c) & 6.9(d)). Among the Janus materials considered, the highest values of the real part of conductivity are consistently observed in the ultraviolet (UV) region. Notably, TaSO and TaSeO exhibit the most prominent peaks, reaching a maximum value in the UV region. This underscores their exceptional ability to conduct light at specific frequencies within the UV spectrum. The absorption peaks for all the structures are predominantly located in the ultraviolet (UV) region (figure 6.10(a)). Notably, TaSP and TaSeP exhibit prominent absorption peaks in the lower energy range of visible light or even extending into the infrared (IR) region. Energy loss function is found to be maximum in between 12eV to 18eV in the UV region (figure 6.10(b)). Regarding reflectivity, diverse peaks are observed across all materials. In the low-energy region ($\omega \rightarrow 0$), TaSP and TaSeP exhibit maximum reflection, while TaSO and TaSeO display minimum reflection (figure 6.10(c)). This variation in reflectivity suggests distinct optical properties and behaviors among the different materials, particularly in response to low-energy light or radiation.

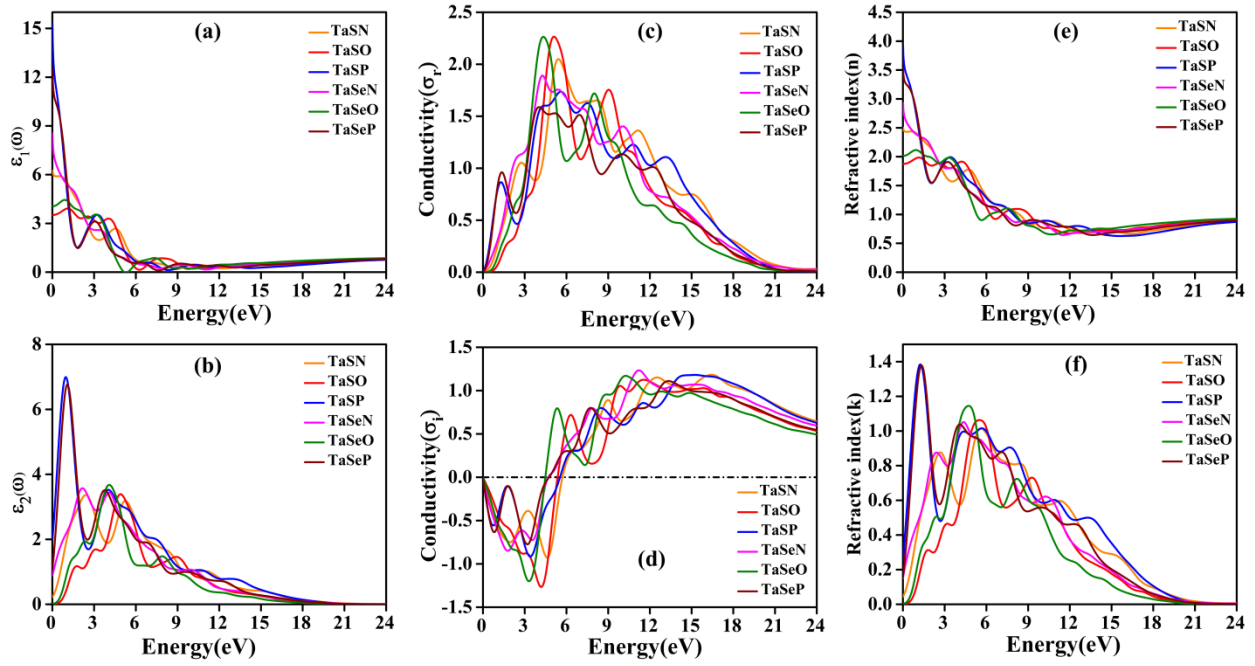


Figure 6.9: real and imaginary part of dielectric function ((a), (b)), optical conductivity ((c), (d)), real and imaginary part of refractive index ((e), (f)).

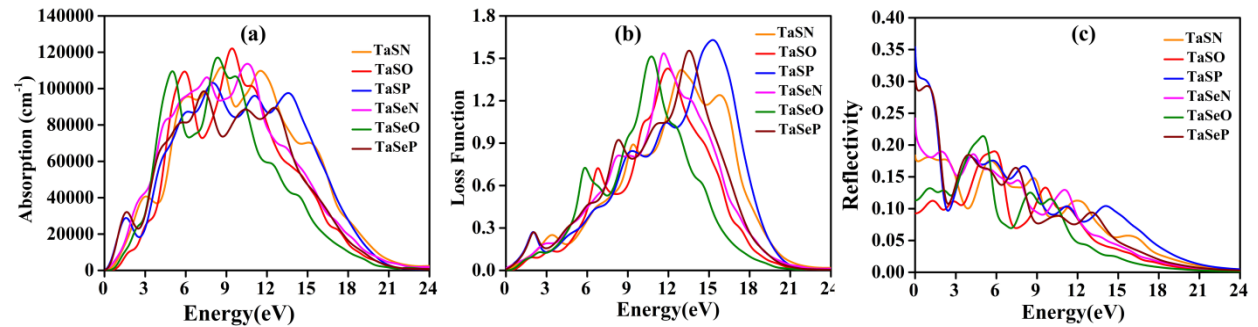


Figure 6.10: (a), (b) & (c) represents Absorption, Loss Function, Reflectivity.

6.4. Conclusion:

Our First principles analysis based on density functional theory (DFT) for TaXY monolayers has unveiled their stability and inherent physical properties. These Janus monolayers exhibit thermodynamic stability, as indicated by positive cohesive energy values. Among them, TaSN stands out with the highest cohesive energy (7.60 eV/atom), suggesting robust bonding between constituent atoms, whereas TaSeP displays relatively weaker bonding with lowest cohesive energy value (5.43 eV/atom). While TaXO monolayers lack mechanical stability, both TaXN and TaXP monolayers demonstrate mechanical stability. Phonon dispersion curves indicate that TaXO and TaXN monolayers are dynamically stable, whereas TaXP monolayers exhibit dynamical instability with imaginary frequencies. The observed dynamical and

mechanical stability of TaXN monolayers has prompted further investigation into their lattice thermal conductivity. The ultra-low lattice thermal conductivity of TaSeN (0.38 W/mK) compared to TaSN (29.71 W/mK) positions it as a promising candidate for applications requiring low thermal conduction. Examining the electronic band structure, we find that TaXO monolayers exhibit metallic behavior, while the remaining monolayers behave as semiconductors. Specifically, TaSN and TaSeN are identified as indirect band gap semiconductors, while TaSP and TaSeP are categorized as direct band gap semiconductors. Moreover, the predicted band gap of TaSN Janus material is 1.42 eV which is ideal for photovoltaic application as we know that Solar spectrum peak is at 1.4 eV. The Raman Effect was observed in semiconducting TaXN and TaXP monolayers, except for TaXO monolayers, which hinder its occurrence due to their metallic characteristics. Our computations reveal the optical characteristics of TaXY monolayers, offering insights into the potential use of these Janus materials in upcoming optoelectronic devices.

References:

- [1] Novoselov, Kostya S., et al. "Electric field effect in atomically thin carbon films." *science* 306.5696 (2004): 666-669.
- [2] Chang, Haixin, and Hongkai Wu. "Graphene-based nanomaterials: Synthesis, properties, and optical and optoelectronic applications." *Advanced Functional Materials* 23.16 (2013): 1984-1997.
- [3] Ponraj, Joice Sophia, et al. "Photonics and optoelectronics of two-dimensional materials beyond graphene." *Nanotechnology* 27.46 (2016): 462001.
- [4] Kara, Abdelkader, et al. "A review on silicene—new candidate for electronics." *Surface science reports* 67.1 (2012): 1-18.
- [5] Acun, Adil, et al. "Germanene: the germanium analogue of graphene." *Journal of physics: Condensed matter* 27.44 (2015): 443002.
- [6] Zhu, Feng-feng, et al. "Epitaxial growth of two-dimensional stanene." *Nature materials* 14.10 (2015): 1020-1025.
- [7] Gogotsi, Yury, and Babak Anasori. "The rise of MXenes." *ACS nano* 13.8 (2019): 8491-8494.
- [8] Banerjee, Anibrata, Bikram Kumar Das, and Kalyan Kumar Chattopadhyay. "Significant enhancement of lattice thermal conductivity of monolayer AlN under bi-axial strain: a first principles study." *Physical Chemistry Chemical Physics* 24.26 (2022): 16065-16074.
- [9] Choi, Wonbong, et al. "Recent development of two-dimensional transition metal dichalcogenides and their applications." *Materials Today* 20.3 (2017): 116-130.
- [10] Cong, Chunxiao, et al. "Optical properties of 2D semiconductor WS₂." *Advanced Optical Materials* 6.1 (2018): 1700767.
- [11] Mohammed, Mohammed H., Ahmed S. Al-Asadi, and Falah H. Hanoon. "Semi-metallic bilayer MS₂ (M= W, Mo) induced by Boron, Carbon, and Nitrogen impurities." *Solid State Communications* 282 (2018): 28-32.
- [12] Lian, Chao-Sheng, Chen Si, and Wenhui Duan. "Anisotropic full-Gap superconductivity in 2M-WS₂ topological metal with intrinsic proximity effect." *Nano Letters* 21.1 (2020): 709-715.
- [13] Luo, Zhaoyan, et al. "Band Engineering Induced Conducting 2H-Phase MoS₂ by Pd-S-Re Sites Modification for Hydrogen Evolution Reaction." *Advanced Energy Materials* 12.12 (2022): 2103823.
- [14] Tang, Qing, and De-en Jiang. "Mechanism of hydrogen evolution reaction on 1T-MoS₂ from first principles." *Acs Catalysis* 6.8 (2016): 4953-4961.

- [15] Das, Arnab, Bikram Kumar Das, and K. K. Chattopadhyay. "Coinage metals doped 1T' WS₂ as efficient bifunctional electrocatalyst towards ORR and HER: A first principles study." *Computational Materials Science* 229 (2023): 112418.
- [16] Terrones, H., and M. Terrones. "Electronic and vibrational properties of defective transition metal dichalcogenide Haeckelites: new 2D semi-metallic systems." *2D Materials* 1.1 (2014): 011003.
- [17] Chen, Wenzhou, et al. "Electronic, magnetic, catalytic, and electrochemical properties of two-dimensional Janus transition metal chalcogenides." *Journal of Materials Chemistry A* 6.17 (2018): 8021-8029.
- [18] Babariya, Bindia, Sanjeev K. Gupta, and P. N. Gajjar. "Theoretical designing of TMDs Janus heterostructures toward efficient photovoltaic and electronic applications." *Surfaces and Interfaces* 42 (2023): 103409.
- [19] Yang, Xiaoyong, et al. "An emerging Janus MoSeTe material for potential applications in optoelectronic devices." *Journal of Materials Chemistry C* 7.39 (2019): 12312-12320.
- [20] Gao, Hui, et al. "Tuning electrical conductance of MoS₂ monolayers through substitutional doping." *Nano Letters* 20.6 (2020): 4095-4101.
- [21] Kuraganti, Vasu, et al. "Manganese doping of MoSe₂ promotes active defect sites for hydrogen evolution." *ACS applied materials & interfaces* 11.28 (2019): 25155-25162.
- [22] Das, Arnab, et al. "Zinc doping induced WS₂ accelerating the HER and ORR kinetics: a theoretical and experimental validation." *Catalysis Today* 423 (2023): 113921.
- [23] Tosun, Mahmut, et al. "Air-stable n-doping of WSe₂ by anion vacancy formation with mild plasma treatment." *ACS nano* 10.7 (2016): 6853-6860.
- [24] Cheng, Y. C., et al. "Spin-orbit-induced spin splittings in polar transition metal dichalcogenide monolayers." *Europhysics Letters* 102.5 (2013): 57001.
- [25] Trivedi, Dipesh B., et al. "Room-temperature synthesis of 2D Janus crystals and their heterostructures." *Advanced materials* 32.50 (2020): 2006320.
- [26] Qin, Ying, et al. "Reaching the excitonic limit in 2D Janus monolayers by in situ deterministic growth." *Advanced Materials* 34.6 (2022): 2106222.
- [27] Smith, N. V., S. D. Kevan, and F. J. DiSalvo. "Band structures of the layer compounds 1T-TaS₂ and 2H-TaSe₂ in the presence of commensurate charge-density waves." *Journal of Physics C: Solid State Physics* 18.16 (1985): 3175.
- [28] Zhang, Lei, et al. "Recent advances in emerging Janus two-dimensional materials: from fundamental physics to device applications." *Journal of materials chemistry A* 8.18 (2020): 8813-8830.

- [29] Navarro-Moratalla, Efrén, et al. "Enhanced superconductivity in atomically thin TaS₂." *Nature communications* 7.1 (2016): 11043.
- [30] Kahraman, Zeynep, et al. "Stable Janus TaSe₂ single-layers via surface functionalization." *Applied Surface Science* 538 (2021): 148064.
- [31] Shi, Wenwu, and Zhiguo Wang. "Mechanical and electronic properties of Janus monolayer transition metal dichalcogenides." *Journal of Physics: Condensed Matter* 30.21 (2018): 215301.
- [32] Falahati, Kiana, Ali Khatibi, and Babak Shokri. "Light-matter interaction in tungsten Sulfide-based Janus monolayers: A First-Principles study." *Applied Surface Science* 599 (2022): 153967.
- [33] Varjovi, M. Jahangirzadeh, et al. "Janus two-dimensional transition metal dichalcogenide oxides: first-principles investigation of W X O monolayers with X= S, Se, and Te." *Physical Review B* 103.19 (2021): 195438.
- [34] Segall, M. D., et al. "First-principles simulation: ideas, illustrations and the CASTEP code." *Journal of physics: condensed matter* 14.11 (2002): 2717.
- [35] Perdew, John P., Kieron Burke, and Matthias Ernzerhof. "Generalized gradient approximation made simple." *Physical review letters* 77.18 (1996): 3865.
- [36] Vanderbilt, David. "Soft self-consistent pseudopotentials in a generalized eigenvalue formalism." *Physical review B* 41.11 (1990): 7892.
- [37] Pfrommer, Bernd G., et al. "Relaxation of crystals with the quasi-Newton method." *Journal of Computational Physics* 131.1 (1997): 233-240.
- [38] Pack, James D., and Hendrik J. Monkhorst. "" Special points for Brillouin-zone integrations"—a reply." *Physical Review B* 16.4 (1977): 1748.
- [39] Wang, Vei, et al. "VASPKIT: A user-friendly interface facilitating high-throughput computing and analysis using VASP code." *Computer Physics Communications* 267 (2021): 108033.
- [40] Kresse, Georg, and Jürgen Hafner. "Ab initio molecular dynamics for liquid metals." *Physical review B* 47.1 (1993): 558.
- [41] Kresse, Georg, and Jürgen Furthmüller. "Efficiency of ab-initio total energy calculations for metals and semiconductors using a plane-wave basis set." *Computational materials science* 6.1 (1996): 15-50.
- [42] Kresse, Georg, and J. J. P. R. B. Hafner. "Ab initio molecular dynamics for open-shell transition metals." *Physical Review B* 48.17 (1993): 13115.
- [43] Du, Yanlan, et al. "Ab initio studies on atomic and electronic structures of black phosphorus." *Journal of Applied Physics* 107.9 (2010).

- [44] Hafner, Jürgen. "Ab-initio simulations of materials using VASP: Density-functional theory and beyond." *Journal of computational chemistry* 29.13 (2008): 2044-2078.
- [45] Li, Yan, Chunying Pu, and Dawei Zhou. "Structure, Stability, and Superconductivity of Two-Dimensional Janus NbSH Monolayers: A First-Principle Investigation." *Molecules* 28.14 (2023): 5522.
- [46] Vajeeston, Ponniah, and Helmer Fjellvåg. "First-principles study of structural stability, dynamical and mechanical properties of Li₂FeSiO₄ polymorphs." *RSC advances* 7.27 (2017): 16843-16853.
- [47] Gu, Xiaokun, et al. "Colloquium: Phononic thermal properties of two-dimensional materials." *Reviews of Modern Physics* 90.4 (2018): 041002.
- [48] Peng, Bo, et al. "Phonon transport properties of two-dimensional group-IV materials from ab initio calculations." *Physical Review B* 94.24 (2016): 245420.
- [49] Bolen, E., E. Deligoz, and H. Ozisik. "Origin of low thermal conductivity in monolayer PbI₂." *Solid State Communications* 327 (2021): 114223.
- [50] Asen-Palmer, M., et al. "Thermal conductivity of germanium crystals with different isotopic compositions." *Physical review B* 56.15 (1997): 9431.
- [51] Zhang, Yongsheng. "First-principles Debye–Callaway approach to lattice thermal conductivity." *Journal of Materiomics* 2.3 (2016): 237-247.
- [52] Fan, Tao, and Artem R. Oganov. "AICON: A program for calculating thermal conductivity quickly and accurately." *Computer Physics Communications* 251 (2020): 107074.
- [53] Fan, Tao, and Artem R. Oganov. "AICON2: A program for calculating transport properties quickly and accurately." *Computer Physics Communications* 266 (2021): 108027.
- [54] Wang, Fancy Qian, et al. "Lattice thermal conductivity of penta-graphene." *Carbon* 105 (2016): 424-429.
- [55] Togo, Atsushi. "First-principles phonon calculations with phonopy and phono3py." *Journal of the Physical Society of Japan* 92.1 (2023): 012001.
- [56] Dabsamut, Klichchupong, et al. "Strain engineering and thermal conductivity of a penta-BCN monolayer: a computational study." *Journal of Physics D: Applied Physics* 54.35 (2021): 355301.
- [57] Li, Qingfang, et al. "Intrinsically low lattice thermal conductivity in layered Mn₃Si₂Te₆." *New Journal of Physics* 25.10 (2023): 103020.
- [58] Ji, Yupin, et al. "The intrinsically low lattice thermal conductivity of monolayer T-Au₆X₂ (X= S, Se and Te)." *Physical Chemistry Chemical Physics* 25.46 (2023): 31781-31790.

- [59] Bhattacharjee, Souvik, and Kalyan Kumar Chattopadhyay. "Laser-induced Fano asymmetry, electron-phonon coupling, and phase transition in lanthanide sesquioxide (Ln_2O_3 ; $\text{Ln} = \text{Eu}, \text{Gd}, \text{Dy}$) nanoparticles: A Raman spectroscopic investigation." *Journal of Applied Physics* 132.21 (2022).
- [60] Hajiyeve, Parviz, et al. "Contrast and Raman spectroscopy study of single-and few-layered charge density wave material: 2H-TaSe_2 ." *Scientific reports* 3.1 (2013): 1-6.
- [61] Valencia-Ibáñez, Santiago, et al. "Raman Spectroscopy of Few-Layers TaS_2 and Mo-Doped TaS_2 with Enhanced Superconductivity." *Advanced Electronic Materials* 8.10 (2022): 2200457.
- [62] Arif Khalil, R. M., et al. "First-principles simulation of structural, electronic and optical properties of cerium trisulfide (Ce_2S_3) compound." *Journal of Electronic Materials* 50 (2021): 1637-1643.

7. Grand conclusions and scopes for future works

7.1. Summary of the present study:

Fuel cells hold tremendous promise as a sustainable alternative energy source for the future.

However, their widespread adoption is hindered by the lack of efficient and cost-effective cathode materials capable of catalyzing the oxygen reduction reaction (ORR). Recent research has increasingly focused on predicting stable forms of acetylene-bonded all-carbon two-dimensional (2D) networks, such as transition metal chalcogenides (TMDs) and their Janus forms, due to their unique properties. Transition metal chalcogenides offer several advantages as electrocatalysts for ORR. Their inherent non-uniform charge distribution and the presence of multiple highly asymmetric metal and non-metal sites make them promising candidates for substitutional doping with various elements, enhancing their catalytic activity. The successful synthesis of different phases of TMDs, including 2H, 1T, and 1T', has further spurred research into their application as electrocatalysts for both ORR and the hydrogen evolution reaction (HER). This study aims to theoretically investigate the electrocatalytic properties of the most stable phases of TMDs and their analogous systems towards ORR and HER, leveraging the potential of transition metal doping. The prospects of utilizing TMDs as confined electrocatalysts for ORR and HER will be explored, offering insights into their practical applicability in fuel cell technology. Moreover, the research also endeavors to discover new Janus forms of tantalum disulfide (TaS_2) and tantalum diselenide (TaSe_2). These materials hold significance not only for their potential in optoelectronics and solar applications but also for catalytic processes, further expanding the scope of their practical utility in various fields. The followings emerged as the notable conclusions from the detailed theoretical studies described in the chapters 4-6 of this thesis:

1. Doping coinage metals such as Cu, Ag, and Au onto the metastable phase 1T' WS_2 emerges as a promising strategy for fabricating cathode materials capable of bifunctional activity, serving both the oxygen reduction reaction (ORR) and the hydrogen evolution reaction (HER) in fuel cell applications. Insights from ab-initio molecular dynamics simulations (AIMD) suggest that the doped structures exhibit notable thermal stability. Moreover, the transfer of charge from the dopant to neighboring atoms significantly enhances the stability of these modified structures. Noteworthy observations reveal higher formation energy and augmented charge transfer within these structures. Additionally, sulfur atoms positioned between wider

tungsten atoms within the 1T' WS₂ phase demonstrate a more favorable energetic disposition for doping compared to those located between narrower tungsten atoms, thereby amplifying the viability of this strategy.

2. The adsorption of oxygen atoms onto doped structures reveals a significant increase in charge transfer, primarily localized at the dopant sites, which holds significant importance in the oxygen reduction reaction (ORR). Our investigation highlights that oxygen adsorption, facilitated through an associative pathway at the dopant site, determines whether the ORR proceeds via a two-electron or four-electron pathway. Notably, pronounced bond stretching or breakage can hinder the two-electron pathway, thereby preventing the formation of toxic H₂O₂ as a byproduct and favoring the exclusive occurrence of the four-electron pathway. These findings emphasize the correlation between increased bond stretching and heightened charge transfer, underscoring their pivotal role in facilitating the ORR process. Among the coinage metals, copper (Cu) doping in 1T' WS₂ demonstrates the most promising bifunctional activity, particularly by favoring the four-electron pathway during the ORR and exhibiting low Gibbs free energy values for the hydrogen evolution reaction (HER) in acidic medium. The lower Gibbs free energy values for doped structures, especially Cu, compared to platinum atoms, were elucidated through an analysis of bonding and antibonding states near the Fermi energy, as obtained from Crystal Orbital Hamiltonian Population (COHP) analysis.
3. The catalytic activity of WS₂ with various transition metals has been extensively studied, but there has been limited exploration regarding doping with different percentages of zinc (Zn). In our research, we conducted theoretical evaluations of the hydrogen evolution reaction (HER) activity, which demonstrated lower overpotential compared to pristine WS₂ when doped with varying percentages of Zn. Similarly, in the case of the oxygen reduction reaction (ORR) under alkaline conditions, low overpotential was observed with low percentage doping of Zn in WS₂. These findings were further validated experimentally in our study.
4. The assessment of the d-band center across various doping percentages provided insight into the catalytic behavior of Zn-doped surfaces. Particularly, when incorporating low concentrations of Zn into WS₂, we observed the rupture of the O-O bond during oxygen molecule adsorption, leading to the highest oxygen adsorption energy. Furthermore, a significant charge transfer was evident between oxygen atoms and sulfur atoms, especially those bonded to the oxygen atoms. These findings indicate that doping WS₂

with metallic elements like Zn activates the sulfur atoms on the upper surface of the WS₂ structure, resembling a sandwich-like configuration with tungsten atoms positioned between sulfur atoms.

5. Janus forms of TaS₂ and TaSe₂ were synthesized by substituting sulfur (S) or selenium (Se) atoms with oxygen (O) and pnictogen atoms like nitrogen (N) and phosphorus (P), resulting in the formation of TaXY monolayers (TaSO, TaSeO, TaSN, TaSeN, TaSP, TaSeP). Stability analysis of these monolayers yielded intriguing results. Specifically, TaXO monolayers demonstrated dynamic stability but were elastically unstable. Conversely, TaXP monolayers exhibited elastic stability but were dynamically unstable in nature. Among these Janus monolayers, TaXN garnered significant attention due to its mechanical and dynamic stability, establishing it as a promising candidate for further investigation. Subsequently, lattice thermal conductivity calculations were performed for TaXN monolayers to assess their capability in conducting heat. Additionally specific heat capacities and their variations with low to high temperatures were also studied for these Janus monolayers.
6. The electronic properties of these Janus monolayers are indeed intriguing, as they undergo a transformation from the inherently metallic nature of TaS₂ and TaSe₂ to semiconductors upon the introduction of pnictogen atoms like nitrogen and phosphorus. This transformation gives rise to TaXN and TaXP monolayers. Of particular interest is the band gap of TaSN, which is approximately 1.42 eV, closely matching the peak solar energy of 1.40 eV. This alignment suggests promising applications in solar energy harvesting and conversion technologies. Moreover, the comprehensive examination of electronic properties, vibrational characteristics including Raman spectra, lattice thermal conductivity, and optical properties highlights the potential applications of TaXY monolayers in optoelectronics.

7.2. Scopes for future works:

With the advancement of experimental techniques, laboratories can now routinely synthesize various phases of transition metal dichalcogenides (TMDs), including the metastable 1T' phase. Both pristine and doped TMDs monolayers, across different phases, have already demonstrated their utility as electrocatalysts for the oxygen reduction reaction (ORR) and hydrogen evolution reaction (HER) in both acidic and alkaline media, showcasing promising results. The findings presented in this thesis undeniably serve as inspiration for the synthesis of promising materials,

such as transition metal-doped 1T' WS₂ and Janus monolayers based on TaS₂ and TaSe₂. The 1T' phases of TMDs monolayers hold considerable potential for application as cathode electrocatalysts in fuel cells, especially in acidic mediums, primarily for HER, owing to their low overpotential comparable to Pt cathodes. Similarly, the 2H phase of WS₂ can be harnessed through transition metal doping in various catalytic reactions, including the nitrogen reduction reaction (NRR), oxygen evolution reaction (OER), CO₂ reduction, and more. Moreover, Janus forms of TMDs have received comparatively less attention both experimentally and theoretically. Thus, there exists significant scope for researchers to explore and discover new Janus forms of TMDs through computational studies and experimental synthesis. Over the past decade, numerous stable forms of TMDs monolayers with exotic properties have been theoretically predicted, with many already synthesized experimentally. The potential for surface modification of these TMDs monolayers and their application as electrocatalysts for ORR, HER, and other crucial reactions, through theoretical or experimental approaches, could potentially mark the dawn of a new era in electrocatalysis based on TMDs.

Appendix

Abbreviations/ Symbols used in the thesis

Abbreviation	Expansion
1/ 2/ 3 D	One/ two/ three dimension(al)
AFC	Alkaline fuel cell
AFM	Atomic force microscope
AIREBO	Adaptive intermolecular reactive bond order
B	Boron
B3LYP	Becke, 3-parameter, Lee–Yang–Parr
C	Carbon
CASTEP	CAMbridge Serial Total Energy Package
CBM	Conduction band minimum
CNT	Carbon nano tube
COHP	Crystal Orbital Hamilton Populations
DBA	Dehydrobenzoannulenes
DFT	Density functional theory
DFT + U	DFT with Hubbard U correction
DMFC	Direct methanol fuel cell
DOS	Density of states
E_{ads}	Adsorption energy
E_b	Activation barrier
E_{ads}^{do}	Di-oxygen adsorption energy
E_F	Fermi energy
E_{for}	Formation energy
EDS	Energy dispersive X-ray spectroscopy
ELF	Electron localization function
ER	Eiley-Rideal
F_{HK}	Hohenberg-Kohn functional
FS	Final state
GCMC	Grand canonical ensemble Monte Carlo method
GDP	Gross domestic product
Gdy	Graphdiyne
GGA	Generalized gradient approximation
GKS	Generalized Kohn-Sham
Gy	Graphyne
\hat{H}	Hamiltonian operator
h-BN	Hexagonal boron nitride
HER	Hydrogen evolution reaction

Abbreviation	Expansion
HF	Hartree-Fock
HOMO	Highest occupied molecular orbital
HOR	Hydrogen oxidation reaction
HPC	High-performance computing
HSE	Heyd–Scuseria–Ernzerhof
ICOHP	Integrated crystal Orbital Hamilton Populations
IS	Initial state
LDA	Local density approximation
LH	Langmuire-Hinshelwood
LUMO	Lowest unoccupied molecular orbital
MCFC	Molten Carbonate fuel cell
MD	Molecular dynamics
MO	Molecular orbital
N	Nitrogen
NM	Noble metal
OER	Oxygen evolution reaction
ORR	Oxygen reduction reaction
PAFC	Phosphoric acid fuel cell
PAW	Projector augmented wave
PBE	Perdew–Burke–Ernzerhof
PBE + D2	PBE functional with Grimme’s dispersive force correction
pCOHP	Projected crystal Orbital Hamilton Populations
PDOS	Projected density of states
PEMFC	Polymer Electrolyte Membrane fuel cell
PGM	Platinum group metal
PW	Plane wave approximation
PW _{scf}	Plane-wave self-consistent field
RHE	Reversible hydrogen electrode
RPA	Random phase approximation
SCAN	Strongly Constrained and Appropriately Normed
SCF	Self-consistent field
SHE	Standard hydrogen electrode
SOFC	Solid oxide fuel cell
TDOS	Total density of states
TEM	Transmission electron microscopy
TM	Transition metal
TMD	Transition metal di-chalcogenide

Abbreviation

TPSS

TST

U

VASP

VBM

vdW

XC

XPS

ZPE

ZT

 η μ χ ψ **Expansion**

Tao-Perdew-Staroverov-Scuseria

Transition state theory

Electrode potential

Vienna *ab-initio* simulation package

Valence band maximum

Van der Waals interaction

Exchange-correlation

X-ray photoelectron spectroscopy

Zero-point energy

Thermoelectric figure of merit

Overpotential

Chemical potential

Electronegativity

Wave function

PhD Thesis

ORIGINALITY REPORT

3%

SIMILARITY INDEX

PRIMARY SOURCES

1	Jinmei Qian, Tongtong Wang, Baorui Xia, Pinxian Xi, Daqiang Gao. "Zn-doped MoSe2 nanosheets as high-performance electrocatalysts for hydrogen evolution reaction in acid media", Electrochimica Acta, 2019	334 words — 1%
2	Bikram Kumar Das, Dipayan Sen, K.K. Chattopadhyay. "Nitrogen doping in acetylene bonded two dimensional carbon crystals: Ab-initio forecast of electrocatalytic activities vis-à-vis boron doping", Carbon, 2016	310 words — 1%
3	pubs.rsc.org	258 words — 1%
4	www.co.bonner.id.us	207 words — 1%

EXCLUDE QUOTES ON
EXCLUDE BIBLIOGRAPHY ON

EXCLUDE SOURCES < 1%
EXCLUDE MATCHES < 10 WORDS